

UNIVERSITY OF BIRMINGHAM

LEAKY WAVE ANTENNAS FOR REMOTE VITAL SIGNS MONITORING AT MM-WAVE FREQUENCIES

by

SOLOMON MINGLE

A thesis submitted to the University of Birmingham for the degree of DOCTOR OF PHILOSOPHY

School of Electronic, Electrical and Systems Engineering

College of Engineering and Physical Sciences

University of Birmingham

December 2022

UNIVERSITY OF
BIRMINGHAM

University of Birmingham Research Archive

e-theses repository

This unpublished thesis/dissertation is copyright of the author and/or third parties. The intellectual property rights of the author or third parties in respect of this work are as defined by The Copyright Designs and Patents Act 1988 or as modified by any successor legislation.

Any use made of information contained in this thesis/dissertation must be in accordance with that legislation and must be properly acknowledged. Further distribution or reproduction in any format is prohibited without the permission of the copyright holder.

Abstract

In this thesis, a novel leaky wave antennas (LWAs) of the Fabry-Perot type (FP) with significantly improved gain and beam scanning capabilities based on periodic metasurfaces for remote vital sign monitoring (RVSM) in the millimetre waveband (50 – 68 GHz) are presented. The LWA design technique presented overcomes the difficulties associated with the fabrication and implementation of traditional designs for millimetre-wave antennas. This technique uses a simple feed between a partially reflective surface (PRS) and a high impedance surface (HIS) to achieve a leaky wave and beam scanning effect for RVSM. Periodic arrays, also known as frequency selective surfaces (FSS) due to their filtering capabilities, were used to determine partial reflections. First, a theoretical approximate model was used to gain an understanding of the physical behaviour of the antenna. The reflection characteristics of PRS and HIS determined using plane wave modal analysis were related to the performance of the antenna. The findings of this study served as guidelines for the development of single and double-layer array designs optimised for both high gain and beam scanning performance. An experimental study on RVSM was conducted using the proposed LWAs and compared with a conventional contact device to verify the accuracy of the results. It was found that the proposed LWAs can detect heart rate and breathing rate with 93% accuracy, which is a good match with the contact device. This research work has contributed to the current knowledge on (i) the design and testing of LWAs with and without HIS configuration to achieve high gains of 20 dBi and 22 dBi for short (1 m) and long (2 m) distances RVSM, (ii) the design of multilayer LWAs with improved bandwidth (8 GHz) and higher gain (24 dBi) for RVSM at 4 m, and (iii) the design and testing of bidirectional LWAs based on dielectric image lines with a gain of 19 dBi and 70^{o} beam scanning through the broadside for single and multiple target RVSM at 1.5 m. The above contributions and findings of the proposed LWAs for RVSM have been published.

To my family especially my wife Mrs Ellen Mingle,

Acknowledgements

I thank my thesis advisor, Prof. Alexandros Feresidis, for his guidance and support during my studies.

Dr Despoina Kampouridou, Dr Muhammad Saqib Rabbani, and senior technician Alan Yates helped me develop my journals, test, and measure RVSM at millimetre wave frequencies, and prototype my antennas. I am grateful for their support.

Publications List

Journal papers:

1. **S. Mingle**, D. Kampouridou and A. Feresidis, "Bidirectional Leaky-Wave Antenna Based on Dielectric Image-Line for Remote Vital Sign Detection at Mm-Wave Frequencies," in *IEEE Open Journal of Antennas and Propagation*, 2022, DOI: 10.1109/OJAP.2022.3201630.
2. **S. Mingle**, D. Kampouridou and A. Feresidis. "Multi-Layer Beam Scanning Leaky Wave Antenna for Remote Vital Signs Detection at 60 GHz" *Sensors 23*, no. 8 (2023): 4059. https://doi.org/10.3390/s23084059.

International conferences:

1. **S. Mingle**, A. P. Feresidis, and K. Despoina, "Beam-Scanning Leaky-Wave Antenna Based on Dielectric Image-Line for Millimetre-Wave Applications", *51st European Microwave Week on Antennas and Propagation*, Excel London, UK, Feb. 13-18, 2022.
2. **S. Mingle**, A. P. Feresidis and S. R. Muhammad, "A Fabry-Pérot Multilayer High Gain Frequency Scanning LWA at 60GHz",16*th European Conference on Antennas and Propagation*, Madrid, Spain, Apr. 7-1, 2022.
3. **S. Mingle**, "Frequency Scannable Leaky-Wave Antenna Design for Remote Vital Signs Radar Application at 60GHz Band". In *2021 International Conference on Electrical, Communication, and Computer Engineering (ICECCE)* (pp. 1-4). IEEE.

Table Of Contents

Abstract ii

Acknowledgements iv

Publications List v

Table Of Contents vi

Chapter 1: Introduction 1

1.1 Background 1

1.1.1 Leaky Wave Antenna Design Structures 1

1.1.2 Periodic Structures 3

1.1.3 Gain Improvement For Doppler Radar At Mm-Wave Frequencies 7

1.2 Motivation And Objectives 9

1.3 Contributions 10

1.3.1 LWA Designs And RVSM Measurements At 60 GHz Bands 10

1.3.2 Gain Improvement Based On Multilayer LWA At 60 GHz Band 11

1.3.3 Development Of Dielectric Image-Line LWA At 60 GHz Band 11

1.4 Challenges And Limitations 12

1.4.1 LWA Computation, Simulation, And Measurement Sensitivity 12

1.4.2 LWA Fabrication And Assembly At Mm-Wave Frequencies 13

1.5 Outline Of Chapters 13

References 15

Chapter 2: Theoretical Background 23

2.1 Ray Optics 23

2.1.1 PRS Operation Design Theory 24

2.1.2 HIS Design Theory 27

2.1.3 LWA Gain And Bandwidth Performance Requirements. 30

2.2 Analysis Of Periodic Structures 35

2.2.1 Frequency Selective Surfaces 36

2.2.2 Electromagnetic Commercial Solvers 37

2.3 Technique For Analyzing Leaky Wave Antennas 38

2.3.1 Leaky-Wave 38

2.3.2 Array Factor Approach 42

2.4 Vital Signs 43

2.4.1 Heart Rate (Pulse Rate) Technique 43

2.4.2 Breathing Rate Technique 45

2.5 Radar Theory 45

2.6 Summary 47

References 48

Chapter 3: Design Of PRS And HIS Periodic Structures For LWA At Millimetre-Wave Frequencies 52

3.1.1 Design Of HIS Unit Cell Operation At 62.5 GHz 54

3.1.2 PRS Unit Cell Design Operation At 62.5 GHz 58

3.2 Valuation Of Losses Within HIS Periodic Structure 61

3.3 Valuation Of Losses Within PRS Periodic Structure 64

3.3.1 Fabrication Considerations 66

3.3.2 Measurements Of HIS And PRS Periodic Surfaces 68

3.3.3 Fabrication Of Dipole Antenna For Exciting LWA At 60 GHz Band 70

3.4 Conclusions 71

References 72

Chapter 4: Leaky Wave Antenna Designs For Remote Vital Signs Monitoring At Millimetre-Wave Frequencies 74

4.1 LWA Designs Base on Periodic Structures For RVSM 75

4.1.1 Beam Scanning Range Analysis With PRS And Ground Plane LWA 77

4.1.2 Beam Scanning Range Analysis With PRS-HIS LWA 78

4.2 Finite Size Leaky Wave Antenna Simulations And Measured Results 81

4.3 Application Of LWA At 60 GHz Band RVSM With Doppler Radar 89

4.4 RVSM Measurements And Discussions 93

4.4.1 RVSM Measurement With PRS - Ground Plane Antenna At 0.6 m 95

4.4.2 RVSM Measurement With PRS - HIS Antenna At 2 m 99

4.5 Sensitivity Of RVSM At 10 GHz Compared To 60 GHz Detection At 1m 103

4.5.1 60 GHz RVSM Measurement Sensitivity At 1m 105

4.5.2 10 GHz RVSM Measurement Sensitivity At 1m 107

4.6 Comparison Of Proposed LWA With Horn Antenna, Patch Antenna And Fabry Perot Antenna At Mm-Wave Frequencies 110

4.7 Conclusions 112

Chapter 5: Multilayer Beam Scanning Leaky Wave Antenna For Remote Vital Signs Detection At Mm-Wave Frequencies 116

5.1 Introduction 116

5.2 Double- Layer Unit Cell (PRS and Plain Dielectric) 118

5.2.1 HIS Unit Cell design 120

5.2.2 Feeding Dipole Design For Multilayer LWA 121

5.3 Multilayer Leaky Wave Antenna Design 123

5.4 Measured Results and Discussion Of Multilayer LWA 127

5.5 RVSM Measurements With Multilayer LWA Doppler Radar 132

5.5.1 Remote Vital Sign Monitoring At 2 m 133

5.5.2 Remote Vital Signs Monitoring At 4 m 139

5.6 Conclusions 142

References 142

Chapter 6: Bidirectional LWA Design Based On Dielectric Image-Line For Remote Vital Sign Monitoring At Millimeter-Wave Frequencies 145

6.1 Introduction 145

6.2 Leaky Wave Antenna Design Procedure 148

6.2.1 Dielectric Image Line Unit Cell Analysis And Design 149

6.2.2 Dielectric Image Line Feed Network 153
6.2.3 Proposed Dielectric Image Line Antenna Design 154
6.3 Simulation Result 154
6.4 Measured Antenna Results And Discussion 157
6.5 Measurement Of Remote Vital Signs With DIL LWA 162
6.6 Antenna Performance Comparison 167
6.7 Conclusions 171
References 172
Chapter 7: Conclusion And Future Prospectives 176
Appendix A: Matlab Programme for RVSM 182

Chapter 1: Introduction

1.1 Background

1.1.1 Leaky Wave Antenna Design Structures

One type of antenna that has recently received a lot of interest is the leaky wave antenna, which uses a travelling wave on a guide structure as the principal radiation mechanism. Their main advantages are usually excellent gain performance, frequency beam scanning, low cost, and simple design requirements [1]. Leaky wave antennas are easy to incorporate owing to their built-in beam scanning and low-profile construction. They may simplify multipoint communications (multibeam needs), surveillance applications, automobile radar systems, and high-gain, low-cost beam scanning mechanisms [2 - 4]. Leaky wave antennas are promising candidates to meet the requirements of modern and emerging mobile mass communication systems (5G), which typically require high gain, antenna efficiency, and dynamic coverage. Furthermore, because tuning technologies can be easily incorporated into antenna design, active beam-steerable leaky-wave antennas for these types of cellular networks are possible [5, 6].

In the last 20 years, applications for high-gain LWAs have been investigated using **microstrip patch arrays** [7 - 9]. The use of patch arrays in printed circuit structures is a significant advantage. However, because of resistive losses and feed radiation, the complicated microstrip feed network that is present in patch arrays suffers from gain loss, sidelobe deterioration, and cross-polarization [10,11]. Gain and efficiency values are particularly affected by ohmic and dielectric losses in the feed lines, as well as losses from radiation, surface waves, and manufacturing tolerance losses. The spurious radiation from the feed line breaks also worsens the side-lobe level and cross-polar radiation.

Slotted waveguide arrays are an efficient and high-gain alternative to planar antennas. Radial Line Slot Arrays (RLSA) are one of many types proposed by Ando et

al. [12, 13]. Currently, they are available commercially in the 12 GHz band for direct broadcast from a satellite (DBS) [14]. Despite this, there are many disadvantages, including high manufacturing costs at millimetre wave frequencies and the requirement of perfect flatness of the plates**.**

Recently, **Fabry-Perot (FP) type leaky-wave antennas (LWAs)** with doubly periodic arrays of conducting elements or apertures in a conducting sheet have been investigated [15 -17]. The name comes from Fabry-Perot interferometers, which are widely used in optics. Resonant cavities are formed by multiple reflections of waves between two parallel reflecting surfaces located close together [18]. As a result of its optical resonant cavity, this device acts as a narrowband frequency filter at discrete frequencies. FP LWAs consist of a metallic-dielectric periodic array placed at approximately half wavelength distance over a metallic ground plane and a low-directivity primary source (e.g., dipole). The passive array acts as a Partially Reflective Surface (PRS), [15 -17], creating a Fabry-Perot-type resonant cavity that significantly increases the gain and directivity of the primary source as shown in Fig. 1.1.1.

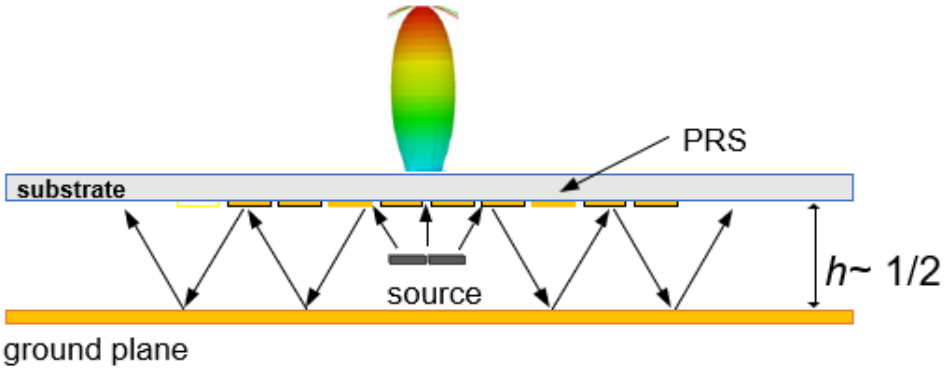


Fig. 1.1.1 Representation of Fabry-Perot (FP) LWA.

Trentini was the first to demonstrate the concept of FP antennas when he investigated how various types of PRSs can increase the directivity of a waveguide aperture in the ground plane. He was also the first to employ a ray optics approximation to describe the antenna operation employing the multiple reflections between the ground plane and the

PRS [15]. James et al. reported the findings of an experiment in which they investigated the influence of multiple-layer arrays on the directional properties of a grounded waveguide aperture and a printed patch antenna [16].

The technique described in the two articles eliminates the often-complicated microstrip conductor networks of patch array antennas. The radiation process relies on the leakage wave and beamforming effect generated by the frequency selective surface (FSS) or partially reflective surface (PRS) in front of the ground plane. Similar leakage waves have been observed in waveguides with partially reflecting walls [19, 20] and dichroic microstrip antenna arrays that overlap [21]. The partial reflection in each of these structures, which allows leakage waves to pass through, can be produced by passive components of periodic arrays (conductive patches or cavities in a conductive plane). In the next part, an introduction to the periodic array structures will be given.

1.1.2 Periodic Structures

Periodic arrays consist of identical components organised in a two-dimensional lattice that is both doubly periodic and planar. They behave like electromagnetic filters when used passively, such as when excited by plane waves [22]. In this situation, they are often referred to as **Frequency Selective Surfaces (FSS)** and are useful in a wide variety of applications, including antennas for both stationary and mobile communication systems [22, 23]. As their name suggests, they selectively allow electromagnetic waves to pass through them, depending on their frequency. More specifically, they exhibit stop-band and pass-band characteristics when illuminated by an electromagnetic wave with an arbitrary angle of incidence. If the angle of incidence becomes 90^{o}, then there is surface wave propagation and hence in this case the structure can be approached as an EBG structure [22, 23].

The geometry of FSS elements can include simple square or dipole components as well as Jerusalem crosses, spirals, loops and other shapes. Reflection and transmission are affected by the geometry and spacing between elements. For conducting periodic elements, a stopband region (i.e., a high reflection coefficient) occurs at the FSS resonance (which is related to the resonant frequency of the metallic elements), while the FSS is completely transparent at other frequencies. Similarly, aperture FSSs exhibit a passband region with complete reflection at frequencies away from resonance [22, 23]. As an example, Fig. 1.1.2 shows the reflection and transmission characteristics of a square aperture FSS.

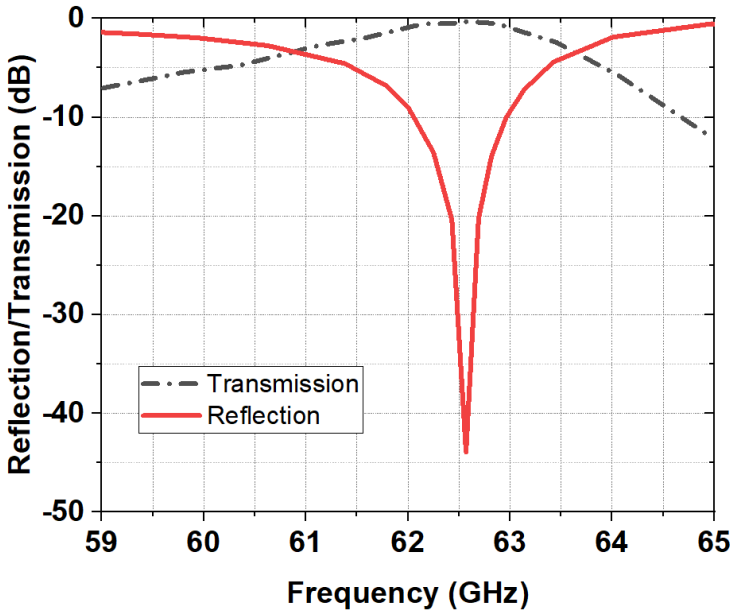
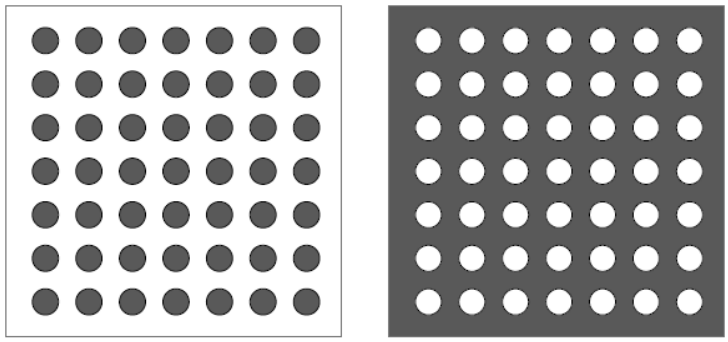


Fig. 1.1.2 Reflection and transmission response of a square aperture FSS array.

For complementary arrays, i.e., arrays with elements of the same shape such that a perfectly conducting plane is formed when the two arrays are superimposed (Fig. 1.1.3), If there is no dielectric substrate, the reflection coefficient of the conducting array will be equal to the transmission coefficient of the aperture array, and vice versa (free-standing FSS).



(a) (b)

Fig. 1.1.3 Examples of complementary FSS arrays, (a) FSS arrays have circular patches. (b) FSS arrays have circular apertures.

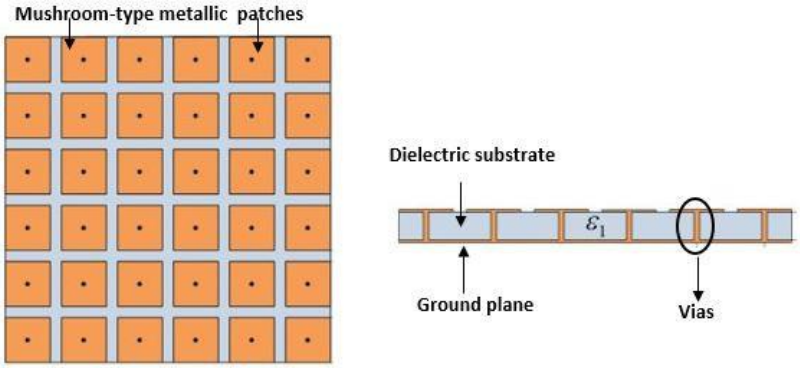
An application of frequency-selective surfaces allows them to be used in fields such as microwave filter technology [22–24], beam splitters [25], multiband reflector arrays [26], radomes [27], and absorbers [28]. In addition, the FSS, which operates as a partially reflecting surface (PRS), has been thoroughly investigated for use in antenna systems [29,30]. Moreover, at frequencies close to resonance, FSS can also be used to create partially reflective surfaces (PRS), which is advantageous for some uses like Fabry-Perot antennas [31–34].

When an FSS is printed on a grounded dielectric substrate in a ground plane, it behaves like a high-impedance surface (HIS) [35]. The ability of high impedance surfaces (HIS) to produce a controlled reflection phase for incident electromagnetic waves has been the subject of numerous research [35,36]. By having a complete zero reflection phase at a certain frequency, they can act like an artificial magnetic conductor (AMC). As a result, at a range of frequencies, the magnetic field tangential to the surface in such structures disappears. “They complement the Perfect Electrical Conductors (PEC), which give reflected plane waves a 180° phase shift.

For example, in Fig. 1.1.4, Sievenpiper [35] proposed printing metallic components in the shape of mushrooms on a grounded dielectric substrate in a two-dimensional periodic array to demonstrate HIS. It consists mainly of metallic patches connected to the ground

plane via vias. It was later shown that HIS can also work without vias [33 - 40], which makes it more difficult to manufacture, especially at higher frequencies. Fig. 1.1.5 shows a typical HIS response structure with an artificial magnetic conductor (AMC) at 62.5 GHz as an example. Resonance occurs between -90^{o} and +90^{o} in the frequency spectrum, which is considered a useful bandwidth for AMC structures (shaded in Fig. 1.1.5).

However, HISs can also be operated at different reflection phase values for different applications. They can be used as cavity antennas to reduce the profile of the antenna [33, 34] or as ground planes in printed antennas [35]. In addition, HIS has also been used in holographic surfaces [40], reflectarrays [41] and polarisation converters [42].



(a) (b)

Fig. 1.1.4 Mushroom HIS Structure Illustration (a) top view (b) side view.

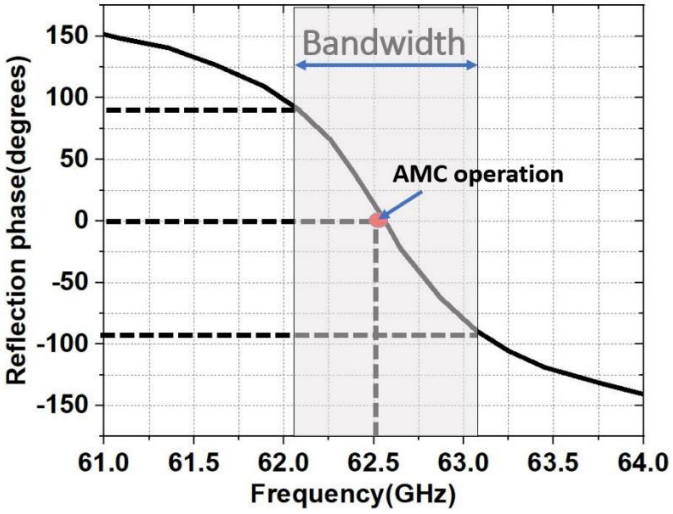


Fig. 1.1.5 Example of a typical HIS reflection phase diagram.

1.1.3 Gain Improvement For Doppler Radar At Mm-Wave Frequencies

In recent studies, dielectrics have been used as **lens antennas** to increase the gain of LWAs [38, 39, 40], which scan from back to front but suffer from broadside radiation due to difficulties with the "open stopband". This was the case with most LWAs, which were unable to radiate properly on the broadside, resulting in a lower gain to operate effectively in the mm-wave frequencies. Huang *et al* [43] remarkably discovered a Dirac leaky wave antenna to solve the open stop band (OSB) problem for a continuous beam scanning leaky wave antenna with an improved gain performance. One of the advantages of a lens antenna is the ability to steer the radiated beam by moving the external feed, due to the spherical symmetry of the lens, avoiding rotating the whole antenna. Nevertheless, it still requires mechanical steering for RVSM, it is bulky and fed externally. A good candidate for the primary source of lenses is **horn antennas.** They are characterized by a broadband operation since they don't have resonant elements and high gain is possible by increasing their size [44]. This has been used for RVSM [44] but requires mechanical steering and is bulky.

Based on the work of [43], Mingle *et al* [45] developed a new form of **bidirectional leaky wave antenna** (BLWA) that has a significant advantage over conventional LWAs due to its ability to transmit with high gain in both the forward and reverse directions over the broadside by adjusting the frequency and has been used for vital sign monitoring with good results. Therefore, the development of high-gain LWA can meet the requirements of frequency sensing to acquire vital signs with high accuracy, resolution, and reliability [46], while being non-invasive, making it an optimal solution for applications such as RVSM [46]. However, to take advantage of the valuable properties of LWAs for RVSM, they must be properly designed and carefully built to reduce manufacturing tolerance.

Leaky Wave Antennas for RVSM Doppler Radar was developed by Lin *et al*, they use the concept of Doppler radar to measure breathing and heart rate remotely [47, 48]. On

this basis, a review of the capabilities of LWAs as radar system sensors that can detect respiration and heart rate is provided. These sensors can detect movement in the chest and, using the Doppler shift principle, compute the patient's heart rate as well as breathing rate. When using a Doppler radar detection system, a high-frequency electromagnetic signal is emitted. The radar system first transmits a signal that is reflected by the target object and then demodulated by the radar system receiver. As the target object moves toward or away from the radar system, the frequency of the reflected signal differs from the transmit frequency due to the Doppler effect. The radar system can detect this frequency difference in the chest and use it to calculate the breathing and heart rate of the moving person.

In the last decade, breath-holding for pulse detection, robust signal processing methods [47–50], and frequency optimization have increased the accuracy of RVSM. Most empirical studies rely on lower microwave frequency Doppler radars, where the electromagnetic wavelength resolution is low, however, microwave (MW) radar antenna systems are enormous so millimetre wave frequencies are preferred which can be incorporated into chips [51] and other technologies such as Wi-Fi, 5G and medical imaging systems [51]. Ka-band frequencies (24 – 40 GHz), which have a shorter wavelength, have also been explored for RVSM but suffer from high resolution [52].

In recent years, mm-wave frequencies have attracted a lot of research attention due to their potential usefulness for RVSM [51 – 56] because of the compactness of the device and an improvement in detection accuracy by using shorter signal wavelengths. The most widely used mm-wave spectrum is the 60 GHz band (57 GHz–66 GHz), which is popular because it is license free [56]. Furthermore, leaky wave antennas have been used in mm-wave sensors due to their low profile, low cost, and ability to be designed into an array to produce high antenna gain [52–56]. The accuracy of RVSM depends on the design of the Doppler radar antenna [52–57]. The antenna's radiation should be focused only on the

target [56], and it should have enough gain to keep the signal-to-noise ratio [56]. Therefore, there are still gaps in the literature for RVSM at 60 GHz, including the study of LWA for RVSM without a high-impedance surface (HIS) for very short distance RVSM and with a high-impedance surface (HIS) LWA for long-distance RVSM applications, as well as a low-cost LWA array architecture that allows accurate and simultaneous acquisition of heartbeat and respiration rate.

1.2 Motivation And Objectives

In the preceding section, we have provided a brief review of several kinds of high-gain antennas, an introduction to leaky wave antennas and some background information on periodic surfaces and metasurfaces, as well as remote vital sign monitoring with Doppler radar. The motivation of this dissertation is to **develop novel leaky wave antennas (LWA) for remote monitoring of vital signs in the millimetre wave spectrum (57-68 GHz)**. The proposed LWA design was subjected to several conventional methods to investigate and evaluate their impact on the overall antenna performance at millimetre wave frequencies. As previously mentioned, these antennas, in comparison to other kinds of antennas, have several distinct benefits. They are planar and easily fabricated. They have a straightforward feeding mechanism, which contributes to their excellent directivity, beam scanning, and efficient performance. They also have good bandwidth characteristics, which is an advantage.

Although much work has already been done on the application of periodic structures, there are still many challenges that need to be overcome, especially for antennas with periodic structures and their operating frequency range. For low microwave frequencies, varactor and PIN diodes have been employed effectively as well as millimetre wave frequencies to scan the beam of antennas, but they require complex bias networks and cause additional losses.

For this reason, **one of the objectives of this thesis was to explore the possibility of designing a novel LWA based on periodic structures (PRS and HIS) without the need for active elements to enable a frequency scanning method that circumvents the above challenges**. These new designs will improve the operation of conventional periodic structures at high frequencies, which will benefit periodic antenna designs and general communication systems. **Another objective of this study is to investigate potential LWA applications in RVSM Doppler radar at mm-wave frequencies by improving detection accuracy due to shorter signal wavelengths, resulting in more targeted signal transmission and reception to avoid interference from unwanted side reflections.** Doppler radar is easier and less invasive than traditional vital sign monitoring devices like electrocardiograms (ECGs), pulse oximeters, and capnography for checking a person's vital signs [58 - 60]. Doppler radar can monitor a person's heart rate and respiration rate in addition to their blood oxygenation levels. Conventional devices require the patient to have the sensors placed directly on their body, which is very uncomfortable for the patient and takes a long time before measurements can be taken [61 - 62].

1.3 Contributions

A novel LWA is developed and tested for use in RVSM using mm-waves in this research. In the current study, RVSM at millimeter-wave frequencies ranging from 57 to 68 GHz was selected as one of the most challenging applications. As a result of this study, the following contributions were made:

1.3.1 LWA Designs And RVSM Measurements At 60 GHz Bands

The first contribution is the development of two novel LWAs that use Doppler radar in the 60 GHz band to remotely monitor vital signs and accurately calculate breathing and heart rates. The design is based on PRS-ground configuration and PRS-HIS

configuration, which provides accurate measurements from a variety of locations and distances up to 2 m. Doppler radar theory, which uses electromagnetic waves to find a target at different distances, was used to investigate the operation of RVSM in the 60 GHz channel. For this purpose, a comprehensive MATLAB programme for processing Doppler radar data was created (see Appendix A). This application was used to clean and extract respiration and heartbeat signals from a noisy received signal. The measurement performance of RVSM data at different distances and locations at 60 GHz was compared to traditional blood pressure machines with good results. In the next section, we will discuss how the higher gain of the LWA helps RVSM to perform better at longer distances.

1.3.2 Gain Improvement Based On Multilayer LWA At 60 GHz Band

The secondary contribution of this work was the development of a novel Fabry-Perot LWA with multiple layers (PRS and Plain dielectric layers) that increases gain and generalises the concept of bandwidth enhancement for RVSM applications. This novel LWA is capable of measuring RVSM over longer distances of 4 m with more beam scanning. It has been shown [63] that by adding another layer and thus forming a double-layer antenna FP the bandwidth can be significantly increased. Despite extensive work on double-layer configurations, there is no study in the literature on the possibility of using additional single dielectric layers to increase antenna gain and bandwidth for RVSM.

1.3.3 Development Of Dielectric Image-Line LWA At 60 GHz Band

The third contribution in this dissertation presents a novel bidirectional LWA based on a dielectric image line (DIL) for RVSM with higher gain and beam scanning performance of 70^{o} at mm-wave frequencies. In this case, the following tactics will be explored:

a substrate with a high dielectric constant is chosen to keep the fields on DIL intact and to reduce the scattered radiation via DIL. A planar substrate-cut microstrip line with a finite feed network is presented at DIL, along with two additional substrate-cut metal strips that increase the scan angle. The antenna performance analysis results have been applied to single and multiple target RVSM. To demonstrate the reliability of RVSM in the 60 GHz band, a person's heart rate and breathing are measured through broadside at different angles and distances to prove the design concept.

1.4 Challenges And Limitations

The main difficulties encountered during the research are discussed in this section. It also describes how these challenges and difficulties were overcome, as can be seen in the following subsections:

1.4.1 LWA Computation, Simulation, And Measurement Sensitivity

The LWA is created by completing several steps, including computing the dimensions using formulas based on the necessary specifications, modelling and CST Microwave Studio simulation, PCB etching fabrication, and assembly. Laboratory tools like the vector network analyzer (VNA), anechoic chamber, cables, connectors, and adapters are used to test the prototype after that. All these stages in LWA design involve approximations and tolerances, which become increasingly important when designing LWAs for mm-wave frequencies and lead to a large gap between predicted and observed performance. As a result, developing LWA at mm-wave frequencies while maintaining close agreement between measured and expected results is a difficult task that occasionally necessitates numerous work repetitions throughout the stages of the design process, which eventually require a significant amount of labour, time, and resources that cannot be reclaimed. To a certain extent, this problem may be mitigated by gaining an

understanding of the tolerance levels involved in the LWA design phases via experience and patience.

1.4.2 LWA Fabrication And Assembly At Mm-Wave Frequencies

A major challenge in this research was the fabrication and assembling of the LWA at millimetre wave frequencies. For an acceptable tolerance level of ±5%, the minimum PCB line width/gap must be more than 0.3 millimetres according to the low-cost laboratory-based PCB etching method [64]. Nevertheless, some industrial PCB etching facilities accept PCB line widths/gaps as low as 0.152 μm with a ± 20% tolerance level [65- 66]. However, for the best antenna performance in terms of ohmic, dielectric, and surface wave losses, a thin PCB substrate is needed for LWA design at mm-wave frequencies. This is because the PCB substrate thickness (h) for LWA design must be a tiny fraction of the operational wavelength (λ) (i.e., $h < \lambda/10$ [64]).

A substrate with a high dielectric constant is chosen to keep the fields on DIL intact and to reduce scattered radiation via DIL. A planar substrate-cut microstrip line with a finite feed network is presented at DIL, together with two additional substrate-cut metal strips to increase the scanning angle. The results of the antenna performance analysis were applied to RVSM with single and multiple targets. To demonstrate the reliability of RVSM in the 60 GHz band, a person's heart rate and breathing are measured through the broadside at different angles and distances to prove the design concept.

1.5 Outline Of Chapters

This thesis focuses on the design and testing of leaky-wave antennas for mm-wave remote vital sign monitoring. It is divided into a total of seven chapters. Chapter 1 introduces the background of the thesis and describes the research motivation. It also discusses current research gaps and recent advances in RVSM.

Chapter 2 presents the theoretical design aspects of LWA at millimetre wave frequencies and their use for RVSM with Doppler radar.

The construction of periodic structures, namely High Impedance Surfaces (HIS) and Partially Reflective Surfaces (PRS), is the subject of discussion in Chapter 3. In the context of this thesis, the LWA was developed using these two periodic structures (PRS and HIS). The structures of PRS and HIS were analysed using a variety of technologies to develop the LWA. For PRS and HIS a ray-optic approach was chosen and studied in more detail, as was the plane wave approximation method used in the microwave studio CST. This has the advantage of focusing on the unit cell rather than the whole structure, which helps to shed light on the behaviour of the structures studied and can also be used to characterise periodic structures. Furthermore, based on the simulated results at 60 GHz frequencies, the values of all losses are compared and investigated before being optimised, fabricated, and tested in the 60 GHz band.

Chapter 4 demonstrates comprehensive LWA designs for RVSM applications using Doppler radar in the 60 GHz band. Results are compared between LWA with HIS and without HIS, and post-processing of RVSM extraction results is examined and compared.

In Chapter 5, a multilayer LWA is designed and analysed to demonstrate the possibility of improving the gain of the proposed LWA design by using an additional plain dielectric layer over the PRSs to increase the gain and bandwidth at 60 GHz. First, a two-layer unit cell was performed in CST to determine the general behaviour of the structure with 95% accuracy. The measurement results of the finite antenna structure and its application in RVSM are shown in this chapter.

The design analysis of bidirectional LWAs with dielectric image line (DIL) for RVSM applications at 60 GHz is discussed in Chapter 6. The unit cell of the dielectric image line (DIL) is subjected to a parametric analysis and the results of this analysis are presented

in terms of antenna performance. This antenna can scan with frequency from left to right through the broadside. The measurement results of the dielectric image lines LWA are presented together with the RVSM results which are in good agreement. Finally, a comparison of all four LWAs in Chapters 4, 5 and 6 was made in terms of gain, directivity, and beam scanning.

In Chapter 7, a summary of the findings of the study is presented, together with some suggestions for further research.

References

[1] D. R. Jackson, A. A. Oliner, C. Balanis, "Leaky-wave antennas" in Modern Antenna Handbook, New York, NY, USA: Wiley, 2008.

[2] D. K. Karmakar, K. P. Estelle, and S. G. Hay, "Fixed-Frequency Beam Steering of Microstrip Leaky-Wave Antennas using Binary Switches," *in IEEE Transactions on Antennas and Propagation,* vol. 64, no. 6, pp. 2146-54, 2016.

[3] D. K. Karmokar, Y. J. Guo, P. Qin, K. P. Esselle and T. S. Bird, "Forward and Backward Beam-Scanning Tri-Band Leaky-Wave Antenna," *in IEEE Antennas and Wireless Propagation Letters*, vol. 16, pp. 1891-1894, 2017.

[4] F. Monticone and A. Alu, "Leaky-Wave Theory, Techniques, and Applications: From Microwaves to Visible Frequencies," *Proc. IEEE,* vol. 103, no. 5, pp.793 – 821, 2015.

[5] M. S. Rabbani, J. Churm and A. Feresidis, "Millimetre-wave beam steerable leaky-wave antenna for 5G systems," *12th European Conference on Antennas and Propagation (EuCAP 2018),* London, pp. 1-4, 2018.

[6] Y. El Gholb, M. Poveda-Garcia, J. L. G. Tornero, J. M. Molina-Garcia-Pardo and N. El Amrani El Idrissi, "A Mobile Terminal Leaky-Wave Antenna for Efficient 5G

Communication," *2019 IEEE-APS Topical Conference on Antennas and Propagation in Wireless Communications (APWC)*, Granada, Spain, 2019, pp. 402-402.

[7] J. R. JAMES and P. S. HALL, 'Handbook of microstrip antennas' (Peter Peregrinus Ltd., London, 1989)

[8] A. Henderson, J. R. James, "Low-cost flat-plate array with squinted beam for DBS reception." *In IEE Proceedings H (Microwaves, Antennas and Propagation)*, vol. 134, no. 6, pp. 509-514. IET Digital Library, 1987.

[9] D. M. Pozar and D.H. Schaubert, Eds: 'Microstrip antennas' (New York: IEEE Press, 1995).

[10] P. S Hall, and C. M Hall, "Coplanar corporate feed effects in microstrip patch array design." In *IEE Proceedings H (Microwaves, Antennas and Propagation)*, vol. 135, no. 3, pp. 180 -186. IET Digital Library, 1988.

[11] E. Levine, G. Malamud, S. Shtrikman and D. Treves, "A study of microstrip array antennas with the feed network," in *IEEE Transactions on Antennas and Propagation*, vol. 37, no. 4, pp. 426 - 434, April 1989.

[12] J. Hirokawa, M. Ando and N. Goto, "Waveguide -Fed Parallel Plate Slot Array Antenna", *IEEE Trans. Antennas and Propag.*, vol.40, No.2, pp.218-223, 1992.

[13] M. Ando, J. Hirokawa, T. Yamamoto, A. Akiyama, Y. Kimura and N. Goto. "Novel Single-Layer Waveguides for High-Efficiency Millimeter-Wave Arrays", *IEEE Trans. Microwave Theory Tech*., vol. MTT- 46, No. 6, June 1998, pp. 792-799.

[14] M. Ando, K. Sakurai and N. Goto, "Characteristics of a Radial Line Slot Antenna for 12 GHz Band Satellite TV Reception", *IEEE Trans. Antennas and Propag*., vol., AP-34, No.10, pp.1269-1272, 1986.

[15] G. Von Trentini, "Partially reflecting sheet arrays," *IEEE Trans. Antennas Propag*., vol. AP-4, no. 4, pp. 666–671, Oct. 1956.

[16] J. R. James, S. J. A. Kinany, P.D. Peel, and G. Andrasic "Leaky-wave multiple dichroic beamformers." *Electronics Letters,* vol. 18. no.25, pp.1209 -1211, Aug. 1989.

[17] A. P. Feresidis, and J. C. Vardaxoglou, “High-Gain Planar Antenna Using Optimized Partially Reflective Surfaces”, *IEE Proc. Microw. Antennas Propag.*, vol. 148, no. 6, Feb. 2001.

[18] S. Kartalopoulos, “Optical Spectral Filters and Gratings”, in Introduction to DWDM Technology: Data in a Rainbow, Wiley-IEEE Press eBook Chapters, 2000.

[19] A. J Robinson, J. C. Vardaxoglou, and R. D. Seager, "Wave guidance and radiation from a hollow tube formed from frequency-selective surfaces," *Electronics Letters*, vol.17, no. 29, pp. 1531-1533. 1993.

[20] J. Vardaxoglou, A. Robinson, and R. Seager, "Towards a new class of waveguiding structures and lightweight horn antennas using passive arrays," In *Proceedings of IEEE International Conference on Electromagnetics in Aerospace Applications, ICEAA, Torino, Italy*, pp. 343-346. 1993.

[21] J. R. James, and G. Andras. "Superimposed dichroic microstrip antenna arrays." In *IEE Proceedings H-Microwaves, Antennas and Propagation*, vol. 135, no. 5, pp. 304-312. IET, 1988.

[22] J. C. Vardaxoglou. *Frequency selective surfaces: analysis and design*. Research Studies Press, 1997.

[23] B. A. Munk. *Frequency selective surfaces: Theory and design*. John Wiley & Sons, 2005.

[24] R. Mittra, C. H. Chan, and T. Cwik, "Techniques for analyzing frequency selective surfaces-a review," *Proceedings of the IEEE*, vol. 76, no. 12, pp. 1593-1615, 1988.

[25] R. Ulrich, "Far-infrared properties of metallic mesh and its complementary structure." *Infrared Physics,* vol. 7, no. 1 37-55, 1967.

[26] V. D. Agrawal, and F.A. Pelow, “Design of a Dischroic Casegrain Subreflector”, *IEEE Trans. Antennas Propag.,* AP-27, no. 4, pp. 466-473, July 1979.

[27] C. J. Larson, “Modified Center Layer Metallic Biplanar Radome Design”, Tech. Rept. AFL-TR-78-28, Ohio State Univ. ElectroScience Lab. Rept. RF 4346-2, Columbus, March 1978.

[28] F. C. Seman, R. Cahill, V. F. Fusco, and G. Goussetis, “Design of a Salisbury Screen Absorber Using Frequency Selective Surfaces to Improve Bandwidth and Angular Stability Performance”, *IET Microw. Antennas Propag.,* vol. 5, no. 2, pp. 149-156, Jan. 2011.

[29] Y. Rahmat-Samii and A. N. Tulintseff, “Diffraction analysis of frequency selective reflector antennas,” *IEEE Trans. Antennas Propag.*, vol. AP-41, pp. 476–487, Apr. 1993.

[30] R. Dickie, R. Cahill, H. S. Gamble, V. F. Fusco, A. Schuchinsky, and N. Grant, “Spatial demultiplexing in the sub-mm wave band using multilayer free-standing frequency selective surfaces,” *IEEE Trans. Antennas Propag.*, vol. 53, pp. 1903–1911, 2005.

[31] A. P. Feresidis, and J. C. Vardaxoglou, “High-Gain Planar Antenna Using Optimized Partially Reflective Surfaces”, *IEE Proc. Microw. Antennas Propag.*, vol. 148, no. 6, Feb. 2001.

[32] Y. J. Lee, J. Yeo, R. Mittra, and W. S. Park, “Design of a High-Directivity Electromagnetic Bandgap (EBG) Resonator Antenna Using a Frequency Selective Surface (FSS) Superstrate”, *Microwave and Optical Technology Letters*, vol. 43, no. 6, pp. 462-467, Dec. 2004.

[33] S. Wang, A. P. Feresidis, G. Goussetis, J. C. Vardaxoglou, "Low-Profile Resonant Cavity Antenna with Artificial Magnetic Conductor Ground Plane", *Electron. Lett.*, vol.40, no.7, pp. 405-406, 1 April 2004.

[34] A. P. Feresidis, G. Goussetis, S. Wang, and J. C. Vardaxoglou, "Artificial Magnetic Conductor Surfaces and Their Application to Low-Profile High-Gain Planar Antennas", *IEEE Trans. Antennas Propag.*, vol. 53, no. 1, pp. 209-215, Jan. 2005.

[35] D. Sievenpiper, L. Zhang, R. F. J. Broas, N. G. Alexopolous, and E. Yablonovitch, "High-impedance electromagnetic surfaces with a forbidden frequency," *IEEE Trans. Microw. Theory Tech.*, vol. 47, no. 11, pp. 2059–2074, Nov. 1999.

[36] G. Goussetis, A. Feresidis and J. Vardaxoglou, "Tailoring the AMC and EBG characteristics of periodic metallic arrays printed on grounded dielectric substrate," *IEEE Trans. Antennas Propagat.*, vol. 54, no. 1, pp. 82-89, Jan. 2006.

[37] H. Mosallaei and K. Sarabandi, "Antenna miniaturization and bandwidth enhancement using a reactive impedance substrate," *IEEE Trans. Antennas Propag.*, vol. 52, no. 9, pp. 2403–2414, Sep. 2004.

[38] Y. E. Erdemli, K. Sertel, R. A. Gilbert, D. E. Wright, and J. L. Volakis, "Frequency-selective surfaces to enhance the performance of broad-band reconfigurable arrays," *IEEE Trans. Antennas Propag.*, vol. 50, no. 12, pp. 1716–1724, Dec. 2002.

[39] Y. Zhang, J. Von Hagen, M. Younis, C. Fischer, and W. Wiesbeck, "Planar Artificial Magnetic Conductors and Patch Antennas," *IEEE Trans. Antennas Propag., Special Issue on Metamaterials*, vol. 51, no. 10, pp. 2704–2712, Oct. 2003.

[40] B. H. Fong, J. S. Colburn, J. J. Ottusch, J. L. Visher, and D. F. Sievenpiper, "Scalar and tensor holographic artificial impedance surfaces," *IEEE Trans. Antennas and Propag.*, vol. 58, no. 10, pp. 3212–3221, Oct. 2010.

[41] J. Huang and J. A. Encinar, *Reflectarray antennas.* Hoboken, NJ: Wiley, 2008.

[42] E. Doumanis, G. Goussetis, J. L. Gomez-Tornero, R. Cahill, and V. Fusco, "Anisotropic impedance surfaces for linear to circular polarization conversion," *IEEE Trans. Antennas Propag.*, vol. 60, no. 1, pp. 212–219, Jan. 2012.

[43] X. Huang, Y. Lai, Z.H. Hang, H. Zheng, & C.T. Chan, "Dirac cones induced by accidental degeneracy in photonic crystals and zero-refractive-index materials," *Nature Materials*, vol.10, no. 8, pp.582-586. 2011.

[44] W. Lv, Y. Zhao, W. Zhang, W. Liu, A. Hu, & J. Miao (2021). Remote measurement of short-term heart rate with narrow beam millimetre wave radar. *IEEE Access*, *9*, 165049-165058.

[45] S. Mingle, D. Kampouridou and A. Feresidis, "Bidirectional Leaky-Wave Antenna Based on Dielectric Image-Line for Remote Vital Sign Detection at mm-Wave Frequencies," in *IEEE Open Journal of Antennas and Propagation*, vol. 3, pp. 1003-1012, 2022.

[46] S. Mingle, "Frequency Scannable Leaky-Wave Antenna Design for Remote Vital Signs Radar Application at 60GHz Band," *2021 International Conference on Electrical, Communication, and Computer Engineering (ICECCE),* Kuala Lumpur, Malaysia, 2021, pp. 1- 4, doi: 10.1109/ICECCE52056.2021.9514229.

[47] C.J. Lin. "Microwave sensing of physiological movement and volume change: A review," *Bioelectromagnetics*, vol.13, no. 6, pp.557-565,1992.

[48] C. Li and J. Lin, "Recent advances in Doppler radar sensors for pervasive healthcare monitoring." In *2010 Asia-Pacific Microwave Conference*, pp. 283-290. IEEE, 2010.

[49] C. Li, Y. Xiao and J. Lin, "Design Guidelines for Radio Frequency Non-Contact Vital Sign Detection, "*29th Annual International Conference of the IEEE Engineering in Medicine and Biology Society*, pp. 1651-1654, 2007.

[50] C.Li, J. Ling, J.Li and Lin, J., Accurate Doppler radar noncontact vital sign detection using the RELAX algorithm. *IEEE Transactions on Instrumentation and Measurement*, vol.59, no.3, pp.687-695, 2010.

[51] T. -Y. J. Kao, A. Y. -K. Chen, Y. Yan, T. -M. Shen and J. Lin, "A flip-chip-packaged and fully integrated 60 GHz CMOS micro-radar sensor for a heartbeat and mechanical vibration detections," *IEEE Radio Frequency Integrated Circuits Symposium*, pp. 443-446, 2012.

[52] N. Birsan and D.P. Munteanu, "Non-contact cardiopulmonary monitoring algorithm for a 24 GHz Doppler radar," *Annual International Conference of the IEEE Engineering in Medicine and Biology Society*, pp. 3227-3230, 2012.

[53] M. Alonso-Delpino, N. Llombart, G. Chattopadhyay, C. Lee, C. Jung-Kubiak, L. Jofre, and I. Mehdi, "Design guidelines for a millimetre wave and terahertz silicon micro-lens antenna". *IEEE Antennas and Wireless Propagation Letters*, 12, pp.8487. Sep. 2013.

[54] H. R. Chuang, H. C. Kuo, F. L. Lin, T.H. Huang, C. S. Kuo and Y. W. Ou, "A 60-GHz millimetre-wave life detection system (MLDS) for noncontact human vital-signal monitoring," *IEEE Sensors Journal*, vol.*12, no.*3, pp.602-609, 2012.

[55] T.Y. J. Kao and J. Lin, "Vital sign detection using 60-GHz Doppler radar system," *2013 IEEE International Wireless Symposium (IWS)*, pp. 1-4, 2013.

[56] J. Gao, K. Li, T. Sato, J. Wang, H. Harada, and S. Kato, "Implementation considerations of patch antenna array for 60GHz beam steering system applications," *IEEE Radio and Wireless Symposium*, pp. 35-38, 2009.

[57] T-M. Shen, T-Y. J. Kao, T-Y. Huang, J. Tu, J. Lin and R-B. Wu," Antenna design of 60-GHz micro-radar system-in-package for noncontact vital sign detection". *IEEE Antennas and Wireless Propagation Letters*, vol.11, 1702-1705, 2012.

[58] L. Sun, Y. Li, H. Hong, F. Xi, W. Cai and X. Zhu, 'Super-resolution spectral

estimation in short-time non-contact vital sign measurement', Review of Scientific Instruments,86(4), p. 044708, 2015.

[59] A. D. Droitcour, T. B Seto, B.K.Park, S. Yamada, A. Vergara, C. El Hourani, T.Shing, A.Yuen, V.M.Lubecke and O. Boric-Lubecke, 'Non-contact respiratory rate measurement validation for hospitalized patients, In 2009 Annual International Conference of the IEEE Engineering in Medicine and Biology Society (pp. 4812-4815). *IEEE*. Sept 2009.

[60] M. Villarroel, A. Guazzi, J. Jorge, S. Davis, P. Watkinson, G. Green, A. Shenvi, K. McCormick, and L. Tarassenko, 'Continuous non-contact vital sign monitoring in the neonatal intensive care unit. Healthcare technology letters, 1(3), p.87. 2014.

[61] L. Goldberger, Clinical Electrocardiography: A Simplified Approach, Chicago: Mosby,1999.

[62] M. Scanlon, "Acoustic monitoring of first responder's physiology for health and performance surveillance," *Proceedings of the SPIE*, vol. 4708, pp. 342-353, 2002.

[63] S. Mingle, M. S. Rabbani and A. Feresidis, "A Fabry-Pérot Multilayer High Gain Frequency Scanning Antenna at 60GHz," *2022 16th European Conference on Antennas and Propagation (EuCAP)*, Madrid, Spain, 2022, pp. 01-04, doi: 10.23919/EuCAP53622.2022.9769293.

[64] Online: [http://www.4pcb.com/pcb-design-specifications/], accessed on 24th Nov. 2021.

[65] Online:(http://www.rogerscorp.com/acs/products/32/RT-duroid-5880 Laminates. aspx), accessed on 24th Nov. 2021.

[66] Online: (http://www.rogerscorp.com/acs/producttypes/35/ULTRALAM-3000-Flexible-Copper-Clad-Laminate-and-Bondply.aspx), accessed on 24th Nov. 2022.

Chapter 2: Theoretical Background

This chapter discusses the theoretical foundations of the proposed Fabry-Pérot-type leaky wave antenna structure, along with the numerical techniques that were used to precisely simulate the antenna. Geometric optics analysis, also known as ray theory, is performed to evaluate the leakage wave and beamforming characteristics of the periodic structures, such as the partially reflecting surface (PRS) and the high impedance surface (HIS), and then to provide useful design guidelines for the performance of high-gain and beam scanning antennas, based on which the PRS and HIS are designed and optimized. The analysis also demonstrates the multiple reflections that take place between the PRS and the ground plane, as well as between the PRS and the HIS, under normal plane wave incidence, with the assumption that the structure is infinite. The periodic full-wave analysis is discussed in Section 2.2 and is performed in CST microwave studio software based on Floquet's theorem, which reduces the computation time of an infinite structure to a single unit cell. This leads to a good estimation of the performance of the proposed periodic structures as well as a large reduction in the time required for the computation. The leaky wave theory and its application to Fabry-Perot antennas are the main topics in Section 2.3. This part also includes an explanation of the leaky wave technique, which provides a better understanding of the function of the antennas as well as helpful design guidelines by predicting the performance of the antenna's characteristics. In Section 2.4, the theory underpinning vital signs, notably heart rate and breathing rate, is described. Section 2.5 presents the Doppler radar approach based on a continuous wave signal transmitted to the patient to acquire reflections of raw data for vital signs estimation.

2.1 Ray Optics

The operation of Fabry-Perot antennas (FP) has been characterised mathematically by a technique called geometrical optics, sometimes referred to as ray optics. This method is

used to describe the ray paths between the transmitting and reflecting beams [1]. This approximation approach assumes that the structure has an infinite size. As a result, it does not take into account the effects of diffraction, and it also does not take into consideration higher-order mode coupling. Trentini [2], was the first person to describe this method. In his work, he demonstrated that increasing the number of partially reflecting plates of various kinds placed in front of a reflecting screen can improve both the directivity and the gain of a waveguide aperture.

Let us consider a straightforward scenario in which a PRS layer is positioned at a cavity height of h_1 in front of a ground plane. A similar conceptual framework can be applied to a situation where we have a PRS layer over a HIS ground plane, both printed on dielectric substrates. It is assumed that the PRS and the HIS array structures are both infinitely large, while the distance between the cavity walls is of the order of one wavelength. To excite the waves that are contained inside the cavity, a dipole fed is employed as the major source of energy. This increases the number of reflections that occur between the two planes, but their amplitudes become smaller. Because of the optical path length, there is a phase shift due to the total reflection that occurs at the ground and the partial reflection that occurs at the PRS. Detail of two case scenarios on the operations of the PRS-Ground plane and PRS-HIS are explained in the next subsection.

2.1.1 PRS Operation Design Theory

In the geometry under consideration, PRS printed on a dielectric substrate (Rogers RT /duroid 5880 with $\varepsilon r = 2.2$ and $\tan\delta = 0.009$) is positioned in front of a ground plane at a cavity height of h_1 (Fig. 2.1.1). The PRS, which has been discussed throughout this chapter, is a one- or two-layer planar periodic array of conducting elements. To obtain an accurate ray-optic approximation, it is assumed that the PRS is infinite as well as in the order of magnitude of a wavelength. The main source is a feeding dipole positioned at

one end between PRS and ground (GND). The operating frequency of the antenna is within the range of leaky-wave frequencies of the PRS. This allows for some of the incident waves to be transmitted via the antenna, while the rest of the wave is reflected toward the ground plane.

The geometry shown below was used for illustration to describe the leakage wave function of the proposed antenna. The waves radiated from the primary antenna travel a considerable distance as they are reflected multiple times between the ground plane and the PRS. A phase shift is produced by the combination of several factors, including the path length, the total reflection at the ground plane, and the phase of the reflection coefficient. The interference caused by waves that are only partially transmitted through the PRS can be used to calculate the amount of power being transmitted.

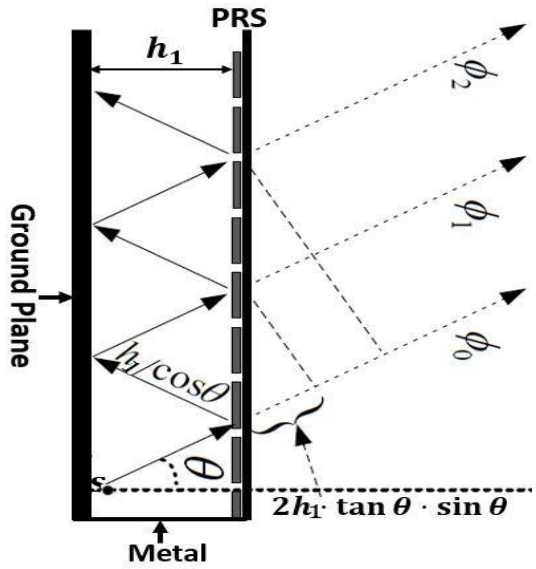


Fig. 2.1.1 Schematic diagram of a single layer FP antenna showing the multiple reflections between the ground and the PRS.

.

Let's assume that a ray is emitted from the dipole which has a radiation pattern $f(\theta)$. The reflection coefficient of the PRS will be $R \cdot e^{i\phi_R}$, where R is the magnitude and ϕ_{PRS}

the phase. If we assume no transmission losses, the amplitude of the transmitted ray will be proportional to $\sqrt{1-R^2}$; the amplitude of the once-reflected ray is proportional to $R\sqrt{1-R^2}$; the amplitude of the twice-reflected ray is proportional to $R^2\sqrt{1-R^2}$ and so on. The electric field intensity (E) in the Fraunhofer zone is the summation of the partial rays, and we may write:

$$E = \sum_{n=0}^{\infty} F(\theta) E_0 R^n \sqrt{1-R^2} e^{i\phi_n} \tag{2.1-1}$$

where ϕ_n the phase angle is composed of the total phase variations during reflections from the ground and the PRS, and the path differences of the partial rays.

The phase difference between the two transmitted beams is the total reflection at the conducting screen ($\phi_{GND} = 180^{\mathrm{O}}\ or\ \pi$) and the partial reflection phase at the PRS (ϕ_{PRS}), both of which produce phase shifts [3]. From Fig. 2.1.1:

$$\phi_0 - \phi_1 = \frac{2\phi_{GND}}{\lambda}(\Delta l) - \phi_{GND} + \phi_{PRS} = \frac{2\phi_{GND}}{\lambda} 2h_1 \left(\tan\theta \cdot \sin\theta - \frac{1}{\cos\theta}\right) - \phi_{GND} + \phi_{PRS}$$

$$= \frac{2\phi_{GND}}{\lambda} 2h_1 \left(\frac{\sin^2\theta}{\cos\theta} - \frac{1}{\cos\theta}\right) - \phi_{GND} + \phi_{PRS}$$

$$= -\frac{2\phi_{GND}}{\lambda} 2h_1 \cdot \cos\theta - \phi_{GND} + \phi_{PRS} \tag{2.1-2}$$

Thus,

$$\phi_n = n(\Delta\phi) = n\left(-\frac{2\phi_{GND}}{\lambda} 2h_1 \cdot \cos\theta - \phi_{GND} + \phi_{PRS}\right) \tag{2.1-3}$$

and since $0 < R < 1$, (2.1-1) is now written [4] :

$$\sum_{n=0}^{\infty} \left(R(\theta) e^{i\Delta\phi}\right)^n = \frac{1}{1 - R(\theta) e^{i\Delta\phi}} \tag{2.1-4}$$

Substituting equation (2.1-4) into (2.1-1) the absolute value of electric field strength is

$$|E| = |E_0|F(\theta)\sqrt{\frac{1-R^2}{1+R^2-2R\cos(\Delta\phi)}} \tag{2.1-5}$$

Therefore, the power pattern becomes,

$$P = \frac{|E|^2}{|E_0|^2} = \frac{1-R^2}{1+R^2-2R\cos\left(\phi_{PRS}-\phi_{GND}-\frac{4\pi}{\lambda}h_1\cos\,\theta\right)}F^2(\theta) \tag{2.1-6}$$

where the magnitude R and the reflection phase on the PRS ϕ_{PRS} depend on the angle of incident θ. Maximum power at boresight (θ = 0) is obtained when the following phase condition is satisfied:

$$\phi_{PRS}-\phi_{GND}-\frac{4\pi}{\lambda}h_1 = 2N\phi_{GND} \text{ where } N = 0,1,2,.. \tag{2.1-7}$$

Rearranging (2.1-7), the equation that determines the resonant distance h_1 between the PRS and the ground plane is:

$$h_1 = \frac{\lambda}{4}\left(\frac{\phi_{PRS}}{\phi_{GND}}-1\right)+N\frac{\lambda}{2} \tag{2.1-8}$$

As an example of the above analysis, a PRS with reflection characteristics operating at the resonance of 62.5 GHz is studied. If the PRS reflection phase at normal incidence is -158.1°, then (2.1-8) holds for $\boldsymbol{h_1}$ = 3.8 mm and n = 2. This is in strong agreement with full-wave calculations predicting resonance at 62.5 GHz with a reflection phase of -158.4° for PRS at this frequency.

2.1.2 HIS Design Theory

In the previous section, High Impedance Surfaces (HIS) were investigated. Most of their applications are based on their capacity to function as artificial magnetic conductors (AMC) when subjected to a certain frequency. Because they do not sustain surface waves at certain frequencies, they also function as electromagnetic bandgaps (EBGs), so two distinct phenomena occur which do not necessarily coincide in frequency [5]. The way

AMCs work in HISs has nothing to do with the resonance of the frequency-selective surface (FSS) array. Instead, it has to do with the resonance of the resonant kind of cavity that is made between the FSS and the ground plane [5, 6] thereby controlling the reflection phase of an incident electromagnetic wave. The schematic diagram of the HIS structure in front of a ground dielectric is illustrated in Fig. 2.1.2. This structure is constructed by a periodic array that is printed on a dielectric substrate that has a thickness of ***t***.

The theory of ray optics is used to develop the AMC power criteria, also known as the resonance condition (2.1-9). This is accomplished by adjusting the phase difference between the direct wave $\boldsymbol{\varphi_o}$ and the reflected wave $\boldsymbol{\varphi_1}$ to 2Nπ [7]. The following equation can be used to calculate the phase difference after the following factors have been considered: the length of the optical path through the cavity; the reflection at the ground plane; and the transmission at the periodic array.

$$\Delta\varphi = \varphi_1 - \varphi_0 = \varphi_T - \frac{2\pi}{\lambda}\cdot t - \pi + \varphi_T - \frac{2\pi}{\lambda}\cdot t - 0$$

$$2\varphi_T - \tfrac{2\pi}{\lambda}\cdot 2t - \pi = 2N\pi, \text{ with } N = 0,1,2,\ldots \qquad (2.1\text{-}9)$$

where ***t*** is the cavity spacing (air or dielectric), λ is the propagation medium's wavelength φ_0 is a direct wave, φ_1 is the reflected wave and φ_T is the phase of the HIS array's transmission coefficient.

It must be mentioned here that the substrate thickness ***t*** for high impedance surface (HIS) is a dielectric fill cavity and will be used throughout the thesis. From (2.1- 9), the substrate thickness ***t*** can be calculated as:

$$\boldsymbol{t} = \frac{2\varphi_T - (2N+1)\pi}{4\pi}\cdot\lambda \qquad (2.1\text{-}10)$$

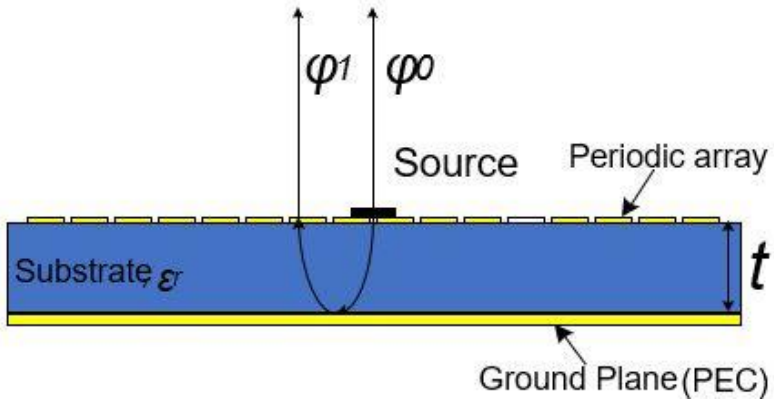


Fig. 2.1.2 High Impedance Surface (HIS) schematic diagram.

As an example of the above analysis, consider a HIS with reflective properties operating at 62.5 GHz. Assuming that the transmission coefficient phase of the HIS array at normal incidence is φ_T = 221.3°, equation (2.1-10) is satisfied for $\boldsymbol{t}$ = 1.75 mm. According to the full-wave simulation, the resonance at this frequency is optimal at 62.5 GHz with a HIS thickness of 1.7508 mm. This is in perfect agreement with the simulation.

Now consider the scenario when a radiation source is put inside the cavity seen in Fig. 2.1.3 between PRS and HIS.

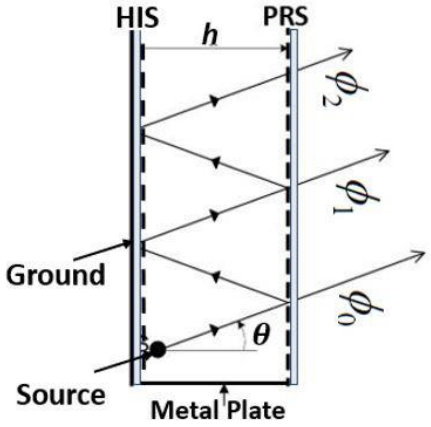


Fig. 2.1.3 Antenna geometry of PRS with HIS structures.

Tracing the reflected and direct wave paths and considering the different phase shifts, the radiation power pattern of the pointing angle from (2.1 - 6) can be rearranged if the ground

plane is now replaced by HIS ground, which shifts the phase of the incident waves according to [2]:

$$P = \frac{1 - R^2}{1 + R^2 - \cos\left(\phi_{PRS} - \boldsymbol{\phi_{HIS}} - \frac{4\pi}{\lambda} \cdot h \cdot \cos(\theta)\right)} \cdot F^2(\theta) \qquad (2.1\text{-}11)$$

where ϕ_{GND} and ϕ_{HIS} denote respectively, PRS and HIS reflection coefficient phase, $\boldsymbol{h}$ is cavity height, R is magnitude reflection coefficient of PRS and λ is the wavelength. The above equation predicts the beam scanning effect as a function of lambda for the proposed LWA, with a fixed resonance cavity height $\boldsymbol{h}$ between PRS and HIS, which can be calculated using (2.1-12):

$$\boldsymbol{h} = \frac{n\lambda_0}{2} + \frac{\lambda_0}{4\pi}(\phi_{PRS} - \phi_{HIS}) \qquad (2.1\text{-}12)$$

To illustrate the above study, consider a HIS with a reflection phase characteristic of 128.79^o operating at 62.5 GHz and the reflection coefficient phase of the PRS array at normal incidence is -157.9^o, then equation (2.1-12) holds for cavity height between PRS and HIS $\boldsymbol{h}$ = 2.90 mm optimized. This is well supported by full-wave calculations of the HIS structure and will be used throughout the thesis.

2.1.3 LWA Gain And Bandwidth Performance Requirements.

The theoretical framework presented in Section 2.1.1 may lead to other important conclusions about antenna gain and bandwidth [8]. To obtain high directivity values for a broad frequency range the phase of the PRS must satisfy the resonant condition within this range. This means that a phase should have a linearly increasing response with frequency as derived from the equation (2.1-7), for the frequency range of interest.

Rearranging Eqn. (2.1-8) into (2.1-6), we have an expression of the directivity or gain - since losses are not taken into account - relative to the primary antenna. The following equation gives the relative gain at boresight ($\theta = 0°$) :

$$G = \frac{P}{F^2} = \frac{(1 - R^2)}{1 + R^2 - 2R\cos\left(\phi_{PRS} - \phi_{GND} - \frac{4\pi f h_1}{c}\right)} \quad (2.1\text{-}13)$$

where P is the pointing angle, F^2 is the radiation pattern of the dipole, G is the gain or directivity, R is the magnitude reflection coefficient of PRS, c is the speed of light, ϕ_{PRS} is the PRS phase and ϕ_{GND} is the ground phase.

The reflection coefficient in equation (2.1-13) is frequency dependent, with magnitude and phase consistent with normal incidence on the PRS. The highest relative gain expression is obtained when $\left(\phi_{PRS} - \phi_{GND} - \frac{4\pi f h1}{c}\right) = 0$. We can derive an expression for directivity or gain in respect of the primary source:

$$G = \frac{P}{F^2} = \frac{1 + R}{1 - R} \quad (2.1\text{-}14)$$

From equation (2.1-14), it can be seen in Fig. 2.1.4 that the directivity increases with R, which means that a highly reflecting PRS placed at the resonant distance will result in a high-directivity antenna.

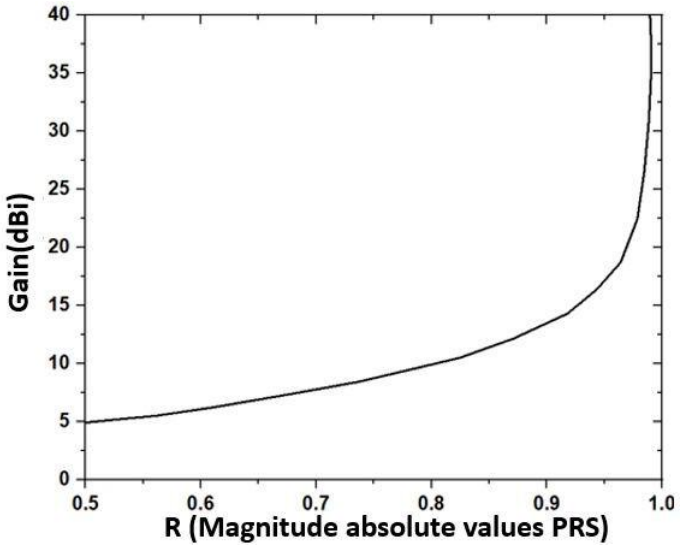


Fig. 2.1.4 Maximum relative gain versus PRS reflection coefficient.

Therefore, the maximum directivity is defined by the PRS reflection magnitude, whereas the bandwidth performance is determined by the reflection phase. Although this technique

is an approximation, it will provide useful information for the design of high directivity broadband FP antennas, as we will see in Chapters 4 and 5.

Another theoretical study relating to the gain and bandwidth is considered in this study if we assume a highly reflecting PRS with $\phi(f) \approx \pi$,

then $\Phi = \phi - \pi - \frac{2 \cdot 2\pi f h_1}{c} = 2kh_1$, where $k = \frac{2\pi f}{c}$ is vector magnitude and $\frac{\Phi}{2} = kh_1$, is the cavity's electrical length.

Since $\cos 2\theta = 1 - 2\sin^2\theta$ [4], Eqn. (2.1-13) is written:

$$G = \frac{(1 - R^2)}{(1 - R)^2 + 4R\sin^2\left(\frac{\Phi}{2}\right)} \qquad (2.1\text{-}15)$$

The visual representation of the antenna's relative gain using a highly reflective screen is given by Equation (2.1-15), versus the electrical length $\Phi/2$, Fig. 2.1.5.

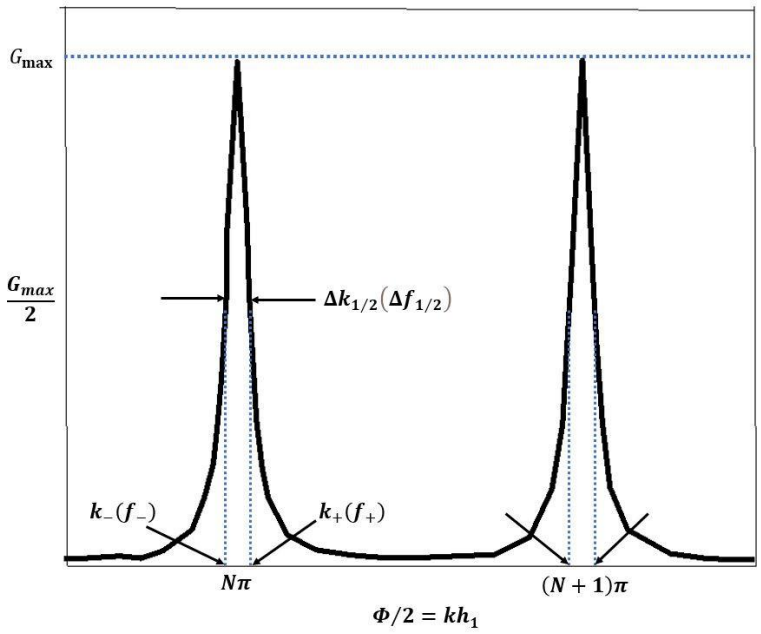


Fig. 2.1.5 Resonant leaky-wave cavity gain characteristics.

The maximum value of the gain is determined by equation (2.1-14) and it is expected that peaks at resonance will be equal to Nπ. The resonance peak can be very high for highly reflective screens, leading to bandwidth reduction. The quality factor, or Q, is a

measure of how selective an antenna is with respect to the frequencies it can efficiently transmit or receive [9]. The higher an antenna's Q factor, the narrower its bandwidth and frequency selectivity. This means that an antenna with a high Q-factor can transmit or receive signals efficiently within a very specific frequency range, but may not perform as well outside that range as shown below:

$$Q = \frac{f_0}{\Delta f_{1/2}} \tag{2.1-16}$$

where $\Delta f_{1/2}$ is the bandwidth characterised at a maximum of half the width, and f_0 is the resonant frequency. The reciprocal of Q is the partial bandwidth (BW), which measures the frequency range in which antenna gain is detectable:

$$BW = \frac{\Delta f_{1/2}}{f_0} \tag{2.1- 17}$$

Equation (2.1-15) can be used to determine the frequencies $f_+$and f_-, at which the gain drops to half its maximum value. For a highly reflective screen, the electrical angle will deviate only slightly from $N\pi$ and one can use the small-angle approximation estimate $\sin(N\pi + \Delta\Phi) \approx \Delta\Phi$.

$$\mathrm{G_{f\pm}} = \frac{G_{\max}}{2}$$

$$\text{or} \quad \frac{(1-\mathrm{R}^2)}{(1-\mathrm{R})^2 + 4\mathrm{R}\sin^2\left(\frac{2\pi \mathrm{f}_\pm}{\mathrm{c}}\mathrm{h}_1\right)} = \frac{1}{2}\frac{1+\mathrm{R}}{1-\mathrm{R}}$$

$$\text{or} \quad \mathrm{f}_\pm = \mathrm{N}\frac{\mathrm{c}}{2\mathrm{h}_1} \pm \frac{\mathrm{c}}{2\mathrm{h}_1}\frac{1-\mathrm{R}}{2\pi\sqrt{\mathrm{R}}}$$

Therefore,

$$\Delta \mathrm{f}_{1/2} = \mathrm{f}_+ - \mathrm{f}_- = \frac{\mathrm{c}}{2\mathrm{h}_1}\frac{1-\mathrm{R}}{\pi\sqrt{\mathrm{R}}}$$

Thus, the fractional bandwidth (FBW) is given by:

$$FBW = \frac{\Delta f_{1/2}}{f_0} = \frac{c}{2\pi f_0 h_1}\frac{1-R}{\sqrt{R}} \tag{2.1-18}$$

Where BW is bandwidth, f_o is fundamental frequency c is the speed of light, and R is the magnitude reflection coefficient of PRS.

In equation (2.1-18), the bandwidth is expressed as a function of the reflection coefficient magnitude and the resonant cavity height. The first valuable piece of information obtained from equation (2.1-18) is that a narrower bandwidth is expected for resonance cavity height (h_1) beyond the first one, i.e., N > 1 in equation (2.1-8). Thus, for the highest available bandwidth, N should be equal to 1 and this will be the case for the rest of the thesis. The dependence of FBW with R obtained from Eqn. (2.1-18) it is plotted as an example in Fig. 2.1.6.

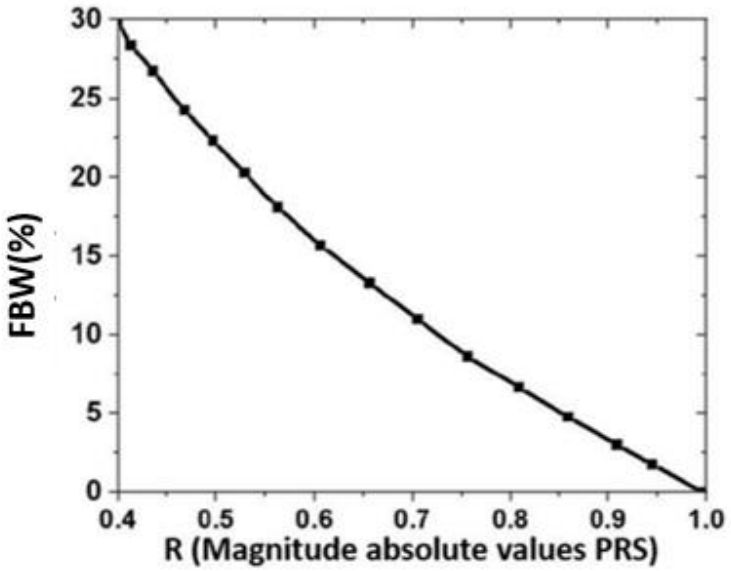


Fig. 2.1.6 Fractional bandwidth as a function of the reflection magnitude of the PRS.

Highly reflective PRS screens, which are needed for high gain, decrease the antenna bandwidth dramatically. This is a result of the resonant nature of the leaky-wave antenna

configuration. However, there is a way to increase the bandwidth even further than the values presented in Fig. 2.1.6.

At this point, it should be recalled that the results presented above are based on the assumption of constant magnitude and phase values of the reflection coefficient with frequency. For a broadband response, the reflection magnitude should ideally be constant so that, according to equation (2.1-14), the maximum gain does not change with frequency. However, it is the phase condition, equation (2.1-8), that determines the frequencies at which this maximum gain occurs, i.e. the operating frequency band of the antenna.

2.2 Analysis Of Periodic Structures

A structure is periodic if it can be generated by an infinite repetition of a basic unit, known as a "unit cell," which is displaced by one or more (up to three) translation vectors. Depending on the number of translation vectors, you can obtain 1-D, 2-D, or 3-D structures. The periodicity of the structure is determined differently in each dimension by the size of the translation vector. The electromagnetic field in each unit cell of a periodic structure has the same amplitude, but there is a phase shift between the individual unit cells as they progress. When this is taken into account, the study of a single cell can be used to simplify and reduce the analysis of an infinite structure. This is possible because the required phase shift is considered. In a real scenario, there can only be structures with a finite size.

Despite this, an array may be said to be periodic if it is sufficiently big, and periodic analysis can be used to provide a decent approximation of the behaviour that is shown by the structure. This will result in a considerable reduction in the amount of time spent computing and calculating.

2.2.1 Frequency Selective Surfaces

Frequency selective surfaces (FSS), according to Chapter 1, are two-dimensional periodic arrays of metallic components or apertures. When these arrays are turned on by an electric field at any angle to the plane of the array, the stopband properties show up first, then followed by passband properties. Thus, the electric field must be perpendicular to the array's plane [7,10]. When a plane wave with energy $\vec{E}_i$ is happening on a lossless FSS array, then the electric fields that are transmitted $\vec{E}_t$, and reflected, $\vec{E}_r$, are linked to $\vec{E}_i$ as follows:

$$E_i = E_r + E_t \tag{2.2-1}$$

$$R = \frac{E_r}{E_i} \text{ and } T = \frac{E_t}{E_i} \tag{2.2-2}$$

where the coefficients of reflection and transmission are depicted as R and T.

FSS can use many parts with different shapes, such as dipoles, cross dipoles, square loops, and square patches. Depending on the shape, each element has different reflection and transmission properties. Metallic components on a dielectric substrate provide stopband properties, while apertures on a conductive plane provide passband properties.

Complementary arrays consist of elements with the same shape. When the two arrays are superimposed, a complete, perfectly conducting plane is formed (Fig. 2.1.1), where the conducting array’s transmission coefficient is equal to the complementary aperture arrays' reflection coefficient. This is a simple case of Babinet's principle [7,10] and other methods like Floquet's theorem can also be used to analyse periodic structures as mentioned above [11,12].

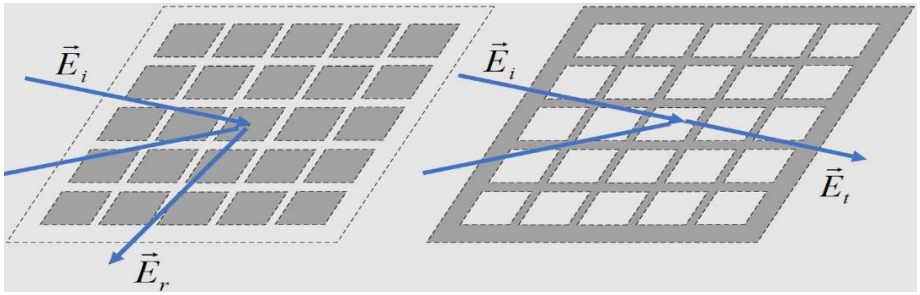


Fig. 2.2.1 Array complements. Reflection capacitive array resonance equals inductive array transmission.

2.2.2 Electromagnetic Commercial Solvers

Many techniques have been used to solve the electromagnetic fields for periodic structures. The most popular numerical methods are based on time domain differential equations such as Finite Difference Time Domain (FDTD) [13, 14], Finite Element Method (FEM) [15] or Transmission Line Matrix (TLM) [16] and frequency domain integral equation methods such as Method of Moments (MoM) [17]. These numerical methods are used by commercial simulation software packages. In this dissertation, CST Microwave Studio™ was used, which is based on the FDTD method.

CST Microwave Studio™ is a 3-D full-wave numerical tool that integrates several electromagnetic solvers. The two solvers used in this work are briefly described here. The finite integral time-domain solver uses an FDTD-like technique that uses the integral form of Maxwell's equations instead of the differential equations. It is based on non-orthogonal meshing schemes that allow the tool to model complicated structures efficiently and rigorously. Since it is a time-domain solver, it is ideal for analysing the structures under investigation in a broadband frequency range. However, it is not suitable for highly resonant structures. The finite element frequency domain solver, on the other hand, is suitable for the analysis of such highly resonant structures. It also contains a special function for the analysis of periodic structures by applying periodic boundary conditions to the unit cell of the structure under investigation. The implementation of periodic

boundary conditions generates the boundaries for arbitrarily shaped unit cells assuming infinitely large structures where a suitable phase shift is introduced between successive periodic elements.

2.3 Technique For Analyzing Leaky Wave Antennas

In addition to the theory of ray optics, the theory of leaky waves may also be used to analyze Fabry-Pero (FP) type leaky wave antennas. This is because the PRS is only partially transparent to electromagnetic waves at frequencies close to its resonance, which results in a leaky wave action. The leaky wave effect caused by the partial electromagnetic transparency of the PRS and HIS at frequencies near resonance is presented in the subsection. This technique may be used to estimate the radiation patterns for structures of limitless size. In addition, a technique for estimating antenna performance based on the array factor is also presented. The tools in this category can help better understand how LWAs work and how they propagate.

2.3.1 Leaky-Wave

The generation of leaky waves is triggered whenever there is a leakage in a structure that is designed to guide waves. As a result of the leakage, they have a complex wave number $\boldsymbol{k}$ that is characteristic of their propagation [18]:

$$k = \beta - j\alpha \tag{2.3-1}$$

where $\boldsymbol{\beta}$ stands for phase constant and $\boldsymbol{\alpha}$ the leakage rate or attenuation constant.

Fast waves, also known as leakage waves, have propagation constants smaller than the wavenumber of free space. They are often caused by surface waves excited inside the structure due to discontinuities running along one side of the structure (Fig. 2.3.1). The ground plane and the PRS together form the waveguiding structure of 2-D Fabry-Perot

antennas (FP). These antennas have a frequency response in two dimensions. Therefore, due to the uniform periodic modulation, discontinuities appear in the PRS.

The attenuation constant, as its name suggests, establishes the amplitude reduction of the propagating wave per metre. A substantial **α** value suggests that the wave attenuates quickly, resulting in a short effective aperture. A low value of **α**, on the other hand, will result in a highly effective aperture. As a result, **α** regulates the beamwidth of the emitted beams. The propagating wave's phase change per metre is represented by the phase constant ***β***, on the other hand. The radiating beam's angle is controlled by the latter, as shown from:

$$\text{Sin}\,\theta = \frac{\beta}{k_0} \qquad (2.3\text{-}2)$$

where ***θ,*** represents the main beam direction of the angle. It is obvious from (2.3-2), the wave number in free space k_0 must be achieved for radiation to occur, given that $\sin\theta \leq 1$ is a result of trigonometry. Equation (2.3-2) depicts the phase constant variation with frequency during beam scanning of leaky wave antennas. It is also clear that a unidirectional leaky wave antenna cannot scan too closely to the broadside. This is because operation near the cutoff frequency of the waveguide would be required for radiation at $\theta \approx 0$. This is a problem that arises naturally with most unidirectional leaky-wave antennas because they are powered by a single source at one end.

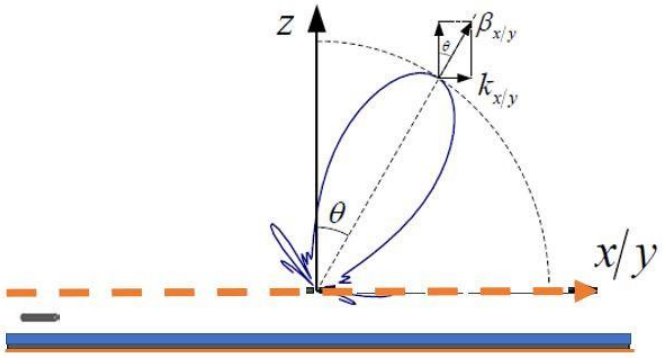


Fig. 2.3.1 Schematic representation of LW radiation in x-y plane.

The relationship between the attenuation constant α and the directivity of an antenna is a measure of how fast the electromagnetic energy transmitted by the antenna moves away from the antenna axis as the wave propagates along the antenna. A smaller value of α means that the energy is propagating closer to the antenna axis, resulting in a smaller beam width and higher directivity. A high directivity antenna radiates most of its power in a narrow beam, while a low directivity antenna radiates power in many directions.

To calculate the total length L of a unidirectional leaky-wave antenna for a typical 90% transmission of radiated power, information such as the operating frequency, the desired beam width, and the characteristics of the antenna substrate is essential:

$$\frac{L}{\lambda_0} = \frac{0.18}{\alpha/k_0} \tag{2.3-3}$$

where λ_0 is the free-space wavelength, L total length of the antenna, K_o ia is the wave number and α is the attenuation constant. The formulas (2.3-2) and (2.3-3) may serve as a rough estimate reference for the design of practical leaky wave antennas in terms of scanning angle, beamwidth, and size.

For periodic leaky wave antennas, an open stopband near $\theta \approx 0$ contributes to the broadside radiation problem. This problem occurs when both the attenuation constant and the phase constant of the fast space harmonics are zero. This is the case for a fundamentally slow leaky-wave antenna. As a result, significant degradation occurs when the antenna radiates toward the broadside [19]. According to [20], for a periodic 1D leaky wave structure, the primary beam can be directed to $\theta = 0^o$ by feeding the antenna symmetrically with one source at the centre of the structure or with two sources at each end, the first realization being the most common (Fig. 2.3.2) leading to bidirectional leaky wave antenna.This antennas radiates or receives electromagnetic waves in two opposite directions along a single axis so that in a bidirectional antenna, the half-power beamwidth (HPBW) is usually the same in both directions.

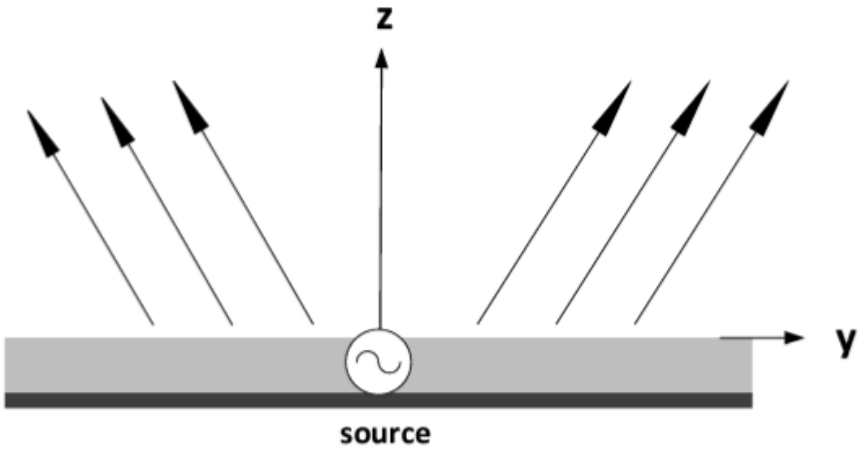


Fig. 2.3.2 Bidirectional leaky wave antenna.

Operating at the open stopband frequency (where β ≈ 0) results in broadside radiation. In this case, the beams that protrude from the structure sides are connected to form a single, symmetrical broadside beam. The same conclusions apply to two-dimensional bidirectional leaky wave antennas with homogeneous or nearly homogeneous geometry, which, if |β|= α [20] may produce a directed pencil beam at the broadside.

In addition, the design principles for the dielectric image line (DIL) leaky wave antenna are described here so that the reader will be able to comprehend the idea that is discussed in Chapter 6. Great care is taken in selecting the width, thickness, and dielectric constant ($\boldsymbol{\varepsilon_r}$) value of the substrate. The design of the dielectric image line unit cell depends on the field constraint and the unit aspect ratio (b = a). This refers to the ratio of the width (b) to the height (a) of the conducting strip and can be calculated using numerical equations to predict whether DIL operates in single-mode or multimode mode [21]:

$$\frac{b}{\lambda_0} \approx \frac{0.32}{\sqrt{\varepsilon_r - 1}} \qquad (2.3\text{- }4)$$

where λ_0 is free space wavelength and ε_r is the dielectric constant, at the design frequency.

Another theoretical equation, known as Bloch-Floquet theory, is used to predict that all potential spatial harmonics can be accommodated by a periodic structure, given as follows [21]:

$$\beta_n(\omega) = \beta_0(\omega) + \frac{2n\pi}{p} \tag{2.3-5}$$

For spatial harmonics n= -1, the dominant beam direction in periodic LWA is [20]:

$$\theta \approx \sin^{-1}\left(\frac{\beta_0(\omega)}{k_0} - \frac{2\pi}{k_0 \times p}\right) \tag{2.3-6}$$

where $\boldsymbol{k_o}$ denotes the free-space wavenumber, $\boldsymbol{p}$ is the periodicity and θ is the angle at the desired frequency.

The radiation pattern can be determined at a fixed frequency [22], and an initial estimate of the period $\boldsymbol{p}$ can be calculated using equations (2.3-6) for a given major beam direction and frequency.

2.3.2 Array Factor Approach

The array factor hypothesis (AF) can be used to accurately define leaky wave antennas. It is a method for analysing the radiation pattern of an array of antenna elements, taking into account the orientation and spacing of the elements and their individual radiation properties. The attenuation factor is determined by the geometry of the array as well as the excitation phase. The properties of the array factor and the total field produced by the array may be modified [23,24] by adjusting the phase between the components in addition to the spacing that exists between them [23,24]. The AF may be calculated if the propagation properties α and β of the antenna are known which can be expressed as :

$$AF = \sum_{n=0}^{N-1} e^{-na\cdot D} e^{jn\left(\frac{2\pi\, \mathrm{D}\cos\gamma}{\lambda} - \beta\cdot D\right)} \tag{2.2-6}$$

where γ depicts the angle from the axis of propagation, i.e., the complementary angle θ. where D_x and D_y represent the periodicity along the x-y axis, and n represents the total number of cells in either the x or y direction.

This theory assumes that structures may be of an endless size; hence, it does not take into consideration the edge effects. In addition to this, it only takes into account the most basic Floquet modes, with the higher modes being treated as if they are ephemeral.

2.4 Vital Signs

Vital signs are a set of physiological measures that are collected to evaluate an individual's fundamental bodily functioning. Commonly measured parameters of vital signs are as follows: heart rate, breathing rate, temperature, and blood pressure [25]. Vital signs are often checked in clinics and during medical emergencies to evaluate a patient's health status. Changes in vital signs may indicate the start of certain physiological disorders. During an activity, vital signs are also utilised to assess overall health. This section explores alternative theoretical techniques for measuring heart rate and respiratory rate. Monitoring heart and respiratory rates at millimetre wave frequencies (56 GHz to 67 GHz) is the focus of this study.

2.4.1 Heart Rate (Pulse Rate) Technique

The heart rate indicates how often the heart beats per minute. It is a measure of the frequency of the heart's contractions, which is controlled by the electrical impulses emanating from the heart's natural pacemaker, which is also known as the sinoatrial node. The normal resting heart rate for adults is usually between 60 and 100 beats per minute [25], but can vary depending on factors such as age, fitness and general health. Regular exercise, stress and certain medications can also affect heart rate. An abnormally high or low heart rate may be a sign of an underlying health condition.

The electrocardiogram (ECG) is the most often used tool for determining the status of the heart [26]. Among heart rate monitors, the electrocardiogram (ECG) is the gold standard, but it has many problems. The electrodes have to be attached to the patient's skin with cables. Movement is difficult because of these connections and in some patients, especially burn victims, the electrodes themselves can irritate the skin. In addition, inappropriate movement artefacts in the ECG signals can also be caused by a loose electrode connection.

Pulse rate can also be monitored with pulse oximeters worn on the fingers. Polar belts, often called electrical chest belts, can be used to monitor heart rate during exercise [27]. The significant changes in chest position between the peak and the rest of the chest are measured with a transducer [28,29]. The position of this device is difficult to reproduce and requires a lot of attention.

Doppler radar for remote measurement of vital signs is a technique in which a Doppler radar system is connected to an LWA to remotely measure a person's physiological parameters, such as respiratory rate and heart rate.The principle of this technique is based on the fact that the human body produces periodic movements due to cardiopulmonary activities, such as the expansion and contraction of the chest wall, heartbeats and blood flow. These movements cause a phase modulation of the radio waves transmitted by the radar and reflected by the body. By analysing the frequency shift of the received signal, the Doppler radar can extract the information about the vital signs of the target. Doppler radar for remote vital sign monitoring has several advantages over other vital sign monitoring methods, e.g., it is non-contact, unobtrusive, maintains privacy and can be used in different environments and conditions. In this thesis, the Doppler radar equipped with high-gain LWAs operates at a distance of 4 metres from the target chest and has been used in this study to monitor heart rate even when the subject was wearing clothing.

2.4.2 Breathing Rate Technique

The average number of breaths an adult takes in one-minute ranges between 16(1/mim) to 24(1/min) based on their overall health [25]. In healthy people, it might drop as low as eight breaths per minute, however, anything beyond this range is often indicative of respiratory issues.

Respiration can be measured using a variety of techniques, ranging from measurement of airflow to assessment of effort or chest movement caused by breathing. The breathing rate is calculated using thermocouples [30], which take the body's temperature in front of the mouth or nose area. Pulse oximetry devices are used to measure oxygen saturation [31]. All these techniques are uncomfortable, and these devices interfere with the measurements.

Doppler radar does not interfere with breathing and can measure breathing rate even when wearing clothes. It is incredibly accurate and can penetrate clothing because the antenna is kept as close to the chest as possible (0.5-2 m). The Doppler technique is therefore recommended to measure respiratory rate. Details of the theory of Doppler radar used to measure vital signs are explained in the next section.

2.5 Radar Theory

Doppler radar is the basis for several types of radar, and this basic idea has direct implications for the operation of the antenna. In this thesis, continuous wave (CW) Doppler radar was used for remote vital sign monitoring because it is a simple and cost-effective solution for detecting moving targets with high sensitivity and accuracy. However, it may not be the best choice for applications that require high imaging performance. In this case, frequency modulated continuous wave (FMCW) radar, pulsed radar and ultra-wideband (UWB) radar may be ideal.

The main advantage of CW Doppler radar is its simplicity of operation, with only one oscillator used for both transmission (TX) and reception (RX), since the bandwidth of the signals used for TX and RX is quite modest. Therefore, the filters in the receiver chain can be simple. Regardless of how far the object is from the radar's field of view, both stationary objects and moving targets can be measured.

In this study, the vector network analyser (VNA) was used together with the LWA antenna as a Doppler sensor for RVSM. The VNA sensors use Doppler shift theory to measure a person's breathing and heart rate. This approach works by analysing the chest wall movement based on mathematical analysis. The desired results are obtained by transmitting a continuous wave (CW) high frequency electromagnetic signal, receiving the reflected signal and demodulating and correlating the phase modulated signal received at the transmitter with the transmitter. The raw data recorded by the person is processed in the time domain by digital filtering, Fourier transform and other signal processing techniques. According to Doppler radar theory, for a transmitted signal $S(t)=\cos(2\pi ft+\theta(t))$, where f and $\theta(t)$ are the frequency and phase of the transmitted wave, respectively, the received baseband signal R(t) can be approximated as follows [32]:

$$\mathrm{R(t)} = \cos\left[\theta(t) + \frac{4\pi x_b(t)}{\lambda} + \frac{4\pi x_h(t)}{\lambda}\right] \qquad (2.4\text{-}1)$$

Because of the periodic nature of $x_b(t)$ and $x_h(t)$, they can be roughly calculated as follows: $x_b(t) = m_b \sin(2\pi f_b t)$ and $\mathrm{x_h(t)} = \mathrm{m_h}\sin(2\pi \mathrm{f_h t})$, where $\mathrm{m_b}$ and $\mathrm{m_h}$ are the displacement amplitudes of chest motion caused by respiration and heartbeat? The frequencies of breathing rate (BR) and heart rate (HR) are f_b and f_h , respectively. In this method, expanding equation (2.4 -1) as a Fourier series gives us [33]:

$$\mathrm{R(t)} = \sum_{\mathrm{i}=-\infty}^{\infty} \sum_{\mathrm{j}=-\infty}^{\infty} \mathrm{J_j}\left[\frac{4\pi \mathrm{m_b}}{\lambda}\right] \mathrm{J_i}\left[\frac{4\pi \mathrm{m_h}}{\lambda}\right] \cos(\mathrm{j}2\pi \mathrm{f_b t} + \mathrm{i}2\pi \mathrm{f_h t} + \theta) \qquad (2.4\text{-}2)$$

From (2.4-2) we can see that the received signal $R(t)$ resembles a time-delayed version of the transmitted signal with phase modulation. The time delay is determined mainly by the distance d_0 between the two-antenna system and the subject. The periodic motion of the target $x(t)$ is superimposed as phase modulation.

Fig. 2.5.1 shows that the chest of a stationary person has periodic motion but no net velocity. A continuous (CW) radar system aimed at the chest as a target receives a signal θ(t) whose phase is modulated by the time-varying chest position x(t). On, multiplying the received signal with the original un-modulated signal from the same source, we can demodulate this phase information affected by the movement of the chest wall during heartbeat and respiration, and therefore heart and respiration rates can be determined. The peak-to-peak chest motion due to respiration in adults ranges from 4 mm to 12 mm, while the peak-to-peak motion due to the heartbeat is about 0.5 mm [33]. A detailed illustration of radar application is provided in Chapter 4.

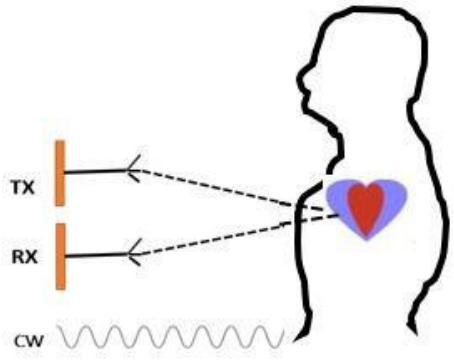


Fig. 2.5.1 Doppler radar with CW mode used for vital signs monitoring.

2.6 Summary

In this chapter, a leaky wave antenna structure was analysed using different methods. Mathematical analysis of the PRS and HIS leaky wave effect was performed using an approximate model of ray optics. This analysis led to the identification of the optimal PRS reflection characteristics for a high gain, broadband antenna. The optimal PRS and

HIS responses are used as a guideline for the design of PRS and HIS arrays in Chapter 3. As a guideline, a summary of several theoretical tools such as antenna theory, array factor, and Doppler radar theory has also been offered. Furthermore, the simulation packages used to predict the performance of the leaky-wave antenna based on the unit cell of PRS and HIS have also been presented. The information provided in sections 2.1 and 2.2 is used in the development and analysis of the antennas mentioned in Chapters 4, 5 and 6. The findings of the study as described in section 2.5 are used for RVSM in Chapters 4, 5 and 6.

References

[1] J. D. Krauss. Electromagnetics. McGraw-Hill, 1953.

[2] G. V. Trentini."Partially reflecting sheet arrays." *IRE Transactions on antennas and propagation,* vol. 4, no. 4, pp. 666-671,1956.

[3] E. Hecht: 'Optics', Addison-Wesley, Reading, Mass., 1990.

[4] S. Abramowitz and A. Stegun, 'Handbook of mathematical functions,' Dover Publications Inc., New York, 1965.

[5] G. Goussetis, A. P. Feresidis and J.C. Vardaxoglou, "Tailoring the AMC and EBG characteristics of periodic metallic arrays printed on grounded dielectric substrate," *IEEE Transactions on Antennas and Propagation* 54, no.1 (2006): 82-89.

[6] A. P. Feresidis, G. Goussetis, S. Wang, and J. C. Vardaxoglou, "Artificial magnetic conductor surfaces and their application to low-profile high-gain planar antennas," *IEEE Transactions on Antennas and Propagation* 53, no.1 (2005): 209-215.

[7] J. C. Vardaxoglou, "*Frequency selective surfaces: analysis and design"*, John Wiley, 1997.

[8] A. P. Feresidis and J. C. Vardaxoglou, "High gain planar antenna using optimised partially reflective surfaces," *IEE Proceedings-Microwaves, Antennas and Propagation*, vol. 148, no. 6 pp. 345-350,2001.

[9] J. T. Verdeyen: 'Laser electronics', Prentice Hall Inc., 1989.

[10] B. A. Munk, "*Frequency Selective Surfaces: Theory and Design*", Wiley-Interscience, 2005.

[11] M. G. Floquet, "Sur les équations différentielles linéaires à coefficients périodiques", *Annales scientifiques de l'École Normale Supérieure,* pp. 47-88, 1883.

[12] D. M. Pozar, "*Microwave Engineering*", 2nd edition, New York: John Wiley & Sons Inc, 1998.

[13] K. S. Yee, "Numerical Solutions of Initial Boundary Value Problems Involving Maxwell's Equations in Isotropic Media", *IEEE Trans. Antennas Propag.*, vol. 14(5), pp. 302-307, May 1966.

[14] A. Monorchio, and R. Mittra, "Time-Domain (FE/FDTD) Technique for Solving Complex Electromagnetic Problems", *IEEE Microw. and guided waves Lett.*, vol 8, no. 2, pp. 93-95, Feb. 1998.

[15] M. N. O. Sadiku, "A Simple Introduction to Finite Element Analysis of Electromagnetic Problems", *IEEE Trans. Educ.*, vol. 32, no. 2, May 1989, pp. 85–93.

[16] C. Christopoulos, "*The Transmission-Line Modeling Method in Electromagnetics*", Morgan & Claypool Publishers, 2006.

[17] R. F. Harrington, "*Field Computation by Moment Method*", New York, NY: Macmillan, 1968.

[18] A. A. Oliner, "*Leaky-Wave antennas*", in Antenna Engineering Handbook, 3rd ed, R. C. Hansen, Ed. New York: McGraw-Hill, 1993, ch.10.

[19] D. R. Jackson, A. A. Oliner, T. Zhao, and J. T. Williams, "Beaming of light at broadside through a subwavelength hole: Leaky-wave model and open stopband effect," Radio Science, vol. 40, no. 6, Dec. 2005.

[20] G. Lovat, P. Burghignoli, D. R. Jackson, "Fundamental properties and optimization of broadside radiation from uniform leaky-wave antennas", IEEE Trans. Antennas Propag., vol. 54, pp. 1442-1452, May 2006.

[21] P. Bhartia and I. J. Bahl, *Millimeter Wave Engineering and Applications*.New York, NY, USA: Wiley, 1984.

[22] T. Zhao, D. R. Jackson, J. T. Williams, Hung-Yu D. Yang, and A. A. Oliner, "2-D Periodic Leaky-Wave Antennas-Part I: Metal Patch Design", IEEE Trans. Antennas and Propag., vol. 53, no. 11, pp.3505-3514, Nov. 2005.

[23] C. A. Balanis, "Antenna Theory: Analysis and Design", Second edition, New York: John Wiley & Sons Inc, 1997.

[24] C. Caloz and T. Itoh, "Array factor approach of leaky-wave antennas and application to 1D/2D composite right/left-handed (CRLH) structures", IEEE Microwave and Wireless Comp. Lett., vol.14, No.6, July 2006, pp. 274-276.

[25] D. L. Gorgas and J. McGrath. "Vital signs and patient monitoring techniques," *Clinical Procedures in Emergency Medicine: 4th ed., (JR Roberts and JR Hedges, Eds.), Philadelphia, Saunders*, pp.3-28,2004.

[26] L. Goldberger, Clinical Electrocardiography: A Simplified Approach, Chicago: Mosby, 1999.

[27] M. Scanlon, "Acoustic monitoring of first responder's physiology for health and performance surveillance," Proceedings of the SPIE, vol. 4708, pp. 342-353, 2002.

[28] W. H. Bancroft Jr. and E. E. Eddleman Jr, "Methods and physical characteristics of the kinetocardiographic and apexcardiographic systems for recording low-frequency precordial motion," *American Heart Journal* vol.7, no.6, pp.756-764,1967.

[29] E. Braunwald and J. K. Perlkoff, “Physical examination of the heart and circulation,” in Heart Disease: A Textbook of Cardiovascular Medicine, (E. Braunwald, D. P. Zipes, and P. Libby, Eds.), New York: W. B. Saunders Company, 2001, pp. 45-81.

[30] B. A. Phillips, M. I. Anstead, and D. J. Gottlieb, "Monitoring sleep and breathing: Methodology: Part i: Monitoring breathing," *Clinics in chest medicine*, vol.19, no.1, pp. 203-212, 1998.

[31] G. Ramachandran, M. Singh, "Three-dimensional reconstruction of cardiac displacement patterns on the chest wall during the P, QRS and T-segments of the ECG by laser speckle interferometry," *Medical and Biological Engineering and Computing*, vol, 27, no.5 pp. 525-530, 1989.

[32] G. Changzhan, et al, "Instrument-based noncontact Doppler radar vital sign detection system using heterodyne digital quadrature demodulation architecture," *IEEE Transactions on Instrumentation and Measurement*, vol.59, no.6, pp. 1580-1588, 2009.

[33] C. Li and J. Lin, "Optimal Carrier Frequency of Non-contact Vital Sign Detectors," *IEEE Radio and Wireless Symposium*, pp. 281-284, 2007.

Chapter 3: Design Of PRS And HIS Periodic Structures For LWA At Millimetre-Wave Frequencies

This chapter covers the design, simulation, and fabrication of the proposed periodic structures in the mm-wave band (58-68 GHz), such as high impedance surfaces (HIS) and partially reflective surfaces (PRS). Applications for these structures include printed antennas [1] and resonant cavity antennas [2, 3], which contain ground planes for profile reduction. HIS and PRS surfaces have been extensively explored for their use in Fabry-Perot leaky wave antennas (LWAs) [3-5] because of their excellent gain performance and easy manufacturing. They provide a suitable option for operation in this band and can be scalable to higher mm-wave frequencies. In addition, they have attracted much attention because of their dispersive properties which make them well-suited for beam scanning applications. For example, static one-dimensional LWAs can enhance beam steering with frequency when a HIS is used as a ground plane [5,6] and the antenna source is placed near one end of the structure [7], which improves the scanning performance. Since various applications require beam scanning at fixed or variable frequencies, various topologies for the electrical reconfiguration of LWAs have recently been presented [8].

In [8], varactor diodes are used to perform a scanning operation on a composite right-handed/left-handed leaky wave antenna. A dynamic HIS is used in the role of the ground plane [9]. A varactor diode embedded in a high-impedance surface (HIS) structure provides changeable reflectivity and permits the scanning of fixed-frequency beams. These diodes are responsible for the HIS's functionality. The use of such adaptive components is limited at mm-wave frequencies because of the significant losses, nonlinearities, and parasitic capacitances they exhibit. Furthermore, tunable HIS surfaces acting as reflectarrays have successfully incorporated Micro-Electro-Mechanical Systems (MEMS) for mm-wave frequencies [10, 11]. However, each element of the periodic

structure needs to have a MEMS component integrated into it to achieve tuning. As a result, the periodic elements decrease in size with frequency, which prevents the incorporation of an electrically large component in the unit cell of the array. This suggests an upper-frequency limit for the technology's applicability. Additionally, research into tunable materials, like liquid crystals [12-15], at higher mm-wave frequencies has produced encouraging results. The main problems with this method of tuning are that liquid crystals are more costly than antennas without tuning components and they take a long time (500ms) [15] to switch between states.

In this chapter, a low-loss method for a frequency-tunable HIS-PRS structure in a dynamic beam-steered mm-wave leaky wave antenna application is described and demonstrated to overcome the above limitations. The HIS and PRS structures proposed here have been used for the development of dynamic beam-steered leaky wave antennas (LWA).The resonant state of the LWA is changed by tuning the operating frequency, which results in a significant change in the reflection phase of the HIS for a range of frequencies (58-68 GHz), which in turn controls the pointing angle of the beam radiated by the antenna.

Alternative designs were investigated and compared with the proposed structures (PRS and HIS) in the simulation software (CST Microwave StudioTM) to calculate the losses in the unit cells and confirm the proposed design. The simulation results showed a dynamic high-impedance surface power with a phase shift of more than 100^{o} at a frequency of 62.5 GHz. This structure is extremely reflective, resulting in LWA power with high gain due to its large reflection coefficient of over 0.9. As a practical application, a dipole antenna with a gain of 9.1 dBi is also presented, which is used to excite the finite LWA structure.

3.1.1 Design Of HIS Unit Cell Operation At 62.5 GHz

An application of the proposed HIS structure that was initially studied is shown in Fig. 3.1.1 and is designed to operate at 62.5 GHz. A PRS is situated at a height of ***h*** above HIS. The HIS unit cell consists of a periodic metal array in two dimensions that serves as the active ground plane. Figures 3.1.2(a, b) and 3.1.2(c) show the proposed HIS's unit cell and boundary condition, respectively.

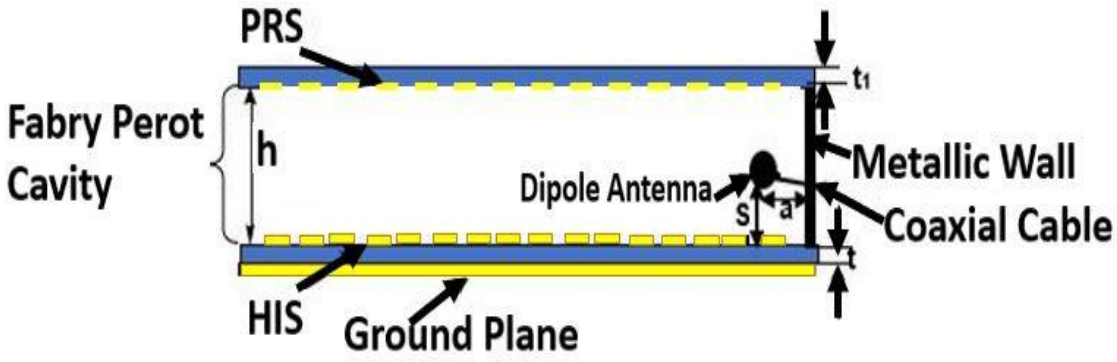


Fig. 3.1.1 Application of the HIS array and PRS array in a Proposed LWA structure (drawn not to scale).

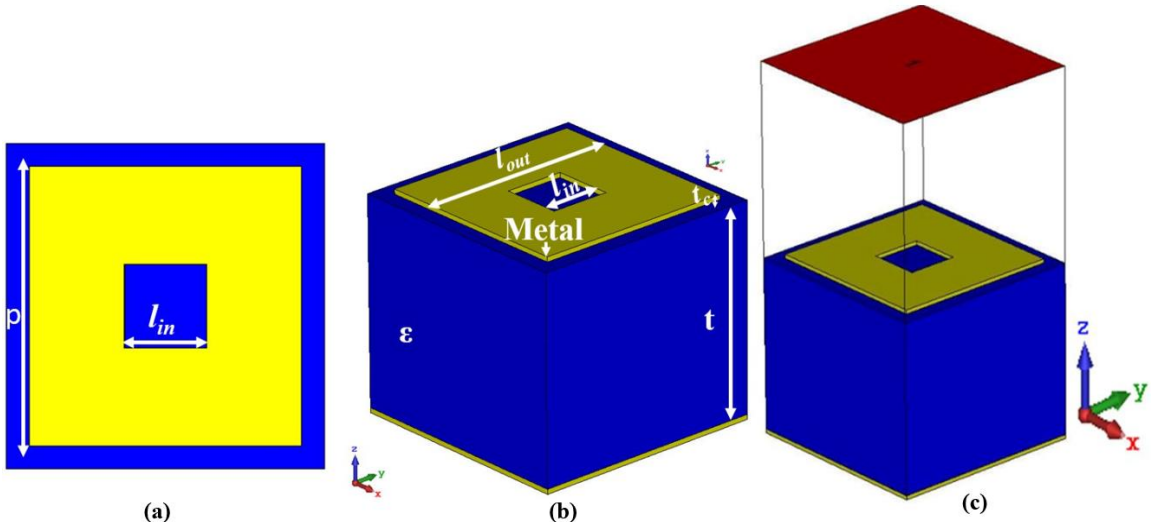


Fig. 3.1.2 HIS Unit cell structure (a) direct point of view from the top, (b) side view (c) unit cell boundary conditions (drawn not to scale).

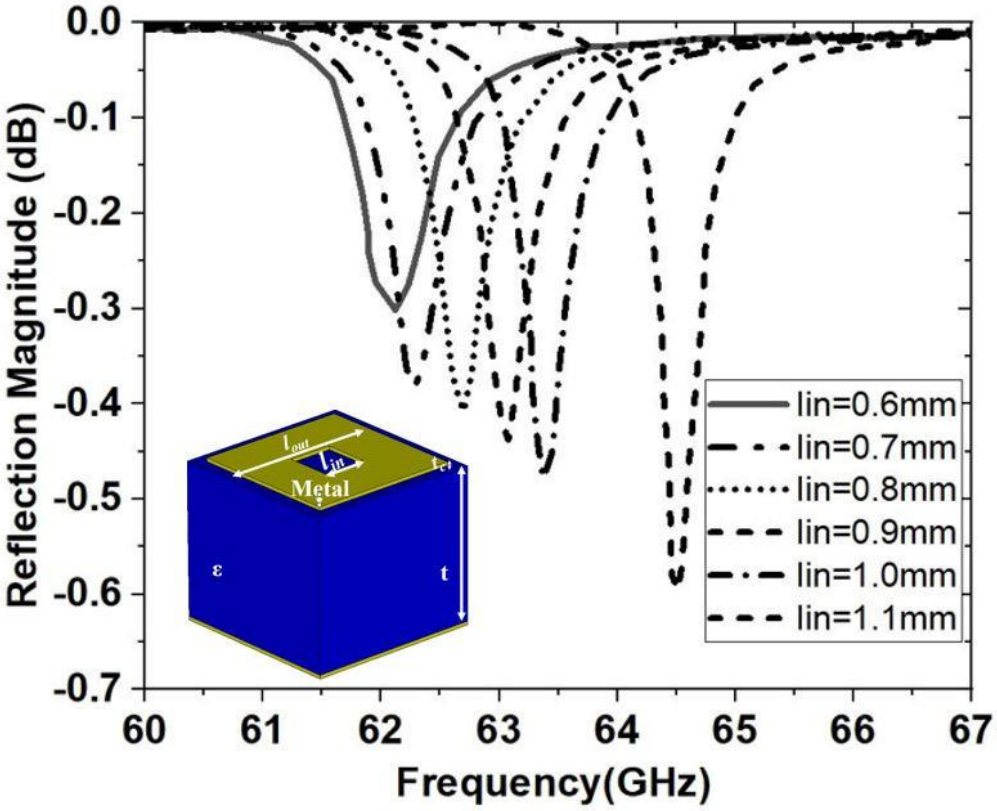
A PRS is placed in front of HIS at ***h***, creating an air cavity between PRS and HIS that provides another level of control over the phase response of the HIS reflection, which depends strongly on the thickness of the cavity and the frequency sensitivity (see Fig. 3.1.1) which is essential for understanding and interpreting information. The substrate is grounded in these HIS structures, creating a cavity filled with dielectric material between the array and the ground plane. The reflection phase can be tuned by changing the frequency.

Various geometries were studied for the proposed configuration, and a metallic element with a square loop was chosen for the HIS array because its reflection phase can change rapidly with frequency. This characteristic is important for the design to make the device more responsive to frequency and to produce a significant phase shift. The proposed design for the HIS consists of a square arrangement of metallic loop elements that are printed on a Roger/Duroid 5888 dielectric substrate with a defined dielectric constant $\varepsilon_r = 2.2$, loss tangent $\delta = 0.0009$ and thickness $t = 1.75mm$ (Fig. 3.1.2a, b).

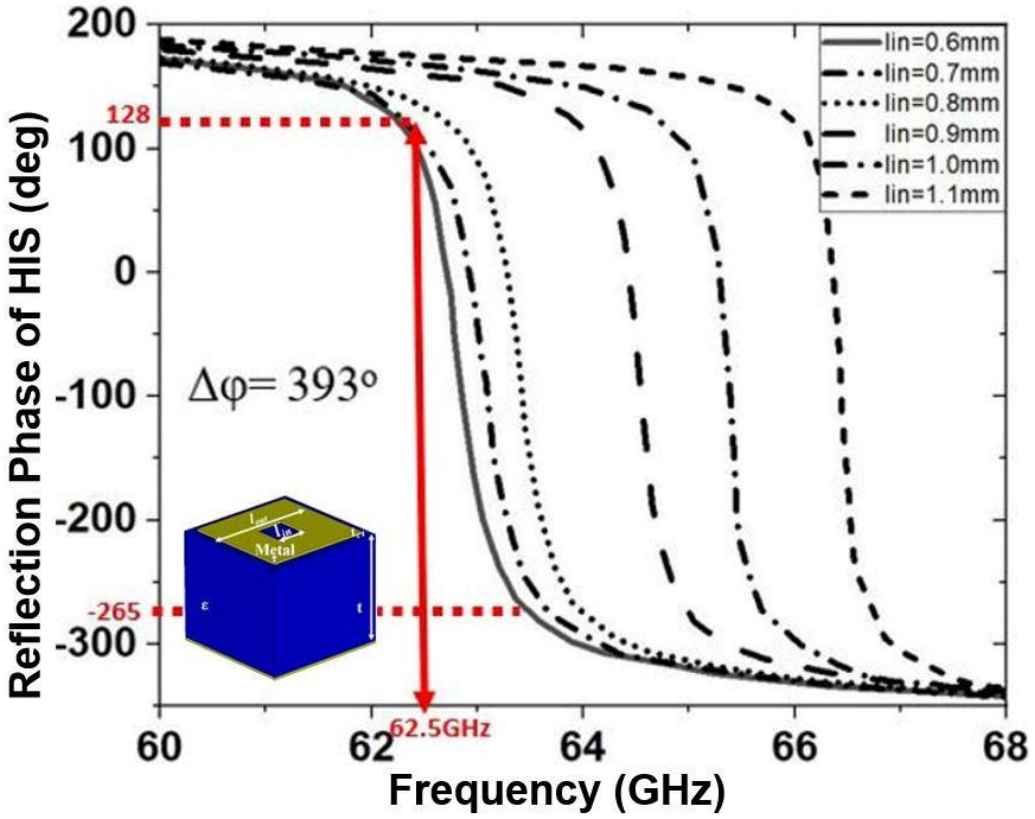
Geometries for six slightly different square loops have been taken into consideration and investigated to evaluate the structure's scanning range performance. For all cases, where the inner dimension of the square loop is different, such as l_{in}*= 0.6mm,* l_{in}*= 0.7 mm,* l_{in} *= 0.9mm,* l_{in}*= 1.0mm,* and l_{in}*= 1.1mm*. All square loops have the same periodicity of p *=1.75 mm* and an outer dimension of l_{out} *=1.5 mm* when parameterized.

In CST microwave Studio™, a thorough wave analysis was carried out to ascertain the proposed designs' reflection properties for regularly incident plane waves. The assumption that the unit cell has an infinite structure leads to periodic boundary conditions being applied to it. The boundaries parallel to the y-axis and the x-axis, respectively, were modelled by a perfect electric boundary condition and a perfect magnetic boundary condition with an open boundary condition in the z-direction.

The simulation results for the six different inner loop dimensions $l_{in} = 0.6\,mm$ to $l_{in} = 1.1\,mm$ are presented in Fig. 3.1.3 and the best HIS structure performance is selected. The selection of the HIS inner loop size $l_{in} = 0.6\,mm$ (Fig. 3.1.3a) for the proposed HIS design was based on empirical and simulation studies which showed that it is optimal to achieve high reflection values and low losses in the desired frequency range (58 - 66 GHz). Moreover, as shown in Fig. 3.1.3(b), a significant phase shift is achieved with $l_{in} = 0.6\,mm$ at the frequency of interest, compared to the rest of the designs, with a maximum of $\Delta\varphi = 393°$ between 60 GHz - 63.5 GHz.



(a)



(b)

Fig. 3.1.3 Simulation result of (a) magnitude reflection coefficient and (b) reflection phase for different inner square loop sizes for operation at 62.5GHz band.

Additionally, it can be shown that there is a trade-off between the largest possible phase shift and the bandwidth when $l_{in} = 0.6\ mm$ is compared to the remainder of the design. More specifically, it can be observed in Fig. 3.1.3(b) that the greater the phase shift, the smaller the bandwidth. Another reason for selecting this dimension is that it is close to the HIS's resonant frequency, resulting in a strong interaction between electromagnetic waves and the HIS. Because of the strong interaction, the reflection coefficient is high, resulting in low losses.

In this case, the square inner loop $l_{in} = 0.6\ mm$ with substrate thickness $t = 1.75\ mm$ and reflection coefficient phase (ϕ_{HIS} =128°) at 62.5GHz was chosen for the proposed LWA design (Fig. 3.1.3b). This satisfies equation (2.1.12) in Chapter 2, Section 2.1.2, and was used to calculate the cavity height $h = 2.90\ mm$ between PRS and the ground HIS.

This claim is supported by the observation that the resonant frequency of the inner square loop, which is at 62.5 GHz for the structure with $l_{in} = 0.6\ mm$, allows low-loss operation with a reflection coefficient above -0.3 dB (Fig. 3.1.3a), while the other parameters lead to higher losses. The reason is that designing an optimal HIS structure requires careful consideration of each of these inner loop parameters to achieve high reflectivity and low loss. It is important to balance the trade-offs between each parameter to achieve the desired performance characteristics for each chosen parameter.

3.1.2 PRS Unit Cell Design Operation At 62.5 GHz

Initially, a single-layer PRS structure implemented in a 2D LWA is being studied (Fig. 3.1.4) The PRS arrays are printed on Roger/Duroid 5888 dielectric substrate with $\varepsilon_r = 2.2, \tan\ \delta = 0.0009$ and thickness $t = 0.5\ mm$. The unit cell is presented in Fig. 3.1.5 (a), (b) and (c) showing the top, side, and bottom views, respectively. The simulation was run using CST software with the boundary conditions shown in Fig. 3.1.5(d), similar to that which was described in Section 2.11.

The boundaries parallel to the x and y axes, respectively, were subjected to perfect electric and perfect magnetic boundary conditions. An open boundary condition was employed for the z-direction. As a result, both x- and y-direction simulations of an infinite arrangement of unit cells are performed. The square patch array's reflection coefficient is computed using the Floquet modal analysis, which is implemented in the CST Microwave Studio software.

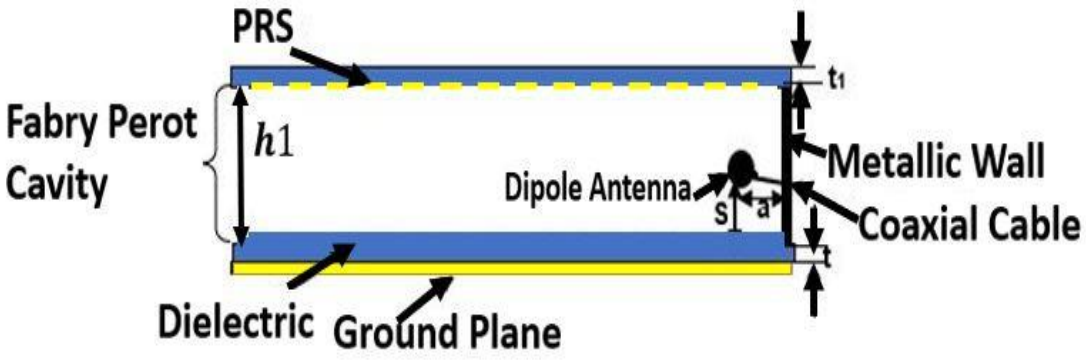


Fig. 3.1.4 Application structure of LWA with PRS array on the top layer and ground plane.

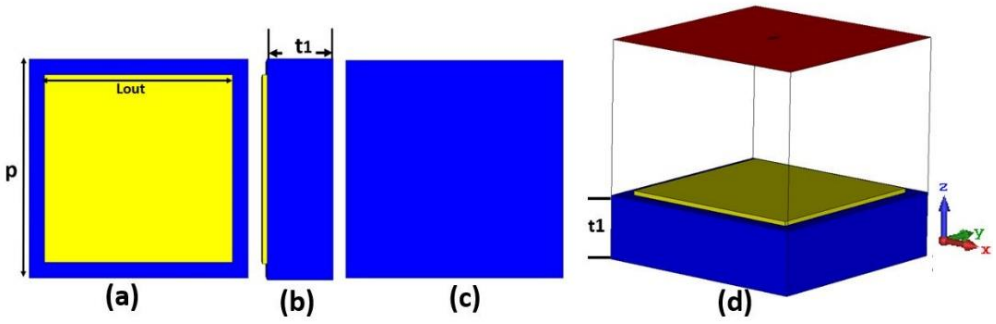


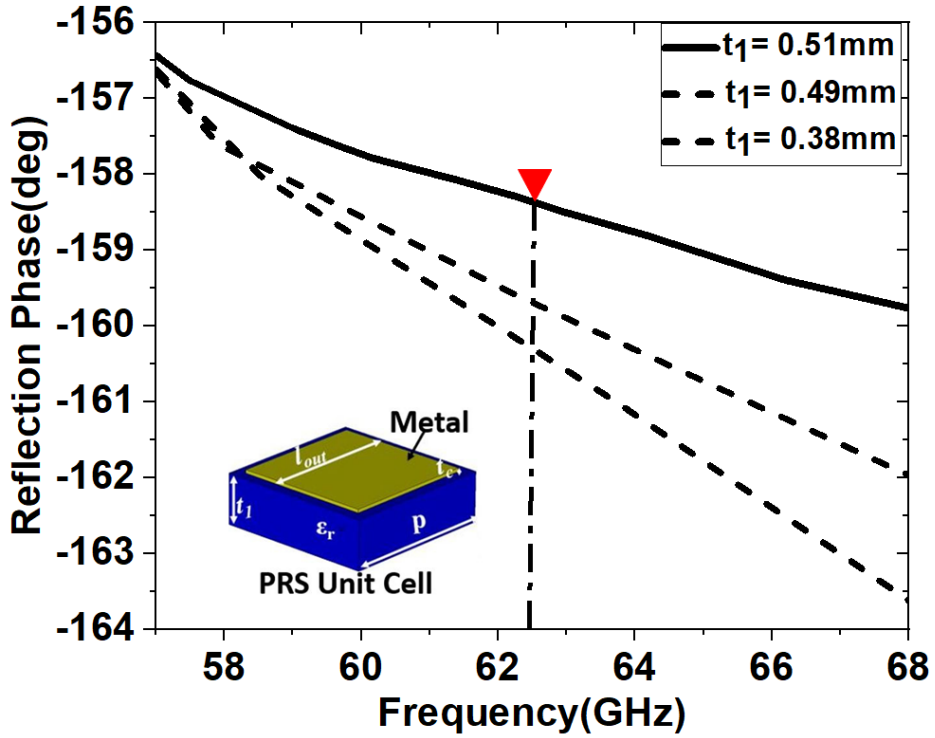
Fig. 3.1.5 Structure of PRS unit cell. (a) top view; (b) side view; (c) bottom view (d) simulation model of the unit cell.

Figure 3.1.6(a-b) shows the simulated phase in addition to the amplitude of the reflection coefficient for three different substrate thicknesses of PRS ($t_1 = 0.51\ mm$, $t_1 = 0.49\ mm$, and $t_1 = 0.38\ m$), which allows us to make an informed decision about the best structure to develop the LWA. The dimensions of PRS were chosen to achieve a high surface reflectance, as described in [5], leading to high directivity with minimum losses.

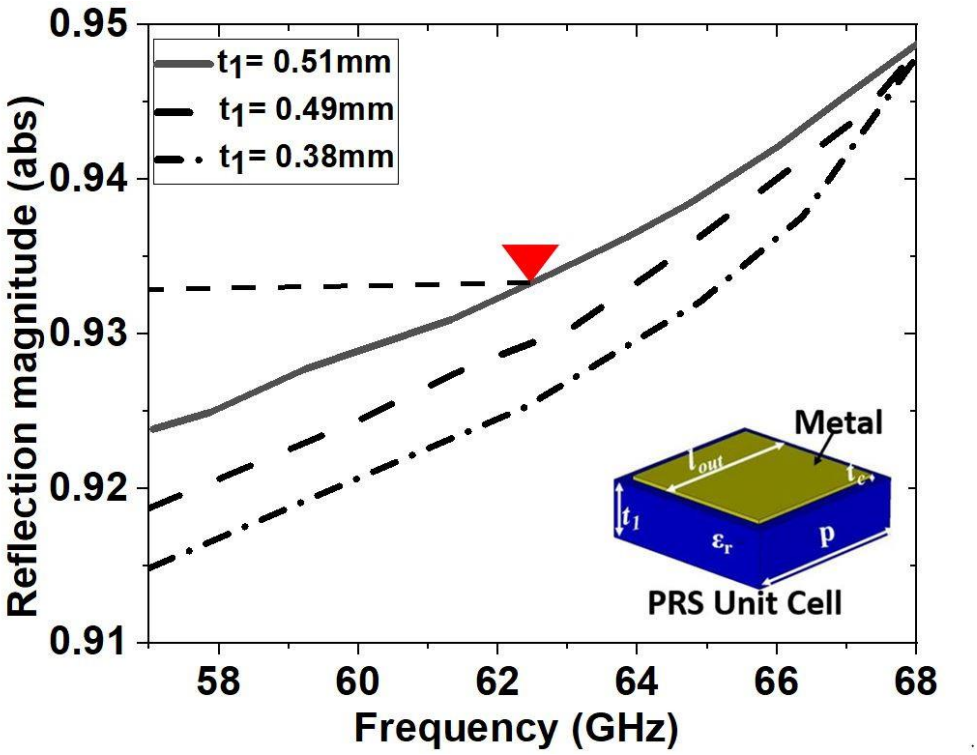
The theory outlined in Chapter 2 states that the resonance conditions must be met or the waves coming out of the cavity must be in phase for the broadside directivity to be at its highest [4]. Thus, a high-gain LWA requires a high reflectivity from PRS. Experience has shown that maximum directivity is achieved when the magnitude of the reflection coefficient (PRS) is between 0.9 and 0.95.

The PRS reflection magnitude coefficient at 62.5 GHz is about 0.94, for a dielectric thickness $t_1 = 0.51mm$, which will result in a large gain, as mentioned in Chapter 2 section 2.1.3, from equation (2.1-14), [See Figure 2.1.4]. Furthermore, the phase of the PRS reflection coefficient is close to -158.4^o at 62.5 GHz. It is also apparent that dielectric thicknesses of $t_1 = 0.38\ mm\ and\ 0.49\ mm$ produce sufficiently excellent values for the reflection magnitude (R= 0.923 and 0.926, respectively). However, due to difficulties in fabrication, this solution was not applied.

The simulation results of the proposed PRS unit cell with thickness $t_1 = 0.51mm$ and a reflection coefficient phase -158.4^o (Fig. 3.1.6) at 62.5GHz, satisfy equation (2.1-8) in Chapter 2 and has been used to calculate the PRS cavity spacing $h_1 = 3.8\ mm$ (Fig. 3.1.4) between PRS and the ground plane, assuming the index n = -2 and ground plane (GND) =180^o.



(a)



(b)

Fig. 3.1.6 PRS response (a) reflection phase and (b) magnitude reflection coefficients of different thicknesses.

3.2 Valuation Of Losses Within HIS Periodic Structure

This section examines the main factors that led to the losses in the proposed configuration and explores the possibility that the losses could have been reduced by choosing a different design that caused fewer losses. This analysis was performed for a design based on a half wavelength, where $l_{in} = 0.60\ mm$. First, simulations were run to test the behaviour of the structure's unit cell in three alternative configurations. First, both metallic and dielectric losses were taken into account, then just metallic losses with the assumption that the dielectric is lossless, and lastly only dielectric losses with the assumption that the metal is lossless. The magnitude of the reflection coefficient is shown for each of the three scenarios in Fig. 3.2.1. It can be observed that the minimum for lossy materials is − 0.95 dB while for lossy dielectric only and lossy metal only it is − 0.08 dB

and − 0.88 dB respectively. This means the losses are mainly attributed to the metal with only a very small part related to the dielectric substrate.

A second investigation was then conducted to examine the losses in two additional alternative configurations. To increase beam scanning, the periodic surface is first turned upside down so that the array is at the top and the AMC cavity is supported by a metallic piezo actuator and partially made of the dielectric substrate and part of the air. To attain the same resonance frequency, the air cavity is now set at 1.382 mm. The lowest reflection value in this situation is -1.78 dB, compared to -0.95 dB which corresponds to the original setup. Furthermore, an air-filled dielectric cavity supported by a metallic piezoelectric actuator is simulated to increase the beam scanning, with the thickness of the cavity now fixed at 2.5 mm, as shown in Fig. 3.2.2(c). The dielectric used is the same as in the original setup, namely Roger/Duroid 5888 with dielectric constants $\varepsilon_r = 2.2$ and $\tan\delta = 0.0009$. In this case, the minimum is equal to - 2.26 dB. Figure 3.2.3 shows the magnitude of the reflection coefficient for all the above setups. The proposed design is greatly advantageous in terms of losses compared with the two other configurations.

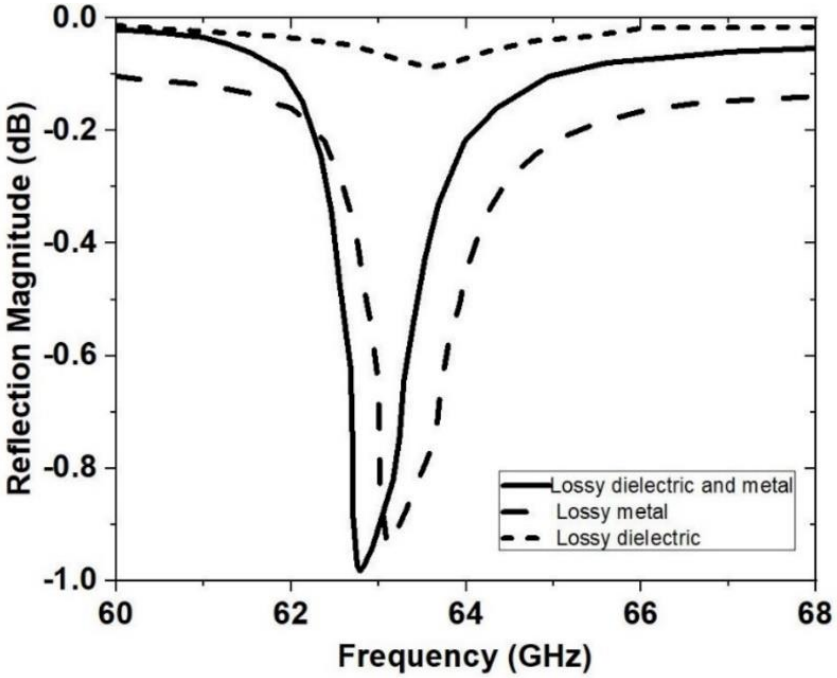


Fig. 3.2.1 Magnitude of the reflection coefficient for lossy and lossless materials.

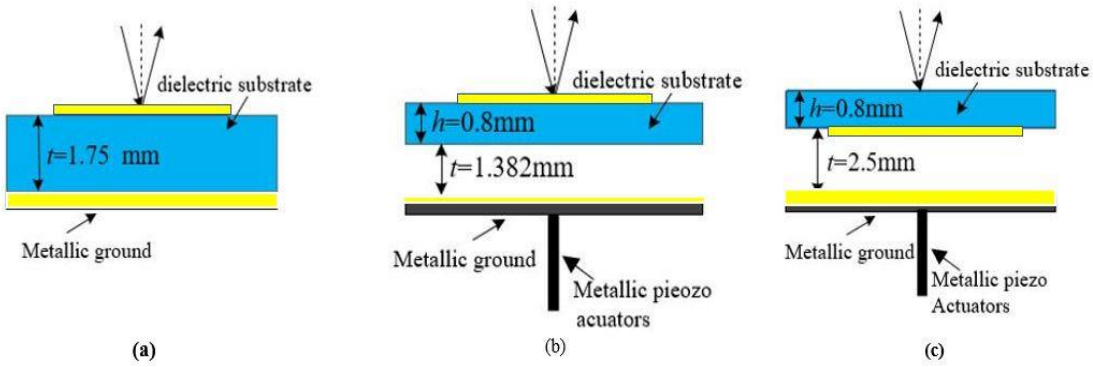


Fig. 3.2.2 Different unit cells configuration (a) the initial design with a cavity filled with dielectric, (b) a design with a metallic piezoelectric actuator holder, a dielectric, and a small air cavity; (c) Use a metallic piezoelectric actuator holder, a dielectric, and a large air cavity in the design.

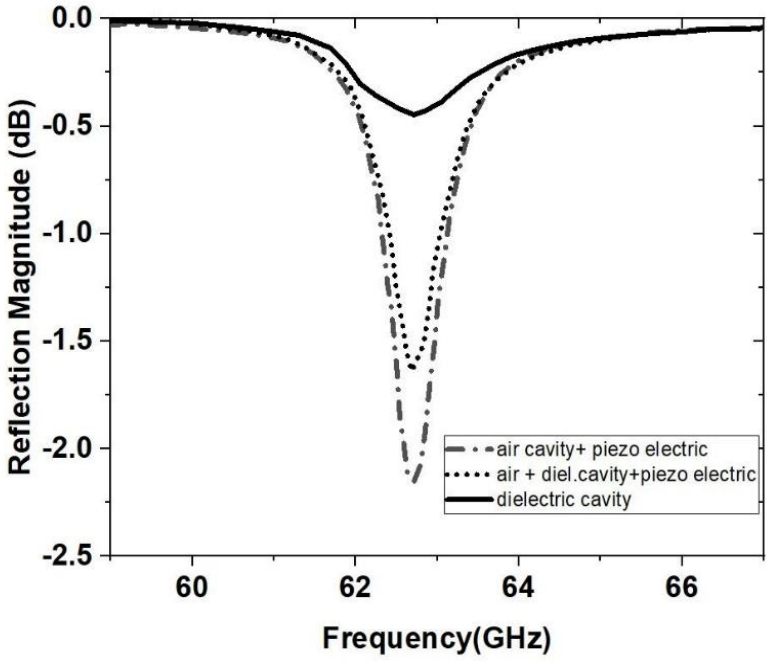


Fig. 3.2.3 The configurations of each reflection coefficient magnitude.

The novelty of the design with only single metal on one side of the dielectric PRS lies in its simplicity and ease of fabrication compared to more complex PRS structures with metal on both sides. By using a single metal dielectric layer, the design can create a phase shift of 180°, resulting in a perfect reflection of the incident waves. This design is easier to fabricate than other PRS structures that may require multiple layers or complex

geometric designs. The use of a dielectric layer in this design also allows some control over the reflected wavefront, as the thickness and material of the dielectric layer can be adjusted to produce different phase shifts.

3.3 Valuation Of Losses Within PRS Periodic Structure

It was previously indicated in Section 3.1.2 that the suggested structure has low losses, which is an essential quality, particularly at higher mm-wave frequencies. Therefore, in this section, an analysis of the main factors contributing to the losses in the proposed PRS structure is performed.

To determine whether metallic or dielectric material losses are more significant, three different cases have been considered. First, the simulation considers both dielectric and metallic losses, then only dielectric losses are considered, and finally, it is assumed that both materials have no losses. This was performed under the conditions of $t_1 = 0.51$ *mm.* The structure's insertion loss at resonance is 0.77 dB when all losses are considered. The subsequent insertion loss is 0.042 dB when only the dielectric losses are considered in the simulations. In conclusion, the insertion loss is calculated to be 0.01 dB when both materials are assumed to be lossless. This means that the metal is responsible for about 0.73 dB, while the dielectric substrates are responsible for only 0.03 dB. However, the total losses shown are incredibly low.

Moreover, another study has been carried out to validate the choice of the dielectric fill cavity in the proposed structure. The most important reason for choosing a dielectric-filled cavity as opposed to a dielectric fill with two meta-surfaces printed on either side of the substrate, is the ability to control the transmission characteristics by changing frequency. However, the reason that the arrays are facing the inside of the cavity and not the dielectric is to avoid losses. It has been shown from simulations that an alternative configuration with the periodic surfaces placed upside-down, so that the arrays are facing

the outside of the cavity (Fig. 3.3.1b), exhibits more losses. A comparison of the transmittance of the two designs is shown in Fig. 3.3.2.

An alternative design with a dielectric thickness of $t_1 = 0.49\ mm$ at the same frequency is compared with the original design with a dielectric constant of $t_1 = 0.60\ mm$. The results, in this case, show that the insertion loss at resonance is 5.44 dB, compared to 0.77 dB for the original design. The reason for the comparisons is to determine which configuration is simple and easy to produce and less lossy which can achieve more phase shifts with frequency. The proposed design has significant advantages in terms of losses compared to the alternative design.

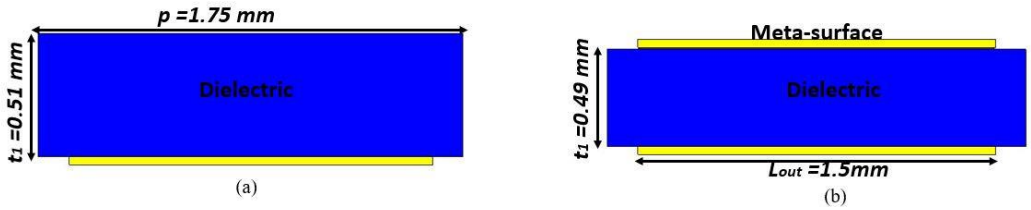


Fig. 3.3.1 Unit cell representation (a) original structure (b) alternative structure.

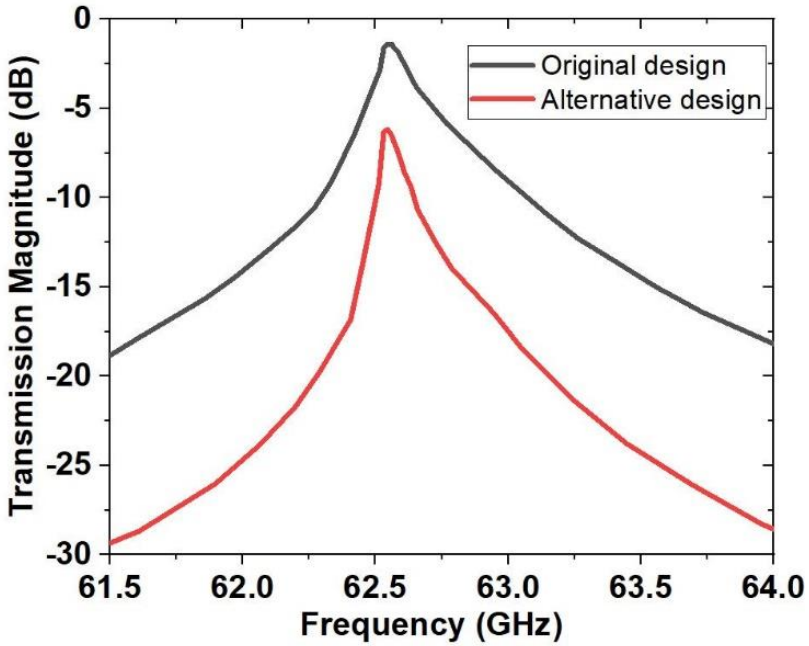


Fig. 3.3.2 Transmission magnitude comparison between the original PRS structure and the alternative design shown in Fig. 3.2.1.

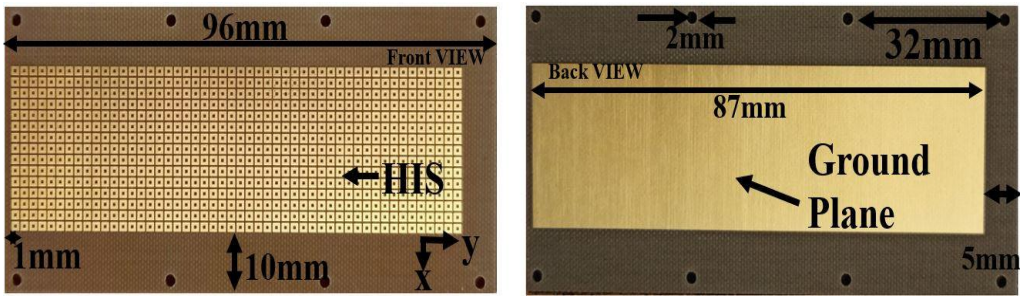
3.3.1 Fabrication Considerations

Several factors need to be taken into account for the actual application of the proposed PRS and HIS structure. To begin with, the arrays must be large enough (~10λ) to prevent diffraction effects and facilitate fabrication. Additionally, it is necessary to assess the impact of surface roughness brought on by high-frequency operation. The two periodic structures were fabricated based on the loss assessment previously performed in Sections 3.2 and 3.3 to validate the simulation results of the claimed properties and make an informed choice. The prototypes of the proposed design HIS with dimensions l_{in}*=0.6mm,* l_{out} *=1.5 mm* and the PRS with dimension l_{out} *= 1.5 mm* were fabricated using commercial photolithography. Commercial photolithography is a process used in the manufacturing of printed circuit boards (PCBs), and other precision electronic components. It is a technique used to transfer a pattern or image onto a substrate (such as PCB) using light and a series of chemical processes.

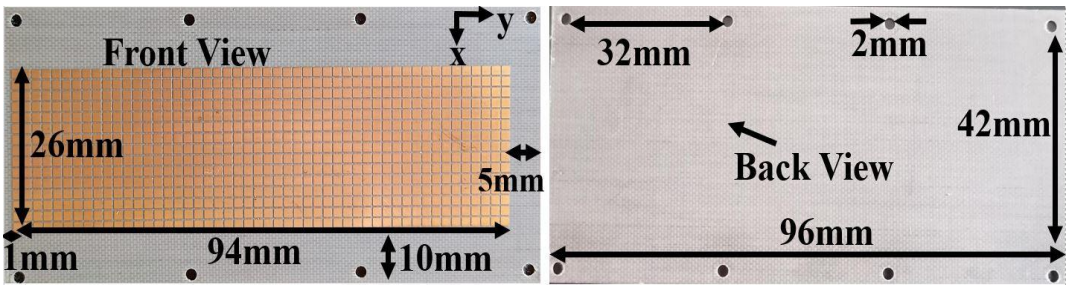
The substrate (Rogers RT /duroid 5880) was a laminated high-frequency with a 0.5oz. (17.5 μm) copper layer on either side. The process begins with dehydrating the dielectric substrate. For this purpose, the substrate was baked for 30 minutes in an oven set at 120°C. Although the bottom and top surfaces are patterned separately, the bottom surface of either HIS or PRS was coated with photoresist during the top surface processing to protect it. The photoresist used was AZ4620, which was baked hard at 120°c for 30 minutes after being spun at 1500 rpm for 30 seconds. The photoresist was then applied to the top surface at the same rate and for the same time. The substrate is then soft-baked at 105° for 9 minutes.

The next step is the patterning of the antenna arrays and patches, which was done using the EVG620 Mask Aligner. The top surface was exposed to UV light with a wavelength of 365 nm or energy of 1000 MJ/cm^2. The UV light is blocked by the opaque parts of the mask, while the transparent parts transmit the UV light and illuminate the surface. The

sample was then exposed to AZ400K developer for 4 minutes after being diluted 1:4 with water. The developer dissolved the parts that had come in contact with the UV light, while the other parts remained in place to prevent wet etching of the underlying copper. After photolithography, the remaining photoresist was strengthened by hard burning at 120°C for 30 minutes. Tranxene CE -100 copper etchant was used to complete the process by removing the areas uncovered by the photoresist. The same procedure was used on the bottom surface to obtain the base surface after removing the protective photoresist with acetone. This time, however, the top surface was covered with the photoresist. The base plate was patterned after it was aligned with the top surface. The front and back views with all dimensions [See Fig. 3.3.3 (a, b)] of the proposed HIS array and PR array structures. For the development of the LWA in the next chapter, a 50 x 15 square loop array of high impedance surfaces (HIS) and a square patch array with partially reflective surfaces (PRS) arrays printed on a 50 x 15 mm^2 substrate from Rogers RT /duroid 5880 will be used throughout the thesis.



(a)



(b)

Fig. 3.3.3 Fabricated 50 x 15 HIS and PRS array (a)front and back view of HIS (b) front and back view of PRS (dimensions are not up to scale).

3.3.2 Measurements Of HIS And PRS Periodic Surfaces

A HIS array of a unit cell with an inner square loop l_{in} = *0.6 mm* and a substrate thickness *t = 1.75 mm* was etched to validate the findings, as well as a PRS array of a unit cell with a thickness t1 = 0.51 mm, which has the same dielectric constant $\varepsilon_r = 2.2$. The overall arrays consisted of 50 x 15 elements. The HIS and PRS properties of the fabricated prototype have been measured (see Fig. Fig. 3.3.5). In the set-up, two standard gain V-band horn antennas were employed to measure the phase of the reflection coefficient from the periodic surface in Fig. 3.3.4. Both antennas were fed from a Vector Network Analyzer (VNA). One was connected to channel 1 and served as the transmitter and the other was connected to channel 2 and served as the receiver. The VNA was calibrated for the frequency range before the measurement began. The horns were positioned at a distance of more than 20 cm from the periodic surface at an angle of incidence/reflection of about 15°. A schematic representation of the measurement setup is shown in Fig. 3.3.4. A reflection measurement was conducted through the S_{21} between the two horn antenna frequency bands.

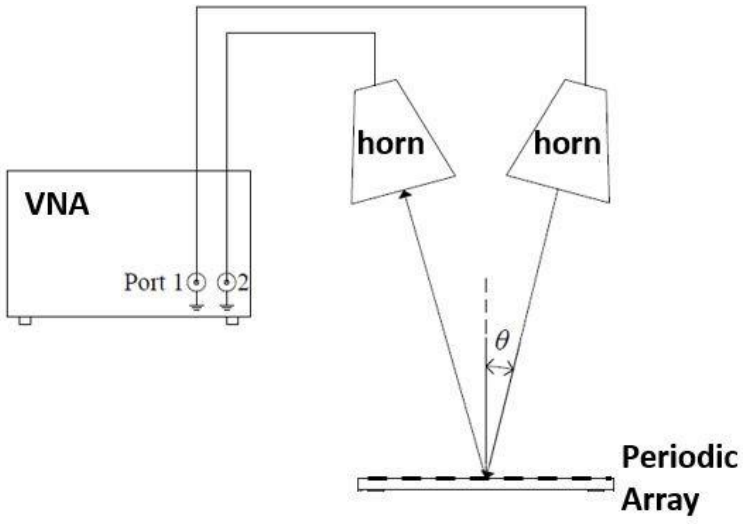
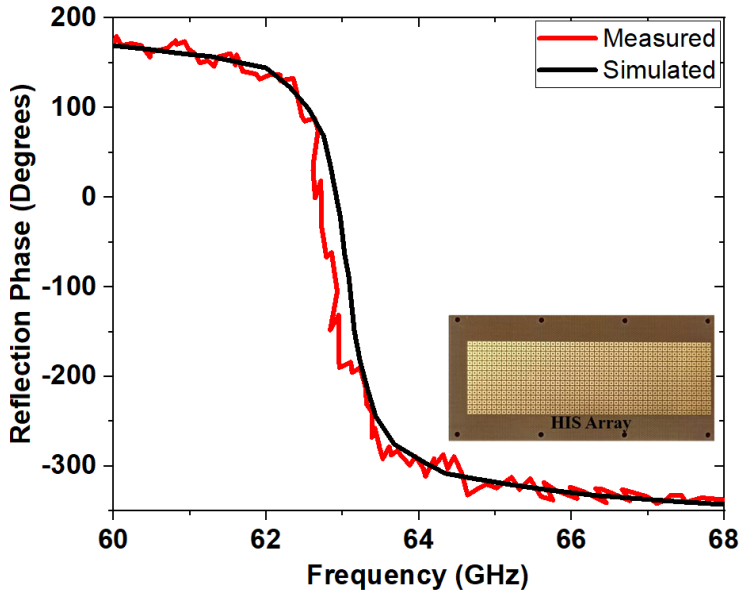


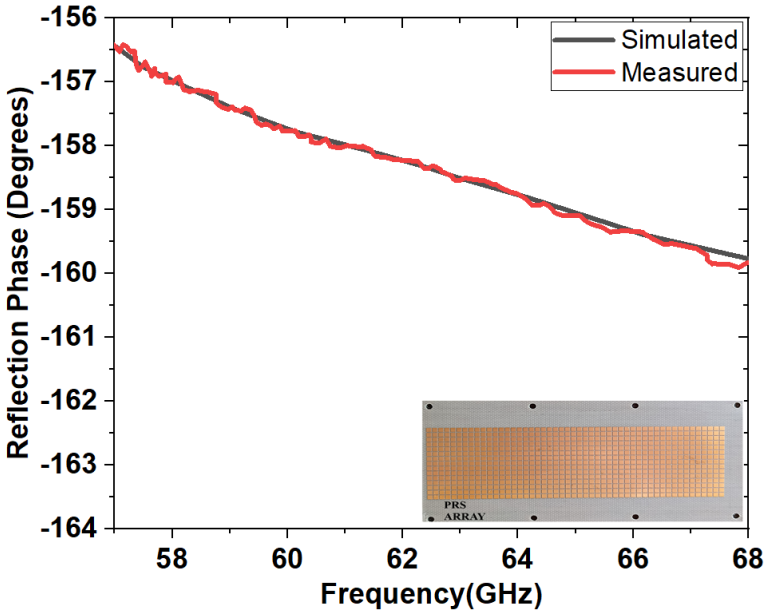
Fig. 3.3.4 Schematic representation of measurement set-up.

The reflection phase of HIS and PRS is measured in the far field with horn antennas at normal incidence. Fig. 3.3.5 shows the measured phase responses. A very good agreement

between measurement and simulation is observed. Note that there are 2 pairs of curves for both periodic arrays representing measurement and simulation. A maximum phase shift of 128^{o} for the HIS array is shown in Fig. 3.3.5(a), and -158.4^{o} for the PRS array in Fig. 3.3.5(b), which are obtained at 62.5 GHz, validating the simulated performance of the proposed design. In the experiment, the dielectric used for the periodic surface was not perfectly flat, resulting in small discrepancies and fluctuations.



(a)

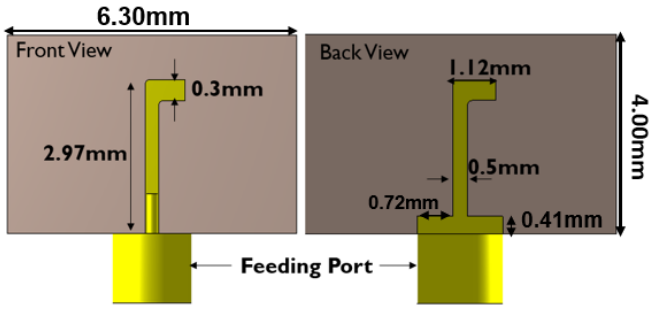


(b)

Fig. 3.3.5 Comparison of simulated and measured phase reflections (a) HIS array (b)PRS array.

3.3.3 Fabrication Of Dipole Antenna For Exciting LWA At 60 GHz Band

In this section, a dipole antenna is printed on a low-loss substrate (RT /Duroid 5880) with a thickness of 0.127 mm, a copper layer thickness of 17.5 μm, and a dielectric constant of 2.2 is presented. As shown in Fig. 3.3.5a, half of the dipole length was etched from top to bottom and the other half from bottom to top to improve the impedance matching of the antenna at the selected feed points. A microstrip line balun with a tapered ground was used to connect the antenna to a normal 50-ohm input. It must be mentioned here that the same etch materials and method was used here as in the previous section. The front and back view of the feeding dipole geometry with dimension is depicted in Fig. 3.3.4a and the fabricated dipole can be seen in Fig. 3.3.5b. A good matching bandwidth S_{11} from 58.4 to 65.7 GHz was observed for the fabricated dipole with a gain of 9.1dBi at 62.5 GHz depicted in Fig. 3.3.6.



(a)



(b)

Fig. 3.3.5 (a) dipole antenna front and rear perspective (b) fabricated dipole.

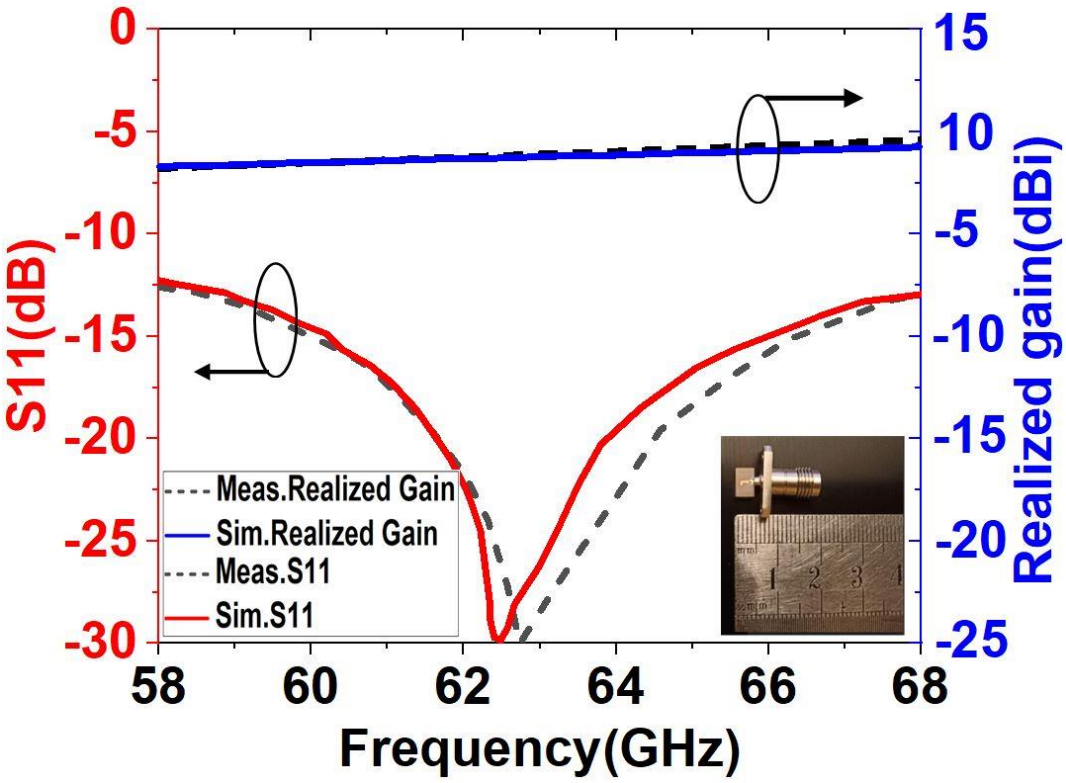


Fig. 3.3.6 (a) dipole antenna simulated and measured gain and S_{11} results.

3.4 Conclusions

In this chapter, low-loss periodic surfaces based on frequency scanning have been demonstrated by simulations and measurement. The proposed HIS structure produces a phase shift of over 128^{o} at 62.5 GHz and a highly reflective PRS reflection magnitude coefficient of 0.9 at 62.5 GHz. One of the best things about the proposed structures is that the losses are very low because no active components are used in the scanning. Application of the proposed frequency-tunable HIS and highly reflective PRS in a 1-D hollow leaky wave antenna (LWA) configuration is presented. The proposed structures have been fabricated and measured where the phases of both arrays are in good agreement. Finally, a printed dipole antenna for LWA excitation has been demonstrated by simulating and measuring with a good gain of 9.1 dBi, a bandwidth of 10 dB, and S_{11} below the -10 dB line, which will be used to excite the LWA in the next chapter.

References

[1] D. Sievenpiper, L. Zhang, R. F. J. Broas, N. G. Alexopoulos, and E. Yablonovitch, "High-impedance electromagnetic surfaces with a forbidden frequency band." *IEEE Transactions on Microwave Theory and Techniques,* vol. 47, no. 11, pp. 2059 - 2074, 1999.

[2] S. Wang, A. P. Feresidis, G. Goussetis, J. C. Vardaxoglou, "Low-profile resonant cavity antenna with artificial magnetic conductor ground plane," *Electronics Letters, vol.* 40, no. 7, pp. 405 - 406, 2004.

[3] A. P. Feresidis, G. Goussetis, S. Wang, and J. C. Vardaxoglou, "Artificial magnetic conductor surfaces and their application to low-profile high-gain planar antennas," *IEEE Transactions on Antennas and Propagation,* vol. 53, no.1, pp. 209 - 215, 2005.

[4] G. Von Trentini, 'Partially reflecting sheet arrays, "Partially reflecting sheet arrays," *IRE Transactions on antennas and propagation, vol,* 4, no. 4, pp. 666 - 671, 1956.

[5] A. P. Feresidis and J. C. Vardaxoglou, "High gain planar antenna using optimised partially reflective surfaces," *IEE Proceedings-Microwaves, Antennas and Propagation,* vol. 148, no. 6, pp. 345-350, 2001.

[6] A. Oliner. "Leaky-wave antennas."Antenna Engineering Handbook", Third Edition, edited by *R. C. Johnson, McGraw Hill*, 1993.

[7] M. García-Vigueras, J. L. Gómez-Tornero, G. Goussetis, A. R. Wiley, and Y. J. Guo, "Enhancing frequency-scanning response of leaky-wave antennas using high-impedance surfaces," *IEEE Antennas and Wireless Propagation Letters,* no.10, pp.7-10, 2011.

[8] S. Lim, C. Caloz, and T. Itoh, “Electronically scanned composite right/left-handed microstrip leaky-wave antenna,” *IEEE Microwave and Wireless Components Lett.*, vol. 14, no. 6, pp. 277-279, June 2004.

[9] R. Guzmán-Quirós, J.-L. Gómez-Tornero, A. R. Weily, and Y. J. Guo, “Electronically steerable 1D Fabry-Perot leaky-wave antenna employing a tunable high impedance surface,” IEEE Trans. Antennas Propag., vol. 60, no. 11, pp. 5046–5055, Nov. 2012.

[10] Online :(http://www.physikinstrumente.co.uk), accessed on 14th Nov. 2021.

[11] E. O. Hammerstad and F. Bekkadal, *A Microstrip Handbook*, ELAB Report, STF 44 A74169, University of Trondheim, Norway, pp. 98 -110, 1975.

[12] O. Bayraktar, O. Civil, and T. Akin, "Beam switching reflectarray monolithically integrated with RF MEMS switch," *IEEE Transactions on Antennas and Propagation*, vol. 60, no. 2, pp. 854-862, 2011.

[13] C. Guclu, J. Perruisseau-Carrier, and O. Civi."Proof of concept of a dual-band circularly-polarized RF MEMS beam-switching reflectarray." *IEEE Transactions on Antennas and Propagation.* vol. 60, no. 11 pp. 5451-5455, 2012.

[14] W. Hu, R. Dickie, R. Cahill, *et al*. "Liquid crystal tunable mm-wave frequency selective surface." *IEEE Microwave and Wireless Components Letters*, vol. 17, no. 9 pp. 667-669, 2007.

[15] G. Perez-Palomino, P. Baine, R. Dickie, M. Bain, J. Encinar, R. Cahill, M. Barba, and G. Toso, "Design and experimental validation of liquid crystal-based reconfigurable reflectarray elements with improved bandwidth in F-band," *IEEE Transactions on Antennas and Propagation*, vol. 61, no. 4, pp. 1704-1713, 2013.

Chapter 4: Leaky Wave Antenna Designs For Remote Vital Signs Monitoring At Millimetre-Wave Frequencies

Doppler radar allows noncontact measurement of breathing and heart rate, making it a more convenient method of monitoring a patient's vital signs than conventional monitoring devices [1,2]. As a result, remote vital signs monitoring (RVSM) is in high demand in the fields of general and speciality healthcare, emergency services, defence, and security services [3 - 6]. However, the reliability and accuracy of the RVSM using a Doppler radar system must be adequately addressed for it to be useful for real-world applications [7 - 9].

In this chapter, two leaky wave antennas (LWAs) with enhanced gain and beam scanning in the 60 GHz band (58 - 68 GHz) are presented for remote detection of a person's breathing and heart rate using the Doppler radar concept. The measured and simulated results of the antennas showed good agreement in all cases. A 39-year-old man's breathing rate (BR) and heart rate (HR) were measured at distances of 0.6 m, 1 m, and 2 m using a PRS and ground plane antenna configuration and PRS-HIS base antenna operation. RVSM makes use of two antennas that are the same, one for transmission and the other for reception in both antenna operations. It was discovered that PRS-HIS's remote vital sign monitoring (RVSM) accuracy is superior to that of PRS and ground plane antenna configuration. Additionally, it has been noted that using higher-gain antennas produces more obvious visual results because the main radar beam is focused on the subject's chest. Furthermore, the sensitivities of a 10 GHz RVSM patch antenna and a 60 GHz RVSM base antenna using the PRS-HIS base antenna are contrasted and compared. For this purpose, patch antenna arrays at 10 GHz were designed and the RVSM measurements were performed.

It was discovered that the respiration and heartbeat signals were 2.35 and 12.96 times stronger, respectively, at 60 GHz than at 10 GHz. This is due to the high gain of 60 GHz compared to 10 GHz. Therefore, the proposed LWA was compared with other RVSM-based work from the recent literature at mm-wave frequency. The main contribution of the proposed LWA is the ability to achieve a 30° beam scan up to 2 metres from the human body with an improved HR accuracy of 93%, which is a significant improvement in the literature compared to other antenna systems used for RVSM except for horn antenna. Additionally, the proposed antenna operates with an enhanced realised gain of 22.3 dBi and a radiation efficiency of 95.5%.

4.1 LWA Designs Base on Periodic Structures For RVSM

In this section, a beam-scanning leaky wave antenna (LWA) is designed as an application of the proposed HIS and PRS structures. The main beam's direction of the LWA is controlled by changing frequency. The HIS structure with $l_{in} = 0.6\ mm$ and the PRS structure with $t_1 = 0.51\ mm$ described in Chapter 3 have been used in this section in a 1D hollow LWAs (Fig. 4.1.1a, b). It is important to remember that highly directive antennas require high reflection magnitude values. The size of the HIS inner loop primarily controls the reflection phase, whereas the PRS aperture size primarily controls the magnitude of the reflection coefficient. As a result, the unit cell's dimensions (Fig. 4.1.1(c)) were carefully chosen to achieve a reflection phase of nearly zero degrees at 62.5 GHz. Periodic boundary conditions in CST simulation software under the assumption of an infinite structure are applied to extracted reflection properties of HIS and PRS arrays.

The PRS and HIS arrays are made up of a 50 x 15 array of square metallic elements and square loop metallic elements, respectively, printed on a Roger 5880 substrate.

The PRS is positioned on top of the ground plane at a distance h_1 = 3.8 mm in the first example of LWA design, as shown in Fig. 4.1.1a, resulting in a resonant cavity type LWA.

In the second LWA design, the PRS is placed on top of the HIS ground at a distance *h = 2.90 mm* as depicted in Fig. 4.1.1b.

As shown in Fig. 4.1.1a, b, the cavity of the antennas is excited by an ideal dipole, and that side is closed off by a vertical metallic ground. The overall profile of the antenna is approximately λ/2.

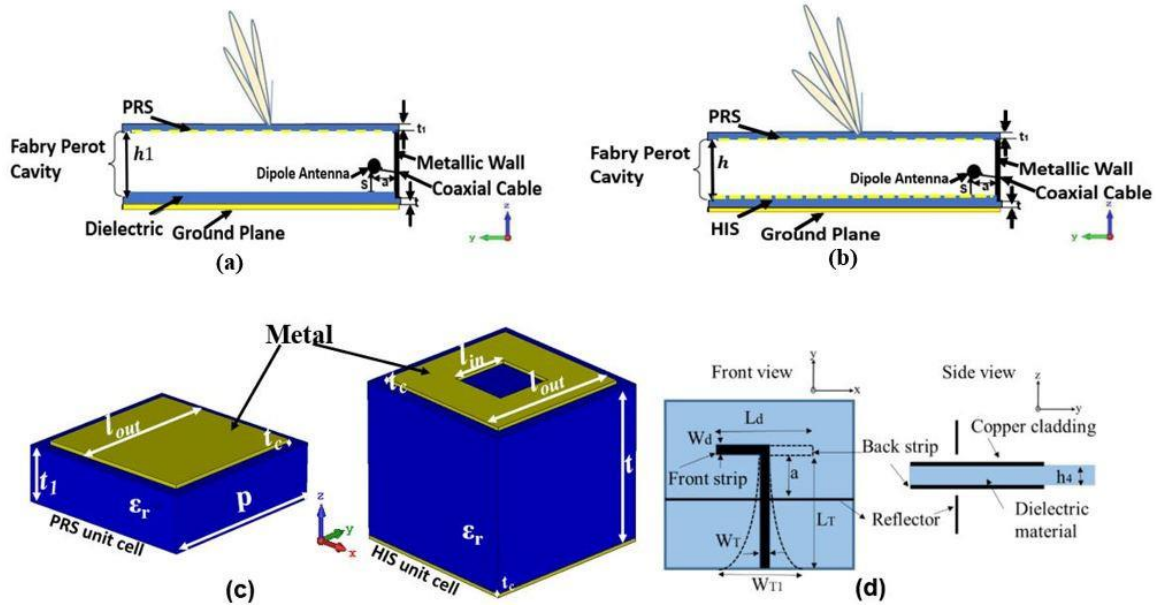


Fig. 4.1.1 Proposed LWAs geometry. (a) LWA without HIS, (b) LWA with HIS (c) PRS and HIS unit cells, and (d) feed dipole antenna (Measurements not to scale).

The antenna works by satisfying a resonance condition to achieve constructive interference and, consequently, high directivity performance, which can be represented using the ray optics technique [10]. The High Impedance Surface (HIS) functions as a ground plane to introduce the necessary phase shift when the frequency is changed, which in turn changes the cavity's resonant condition and, as a result, regulates the pointing angle of the antenna's radiation beam for a range of frequencies.

Fig. 4.1.1(c) depicts the HIS and PRS unit cells with different thickness substrates $t = 1.75mm$ and $t_1 = 0.52mm$ respectively and are commercially available. The periodicity of PRS corresponds to the periodicity of the HIS array ($p = 1.75mm$), while the size of the patch is $l_{out} = 1.50\ mm$. The PRS's dimensions were selected to produce high directivity by generating large reflectance values from the surface. The dimensions of the feeding dipole antenna (Fig. 4.1.1d) are as follows: $L_d = 2.24\ mm$, $Wd = 0.3\ mm$, $LT = 2.97\ mm$, $WT = 0.3\ mm$, $WT\ 1 = 1.44\ mm$, with 17.5 μm substrate thickness and a surface area of 6.30 mm × 4.0 mm. In Fig. 4.1.1 (a, b), ***s*** and ***a*** are 0.6 mm and it denotes the separation between the dipole and HIS array or ground and the metal wall respectively.

4.1.1 Beam Scanning Range Analysis With PRS And Ground Plane LWA

In this section, we used analytical equations to analyze the beam scanning range for the first case of the proposed leaky wave antenna (LWA) without HIS, i.e., PRS and ground plane configuration structure. A simple approach to plane wave analysis based on infinite arrays can be used to obtain a comprehensive picture of the range of antenna beam scanning that can be achieved without the sensitive HIS structure. The radiation pattern of the LWAs is described by an earlier equation (2.1- 6) developed in [10, 11], which also takes into account the ground reflection phase (φ_{GND}).

The performance of PRS and ground plane antenna configurations in the simulation is presented. As can be seen in Fig. 4.1.2, a continuous beam scanning mode was generated between 60 and 66 GHz, covering 10^o to 28^o. From equation (2.1- 6), it can be seen that lambda (λ) is a function of frequency, resulting in beam scanning as the frequency changes. The analytical result of the antenna without the HIS structure shown in Figure 4.1.2, has a beam scan of approximately $\Delta\theta = 18°$ and a bandwidth of 6 GHz.

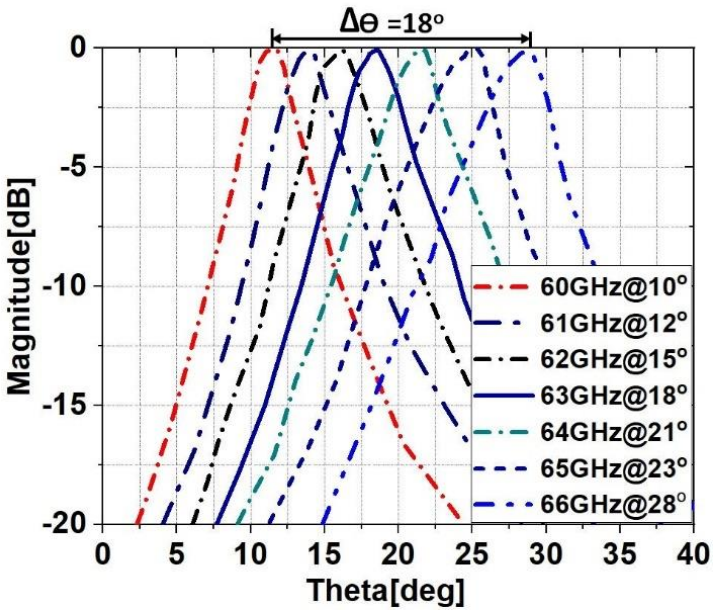


Fig. 4.1.2 Frequency scanning of the LWA without HIS from 60 GHz to 66 GHz calculated theoretically for $h_1 = 3.38$ *mm.*

This confirms the theoretical analysis in Chapter 2 section 2.1.1, where higher-order resonance cavity heights for LWA without HIS were used.

The simulation study shown in Fig. 4.1.2. with a cavity height $h_1 = 3.8$ *mm* improves return loss and moderate-high gain performance for PRS and ground plane antenna configuration. The cavity thickness $\boldsymbol{h_1}$ depends on the phase reflections of the PRS and the ground plane [11].

4.1.2 Beam Scanning Range Analysis With PRS-HIS LWA

It must be mentioned here that similar analytical equations with slight modifications are used for the analysis of the PRS and HIS leaky wave antenna configuration. For this reason, the ground phase (φ_{GND}) in Equation (2.1- 6), is replaced with a HIS phase ($\boldsymbol{\varphi_{HIS}}$), then a new pointing angle could be expressed as:

$$P = \frac{1 - \mathrm{R}^2}{1 + \mathrm{R}^2 - 2\mathrm{R}\cos\left(\varphi_{PRS} - \boldsymbol{\varphi_{HIS}} - \frac{4\pi}{\lambda} \cdot h \cdot \cos(\theta)\right)} \cdot F(\theta)^2 \qquad (4.1-1)$$

where P is the pointing angle, F^2 is the radiation pattern of the dipole, P is the pointing angle, R is the magnitude reflection coefficient of PRS, h is cavity height, ϕ_{PRS} is the PRS phase and ϕ_{HIS} is the phase reflection of HIS.

The term $F(\theta)^2$denotes the radiation pattern of the dipole over a ground plane and it is assumed to be 1 in calculating the pointing angle (*p*) and comes from (4.1-1), which can be expressed in (4.1-2).

$$F(\theta) = \cos\left(\theta + \frac{\pi}{2}\right) cos\left(\frac{1}{2}k \cdot acos\left(\theta + \frac{\pi}{2}\right) + \pi\right) \qquad (4.1-2)$$

where ***a*** denotes the separation between the dipole and the metal wall and ***k*** denotes the wavenumber (see Fig. 4.1.1 a, b).

In this investigation, it was found that unidirectional LWA can be generated by exciting the antenna cavity with a dipole on one side of the cavity and terminating the cavity with a vertical metallic ground (Fig. 4.1.1 b).

A continuous beam scanning performance from 3º to 33º was determined for PRS and HIS antenna configuration operation from 58 GHz – 66 GHz (Fig. 4.1.3). The beam scanning range obtained for PRS and HIS-based LWA is $\Delta\theta = 30^o$. This analysis shows that the HIS-based LWA with a cavity height of ***h*** = *2.90 mm* achieve larger beam scanning, resulting in a high gain that can be useful for longer-range RVSM detection.

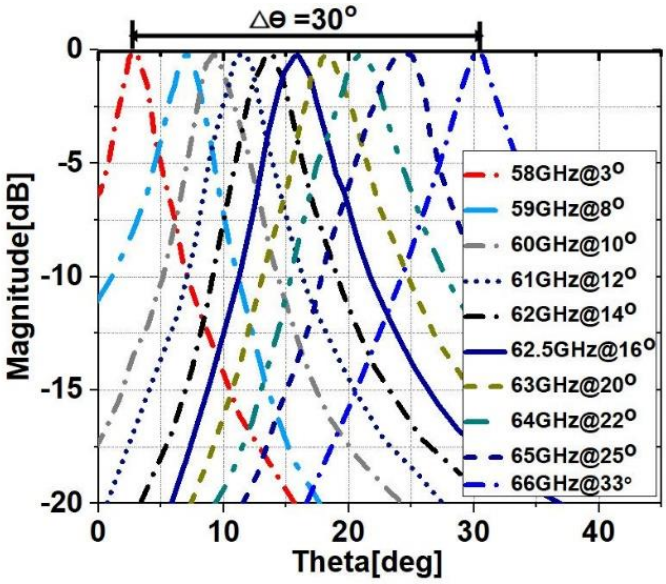


Fig. 4.1.3 Estimated theoretical HIS-based frequency scanning of the LWA from 58 GHz to 66 GHz for ***h*** = *2.90 mm*.

The phases of the reflection coefficient of PRS and HIS (φ_{PRS} and $\boldsymbol{\varphi_{HIS}}$) was considered in the antenna simulation design, which is crucial for determining the cavity thickness ***h*** between PRS and HIS array. In the next section, the performance of the measured and simulated results of the two proposed LWAs for RVSM is presented.

The key parameter determining the scanning range for remote vital sign monitoring using a leaky wave antenna is the **operating frequency** of the radar source. By adjusting the operating frequency within a certain band, the beam of the antenna can be scanned over a desired angular range to detect vital signs of multiple targets. Another key parameter that determines the frequency scanning range of LWAs is the dispersion of the waveguide, which is a measure of the variation in the phase velocity of the RF signal as it travels along the waveguide. The dispersion of the waveguide determines the phase shift of the propagating signal and thus the direction of the beam, which can be controlled by the design of the LWA (i.e., the shape, size, and material properties of the waveguide). By optimizing the design of the waveguide, it is possible to achieve a wide frequency scanning range and high beam steering accuracy.

4.2 Finite Size Leaky Wave Antenna Simulations And Measured Results

This section discusses the proposed LWA measurement, which was performed in an anechoic chamber. The realised gain of the proposed leaky wave antennas (PRS-ground antenna and PRS-HIS antenna configurations) was determined using the gain comparison method. This method requires two antennas: one as a receive antenna with a known gain (in our case, a horn antenna) and another as a transmitter antenna with an unknown gain (our proposed LWA). The antennas were placed at a far-field distance of 2 m. Friis' equation was then used to calculate the gain of the antennas. A schematic diagram of the setup in the anechoic chamber is presented in Fig. 4.2.1.

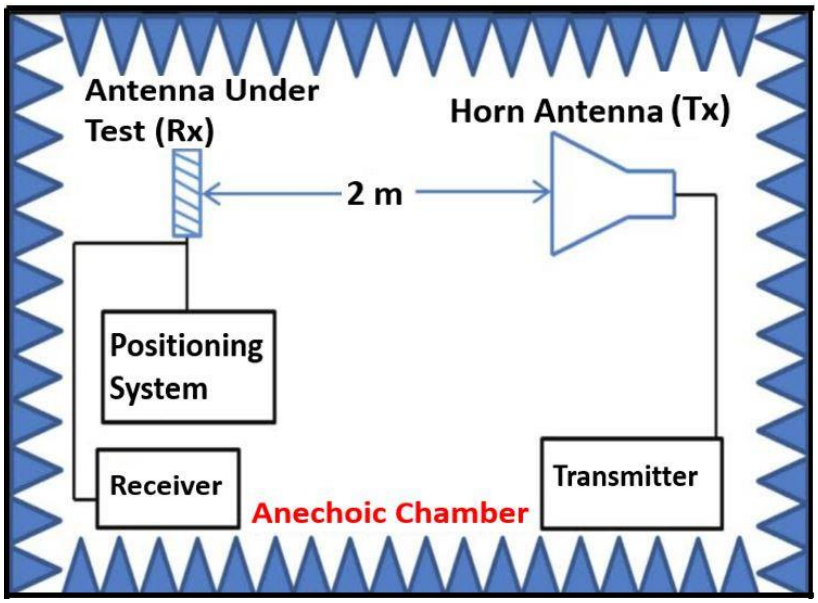


Fig. 4.2.1 A schematic setup of gain and radiation pattern measurement in the anechoic chamber.

An anechoic chamber (Fig. 4.2.1) is a space that absorbs all sound waves and electromagnetic radiation, creating an environment in which measurements can be made without interference from external sources. To measure the gain of an antenna in an anechoic chamber, the following steps are performed: The antenna is mounted on a rotating platform and connected to a transmitter or receiver. The signal is measured at different points while it is rotated in a full 360-degree circle using a calibrated receiving

antenna. The collected data is used to calculate the gain of the antenna, which is usually expressed in decibels (dB). The measurements were repeated at different frequencies to determine the frequency response of the antenna. To ensure accurate measurements, the VNA and the other equipment used were carefully calibrated and controlled to produce accurate results.

The antenna with the PRS and ground plane design obtained roughly 20 dBi gain, whereas the antenna with the PRS and HIS configuration achieves 22 dBi gain. Fig. 4.2.2 shows the fabricated inside view of the leaky wave antennas, where (a)-(b) and (c)-(d) are two duplicates of the leaky wave antenna (LWA) without HIS elements and the leaky wave antenna (LWA) with HIS elements, respectively.

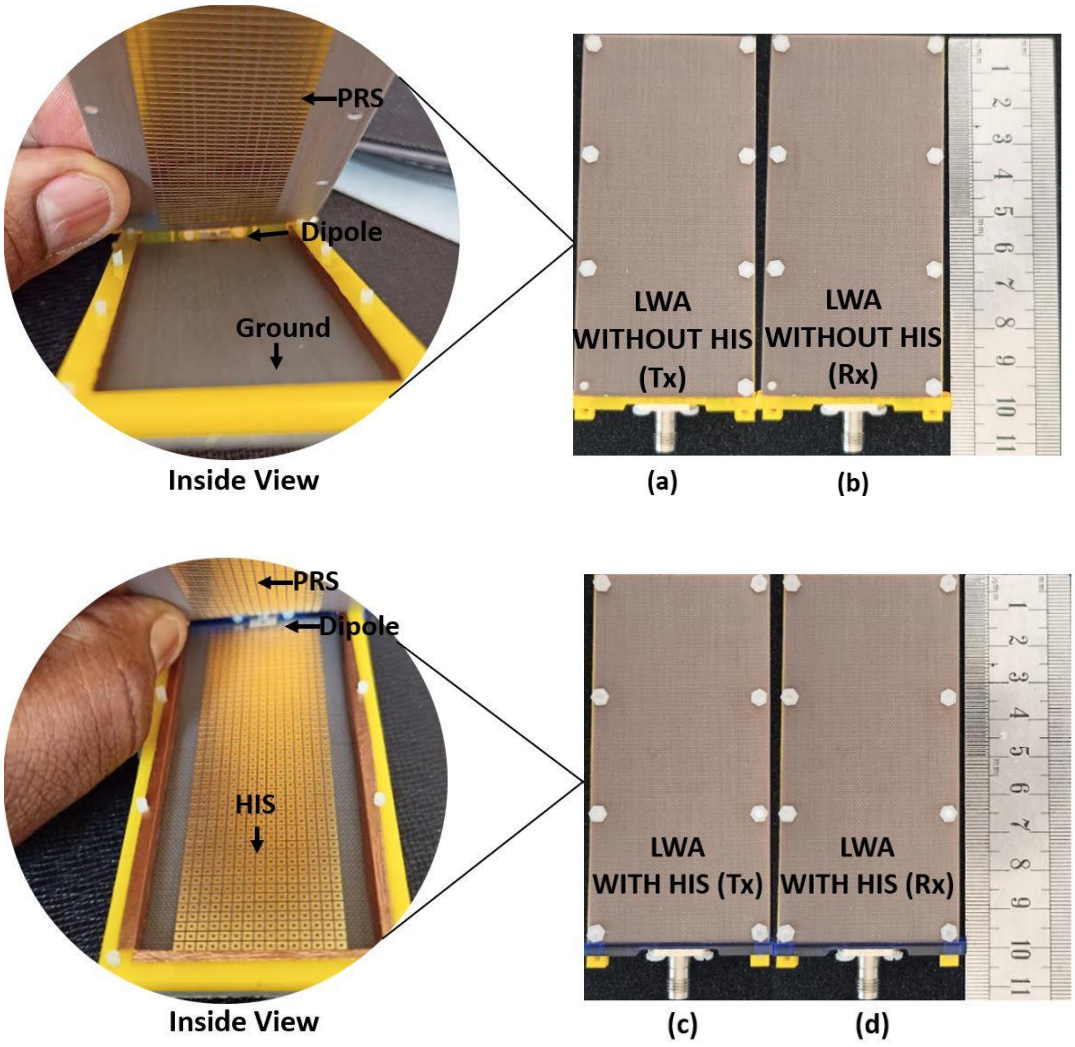
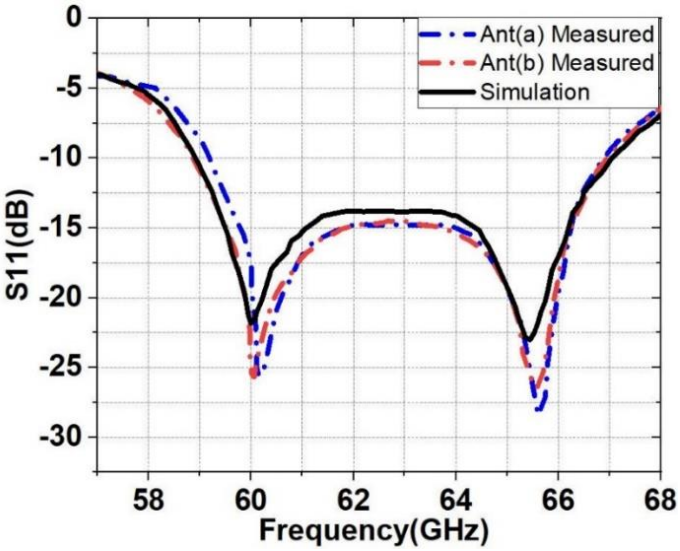
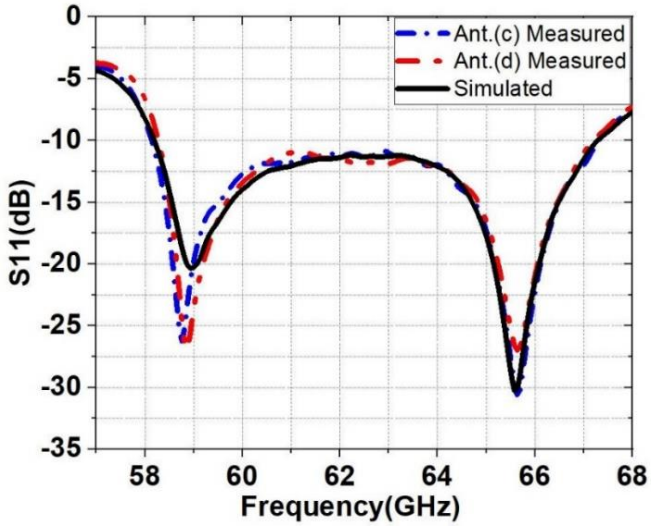


Fig. 4.2.2 Fabricated LWA **without HIS (a)-(b**) and LWA **with HIS (c)-(d)** for RVSM.

The antenna arrays were fabricated using a low-loss RT/Duroid 5880 substrate with a dielectric constant of $\varepsilon_r = 2.2$. A conventional and inexpensive method of producing printed circuit boards was used to build the antenna layers. The housing for the coaxial feed and the whole antenna assembly is made of PTFE, which has a low loss. PTFE is a fluoropolymer made from tetrafluoroethylene. It is great for a wide range of uses, such as making antenna enclosures that are easy to put together and measure. The external connector is made up of a 1.85 mm flanged launcher and a GB185 glass bead. The size of each array produced exceeds the 152 μm linewidth/gap PCB etch limit for ease of fabrication. The PRS and HIS boards were attached to the frame with a total of eight plastic screws, one in each corner of the board. In addition to the frame, plastic spacers were used to keep the boards straight and evenly spaced. The plastic spacers used on the prototype antenna had a tolerance of about ± 0.05 mm, similar to the PCB. Figures 4.2.3 (i) and (ii) depict the simulation and measured return loss values (S_{11}) of leaky-wave antennas PRS and ground plane, as well as the PRS-HIS antenna configuration, respectively. The simulation and the measured S_{11} results exhibit a high degree of agreement, as can be seen in Fig. 4.2.3. The antennas in Figure 4.2.3 (i) and (ii) have resonances that are centred between 58.75 GHz and 66 GHz. Therefore, 58 GHz and 66 GHz frequency tones have been respectively selected for the RVSM when antennas 4.2.3(i) and 4.2.3(ii) are employed.



(i)



(ii)

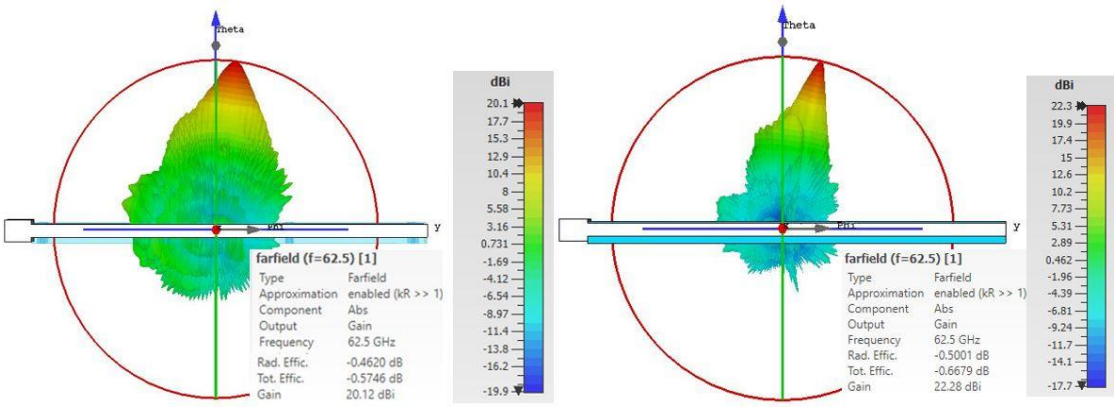
Fig. 4.2.3 Simulated and Measured S_{11} values for **(i)** LWA without HIS and **(ii)** LWA with HIS.

The two matching points of S_{11} observed in Fig. 4.2.3, mean that the antennas are well-matched to the transmission line and there is a minimal reflection of the transmitted signal. In other words, the impedance of the antenna matches the impedance of the transmission line, and as a result, the signal can pass through the line without any significant loss or distortion. This is an important factor in the antenna system design because any mismatch between the antenna and transmission line can result in signal loss, signal distortion, or damage to the transmitter or receiver. Measurements and optimizations of the S_{11} parameter were performed to ensure that the proposed antennas

operate at maximum efficiency and that the transmitted and received signals are of the highest possible quality for RVSM.

The simulated 3D far-field radiation (FRP) patterns for the proposed antennas, which are a graphical representation of the antenna's radiation characteristics, are shown in Fig. 4.2.4 (a) and (b). The radiation intensity is usually represented by a colour scale, with different colours indicating different intensity levels. These patterns are useful for a variety of applications, including antenna design, optimisation and testing. By analysing the far-field radiation pattern of an antenna, designers can evaluate its performance, identify problems or limitations, and optimise the design to achieve the desired radiation characteristics.

The simulated 3D far-field plot also provides a way to compare the radiation characteristics of an actual antenna with the predicted characteristics. By comparing the measured radiation pattern of an antenna with the simulated plot, any discrepancies or problems that may need to be addressed can be evaluated and identified.



(a) (b)

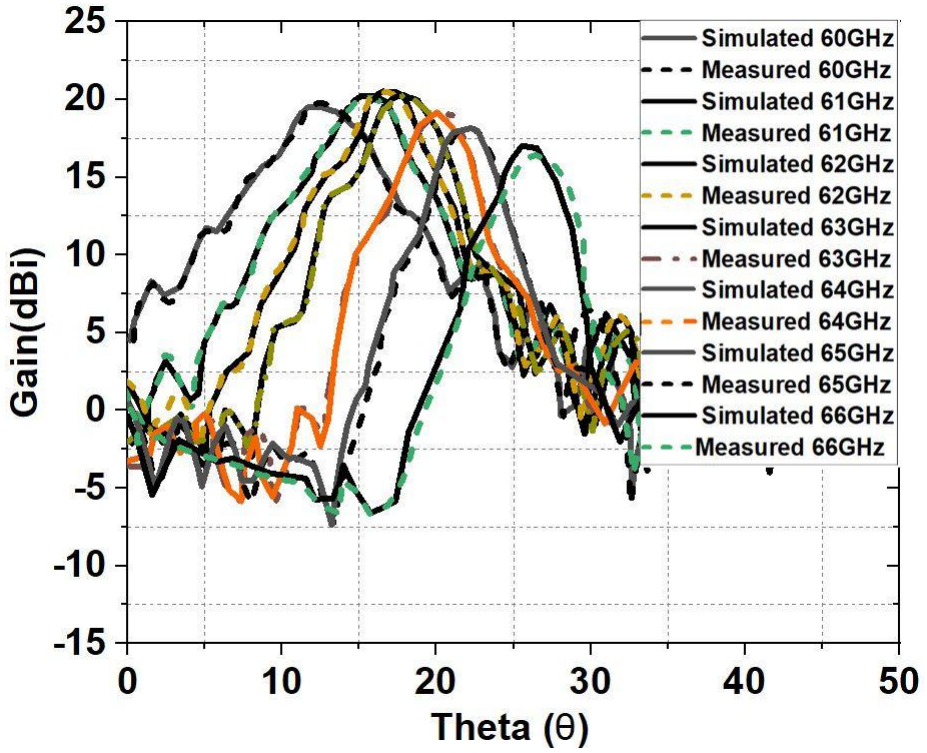
Fig. 4.2.4 Simulation 3-D FRP of LWAs (a) LWA without HIS (b)LWA with HIS.

The results of all measured antennas for S_{11} and the far-field radiation pattern (FRP) are within the tolerance for PCB fabrication [12-13]. Some distortions are seen for the

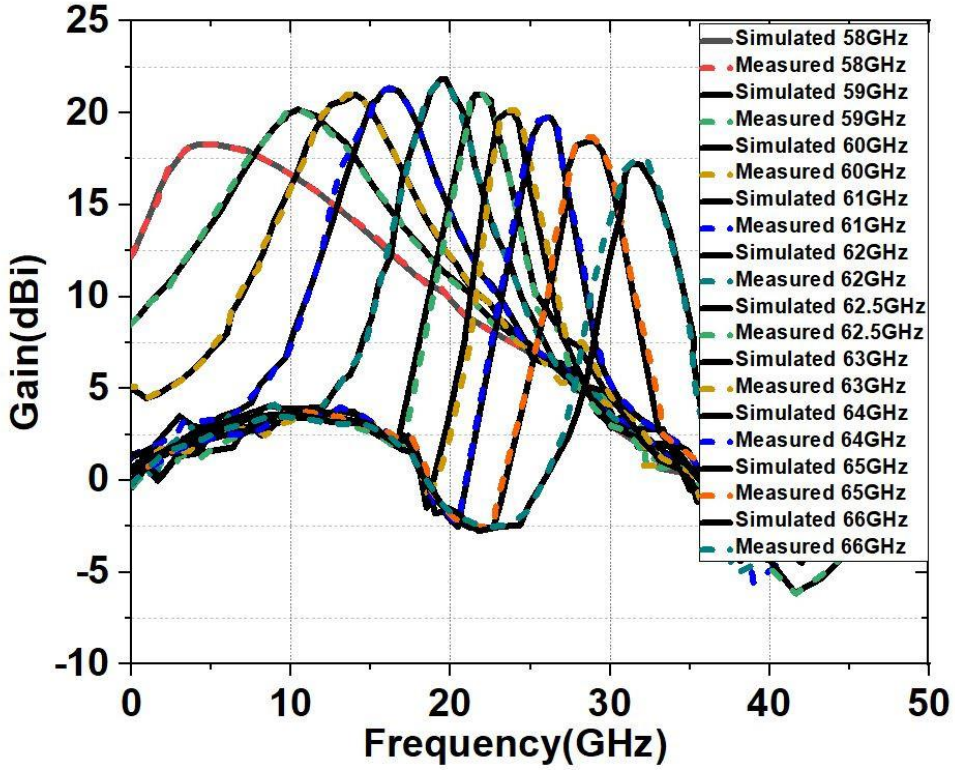
antennas in Figs. 4.2.4(b) and 4.2.5(a), which are brought on by reflections from the test fixtures and the environment [13–14]. Figure 4.2.5 presents the 2D results of simulations and measurements conducted on the FRP in H planes at the frequencies of interest. According to Figs. 4.2.5, the primary radiation lobes of the antennas are directional and scan with frequency in the H-planes.

The antennas' simulated and the measured gain can be seen in Fig.4.2.6 and is summarized in Table 1. It is self-evident that the gain has increased due to the use of PRS and HIS antenna configuration compared to PRS and ground plane antenna configuration. However, since only a single tone frequency is used for the detection method, the bandwidth (BW) is not critical for our current application of RVSM. The efficiency of the antennas is increased in both scenarios, reaching a maximum of 92.87% for LWA without HIS and 95% for LWA with HIS at 62.5 GHz (See Fig. 4.2.7) with fewer side lobes.

The efficiency of an antenna is the ratio between the power radiated by the antenna and the power supplied to the antenna. There are different methods to estimate the efficiency of an antenna. In this research, we use computer simulation software in CST to accurately estimate the efficiency of the proposed antenna. An electromagnetic field solver in CST model the antenna's behaviour and predict its performance as shown in Fig. 4.2.7.

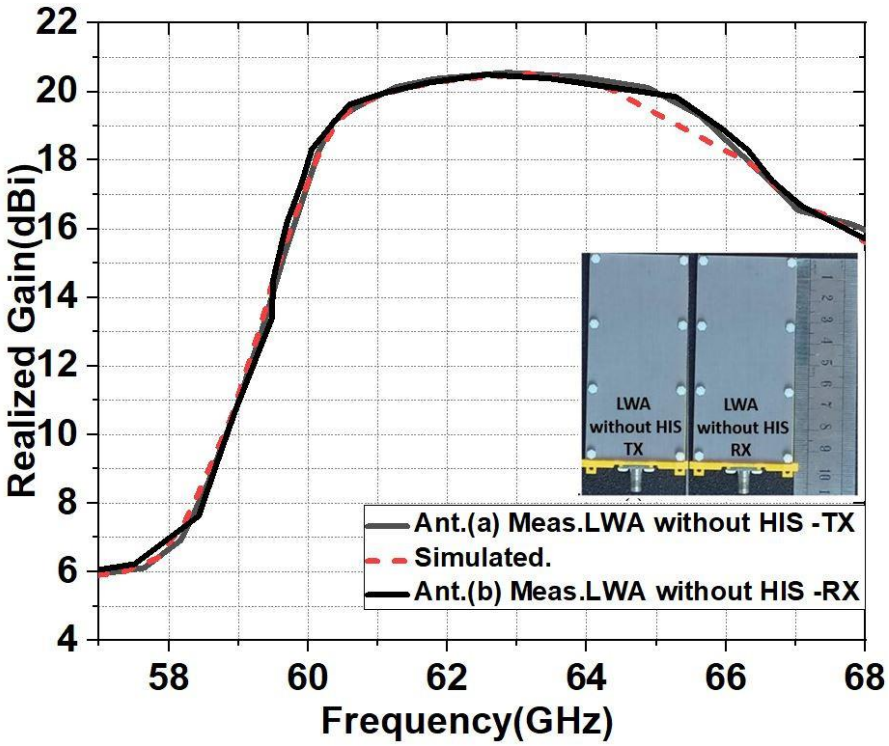


(a)

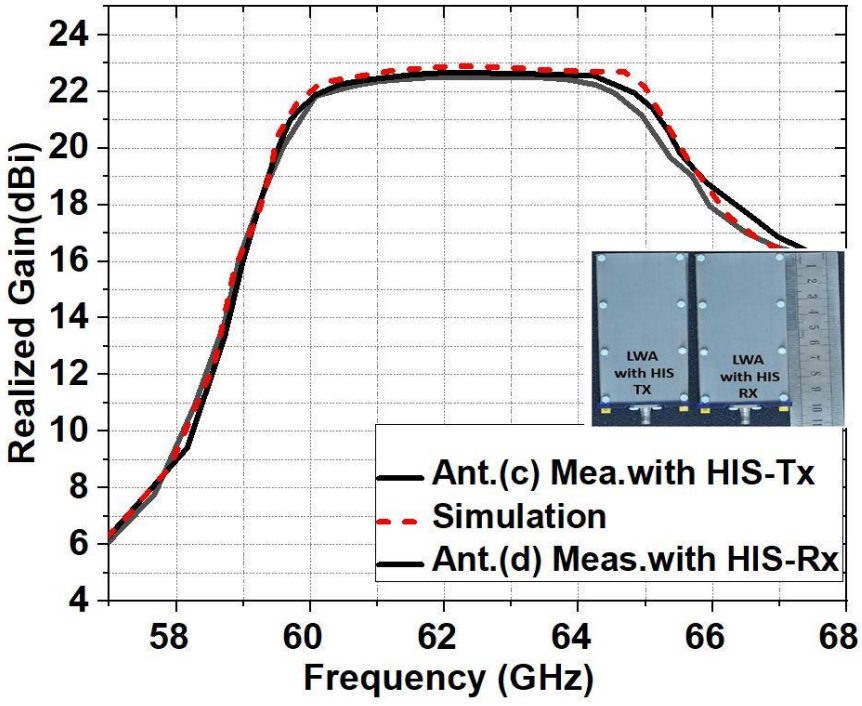


(b)

Fig. 4.2.5 Measured and simulated beam scanning LWAs (a) without HIS and (b) with HIS.



(a)



(b)

Fig. 4.2.6 Simulated and Measured gain of LWAs (a)without HIS and (b) with HIS for RVSM.

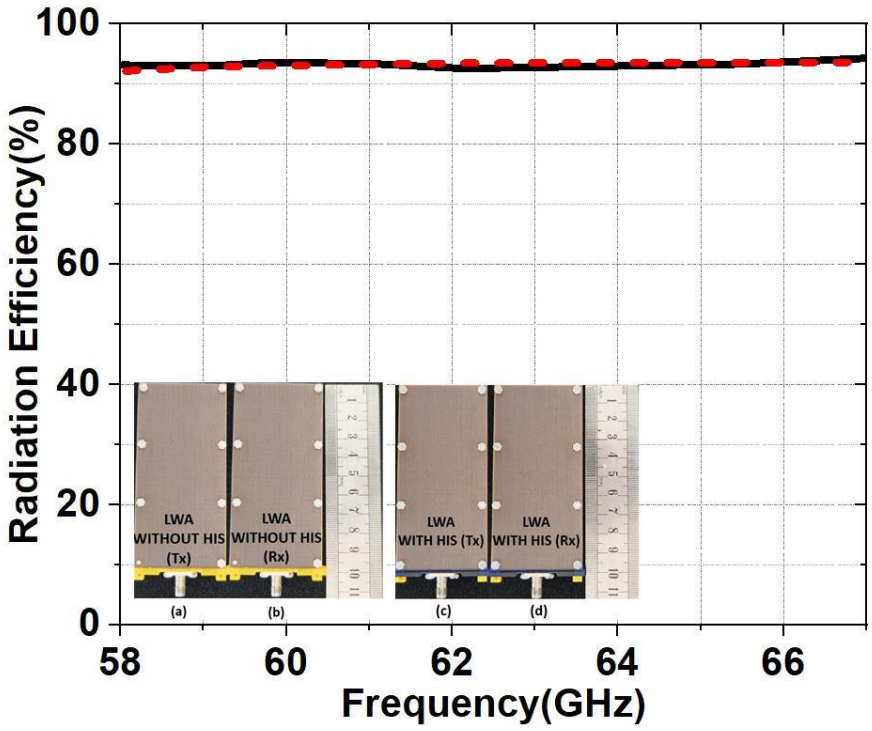


Fig. 4.2.7 Radiation efficiency of LWAs without and with HIS for RVSM.

Table 1. Performance Of Simulated And Measured Antennas

Performance features	Operating band (S_{11}< -10dB)	Gain (dBi)	Beam scanning	HPBW
Ant.(a) Measured	59.8 GHz and 67 GHz	20.1	18^o	12^o -5^o
Ant.(b) Measured	59.8 GHz and 67 GHz	20.1	19^o	14^o -6^o
Simulated	59 GHz and 66.9 GHz	20.6	18^o	9^o - 4^o
Ant. (c) Measured	58.35 GHz and 67 GHz	22.3	29^o	13^o - 6^o
Ant.(d) Measured	58.50 GHz and 67 GHz	22.2	30^o	14^o - 7^o
Simulated	58.34GHz and 66.4GHz	22.3	30^o	9^o - 6^o

4.3 Application Of LWA At 60 GHz Band RVSM With Doppler Radar

Figure 4.3.1 depicts a block diagram of the various steps of the RVSM process when Doppler radar is used to detect vital signs. A transmitting antenna (Tx) transmits a continuous electromagnetic wave with a single frequency tone. At a predetermined distance (d), the wave is reflected off the person's chest and is picked up by a reception

antenna (Rx). The quasi-periodic vibration of the chest brought on by breathing and heartbeat phases modulates the signal received.

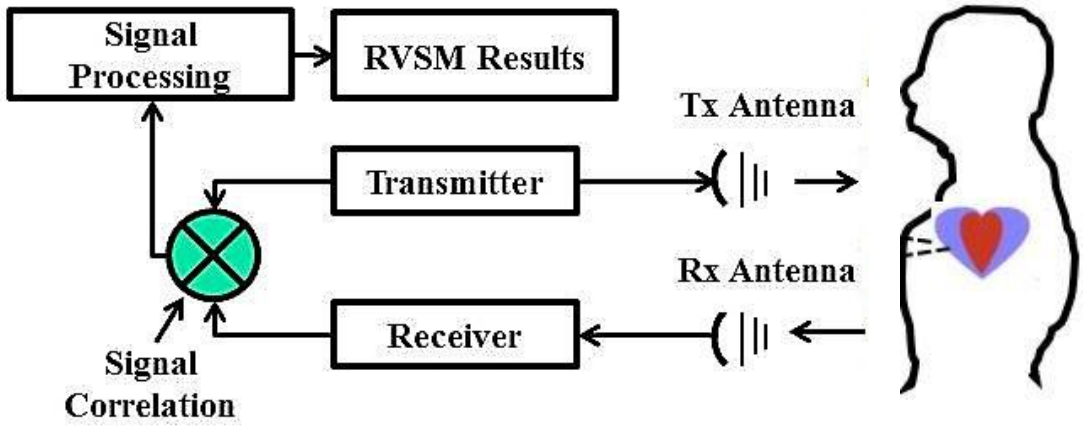


Fig. 4.3.1 RVSM signal processing diagram.

At the receiver (Rx), this phase-modulated signal is demodulated and correlated with the radiated signal, and the resulting data is stored for some time. The subject's respiration rate and heart rate are then determined by processing the raw data from the time domain using a variety of signal processing methods, such as the Fourier transform and digital filtering.

Doppler radar theory allows for an approximate calculation of the received baseband signal R(t) for a transmitted signal $S(t) = \cos(2\pi ft + \theta(t))$, where f and $\theta(t)$ are the frequency and phase of the [15]:

$$R(t) = \cos\left[\theta(t) + \frac{4\pi x_b(t)}{\lambda} + \frac{4\pi x_h(t)}{\lambda}\right] \qquad (4.4.-1)$$

where $\theta(t)$ denotes the overall phase shift brought on by ambient reflections, the signal path (d), and any lingering phase noise. The signals of the chest vibrations based on the operating wavelength caused by respiration and heartbeat are denoted as $\lambda, x_b(t)$ and $x_h(t)$ respectively. The $x_b(t)$ and $x_h(t)$ are periodic which can be estimated in the calculation as $x_b(t) = m_b \sin(2\pi f_b t)$ and $x_h(t) = m_h \sin(2\pi f_h t)$ where m_b and m_h are respiration and heartbeat cause the displacement amplitudes of chest motion

respectively. The BR and HR frequencies are denoted by f_b and f_h, respectively. In this method, the Fourier series expansion of equation (4.4-1) yields [16]:

$$\mathrm{R(t)} = \sum_{\mathrm{i}=-\infty}^{\infty} \sum_{j=-\infty}^{\infty} \mathrm{J}_j\left[\frac{4\pi \mathrm{m_b}}{\lambda}\right] \mathrm{J_i}\left[\frac{4\pi \mathrm{m_h}}{\lambda}\right] \cos(j2\pi f_b t + i2\pi f_h t + \theta) \qquad (4.4.-2)$$

where $J_n(X)$ is a first-order Bessel function with argument X. The above equation can be written using the first positive harmonics of $\mathrm{f_b}$ and $\mathrm{f_h}$:

$$\begin{aligned} R(t) \quad &= J_1\left[\frac{4\pi m_b}{\lambda}\right] J_0\left[\frac{4\pi m_h}{\lambda}\right] \cos\left(2\pi f_b t + \theta\right) \\ &+ J_0\left[\frac{4\pi m_b}{\lambda}\right] J_1\left[\frac{4\pi m_h}{\lambda}\right] \cos\left(2\pi f_h t + \theta\right) \end{aligned} \qquad (4.4.-3)$$

where $\mathrm{J_1}\left[\frac{4\pi \mathrm{m_b}}{\lambda}\right] \mathrm{J_0}\left[\frac{4\pi \mathrm{m_h}}{\lambda}\right]$ and $\mathrm{J_0}\left[\frac{4\pi \mathrm{m_b}}{\lambda}\right] \mathrm{J_1}\left[\frac{4\pi \mathrm{m_h}}{\lambda}\right]$ are, respectively, the amplitudes of the R(t) phase variations caused by breathing and heartbeat. The main information regarding the 60 GHz band's suitability for RVSM is provided in equation (4.4-3), which will be used to analyze and visualize the key RVSM parameters at 60 GHz.

To analyze and visualize the key RVSM parameters, Fig 4.3.2(a) displays the graph of $\mathrm{J_0(X)}, \mathrm{J_1(X)}$ and the combination of the parameters X to 30. It can be shown that $\mathrm{J_0(X)}$ and $\mathrm{J_1(X)}$ are periodic operations with some phase shift, and the peak amplitude of their product is much shorter than the individual maximum amplitudes, and it passes through zero values twice as compared to single $\mathrm{J_0(X)}, \mathrm{J_1(X)}$ curves. However, for larger values of argument X, in this particular case, the intensity of the received BR and HR signal is composed of a combination of $\mathrm{J_0(X)}$ and $\mathrm{J_1(X)}$, but at various parameters of the argument X which are regulated by $\mathrm{m_b}$ and $\mathrm{m_h}$ as shown in equation (4.4-3). For our present RVSM scenario at 60 GHz-band, λ is around 4.8 mm, $\mathrm{m_b} = (8 - 12)\mathrm{mm}$ and $\mathrm{m_h} = (0.2 - 0.5)\mathrm{mm}$ for a person at rest with regular breathing [17]. Fig.4.4.2. (b)-(d) illustrate the phase-amplitude fluctuations of the R(t) signal for various combinations of

m_b and m_h with BR and HR combined. As shown in Fig. 4.4.2. (b), the highest R(t) amplitude is about 40, which is sufficient for RVSM detection. However, there is a zero or null line with a chest amplitude of about 9.9 mm. A comparable zero line is only visible for the signal BR in Figure 4.4.2(c). However, Fig. 4.3.2. (d) the obtained HR signal contains two null lines at 8.8 mm and 11 mm of chest displacement, and the maximum phase amplitude of the heartbeat is approximately one-third that of respiration. It is possible that these undesirable m_b and m_h combinations will exist, leading to the null detection points, but this is highly unlikely (see equation (4.4-3). Nevertheless, a small modification can be made by varying λ to avoid these points [16]. In summary, RVSM in the 60 GHz band has a high possibility to detect BR and HR, although BR may be easier to distinguish from the HR signal.

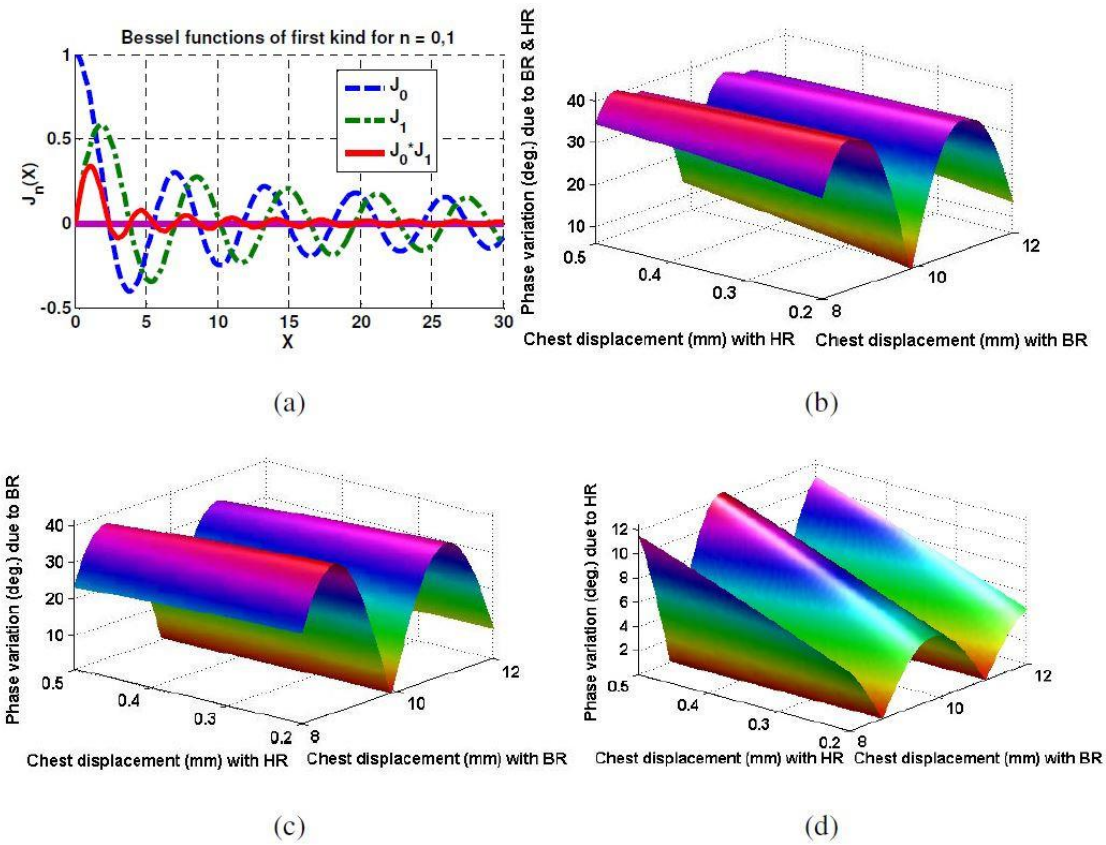


Fig. 4.3.2 (a) Representations of Bessel functions for the argument X with their combination $J_0(X)$ of $J_1(X)$ for magnitude and phase-amplitude of R(t) in equation (4.4-

3) result from different combinations of m_b and m_h (b) combination of both BR and HR, (c) signal for BR only, and (d) signal for HR only.

4.4 RVSM Measurements And Discussions

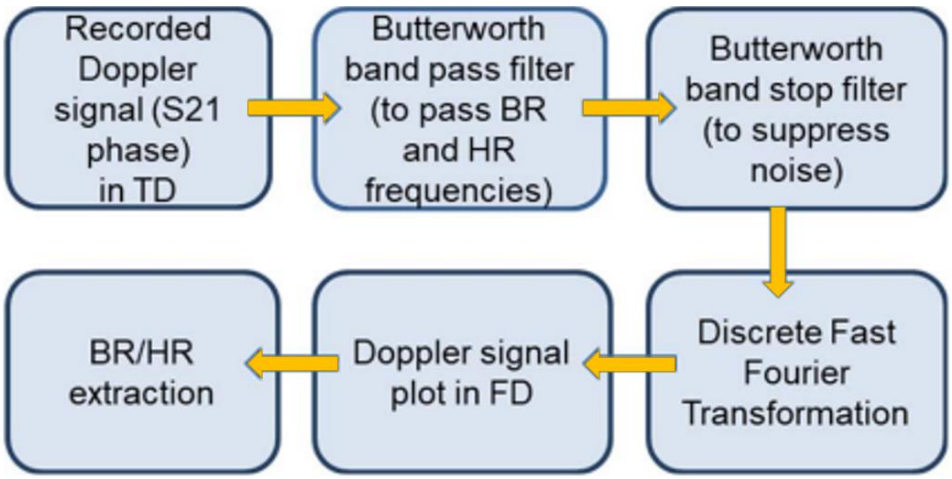
Figure 4.4.1 shows the experimental setup for RVSM measurements in the 60 GHz band. The RVSM transceiver used is the Rohde & Schwarz VNA 67 GHz, which uses two similar antennas, one for transmitting and the other for receiving the reflected signal from the subject. The Vector Network Analyzer (VNA) is a sophisticated electronic instrument that has a built-in mixer to correlate the received and transmitted signals, which is an advantage as no external components are required. In addition, the VNA offers a wide range of parameters, such as frequency, power, etc., which can be easily varied. For example, the VNA can measure the S21 phase of the received reflected signal.

Prior to data collection, the VNA was programmed with Microsoft Visual Basic and connected to a laptop via a GPIB-to-USB converter. The antennas were spaced 20 cm apart and pointed at the subject's chest. The test subject was wearing normal clothing. He was then asked to sit on a chair and point the antenna at his chest at various distances and positions. He was asked not to move or speak during the entire experiment. The subject's position was adjusted by checking whether the respiratory signal was visible on the VNA when the subject was breathing normally and whether the respiratory signal was visible on the VNA when the subject was not breathing.

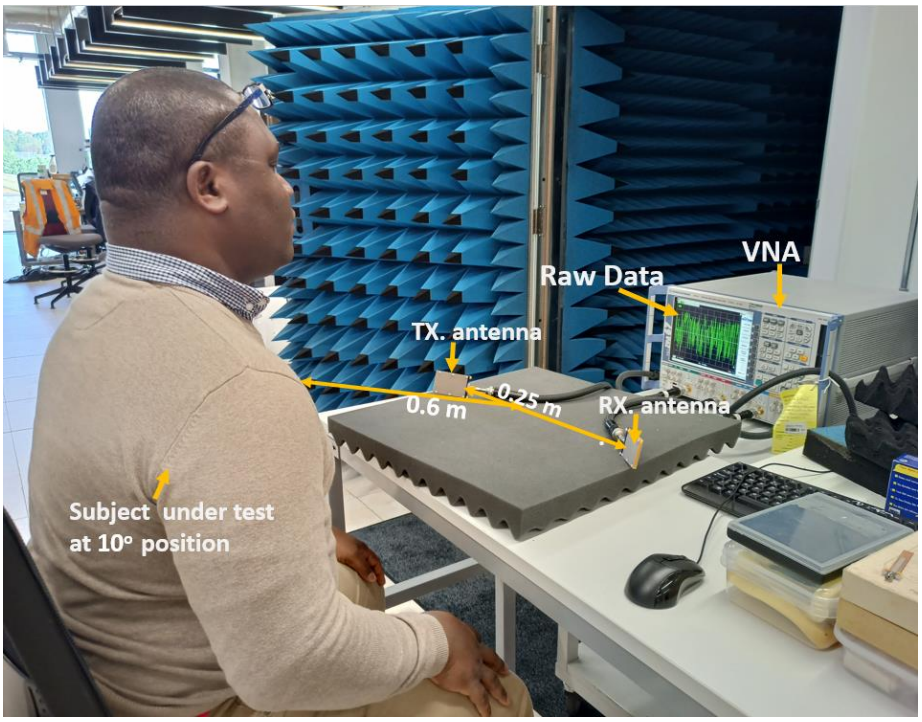
For the actual experimental measurements, the subject was asked to breathe normally for 5 minutes. Then the VNA generates electromagnetic waves that the antenna emits, which interact with the subject's body. The antenna receives the reflected waves, and the VNA calculates their S_{21} phase. The data were collected continuously at specific time intervals (60 seconds). The data is then stored locally and sent to the computer connected to the VNA for further analysis.

The targeted BR and HR information is then extracted from the recorded data after it has been acquired and processed in Matlab using various digital signal-processing techniques. All experiments were performed in a normal laboratory environment. The signals received from the VNA contained the raw data of the heart rate and breathing rate, which were separated in the first stage. This was achieved by first passing the signal through the cutoff frequencies of a 10^{th}-order Butterworth bandpass filter, with an expected BR of 10(1/Min) - 41(1/Min), and then through an 8^{th}-order Butterworth bandstop filter, with a predictable minimum heart rate of 61(1/Min) and a maximum threshold heartrate cutoff of 98(1/Min). The filters were selected based on the most accurate results after examination [18]. The discrete fast Fourier transform (DFFT) that generated the BR and HR was used after filtering to calculate heart rate and respiratory rate over a period of several seconds. The criteria were determined using the highest and lowest average heart and respiratory rates. The most important components of digital signal processing are the discrete fast Fourier transform (DFFT) and the digital filtering of the recorded raw data in the time domain.

The manually recorded results were compared with the measured values from BR and HR. The manual count was performed using a stopwatch and a hospital blood pressure machine) for the heart rate. The complete RVSM MatLab code is published in Appendix A. In the next sections, we will compare the performance of the RVSM with the two different antennas.



(a)



(b)

Fig. 4.4.1 RVSM Doppler system (a) Digital signal processing block diagram (b) 60 GHz bands experimental set-up.

4.4.1 RVSM Measurement With PRS - Ground Plane Antenna At 0.6 m

Using the PRS-Ground Plane Antenna configuration which is also known as LWA without HIS was used to perform RVSM measurements in this section to validate the design concept. As previously stated, two antennas are used in RVSM operation. One antenna is used for signal transmission and the other for reception. It has been shown that

with the LWA without HIS (i.e., PRS and Ground Plane Antenna configuration), the vital signs can only be detected accurately over a very short distance [1]. The PRS-Ground plane antenna configuration or LWA without HIS has a moderate gain (20.1 dBi), moderate transmit power, and minimal beam scanning requirements(18^o) which can meet the needs of short-range applications. The angular range for RVSM detection was set at 0.6 m for efficient and accurate detection. To demonstrate that the LWAs are effective without HIS, the experiments are done in three stages using the best radiation angles. The subject is placed 0.6 m away from the LWA, and the RVSM measurements are taken at three different angles: 10°, 15°, and 20° in front of the Tx/Rx antennas.

The S_{21} phase data (demodulated Doppler signal in the time domain (TD)) are recorded at 61 GHz for each angular position. During the recording of the reflection coefficient phase (S_{21}), HR and BR were measured for 60 seconds. Then the results are repeated at 62.5 and 66 GHz. Figures 4.4.2 – 4.4.4 show that we now have three sets of S_{21} phase data for 61, 62.5, and 66 GHz at the three angles indicated. Plots in the left column in each figure depict the Doppler signal recorded in the time domain (TD), while plots in the right column (RHS) depict the corresponding treated signal in the frequency domain (FD) (Figs. 4.4.2-4.4.4). The first and second highest peaks indicate the predicted respiratory rate (BR) and heart rate (HR), respectively. A summary of the RVSM measurement with PRS-Ground LWA is shown in Table 2. The results agree well with the predicted values and show that BR and HR are consistent within their ranges for an average person (a 39-year-old man) [19].

A conventional method for measuring breathing rate and heart rate using manual count and blood pressure monitor was compared with the Doppler radar technique and are in good agreement (see Fig. 4.4.5). The RVSM detection performance of the proposed antenna is adequate in an angular range of 18° at a short distance of 0.6 m. However, it is essential to highlight that some of the HR and BR signals that are detected are not much

stronger than the background signals. This indicates that RVSM may be incorrectly detected in a noisy setting, but not in a laboratory. In addition, when the subject moved 20^{o} away from the antenna, the findings were inaccurate beyond 0.6 m. Therefore, for long-distance (up to 2 m) monitoring, the LWA with HIS-based (PRS-HIS) operation is investigated and presented in the next section.

Table 2. RVSM Measurement Of BR And HR **Without-HIS**-Based LWA Operation At 10^{o},15^{o},20^{o} For Each Frequency

61 GHz	62.5 GHz	66 GHz	Manually Counted. BR & HR Range with Hospital Machine		Max. Error
BR-HR (1/min)	BR-HR (1/min)	BR-HR (1/min)	BR (1/min)	HR (1/min)	BR-HR (1/min)
20-72	19 -78	21-79	18 -22 (avg.20)	78 - 80 (avg. 79)	5% - 3.4%

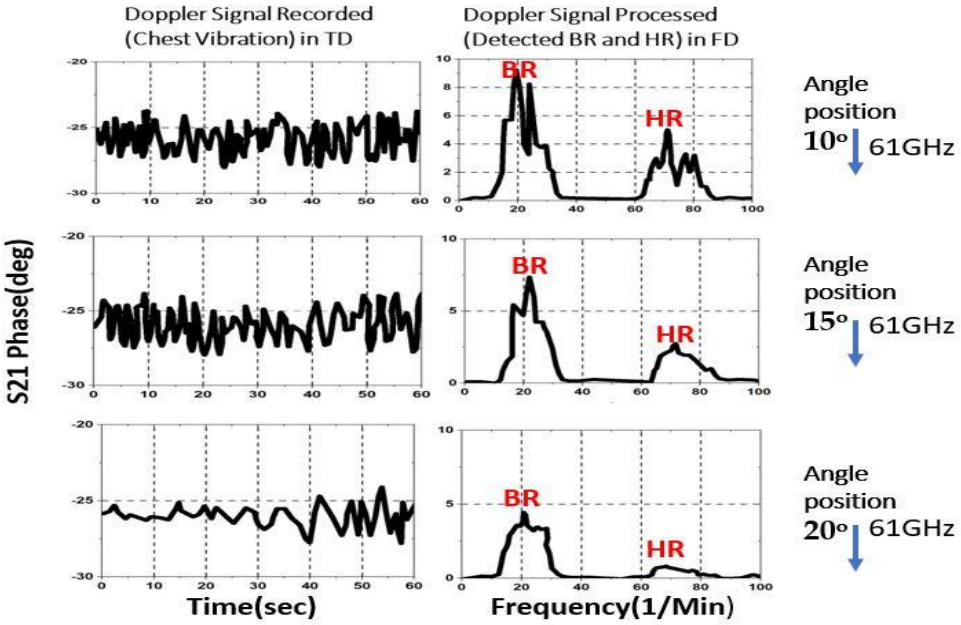


Fig. 4.4.2 RVSM measurement at 61 GHz from various positions at 0.6 m distance.

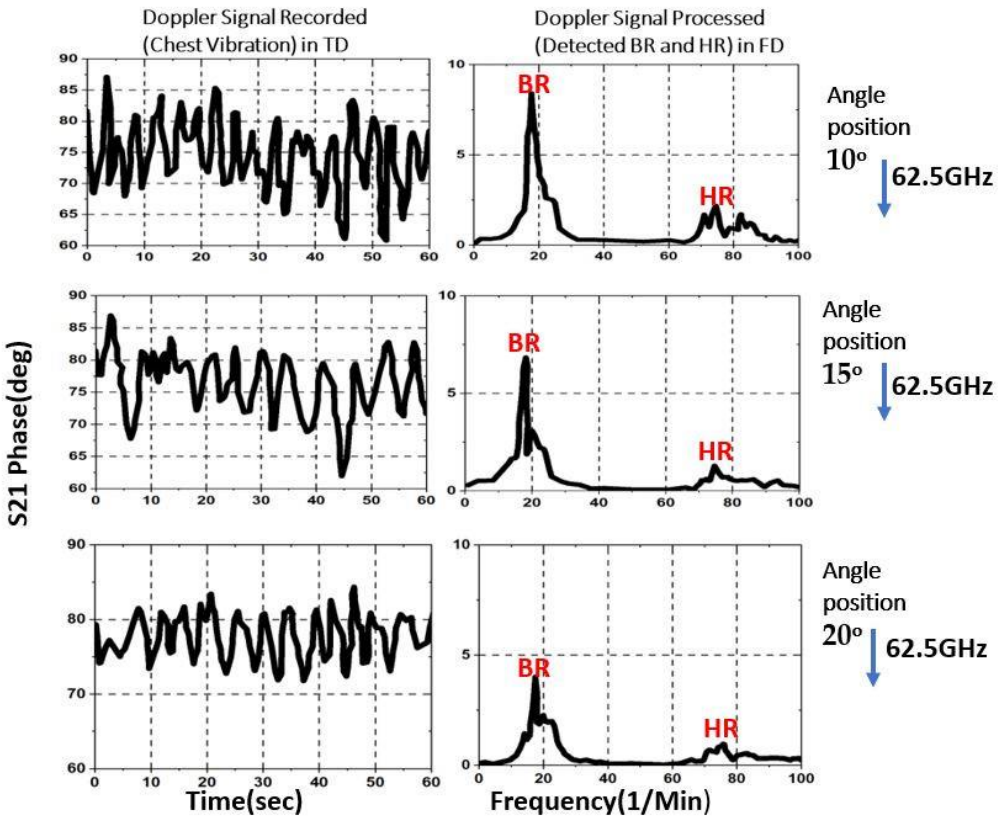


Fig. 4.4.3 RVSM measurement at 62.5 GHz from various positions at 0.6 m distance.

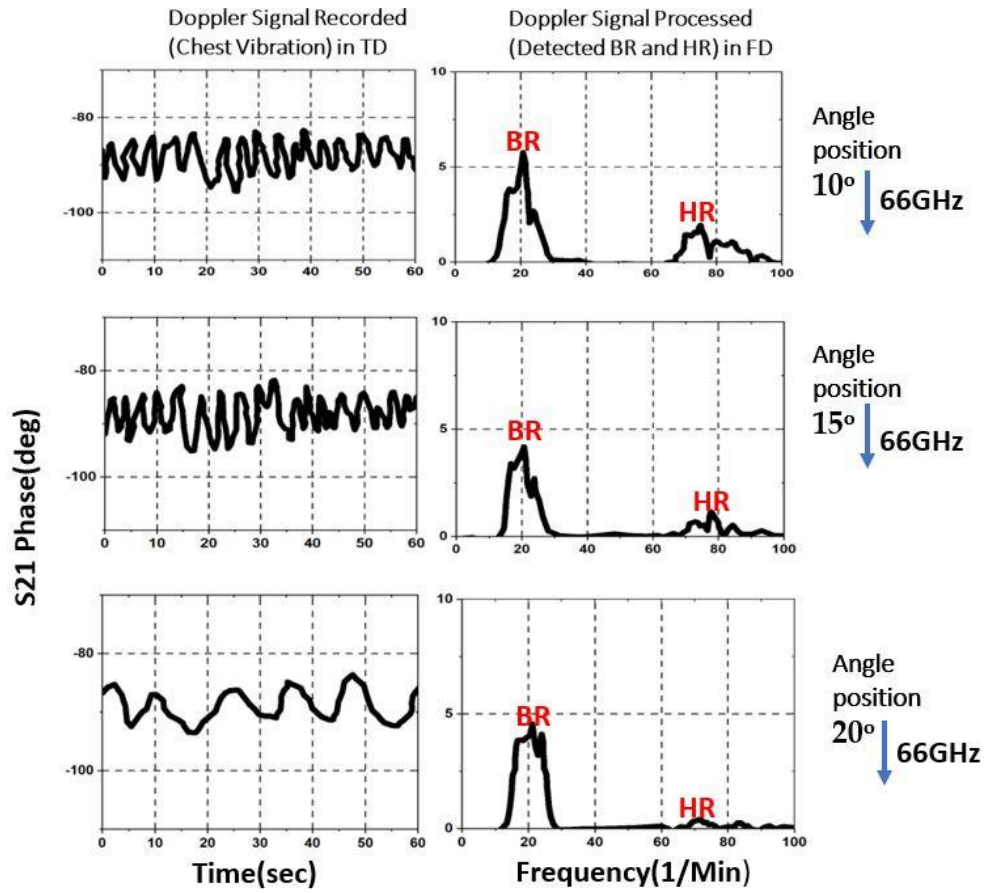


Fig. 4.4.4 RVSM measurement at 66 GHz from various positions at 0.6 m distance.

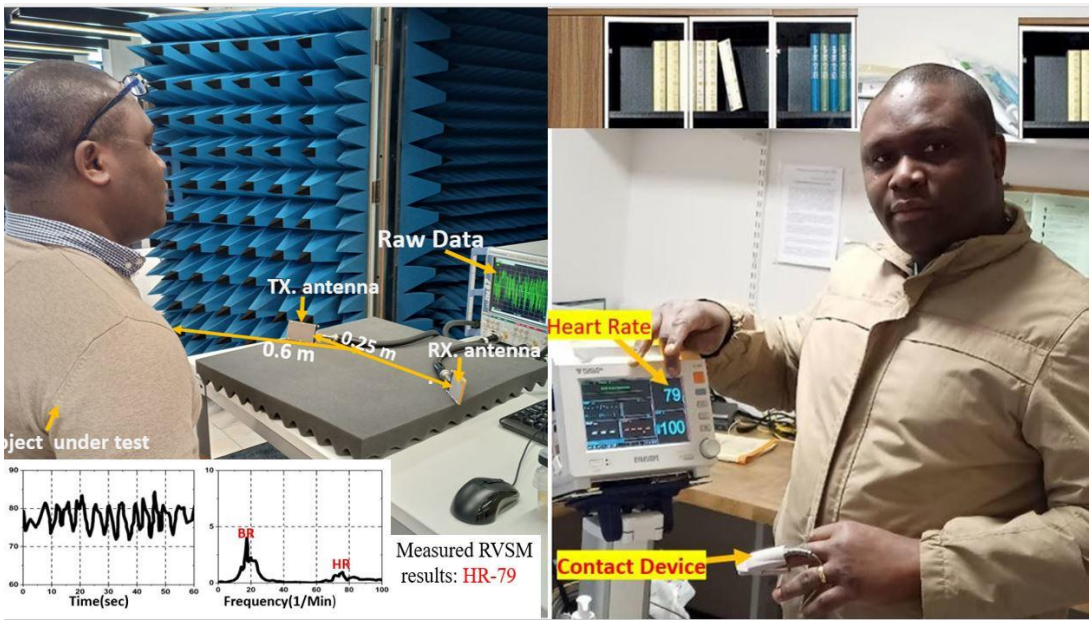


Fig. 4.4.5 Validation of RVSM results compared with hospital blood pressure machine.

4.4.2 RVSM Measurement With PRS - HIS Antenna At 2 m

For long-distance RVSM applications, two similar HIS-Based LWAs have been implemented experimentally for the detection of breathing (BR) and heart rate (HR). During the implementation, the transmitting antenna sends the electromagnetic wave to the target chest and the reflected signals are received by the receiving antenna. Both antennas are placed at the same distance of 2 m away from the subject's chest. The space between the two antennas is about 0.25 m. The S_{21} phase is measured for 60 seconds with each of the antenna designs shown in Fig. 4.2.1(c)-(d). As previously described in Section 4.3, the HIS-based LWA has a high gain and improved beam scanning.

During the measurements, the subject is positioned 5^{o}, 10^{o}, 15^{o}, 20^{o}, 25^{o}, and 30^{o} at 2m from the transmit and receive antennas (Tx/Rx), while the S_{21} phase data (demodulated Doppler signal in the time domain (TD)) for each angular location is captured at 58 GHz. The measurements are then carried out once again for 60 GHz, 62.5 GHz, 64 GHz, and 66 GHz. Consequently, we acquire five sets of S_{21} phase data for the supplied six angular locations at 58, 60, 62.5, 64, and 66 GHz, as shown in Fig. 4.4.6-4.5.0. Table 3 depicts the measured BR and HR with **PR-HIS**-based LWA.

In each figure, the plots in the left column show the Doppler signal in the time domain (TD), and the plots in the right column show the same signal after it has been processed in the frequency domain (FD). Each plotted peak of the processed data represents the expected BR signal at 20 (1/Min) amplitude, while the second amplitude peak signal at around 81 (1/Min) represents the anticipated HR. The measured BR and HR signals have amplitudes that are sufficiently higher than the resulting noise levels for the subject locations at both high and low angles, i.e., 5^{o} and 30^{o}, as shown in Figures 4.4.6 - 4.5.0. Both the BR and HR values are within the ranges that were predicted and match the results from the manual count and the blood pressure monitor, which were already mentioned. The sensitivity of the proposed antenna for RVSM at 2 m is satisfactory over the angular range of 5^{o} to 30^{o} when the operating frequency is tuned from 58 GHz to 66 GHz.

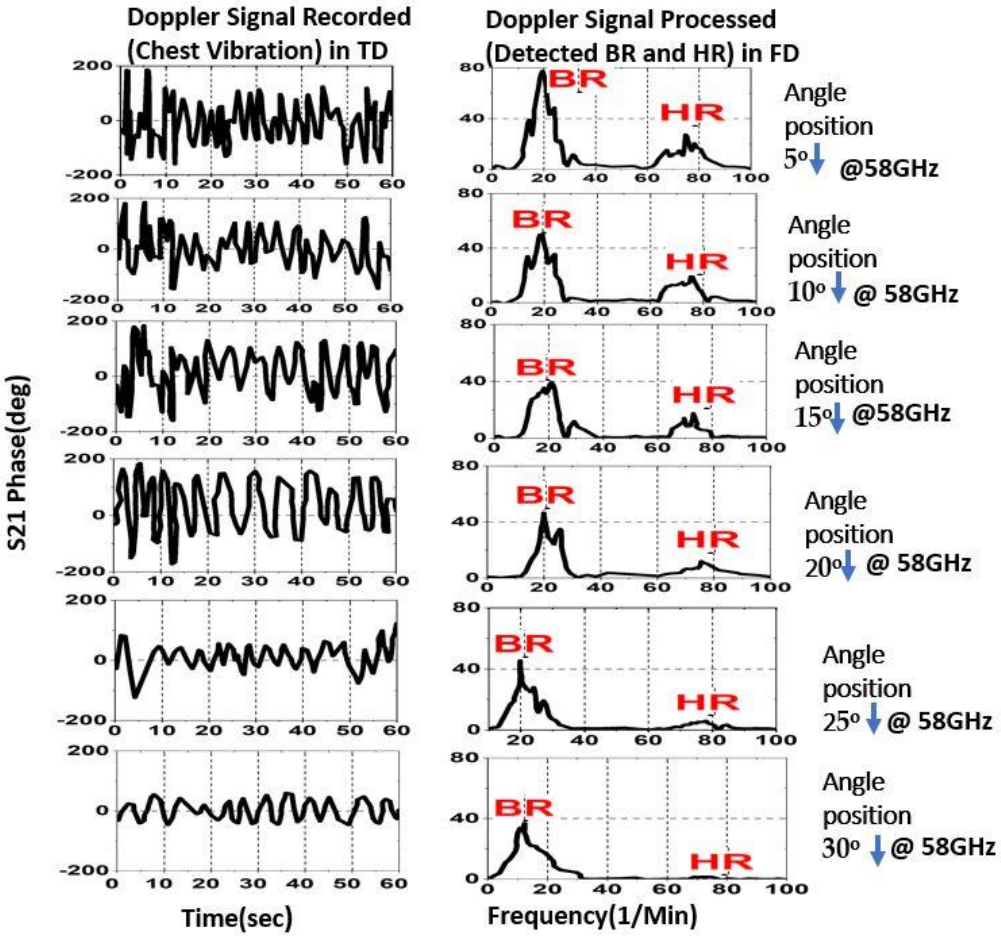


Fig. 4.4.6 RVSM Measurement at 58 GHz from a 2 m distance.

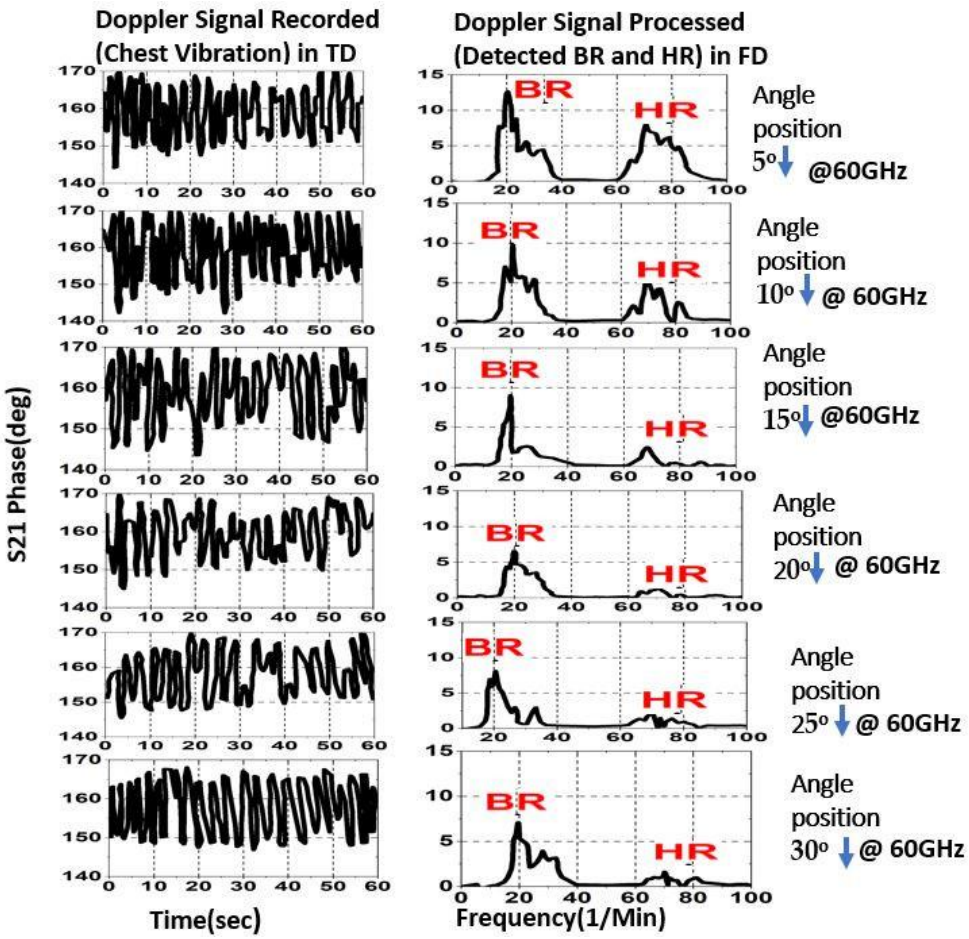


Fig. 4.4.7 RVSM Measurement at 60 GHz from a 2 m distance.

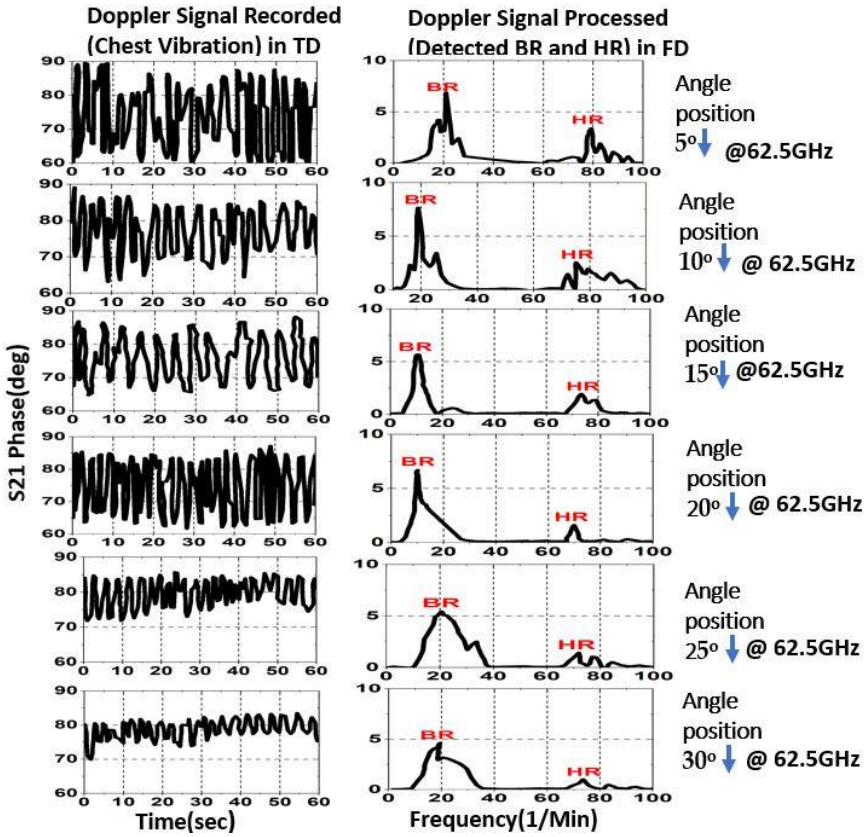


Fig. 4.4.8 RVSM Measurement at 62.5 GHz from a 2 m distance.

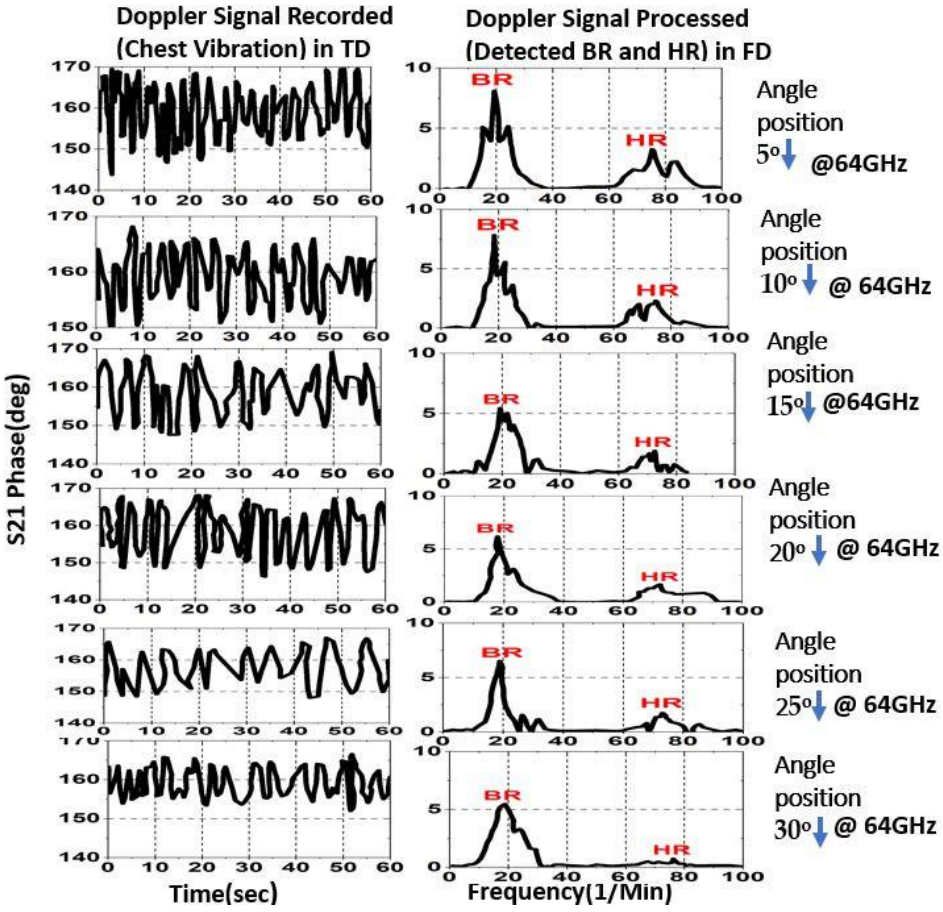


Fig. 4.4.9 RVSM Measurement at 64 GHz from a 2 m distance.

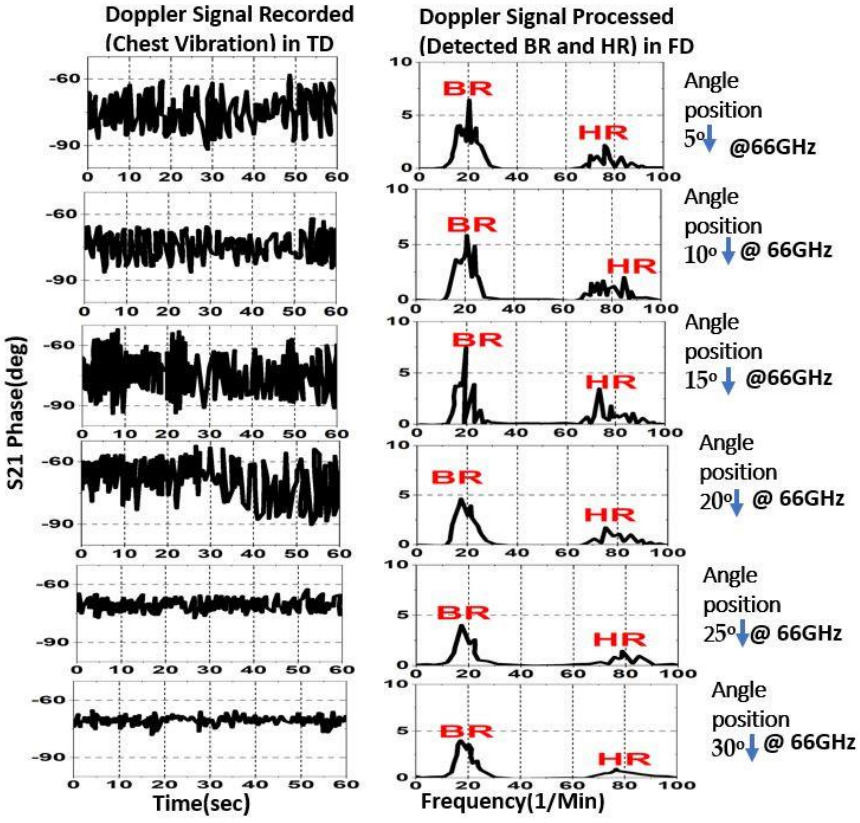


Fig. 4.5.0 RVSM Measurement at 66 GHz from a 2 m distance.

Table 3. Measured BR And HR **With-HIS** Based LWA Operation Results Of 5º,10º,15º,20º, 25º, and 30º For Each Frequency.

58 GHz	60 GHz	62.5 GHz	64 GHz	66 GHz	Manually Counted BR & HR range with Hospital Machine		Max. Error
BR-HR (1/min)	BR-HR (1/min)	BR-HR (1/min)	BR-HR (1/min)	BR-HR (1/min)	BR (1/min)	HR (1/min)	BR-HR (1/min)
20 -79	19 -75	19-78	19 -79	20 - 80	19 -20 (avg.20)	78 - 80 (avg. 79)	5% - 1%

It can be noticed that, at high frequency for example in Fig. 4.5.0, the breathing rate (BR) and the heart rate (HR) measurement at 66 GHz from a 2 m distance shows clear peaks at 5º up to 25º. This shows the good performance of the LWA directivity and its sensitivity. Table 3 above also shows the consistency and accuracy of the measurement results. For example, in the range of 60 GHz – 64 GHz, BR and HR are 19 (1/min) and 79(1/min), respectively, compared to manual or contact device measurements.

4.5 Sensitivity Of RVSM At 10 GHz Compared To 60 GHz Detection At 1m

In a new experiment, the PRS and HIS-based LWA configuration shown in Figure 4.2.1 (c)-(b), also known as the HIS-based LWA antenna, is used for 60 GHz RVSM measurements, and compared with a conventional microwave patch antenna at 10 GHz for a short distance of 1 m.

This experiment was conducted to determine if RVSM in the 60 GHz band has better detection sensitivity than 10 GHz RVSM at the microwave frequency level. Figure 4.5.1 shows the design parameters of a microstrip patch antenna from Rabbani et al. [2] at 10 GHz, which was used for RVSM based on the same Roger 5880 material, but with a substrate thickness of h = 1.57 mm [14]. The 10 GHz antenna has the following dimensions: L= 9.03 mm, W= 34.35 mm, LT1= 15.39 mm, LT2= 9.03 mm, WT1= 8.1 mm, and WT2 = 4.05 mm.

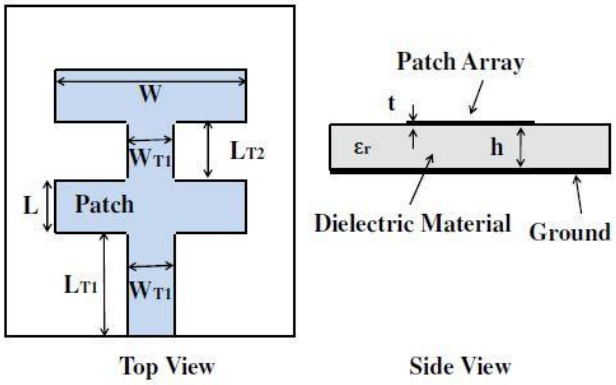
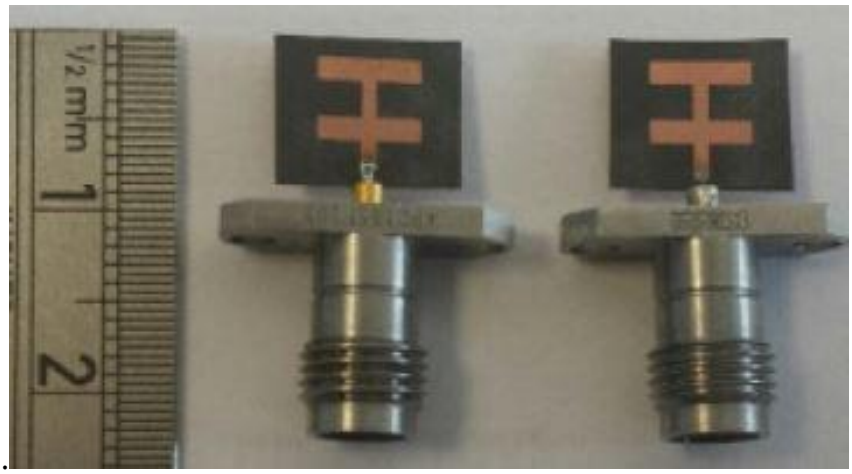
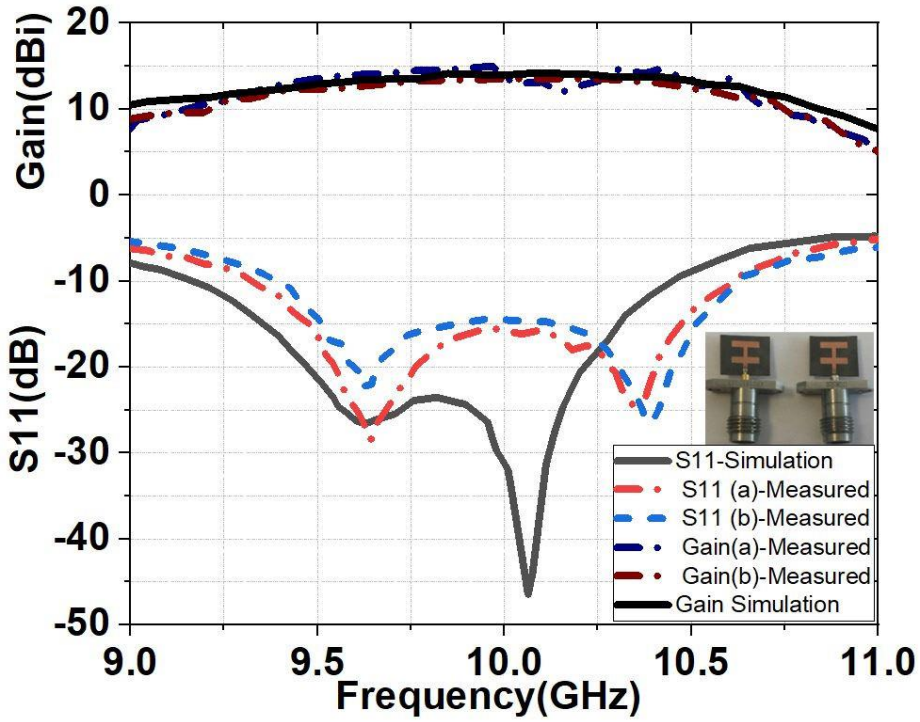


Fig. 4.5.1. The suggested patch antenna array structures top and side view (Fig. not drawn in scale) [2].

The two manufactured copies of the 10 GHz antenna are depicted in Fig. 4.5.2 (a-b), and the S_{11} measured and simulation results as well as the gain are depicted in Fig. 4.5.2 c, respectively. The S_{11} beamwidth (BW) of the antennas depicted in Fig. 4.5.2 (a) and (b) was measured to be approximately 1.2 GHz, which is close to the simulation BW of 1.28 GHz and all the measured and simulation results are in good agreement. The measurement of the patch antenna was conducted at a frequency of 10 GHz, and the measured S_{11} results for the antennas are less than -10 dB. The measured gains of the antennas in Fig. 4.5.2 (a) and (b), are 13.91 dBi and 13.68 dBi, respectively, which agree exactly with the calculated gain of 13.84 dBi (Fig. 4.5.2c). The far-field radiation pattern (FRP) where the half-power beamwidth of the antenna is between 32^o and 43^o and its main lobes are aligned in the 0^o direction depicted in Fig. 4.5.3.

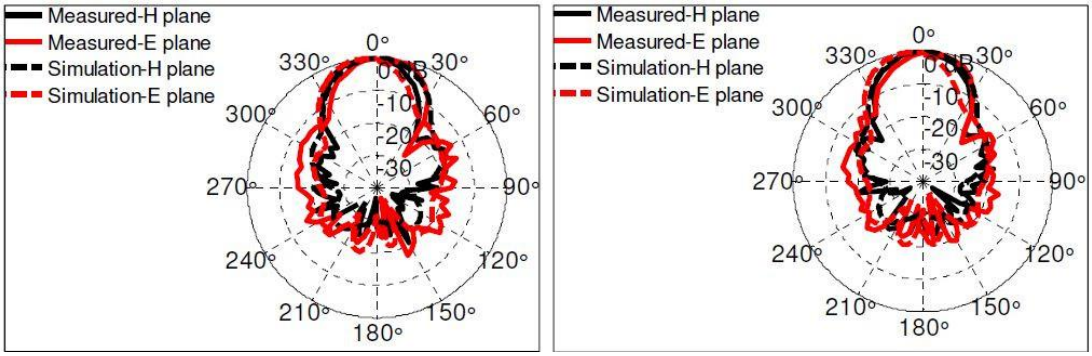


(a) **(b)**



(c)

Fig. 4.5.2. Results of 10 GHz antenna measurements. (a) and (b) show the two copies of the fabricated antennas; (c) show the results of simulation and measurement of S_{11} and gain.



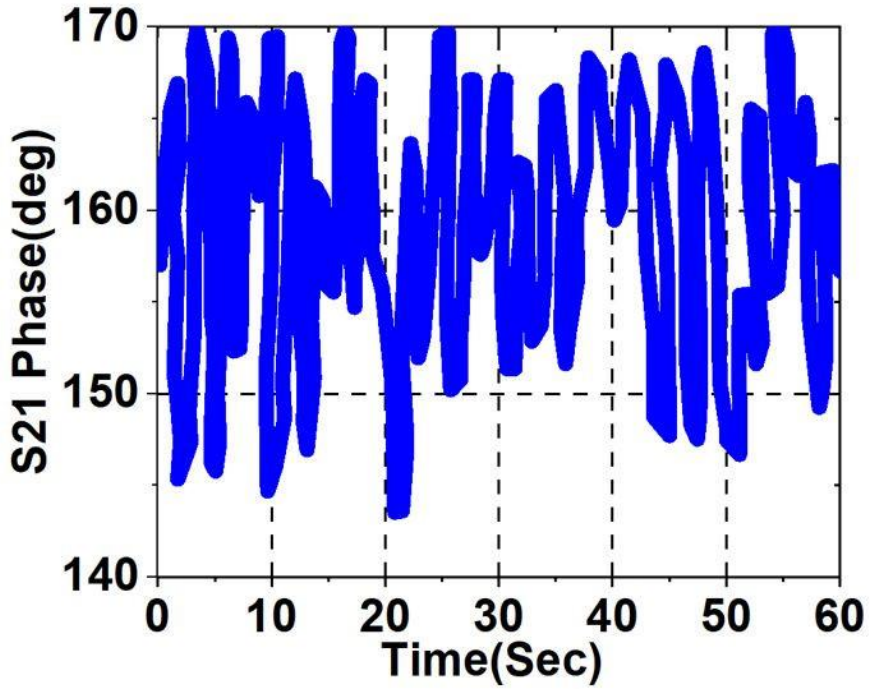
(a) (b)

Fig. 4.5.3. Measured and Simulation antenna of the Fairfield Radiation pattern at 10 GHz depicted in (a) Fig 4.5.2(a)-(b).

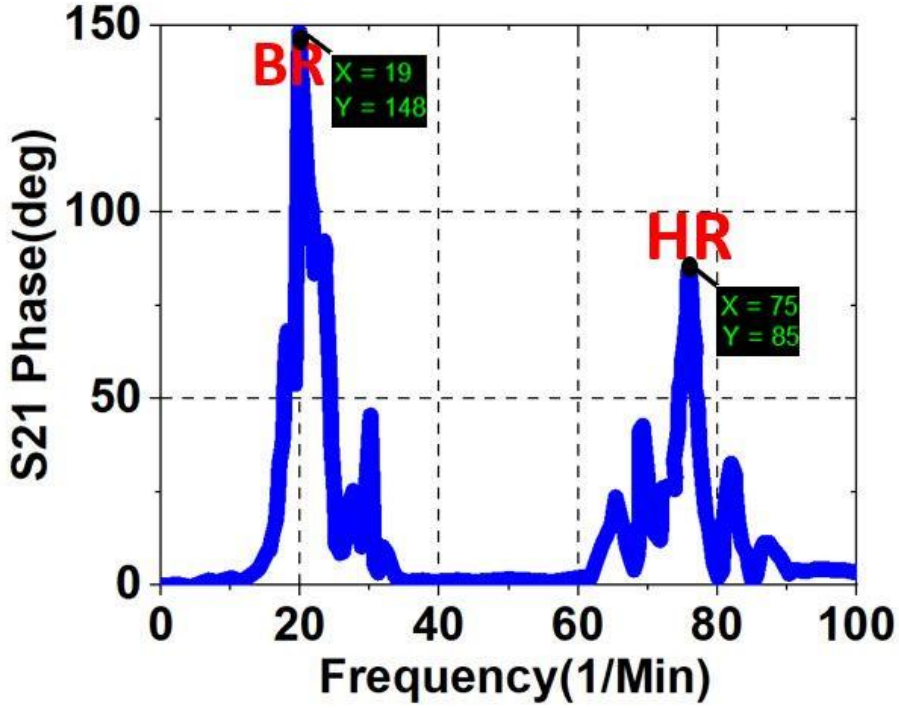
4.5.1 60 GHz RVSM Measurement Sensitivity At 1m

The outcomes of the RVSM at 60 GHz are shown in Figure 4.5.4, where (a) the raw RVSM data is recorded in the time domain and (b) the data points processed are recorded

in the frequency domain. The BR and HR values are 19 (1/min) and 75 (1/min), respectively, as shown in Fig. 4.5.4(b). The results obtained with the manual count and blood pressure device agree with the measured BR and HR values.



(a)



(b)

Fig. 4.5.4 60GHz RVSM measurement at 10^{o} for a 1 m distance. (a) collected raw data; (b) identified frequency peaks for BR and HR.

4.5.2 10 GHz RVSM Measurement Sensitivity At 1m

The RVSM experiment for the 10 GHz antenna is set up in Fig. 4.5.5, and the outcomes are displayed in Fig. 4.5.6, where (a) denotes the time domain raw data recorded and (b) denotes the frequency domain processed data. The measured BR and HR were 20 and 75, respectively, per minute. As seen in Fig. 4.5.6(b), the detected BR and HR have amplitudes of 49 and 8, respectively. It is evident from comparing Figs. 4.5.4(b) and 4.5.6(b) that the BR and HR values detected at 60 GHz are significantly higher (115 and 46, respectively) than those detected at 10 GHz (49 and 8). As a result, BR and HR have a detection sensitivity at 60 GHz which is approximately 2.35 and 12.96 times higher than that at 10 GHz. Additionally, the intermodulation between the amplitudes of BR and HR as shown in equations (4.4-2) and (4.4-3) explains why the sensitivity of HR has improved significantly more than that of BR. This allows the 60 GHz Doppler radar to detect the HR signal, which is typically weaker in the noise, with great clarity.

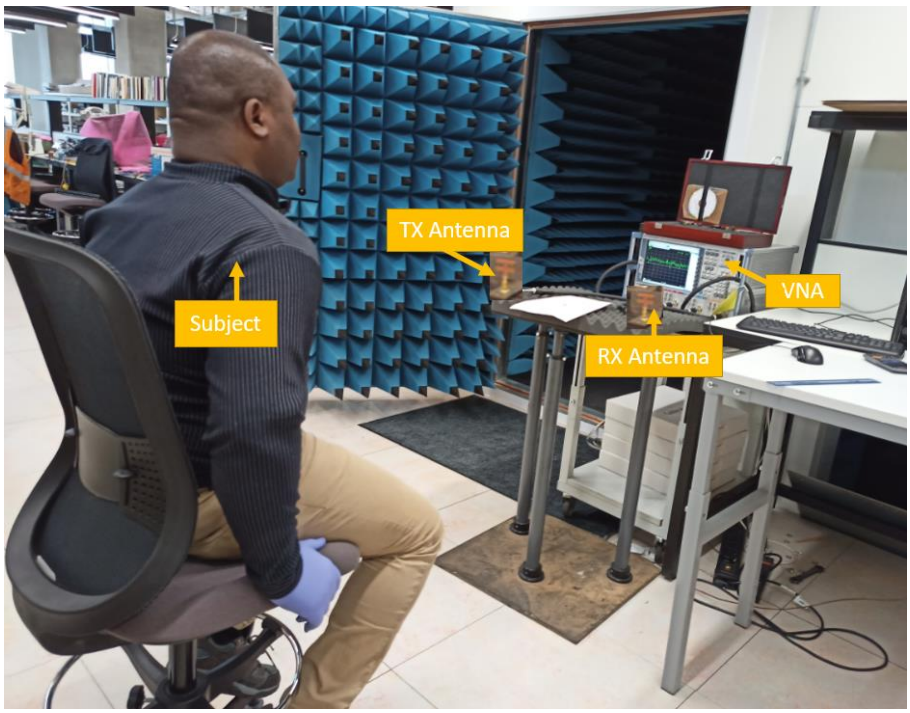
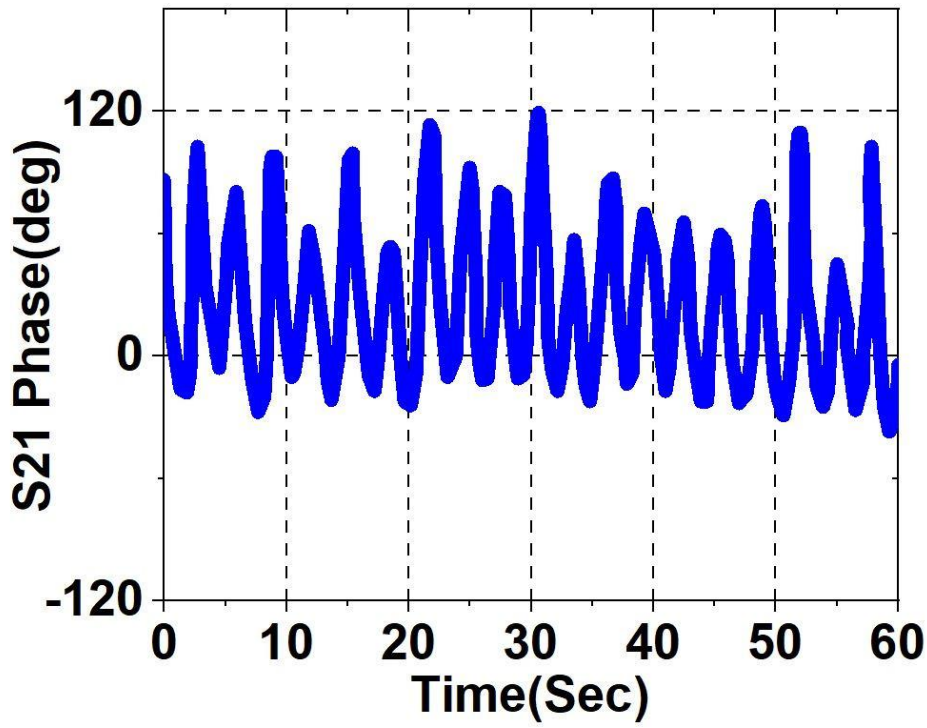
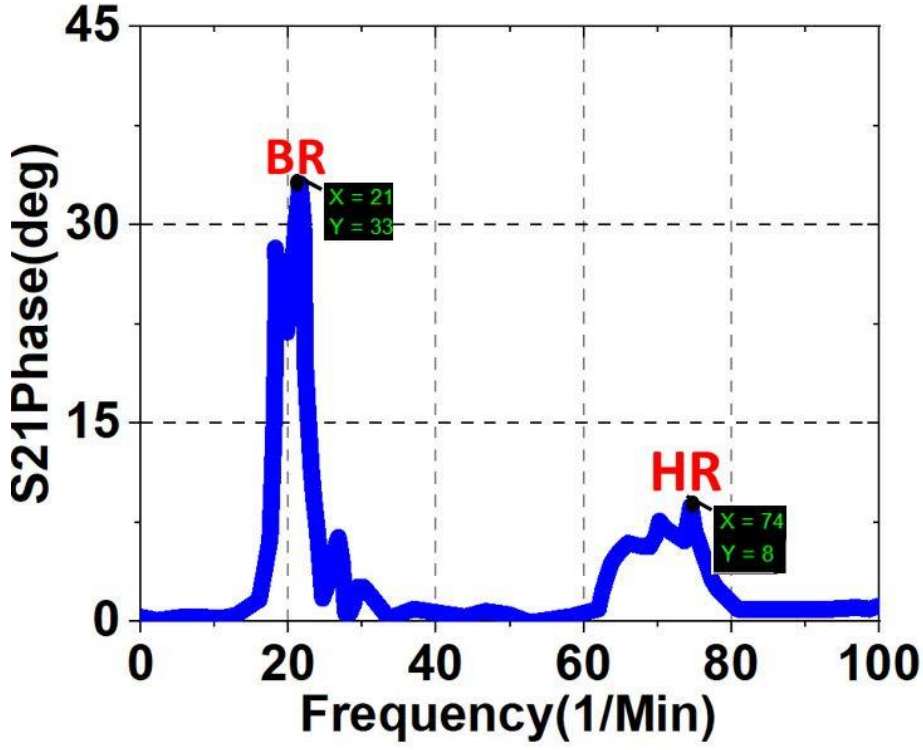


Fig. 4.5.5 RVSM experiment setup at 10 GHz from 1 m distance.



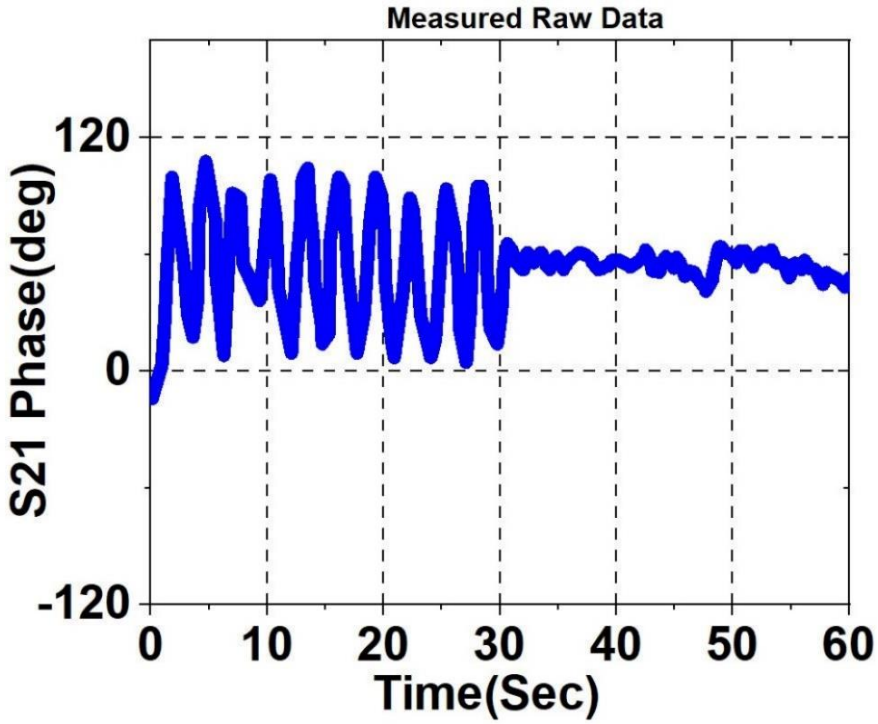
(a)



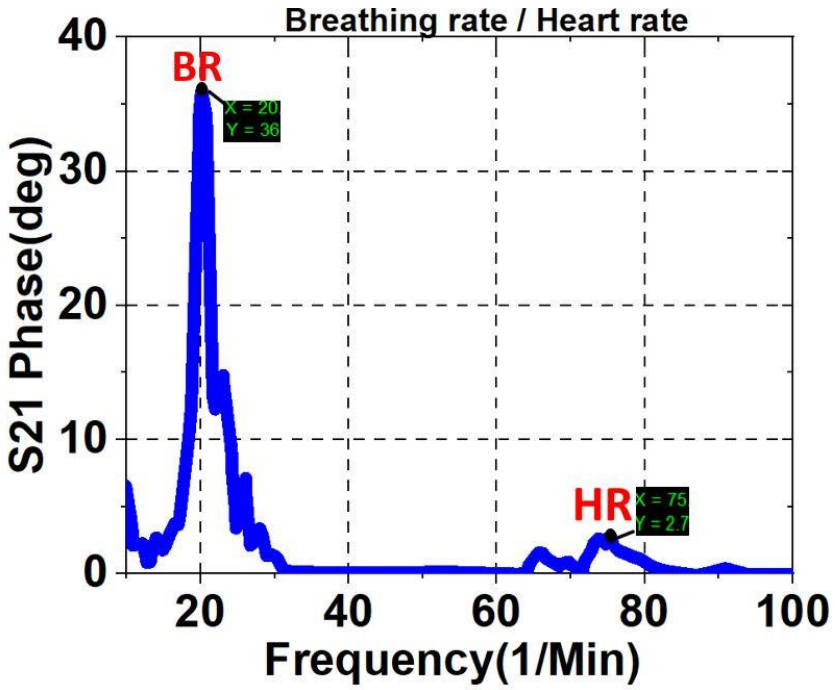
(b)

Fig. 4.5.6 10 GHz RVSM at a distance of 1 m. (a) captured raw data and (b) BR and HR frequency peaks were found.

Finally, the impact of breath holding on the accuracy of the HR result as well as on the received phase modulated waveform is discussed. To achieve this, an experiment using the same antennas as those shown in Fig. 4.5.2(a)-(b) is carried out at 10 GHz. The subject breathed normally for the first 30 seconds of data acquisition with the 10 GHz patch antenna and then stopped breathing for the remaining 30 seconds. Figures 4.5.7(a) and (b) show, respectively, the processed data in the frequency domain and the received phase modulated signal in the time domain. As seen in Fig. 4.5.7(a), the BR signal predominates in the amplitude of the first half of the recorded data, disappearing in the second half of the data to leave the HR signal dominant but with a relatively very small amplitude. The measured BR (20/min) and HR (75/min) signal peaks' amplitudes are clearly shown in Fig. 4.5.7(b). The detected HR signal is more obvious in Fig. 4.5.7(b) than it is in Fig. 4.5.6(b), as can be seen by comparing the two figures. Therefore, breath holding for a certain time is used in RVSM to improve the accuracy of the HR signal [13]. Similarly, high gain with beam scanning has been performed for RVSM in [20] and [21].



(a)



(b)

Fig. 4.5.7. (a) The frequency-domain processed signals BR and HR and (b) the time-domain received phase-modulated signal.

4.6 Comparison Of Proposed LWA With Horn Antenna, Patch Antenna And Fabry Perot Antenna At Mm-Wave Frequencies

In this comparative analysis, an examination will be conducted on the merits and demerits of every type of antenna along with their RVSM efficiency at millimetre wave frequencies. Although horn antennas are ideal for high gain and directional radiation, they cannot scan with frequencies when the subject under test shifts location, while patch antennas, which have a low profile can result in more loss in wideband applications and lack scanning capabilities. The proposed Fabry-Perot LWA are suitable for high gain, low side lobes, and more beam scanning, which is appropriate for continuous frequency-tunable beam patterns for RVSM applications.

Table 4 compares this work with others from the recent literature on RVSM applications at millimetre wave frequencies. Overall, the main contribution of our proposed LWA scan with a frequency of up to 30^{o} at a distance of 2 m from the human body with an improved

estimated accuracy of 93%, which is a significant improvement over other antennas n the literature for RVSM, except the horn antenna. The proposed antenna operates with an improved realised gain of 22.3 dBi and a radiation efficiency of 95.5% compared to the horn antenna. The achieved bandwidth of the proposed LWA is more limited compared to [7], [13] and [21] due to the well-known trade-off between gain and beam aperture, but in the present application, the bandwidth is not important since a narrow beam is required to focus on the object chest for RVSM.

Table 4. Comparison Of Proposed LWA with Literature

	[7]	[13]	[20]	[21]	**This Work**
Antenna Type	Horn	P. A	F. P	F. P	**Fabry Perot**
Frequency (GHz)	60	57-66	62- 65	$50-66$	$\mathbf{58-66}$
Radiation efficiency (%)	94	94	95	83.2	**95.5**
Scanning range (˚)	0	-	12	70	**30**
Gain (dBi)	24	14	20.1	19.3	**22.3**
Bandwidth (GHz)	12	14	3.38	16	**8**
RVSM distance (m)	1	-	3	1.5	**2**
RVSM accuracy (%)	98.4	-	90.8	95	**93**

Furthermore, the realised gain of our proposed antenna makes it suitable not only for RVSM but can also be used for various other applications, such as 5G communications and IoT. Other similar antennas in the literature, especially [7],[13] and [20], have high radiation efficiency, but the proposed design has a suitable configuration that works as an LWA with superior characteristics at millimetre-wave frequencies with lower fabrication

costs. For example, in [13], there were slight differences between the simulated and observed results due to the air gap between the ground plane and the dielectric layer during fabrication. An epoxy was used to close that gap between the two layers which adds up to the cost. Therefore, the radiation on the broadside was not considered and no RVSM was performed.

4.7 Conclusions

Two leaky wave antennas based on the PRS-Ground plane and PRS-HIS configuration have been developed for accurate RVSM in the 60 GHz band, with improved gain and radiation characteristics. The results of the antenna measurements and simulation matched perfectly. The Doppler radar technique was utilised to evaluate the 60 GHz channel's suitability for the RVSM application. RVSM measurements were performed with each of the proposed antennas, thus, (i) Leaky-wave antenna without HIS (PRS - Ground plane antenna), in which a duplicate of the same antenna is made, one of which serves as the transmitting LWA (Tx) and the other as the receiving LWA (Rx), and is located 0.6 m away from the subject's chest; and in (ii) a HIS-based leaky wave antenna (PRS and HIS configuration), two similar LWAs, one for Tx and the other for Rx, were also placed at different distances up to 2 m from the subject to observe the accuracy of the results. Throughout data collection, both BR and HR were observed in the patient, who was breathing normally. For accurate detection of HR, it is necessary to hold your breath. In each case, the measured results demonstrated extremely accurate, unambiguous, and reliable RVSM detection using basic digital signal processing techniques. Overall, the main contribution of the proposed LWA scan with frequency up to 30^{o} to a distance of 2 m from the human body with an improved RVSM accuracy of 93%, which is a significant advantage over other antennas in the literature and close to the horn which has been used for RVSM application.

References

[1] D. Obeid, G. Zaharia, S. Sadek, and G. El-Zein, “Microwave Doppler radar for heartbeat detection vs electrocardiogram”. *Microwave and Optical Technology Letters*, vol.54, no.11, pp.2610-2617, Nov 2012.

[2] M. S. Rabbani, and H. Ghafouri-Shiraz, “Ultra-Wide Patch Antenna Array Design at 60 GHz Band for Remote Vital Sign Monitoring with Doppler Radar Principle”. *Journal of Infrared, Millimeter, and Terahertz Waves*, vol.38.no.5, pp.548-566. May 2017.

[3] C. Gu, “Short-range noncontact sensors for healthcare and other emerging applications: A review”. *Sensors*, vol.*16.no.*8, p.1169. Aug. 2016.

[4] A.D. Droitcour, T. B Seto, B.K. Park.S. Yamada, A. Vergara, C. El Hourani, T. Shing, A. Yuen, V.M. Lubeck, and O. Boric-Lubeck, “Non-contact respiratory rate measurement validation for hospitalized patients”. *In Engineering in Medicine and Biology Society, 2009. EMBC 2009. Annual International Conference of the IEEE*.pp. 4812-4815. IEEE. Sept. 2009.

[5] M. Villarroel, A. Guazzi, J. Jorge, S. Davis, P Watkinson, G. Green, A. Shenvi, K. McCormick, and L. Tarassenko, “Continuous non-contact vital sign monitoring in the neonatal intensive care unit”. *Healthcare technology letters*, *1*(3), pp. 87-91. Sep. 2014.

[6] S. Suzuki, T. Matsui, M. Kagawa, T. Asao, and K. Kotani, “An approach to non-contact vital sign monitoring using dual-frequency microwave radars for elderly care”. *Journal of Biomedical Science and Engineering*, vol.6 no.7, pp. 704. Sep. 2013.

[7] Z. Yang, P. H. Pathak, Y. Zeng, X. Liran, P. Mohapatra, “Monitoring vital signs using millimeter-wave”. *In Proceedings of the 17th ACM international symposium on mobile ad hoc networking and computing*. pp. 211-220. Jul. 2016.

[8] T. Y. J. Kao and J. Lin, “Vital sign detection using a 60-GHz Doppler radar system”. In *Wireless Symposium (IWS), 2013 IEEE International*.IEEE., pp. 1-4. April 2013.

[9] V. Li, M. Lubeck, O. Boric-Lubeck, and J. Lin, “A review on recent advances in Doppler radar sensors for noncontact healthcare monitoring”, *IEEE Transactions on microwave theory and techniques,* vol. 61, no. 5. pp. 2046-2060. Sep. 2013.

[10] G. Von Trentini, “Partially reflecting sheet arrays,” IRE Trans. *Antennas Propag.*, vol. 4, no. 4, pp. 666–671, Oct. 1956.

[11] A. P. Feresidis, G. Goussetis, S. Wang, and J. C. Vardaxoglou, “Artificial magnetic conductor surfaces and their application to low-profile high-gain planar antennas,” *IEEE Trans. Antennas Propag.,* vol. 53, no. 1, pp. 209–215, Jan. 2005.

[12] J. Gao, K. Li, T. Sato, J. Wang, H. Harada and Kato, S,” Implementation considerations of the patch antenna array for 60GHz beam steering system applications”. *In Radio and Wireless Symposium.* IEEE. pp. 35-38. Jan. 2009.

[13] M. S Rabbani and H. Ghafouri-Shiraz, “Improvement of microstrip patch antenna gain and bandwidth at 60 GHz and X bands for wireless applications”. *IET Microwaves, Antennas & Propagation,* vol.10.no.11, pp. 1167-1173. Jan. 2016.

[14] M. S Rabbani and H. Ghafouri-Shiraz, “Size improvement of rectangular microstrip patch antenna at MM-wave and terahertz frequencies”. *Microwave and Optical Technology Letter*s, 57(11), pp. 2585-2589. July 2015.

[15] C. Gu, C. Li, J. Lin, J. Long, J. Huangfu, and L. Ran, “Instrument-based noncontact Doppler radar vital sign detection system using heterodyne digital quadrature demodulation architecture”. *IEEE Transactions on Instrumentation and Measurement,* 59(6), pp. 1580-1588. June 2010.

[16] C. Li, and J. Lin, “Optimal carrier frequency of non-contact vital sign detectors”. *In Radio and Wireless Symposium, 2007 IEEE* (pp. 281-284). IEEE, Jan. 2007.

[17] D. Obeid, S. Sadek, G. Zaharia, and G. El Zein, “Multitunable microwave system for touchless heartbeat detection and heart rate variability extraction”. *Microwave and optical technology letters*, *52*(1), pp. 192-198. Nove. 2010.

[18] M. S. Rabbani, “Microstrip antenna design with improved fabrication tolerance for remote vital signs monitoring and WLAN/WPAN applications at mm-wave and THz frequencies,” PhD dissertation, University of Birmingham, 2018.

[19] NHS. Online at: http://www.nhs.uk/chq/Pages/2024.aspx, accessed on July 7th, 2022.

[20] M. S. Rabbani, J. Churm and A. P. Feresidis, "Fabry–Perot Beam Scanning Antenna for Remote Vital Sign Detection at 60 GHz," in *IEEE Transactions on Antennas and Propagation*, vol. 69, no. 6, pp. 3115-3124, June 2021,

[21] S. Mingle, D. Kampouridou and A. Feresidis, "Bidirectional Leaky-Wave Antenna Based on Dielectric Image-Line for Remote Vital Sign Detection at mm-Wave Frequencies," *in IEEE Open Journal of Antennas and Propagation*, vol. 3, pp. 1003-1012, 2022.

Chapter 5: Multilayer Beam Scanning Leaky Wave Antenna For Remote Vital Signs Detection At Mm-Wave Frequencies

Abstract-In a typical dynamic scenario where a patient desire continuous RVSM reception during sleep or in an office, an analysis of antenna specifications is provided by Doppler radar (DR). The antenna was produced following the drawn design specifications and offers accurate RVSM up to a 4 m distance, high gain (> 24 dBi), and wide beam scanning (30^{o}) over the operating frequency band (58–66 GHz) compared to horn antenna which has less beam scanning, shorter RVSM range at 1m as well as other antennas in literature. The subject undergoing health monitoring continuously has the freedom to move up to 1m away from the fixed sensor position. To confirm the suitability of the proposed antenna for a dynamic RVSM application, extensive RVSM measurements were performed at 2 and 4 meters from the subject using the Doppler radar technique with the FPC LWA. It has been found that varying the operating frequency from 58 to 66 GHz led to 93% accuracy of both breathing rate (BR) and heartbeat rate (HR) measurements within 30^{o} of the radar cross-section area.

5.1 Introduction

Designing a suitable antenna for health monitoring wireless sensors in the 60 GHz range is a difficult challenge [1–3]. The conventionally low microwave frequency range of Doppler radar (2.4, 5.7, and 10 GHz) makes it challenging to detect heartbeats due to the small amplitude of heartbeat vibrations in the chest (0.2 mm) [1]-[7]. High-directivity and efficient antennas are recommended because they are better able to compensate for path loss and significantly lessen interference from lateral reflections brought on by unintended movement [8]. Controlling the main beam of the LWA is essential for

continuous health monitoring with a fixed-position sensor, particularly when frequent patient movement is anticipated, such as when the patient is working or sleeping [9, 10]. The proposed LWA of the Fabry-Perot-Cavity (FPC) type, which has an inherently narrow operating bandwidth, is recommended for RVSM because of its directivity and the ability to focus the main radiation beam on the patient. Fabry-Perot cavity antennas (FPAs) are a good alternative to traditional antennas such as planar microstrip patch arrays or slot array antennas because of their high directivity properties. As mentioned in Chapter 1, the antenna gains and bandwidth of FPC antennas can be increased using a technique described in [11]. It has been demonstrated that a double-layer (PRS and plain dielectric) Fabry-Perot Cavity type antenna can attain a higher gain, more beam scanning and broader bandwidth than a single-layer antenna.

In this chapter, we propose a multilayer leaky wave antenna (LWA) of the Fabry-Perot type with a high gain (24.3 dBi) greater than previous designs for long-range remote vital sign monitoring (RVSM) in a dynamic environment using Doppler radar (DR). The multilayer part of the proposed LWA is made up of periodic partially reflective surfaces (PRS) and plain dielectric, extending the work that had already been done and greatly improving the FPC antenna's directivity-bandwidth performance. Fig. 5.1.1 demonstrates an example of the multilayer LWA used for remote vital signs monitoring in a dynamic environment.

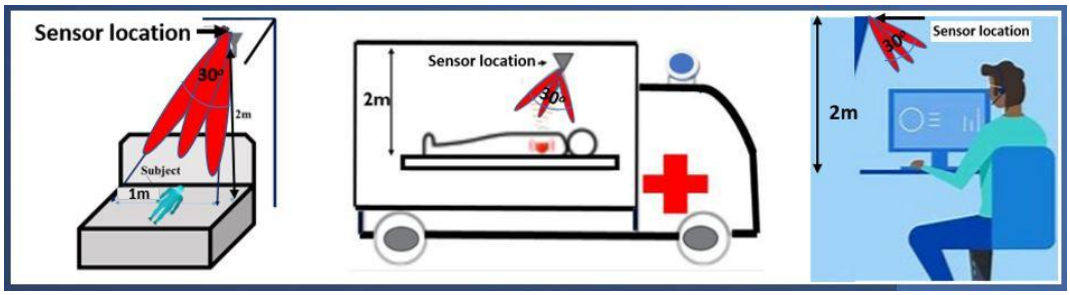


Fig. 5. 1.1. Multilayer LWA applications for RVSM.

Initially, a multilayer-layer antenna is investigated and studied, consisting of Partially Reflective Surfaces (PRS) and plain dielectric layers placed in front of a High Impedance

Surface (HIS) behaving as ground forming two open cavities. The PRS layer is made of square metallic patches and the HIS behaves as the ground is made of a square metallic loop. The PRS and HIS array's reflection properties, which are discovered through periodic analysis, serve as the foundation for the antenna performance. To improve the gain and bandwidth (BW) of FPC antennas, we demonstrate for the first time the design and application of a two-layer structure (PRS and plain dielectric). Consequently, we simplify the idea of Fabry-Perot cavity antennas with PRS and plain dielectric layers. The geometry of the proposed structure was optimized, and a full-wave simulation was performed in CST Microwave Studio. A prototype was built and tested to validate the simulation results, which are in agreement with the measured results.

5.2 Double- Layer Unit Cell (PRS and Plain Dielectric)

Firstly, a double-layer consisting of PRS and Plain dielectric is designed which is then placed in front of a HIS acting as the ground plane which has already been described in Fig. 5.2.1 for the multi-layer leaky wave antenna. A 1.75 mm thick dielectric substrate with a relative dielectric constant of 2.2 and a loss tangent of 0.0009 is used to print both the PRS and the plain dielectric. Fig. 5.1.1 depicts the structure of the unit cell. Metallic square components were chosen for the proposed PRS design because of their magnitude reflection. The dimensions of each layer are shown in Fig. 5.1.1 (a) with periodicity $P = 1.75mm$ and patch element dimensions $l_{out} = 1.50\ mm$. Fig. 5.1.1 (b) depicts the cross-section of the unit cell, where $h = 1.25\ mm$ cavity height between the PRS layer and the plain dielectric layer. These dimensions were chosen to create a reflection phase response with a positive gradient as was described in Section 2.1 and to produce high gain across a broad frequency range. Periodic boundary conditions were set up in CST Microwave Studio™ to extract the reflection coefficients and optimize the dimensions following this design strategy, which was first mentioned in [11].

The complex reflection coefficients are shown in Fig. 5.1.2 along with the ideal phase, which was calculated in CST and using equations (2.1-12) to obtain a cavity height of 2.91 mm from the ground plane. It can be seen that the reflection magnitude hits a minimum at 62.5 GHz. This suggests that the transmission is slightly enhanced at the resonant frequency. Equation (2.1-14) makes it clear that the observed high reflectance values lead to an antenna with high directivity, which can be achieved with the multilayers proposed here, such as PRS and dielectric. Additionally, between 62.3GHz and 63.1 GHz, a phased increase in the reflection phase is attained (see Fig. 5.1.2). Finally, at 62.59 GHz, the two-phase curves overlap, indicating high directivity.

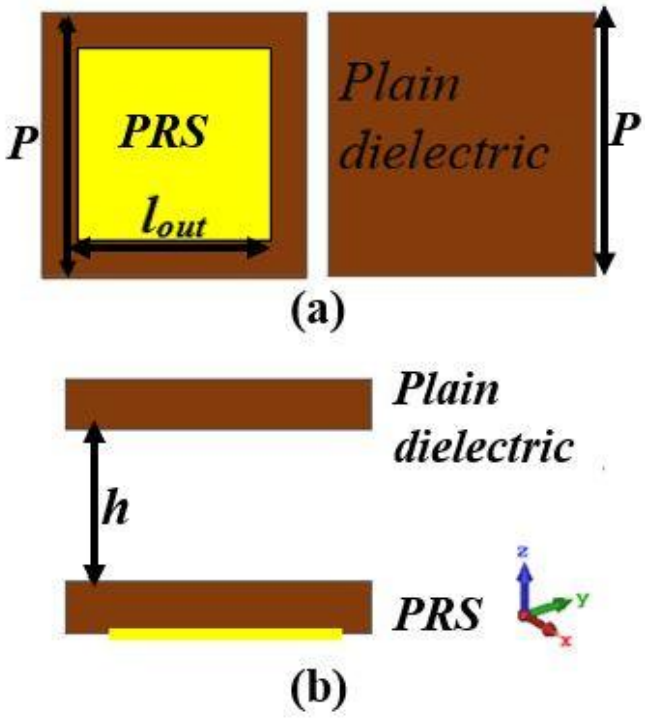


Fig. 5.1.1 (a) Parameters of PRS and Plain dielectric Unit cell and (b) side view PRS and Plain Dielectric layers in z-y coordinate axis.

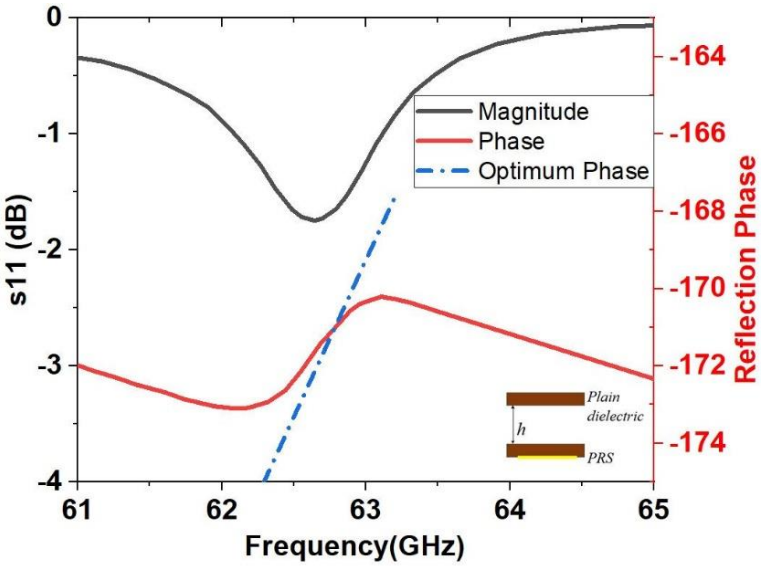


Fig. 5.1.2 Two-layer (PRS and plain dielectric) reflection coefficients with *h = 1.25mm*, *p* =1.75 mm.

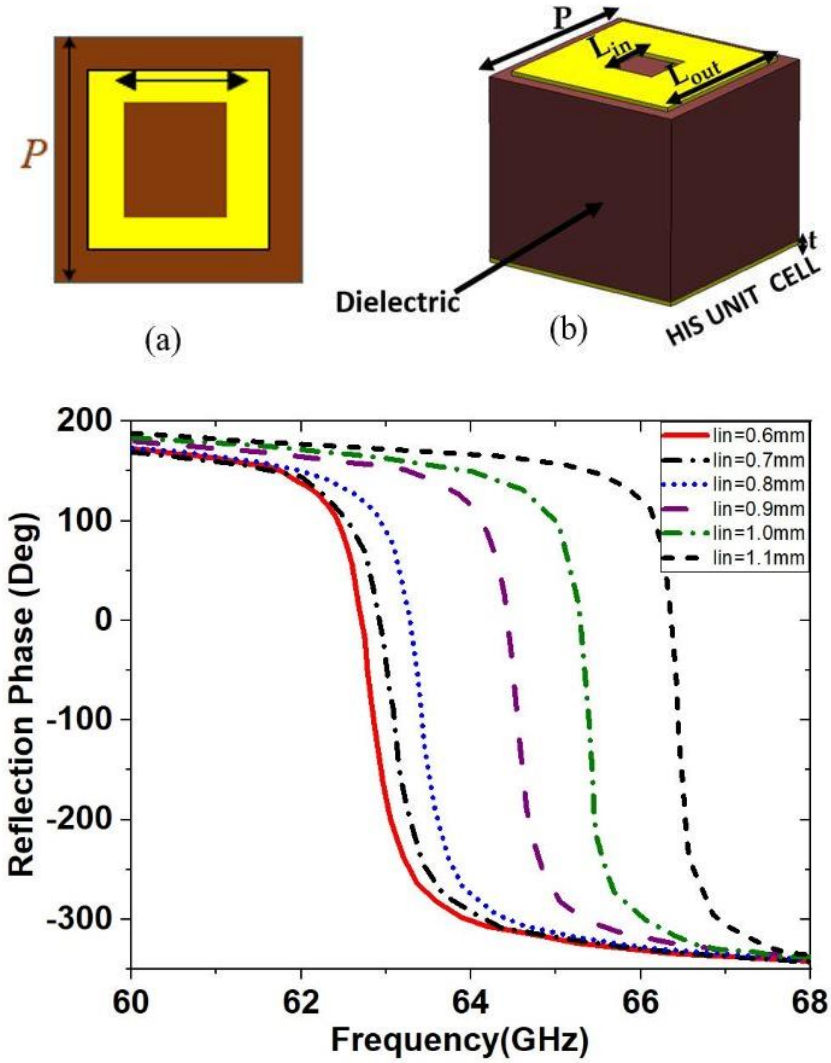
5.2.1 HIS Unit Cell design

The proposed HIS unit cell is a square loop geometry developed to operate in the 60GHz band demonstrated in Fig.5.1.3(a). It is made up of a ground plane at the bottom and a 2D periodic metallic array at the top filled with a dielectric. The substrate is grounded in the implementation of HIS structures, subsequently creating low-loss characteristics and sensitivity to frequency change. In addition, it generates reflective waves with a wide range of phase shifts at different frequencies and reflects waves with zero phase shifts at a specific frequency, as described in Chapter 1.

The array elements were printed on a dielectric substrate with a copper cladding thickness of *t = 0.175 mm* (Fig. 5.1.3b). The square loop's periodicity and outer diameter are similar to those used in Chapter 4 as well. In CST, a full-wave analysis was done based on how the proposed designs reflect plane waves that hit them normally, using periodic boundary conditions at the unit cell level and assuming that the structure is infinite.

It can be observed that a significant phase shift of φ = 120.8◦ was obtained at 62.5Hz in Fig. 5.1.3c, which is within the frequency of interest for this project. Compared to the

other metasurface square loops, the phases drift away and can lead to more losses, as discussed earlier in Chapter 3.



(c)

Fig. 5.1.3 (a)Top view of the proposed HIS unit cell periodic surface (b) perspective or side view of the proposed HIS unit cell (c)Simulated reflection characteristics of the different HIS meta-surfaces inner square loop from l_{in} = 0.6 mm to 1.1mm with similar substrate thickness h_3 = *1.75 mm.*

5.2.2 Feeding Dipole Design For Multilayer LWA

This section presents an optimized fed dipole antenna used to excite the multilayer leaky wave antenna. As previously mentioned, we choose a printed dipole antenna (DPA) with microstrip feed due to its ease of scaling to higher frequencies and being less

expensive to manufacture. In Figure 5.1.4, a microstrip line with a loss tangent of $\delta = 0.009$ and a dielectric constant of $\varepsilon_1 = 2.2$ is printed on a 1.7 mm thick dielectric substrate. The feed is etched off the substrate, which has the ground plane printed on the opposite side. The same figure shows the back view parameters of the microstrip-printed dipole antenna line. To evaluate the benefits of the improved feed dipole structure, the near-field distribution is examined. Fig. 5.1.5 shows the cross-section of the electric field at 62.5 GHz for two-sided microstrip line-fed patches. It was observed that the optimized two-sided microstrip patches provide a more uniform near-field distribution than non-optimized patches. The directivity of the antenna is improved by this effect, which is especially advantageous for the FP antennas proposed in this chapter. The fed dipole antenna was simulated and measured to determine the operating frequency and bandwidth of the proposed feed dipole structure. Figure 5.1.6 shows the S_{11} response and gain of the feeding dipole antenna. The S_{11} response is less than -10 dB from 59 GHz to 66 GHz, which is equivalent to a fractional bandwidth of 9.6%. In this case, two minima occur at 60 GHz and 62.5 GHz, which correspond to the structure's double resonance (Fig. 5.1.6.). The maximum gain of the feeding dipole antenna is 9.23 dBi, and if it is used to excite the multilayer leaky wave antenna, this gain should increase even further. It's worth noting that the optimization that resulted in the design shown here was also done with the entire FP antennas to ensure that the final antenna prototypes worked properly. Table 1 shows the parameters of the fed dipole patch antenna chosen to resonate in the frequency range of interest.

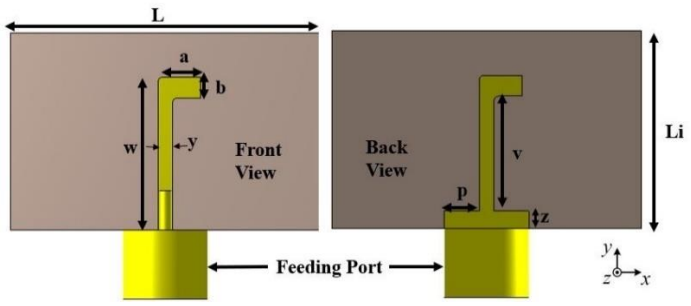


Fig. 5.1.4 Feeding dipole antenna structure with parameters (optimized).

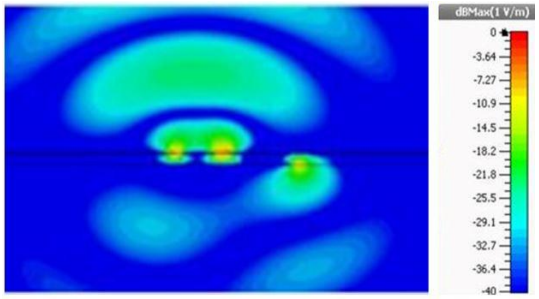


Fig. 5.1.5 Electric field distribution (YZ plane) with two-sided optimized patches.

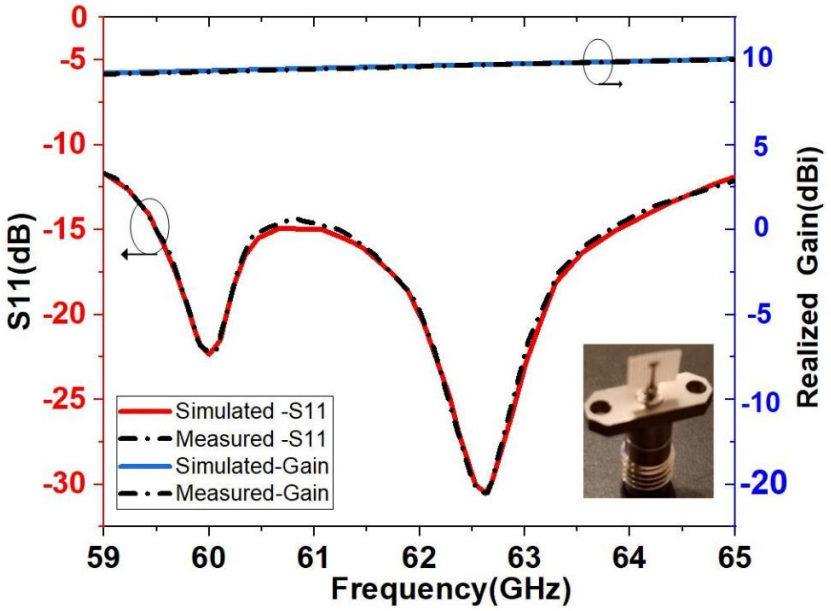


Fig. 5.1.6 The feeding PDA structure. Simulated and measured S_{11} and realized gain.

Table. 1 Feeding Dipole Structure Parameter And Values (mm)

Parameters	a	b	L	Li	p	v	y	z
Value	1.10	0.28	6.10	3.89	0.68	2.13	0.42	0.34

5.3 Multilayer Leaky Wave Antenna Design

A finite-size multilayer Fabry Perot Cavity (FPC) antenna was developed based on the optimized HIS, PRS and plain dielectric designs. The structure was built with a double layer (PRS and Plain dielectric) in front of a metallic HIS ground plane (Fig. 5.2.1a). A printed dipole antenna (Fig. 5.1.4) is inserted internally between PRS and the HIS ground plane, and this side is terminated by a vertical metallic ground (Fig. 5.2.1a, b) to provide a unidirectional FPC LWA. The dimensions of the feed dipole (3.89 mm x 6.10 mm) were

chosen to provide a satisfactory match in the frequency range of interest. The overall multilayer leaky wave antenna dimensions are 95.4×46 mm^2 with an array of 50 ×15 patch elements printed on Roger 5880 and a plain dielectric (Fig. 5.2.1c). The cavity height between the HIS array and the first layer PRS array is $h_1 = 2.91$ mm whilst the remaining parameters $h = 1.29$ *mm* which is the cavity between PRS and plain dielectric, $l_{in} = 0.6$ mm and l_{out} = 1.5mm are unit cell values, as already described in section 5.1.1.

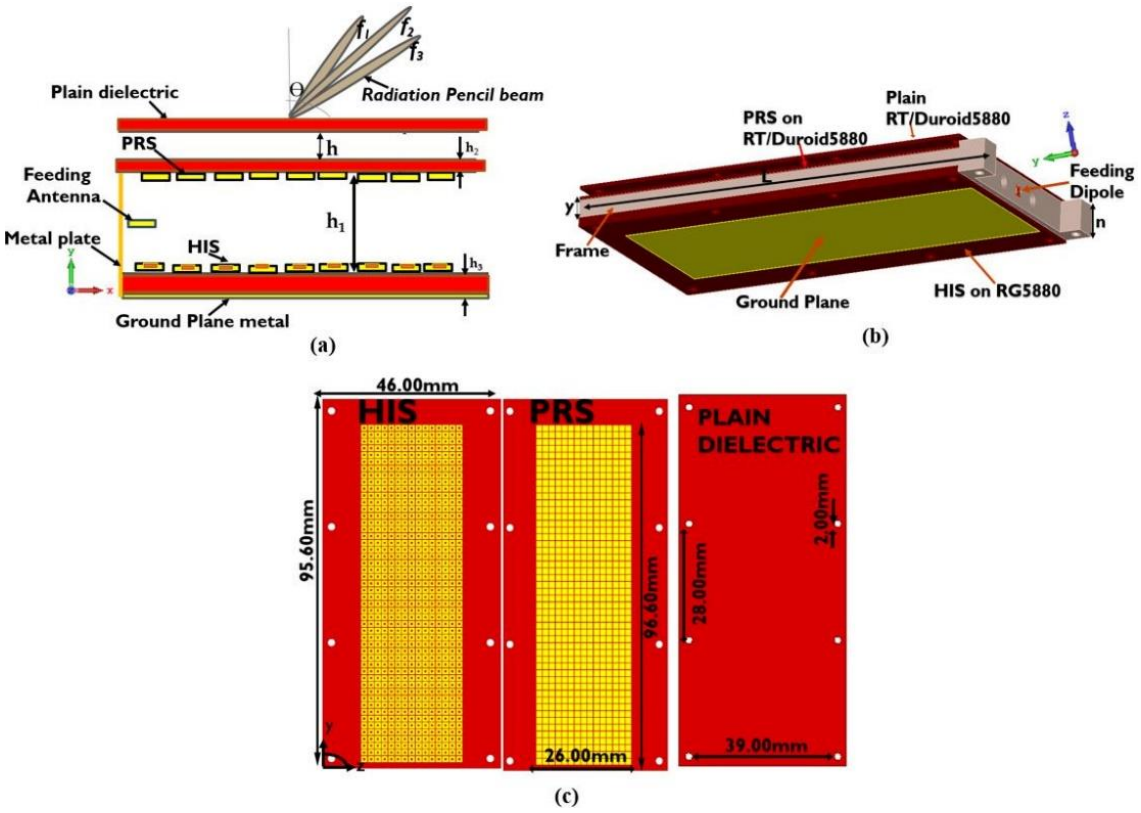
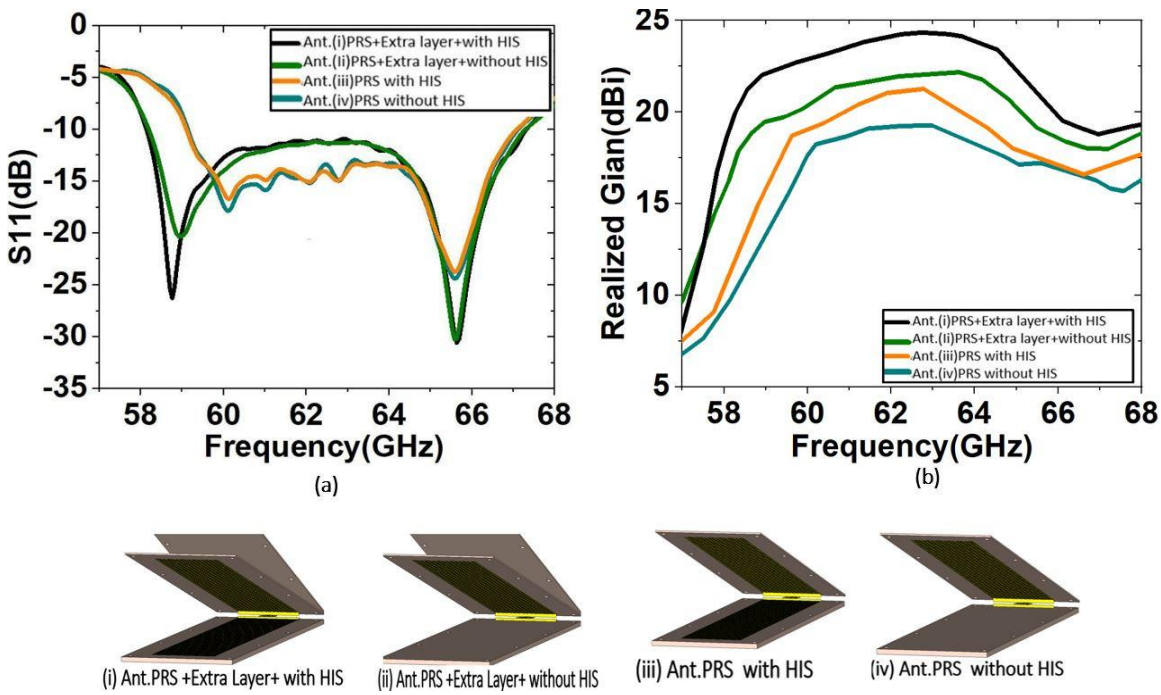


Fig. 5.2.1 Proposed multilayer LWA structure. (a) The geometry of double layer LWA (b) Side view of the LWA with a frame along xy plane where $y = 5\ mm, n = 5.2$ mm and $L = 95.5\ mm$. (c) 3D view of the HIS, PRS and Plain dielectric structure.

The concept of the proposed multilayer LWA also known as double layer LWA was compared with four different antenna configurations by way of simulation in CST Microwave Studio to justify the proposed design. The S_{11} response for the proposed multilayer LWA compared to the three different configurations is shown in Fig. 5.2.2 (a). The proposed multilayer LWA S_{11} has a much wider frequency range than the other

antenna configurations in the previous chapter and covers the entire operating bandwidth while maintaining an S_{11} of less than -10 dB. In Fig. 5.2.2b (black line), the directivity of the proposed antenna simulation with the highest gain of 24 dBi at 62.5 GHz is shown in comparison to other configurations.

The proposed antenna's 3 dB directivity bandwidth is 10.2%. The directivity of the proposed antenna shows two peaks that coincide with the two resonant cavities. This is expected since the resonance condition is met (see Fig. 5.1.2) and the reflection phase response of PRS and the plain dielectric is nearly optimal in this frequency range. Moreover, the directivity and S_{11} of the proposed multilayer LWA in Figure 5.2.2(a-b) show excellent matching performance with smaller deviations between the directivity and gain.

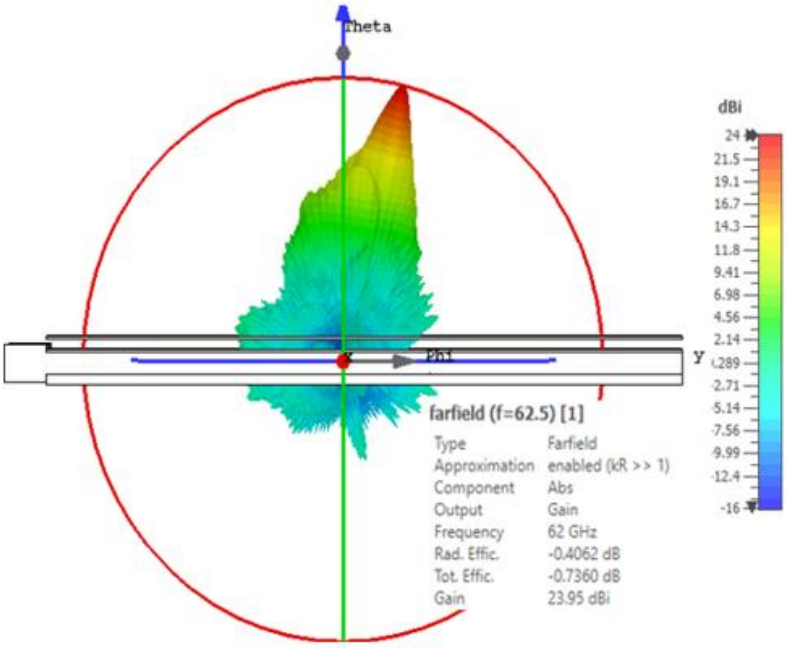


(c)

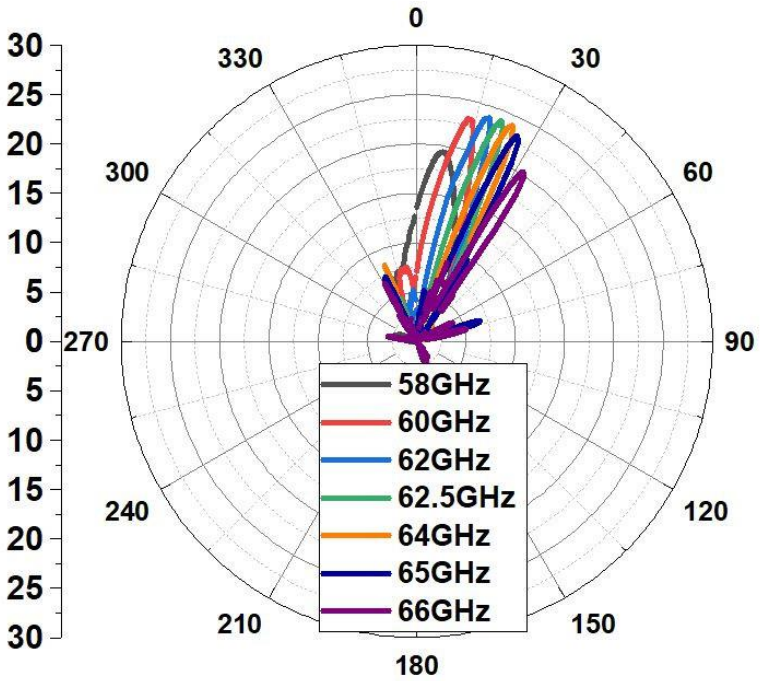
Fig. 5.2.2 Simulated LWA models (a) S_{11} and (b) realized gain for four different LWA configurations (c) inside view of all for LWA configuration.

The proposed multilayer LWA was developed to take advantage of the high-impedance surface (HIS). By using HIS as a phase shifter or reflector and an extra plain dielectric layer, the proposed LWA can be optimised for maximum gain. The advantages of this design are a gain of 24.3 dBi, more beam scanning (30^{o}) and a relatively small size due to the length, width, shape, and substrate properties. These features also contribute to improved functionality and performance. Nevertheless, an LWA without HIS and an additional layer can be more complicated, costly, and lossy. The proposed LWA design can be seen in Fig. 5.2.2 (c)i achieves improved gain, bandwidth, and beam scanning while maintaining its compactness and efficiency of 95% compared to the other antennas.

Fig.5.2.3(a)-(b) shows the simulated 3-D radiation patterns in the far-field (FRPs) of the proposed multilayer LWA at 62.5 GHz and 2-D FRPs in the E-plane at different frequencies operating within the frequency band. Table 2 compares the proposed multilayer LWA with other antenna configuration cases to prove our design concept.



(a)



(b)

Fig.5.2.3 Proposed Multilayer antenna simulation results. (a) Far-field radiation patterns in 3-D at 62.5GHz (b) far-field radiation patterns 2-D plot in the E-plane at different frequencies.

Table 2. Proposed Simulated Antenna Results Compared To Three Antennas Performance.

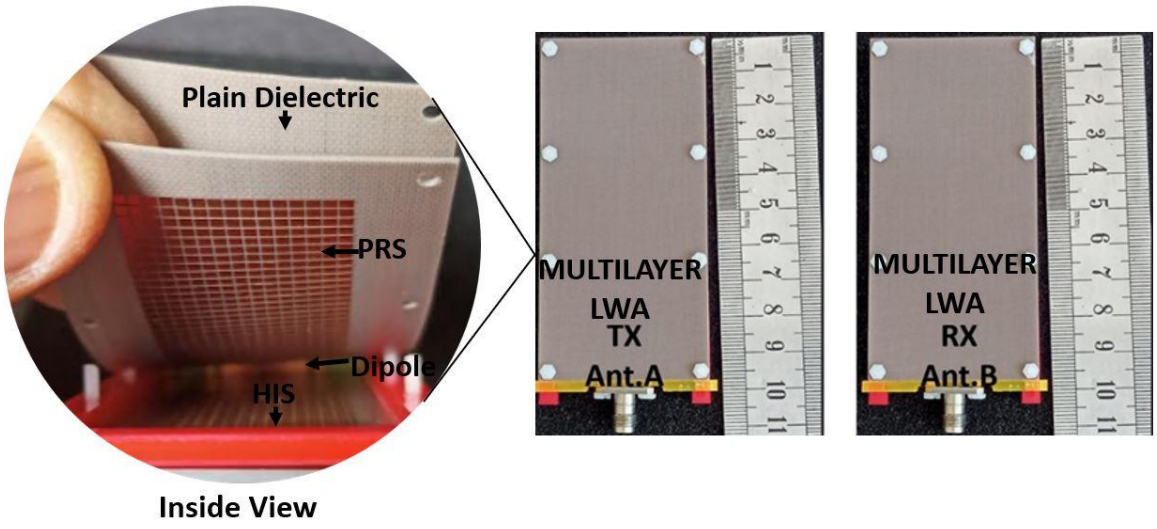
Antenna type	Operating Band $S_{11<}$ -10dB	Realized Gain(dBi)	Beam angles(deg)
with HIS	58GHz - 67GHz	22	10^o – 33^o
without HIS	60GHz - 66.6GHz	19.8	13^o – 33^o
with HIS and Plain dielectric	***58GHz -66.7GHz***	***24.3***	***4^o – 34^o***
without HIS and dielectric	60GHz - 66.7GHz	18	12^o – 33^o

5.4 Measured Results and Discussion Of Multilayer LWA

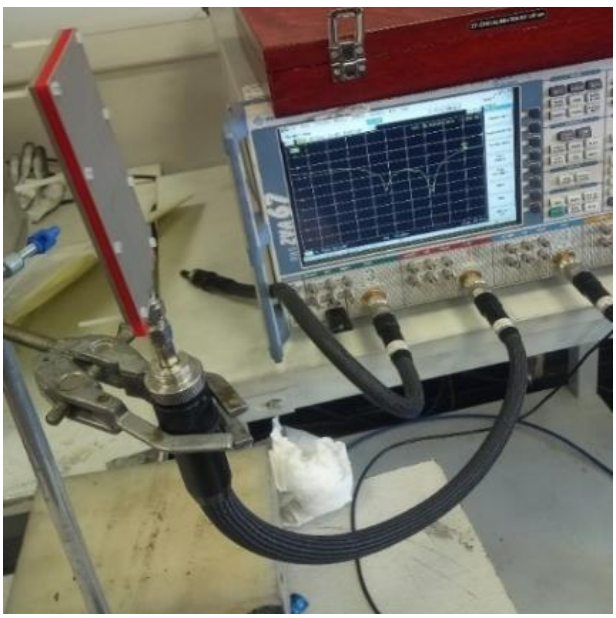
The entire multilayer LWA structure, as well as the coaxial feed, is encapsulated in a low-loss polytetrafluoroethylene (PTFE) for easy assembly and measurement purposes. The antenna PCB layers have been designed to fit into a micro-milled PTFE frame. For

the external connection, a 1.85 mm female flanged launcher (connector) with a GB185 glass bead was employed to achieve impedance matching. The antenna layers were fabricated using a conventional, low-cost PCB fabrication method.

Two prototypes of this antenna were fabricated with high precision for RVSM application (Fig.5.3.1a) and are referred to as antenna A and antenna B, respectively. The inside view of the proposed multilayer LWA is also shown in this section to enable the potential reader to understand the configuration of the antenna.



(a)



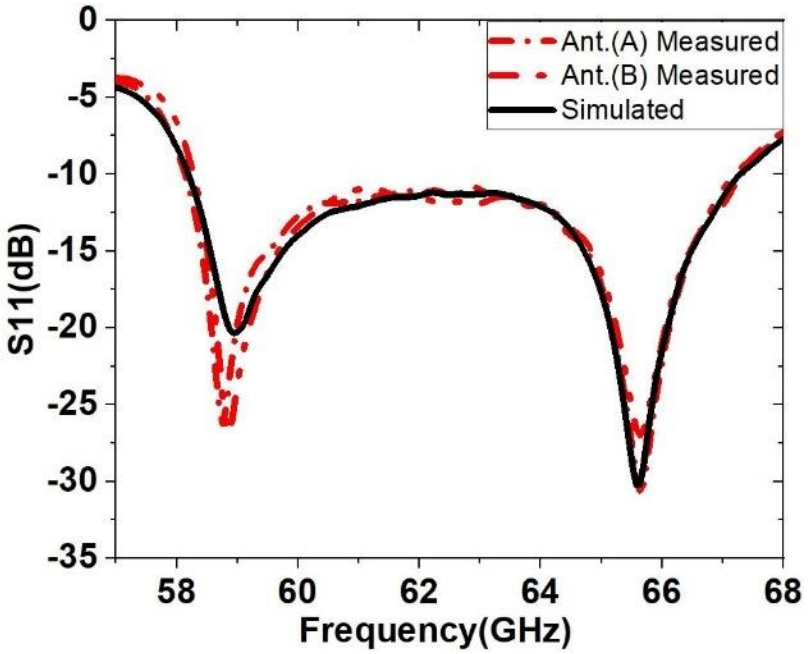
(b)

Fig. 5.3.1 **(**a) Manufactured LWA prototype inside view with external connectors (ant. A and ant. B). (b) S_{11} measurement setup.

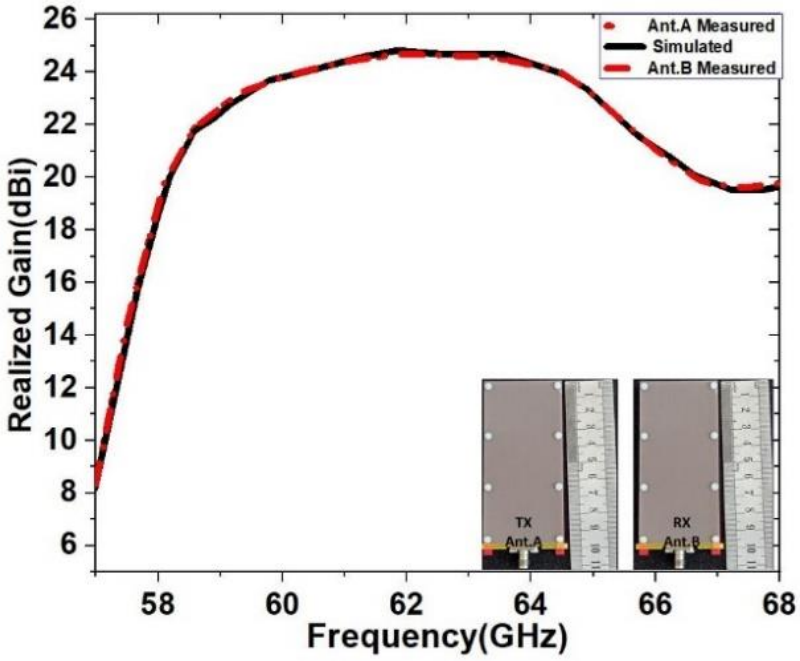
The setup for the S_{11} measurement shown in Fig. 5.3.1b demonstrates how much power is reflected from the antenna and is therefore known as the reflection coefficient or return loss. If S_{11} = 0 dB, then all the power is reflected from the antenna, and nothing is radiated. If S_{11} = - ∞ dB, then all the power is radiated from the antenna, and nothing is reflected. The lower the value of S_{11}, the better the performance of the antenna.

To measure the S_{11} of the proposed LWA with a VNA, we first connect the antenna port to port 1 of the VNA using a suitable coaxial cable and adapter. A suitable frequency range for the antenna on the VNA is set, such as 57–67 GHz for a short-wavelength LWA. The VNA was then calibrated with a calibration set consisting of a short circuit, an open circuit, and a matched load. The reason for the calibration was to eliminate errors due to cable loss or mismatch. The S_{11} of the antenna is then measured by observing the magnitude and phase of the reflected signal on the VNA display. The magnitude has been recorded on a logarithmic scale in decibels. The phase can be recorded in degrees or radians. The performance of the S_{11} measurement results was therefore analysed and evaluated to determine the resonant frequency, bandwidth, impedance, and radiation efficiency of the proposed antenna.

In comparison with the simulations, Fig.5.3.2 shows an agreement of the measured S_{11} and the realized gain for both antennas ‘A’ and ‘B’ that will be used for remote vital signs applications. The results from simulations and measurements are satisfactory, reliable and meet the design specification for RVSM application. The measured S_{11} value is still below -10 dB for all the frequency ranges of interest, except for a small deviation up to -25.2 dB and -28 dB at about 59 GHz and 59.9 GHz, respectively. The measured S_{11} bandwidth and peak gain of antenna ‘A’ is 8.55 GHz and 23.98 dBi, respectively, and are very close to those of antenna ‘B’ (8.73 GHz and 24 dBi, respectively).



(a)

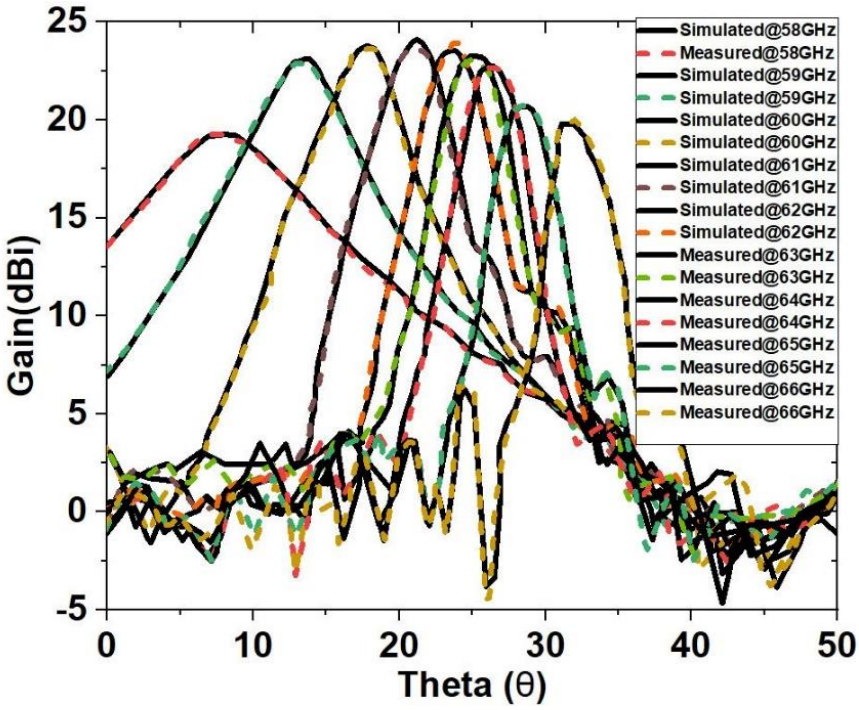


(b)

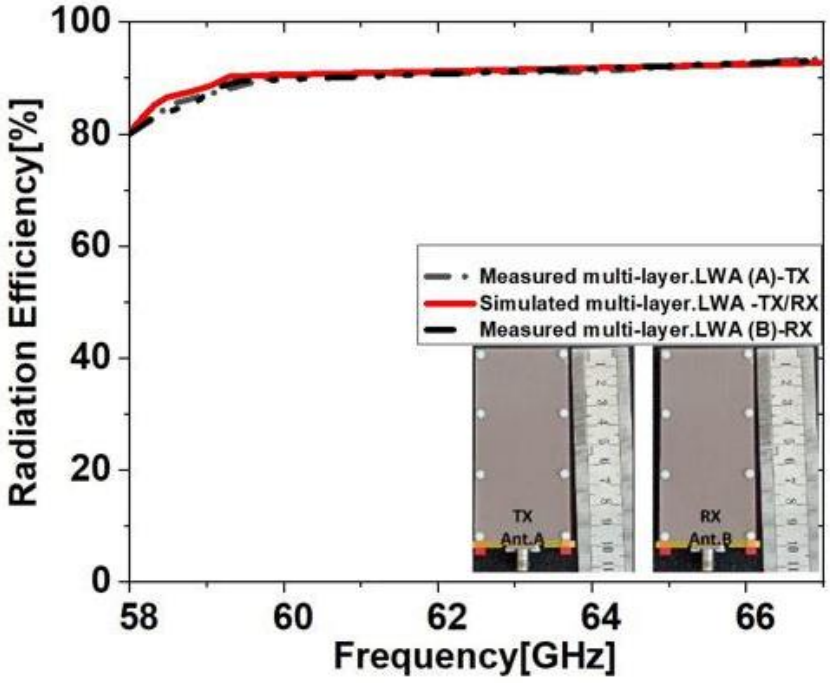
Fig. 5.3.2 Measured LWA results compared to simulated in (a) S_{11} and (b) Realized gain.

The measured radiation patterns for antenna A, similar to antenna B, are shown in Fig. 5.3.3a. The antennas achieve the expected beam scanning range of 30^{o} over the entire operating frequency spectrum (58 GHz - 66 GHz). The radiation efficiency measurement (see Fig. 5.3.3.) of the proposed multilayer LWA remains high at 95.5% in the frequency

range of 58 to 67 GHz, with a half-width beam (HPBW) that ranges from 13 ^{o} to 5^{o} shown in Table 3 in comparison with the simulations results in Fig. 5.2.2b



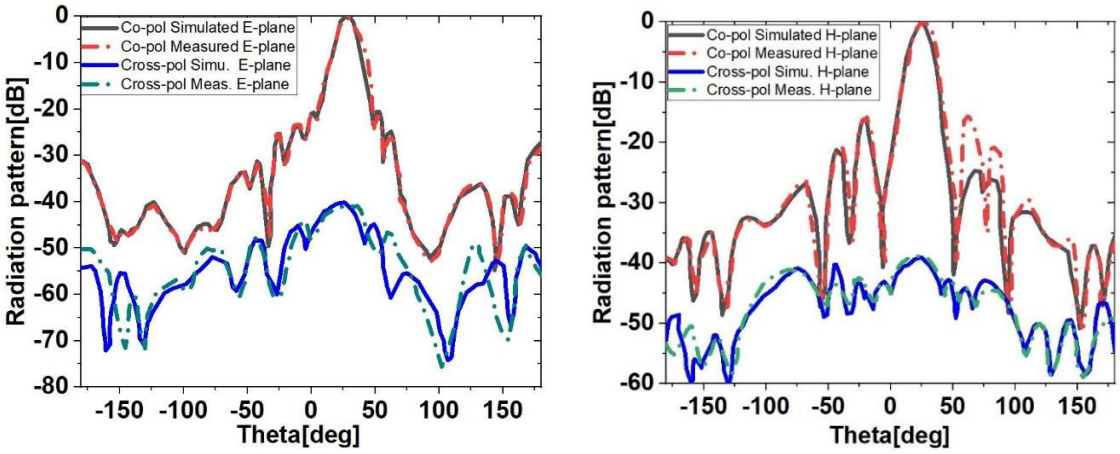
(a)



(b)

Fig. 5.3.3 Measured and simulated (a) Far-field radiation pattern (FRPs) in the E-plane of ant. A . similar to antenna B (b) radiation efficiency of ant. A and ant. B.

Inconsistencies in the fabrication and gain measurements performed, such as interconnector losses, reflections from the environment, and misalignment of the antenna layers, explain the small beam angle shift of 0.1° and 1° between the measured and simulated results (see Table .3) at some frequencies. The resulting antenna characteristics satisfy the RVSM criterion as described in Section 1. The co-pole and cross-polar level at 62.5 GHz is also shown in Fig. 5.3.4 and is still below -40 dB in both the E and H planes. A comparable cross-polar level which is unwanted radiation can be expected for other frequencies as well. The above measurement is summarized in Table 3.



(a) (b)

Fig. 5.3.4 Measured and simulated copolar and cross-polar (a) E-plane and (b) H-plane radiation patterns at 62.5GHz.

Table 3. Performance Of Measured Multilayer Leaky Wave Antennas.

	Operating Band $S_{11<}$ -10dB	Realized Gain(dBi)	Beam angles(deg)	HPBW (deg)
Ant. A (measured)	58.95GHz – 66.5GHz	24.2	4° – 34°	13° - 5°
Ant. B (measured)	58.9GHz – 66.3GHz	24.12	4.2° – 34.3°	14° - 8°
Simulated	58GHz – 66.7GHz	24.0	5° – 36°	9° - 5°

5.5 RVSM Measurements With Multilayer LWA Doppler Radar

In this section, the principles of Doppler radar and all the steps used in Chapter 4 were applied to extract the vital signs using the multilayer LWA. In conclusion, a Doppler radar

transmits a one-tone electromagnetic (EM) signal for a predetermined period using it's transmitting antenna (Tx) (multi-layer LWA). The electromagnetic signal that bounces off the person's chest at a certain distance is picked up by the other multilayer LWA used for reception (RX).

The quasi-periodic oscillations of the chest caused by breathing and pulse gradually change the received signal's phase over time. During the demodulation process, the signal that was sent and the phase-modulated signal that was received is merged. The product is a signal that has characteristics that are similar to those of the baseband signal that was captured in the time domain (TD) by the Rx [12]:

$$R(t) = \cos\left[\theta(t) + \frac{4\pi x_b(t)}{\lambda} + \frac{4\pi x_h(t)}{\lambda}\right] \qquad (5.4-1)$$

where $\theta(t)$ is the complete phase shift caused by the signal direction consisting of reflections from the subject and surrounding as well as remaining phase noise; the operating wavelength is denoted by λ, and the chest vibration displacements caused by breathing and heartbeat, respectively, are denoted by $x_b(t)$ and $x_h(t)$. By extending it in a Fourier series, as described in [13], it is possible to convert the recorded and demodulated received signal into the frequency domain (FD). Matlab is then used to apply the necessary digital filters to isolate the desired BR and HR signals from the noise and unwanted harmonics that were produced as a result. The details of this process are already explained in Chapter 4.

5.5.1 Remote Vital Sign Monitoring At 2 m

For our RVSM measurements, we use the Rohde & Schwarz ZVA67 GHz Vector Network Analyzer (VNA) and the multilayer leaky wave antennas that we have proposed. These antennas serve as Tx and Rx antenna modules. The VNA offers users the ability to

set the operating frequency within the desired range, which in this case ranges from 58GHz to 65 GHz. To verify the range of the proposed beam scanning antennas for vital sign detection from a stationary location in the range of 2 m to 4 m, a complete setup of the tests shown in Fig. 5.4.1 was performed. First, we look at the 2 m RVSM measurements.

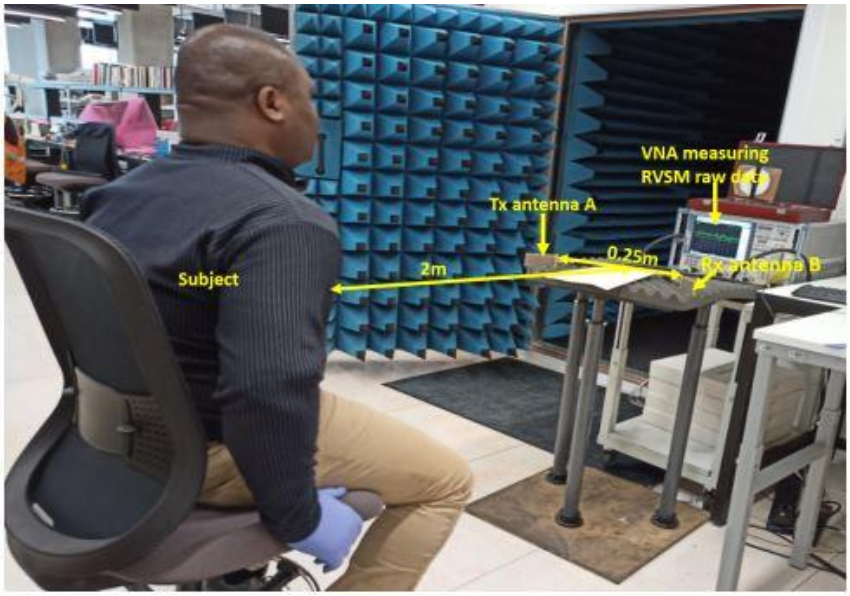


Fig. 5.4.1 RVSM experiment measurements at 2m.

A comprehensive set of experiments was conducted to validate the 2-meter coverage of the proposed stationary beam-scanning antennas for vital sign detection. The transmission (Tx) and reception (Rx) of electromagnetic waves in the 57 - 66 GHz frequency range of the VNA were both calibrated to 0 dBm, allowing 201 measurement points to be acquired, when the subject sits in front of the antennas at a 2m radial distance and angular position demonstrated in Fig. 5.4.1. A 60-second continuous waves (CW) time sweep with a tone within one minute is executed. The electromagnetic (EM) signals are transmitted to the chest from the Tx antenna, which can be found on port 1 of the VNA. This takes place during the sweep period. The Rx antenna, which can be found connected to Port 2 of the VNA, receives electromagnetic signals. The VNA records the phase-demodulated signal, which is also referred to as the S_{21} phase, and stores it for a

period of sixty seconds. The required BR and HR values are then determined by running the acquired S_{21} phase data through a signal processing program in MATLAB. During signal processing, Bandpass filters are used to pass the breathing rate (BR) and heart rate (HR) frequencies, followed by a notch filter, also known as tenth-order Butterworth digital filters, which are used to reduce noise, read data, and output display commands. The discrete fast Fourier transform (DFFT), bandpass filters, and notch filters are the key elements that make up the software that analyses the signals. The DFFT is responsible for converting the TD signal to the FD signal. To justify RVSM detection capabilities under the proposed antenna beam steering, we are interested only in the average results for BR (1/Min) and HR (1/Min) in the frequency domain (FD) and not BR and HR waveforms in the time domain. Consequently, no electrocardiogram (ECG) is required to compare Doppler radar waveforms with beam steering RVSM results.

During the experiment, the subject sat 2 m in front of the Tx/Rx antennas at three distinct angular locations, namely 5°, 15°, and 30°, and S_{21} phase data (demodulated Doppler signal in TD) are captured at 58 GHz for each of the angular positions. The tests are then repeated at 62.5 GHz, 64 GHz, and 66 GHz. We collect four sets of S_{21} phase data in this way for the three angular locations at 58 GHz, 62.5 GHz, 64 GHz, and 66 GHz. The experiment's findings are shown in Figs. 5.4.2 - 5.4.5, respectively. The plots on the left side of each image show the recorded Doppler signal in the time domain (TD), while the plots on the right side show the corresponding processed signals in the frequency domain (FD). The first peak in each processed data plot occurs at a frequency of about 20 (1/min) and indicates the predicted amplitude of the BR signal. The second peak in each plot occurs at a frequency of about 80 (1/min) and indicates the expected amplitude of the HR signal.

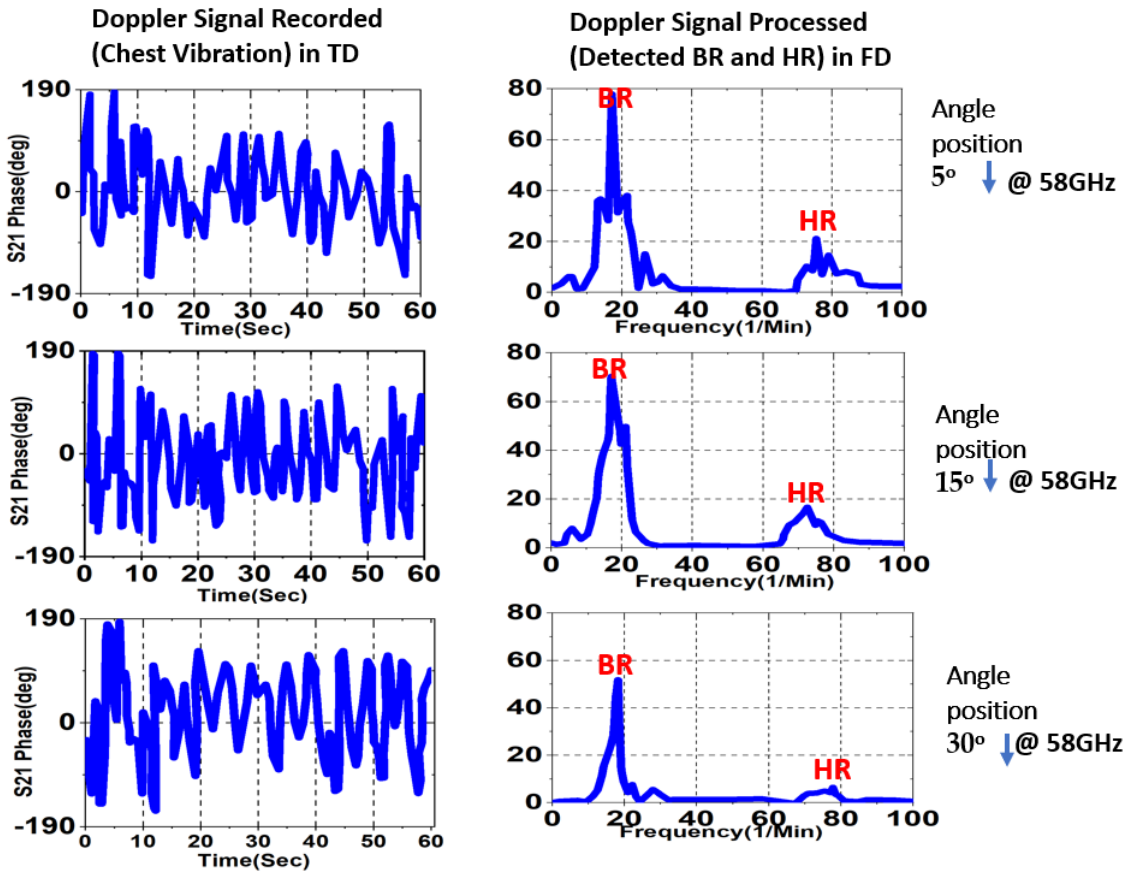


Fig. 5.4.2 RVSM Measurements from a 2 m distance at 58 GHz.

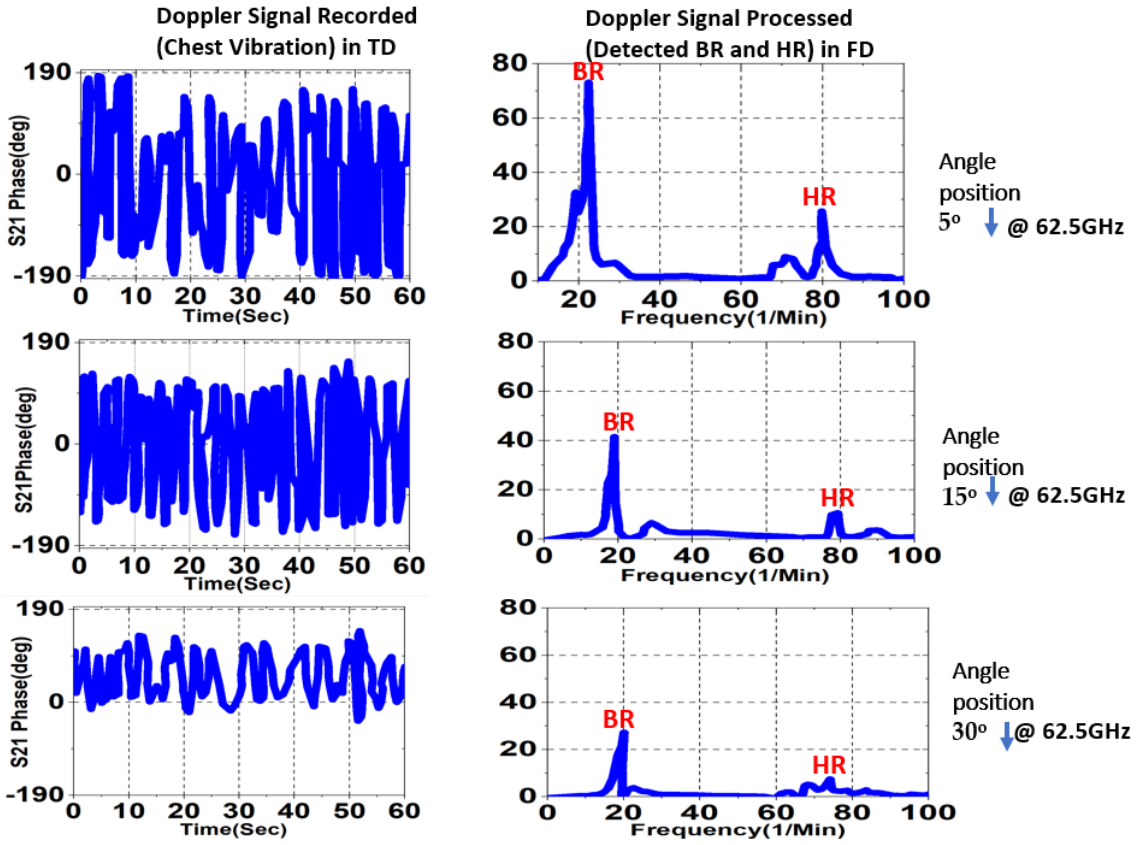


Fig. 5.4.3 RVSM Measurements from a 2 m distance at **62.5** GHz.

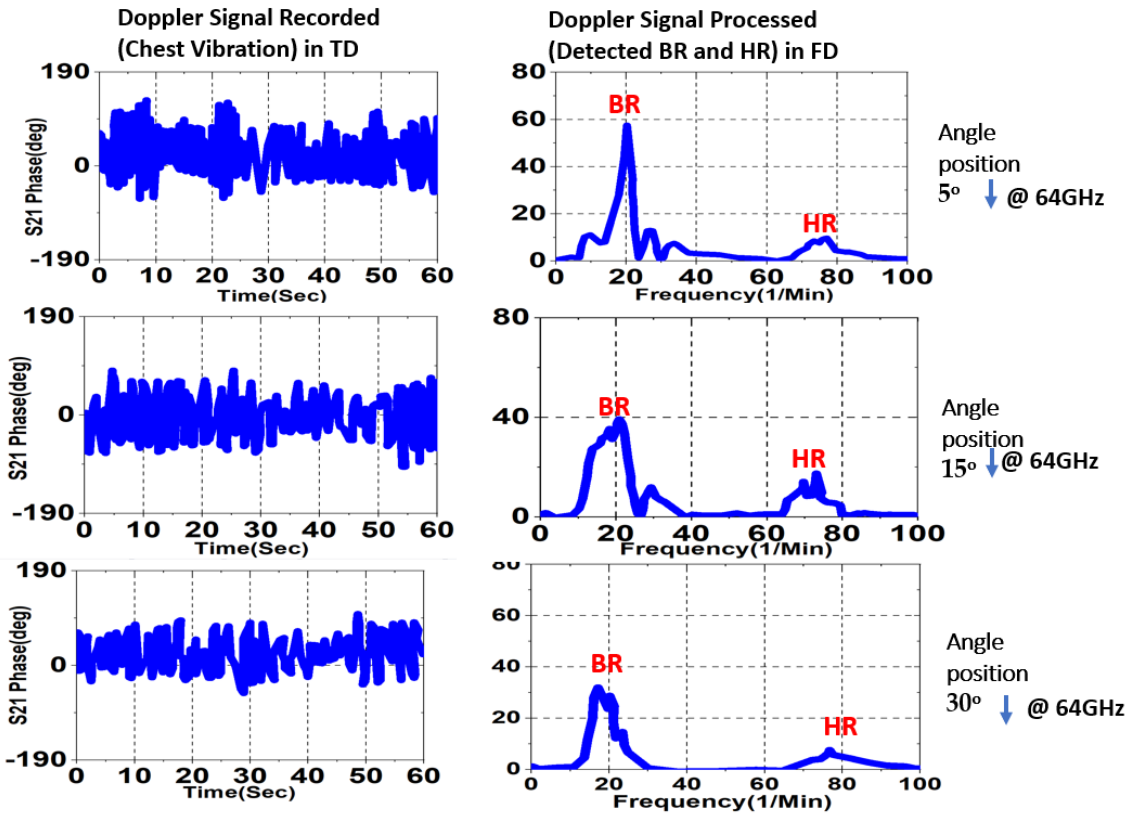


Fig. **5.4.4** RVSM Measurements from a 2 m distance at 64 GHz.

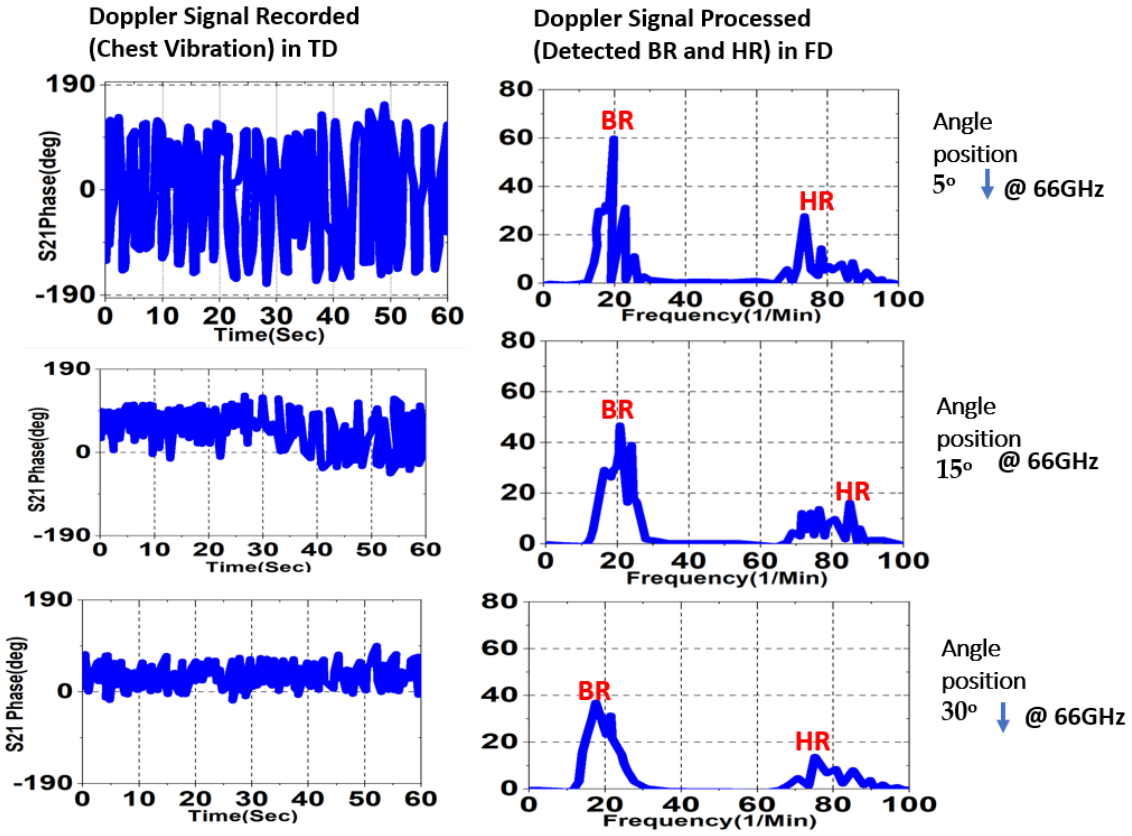


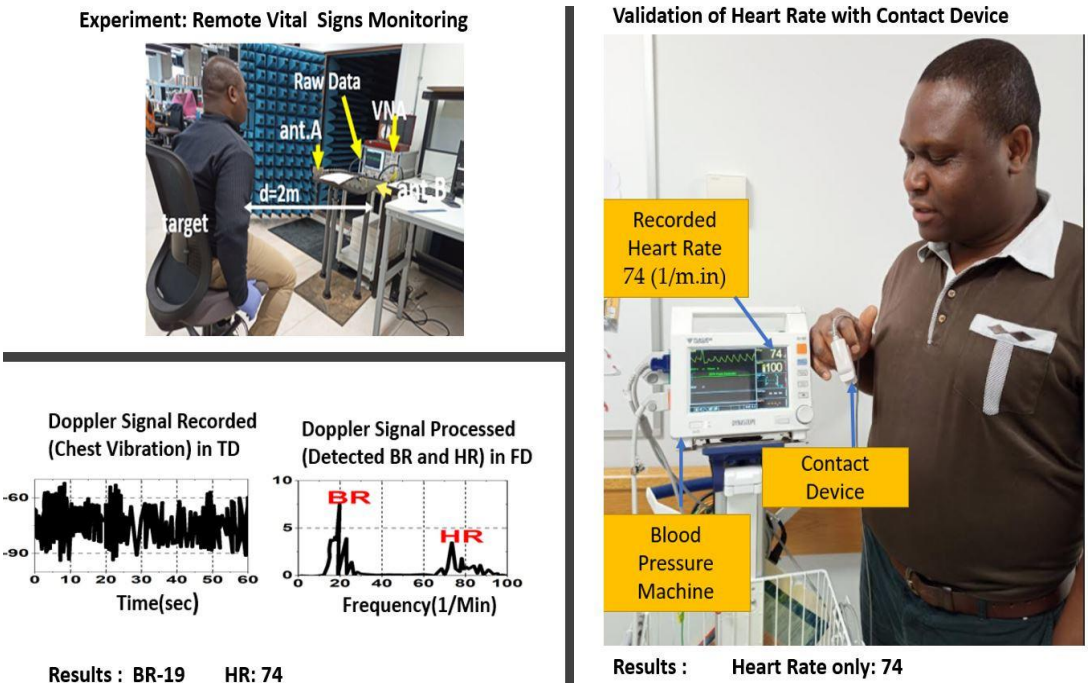
Fig. **5.4.5** RVSM Measurements from a 2 m distance at 66 GHz.

It is clear from looking at Fig. 5.4.2 that for the subject at lower angular positions specifically 5° and 10°, the detected BR and HR signals have sufficiently higher amplitudes than the noise levels due to the proposed antenna's high gain performance. These results are consistent with expectations [see Table 3] at a frequency of 62.5 GHz, where the radiation beam of the antenna is centred at an angle of about 20^{o} and has a high-power beam width of more than 12^{o}. It can be shown in Figures 5.4.2 – 5.4.5 that when measurements are taken at higher angular locations and higher operating frequencies, the detected Doppler signal has the maximum amplitude in comparison to the levels of background noise. Table 4 summarizes all the results and findings of the RVSM. According to the data shown in Table 4, all of the calculated BR and HR values are reliably located within the predicted value range, with a comparatively little margin of error of 0.3% when compared to their mean reference values.

Table 4. Measured BR And HR At Various Positions With Respective Beam Angles At 5^{o},15^{o} and 30^{o} For Each Frequency.

58 GHz	62.5 GHz	64 GHz @	66GHz @	Manual Counted BR Contact Device HR		Maximum Error
BR – HR (1 / min)	BR – HR (1 / min)	BR – HR (1 / min)	BR – HR (1 / min)	BR (1 / min)	HR (1 / min)	BR – HR (1 / min)
19 - 78	20 - 80	20 -79	19-80	19 -20 (avg.20)	74 – 80 (avg.79)	5% - 0.3%

To authenticate the heart rate of our data, we compared it to those of a traditional hospital blood pressure monitor used on patients daily [See Fig. 5.4.6]. Results obtained with the traditional hospital sphygmomanometer (a contact device) agree well with remote vital signs obtained with Doppler radar technology. The DR signal is constantly captured during the time window process; however, signal processing is only performed to the most recent period (for example, 60 seconds for a pulse resolution of 1/min), and findings are updated after a small-time delay (for example, every 5 s). Simple signal processing based on the Fourier transform is employed to provide time-averaged and high-resolution RVSM results [13].

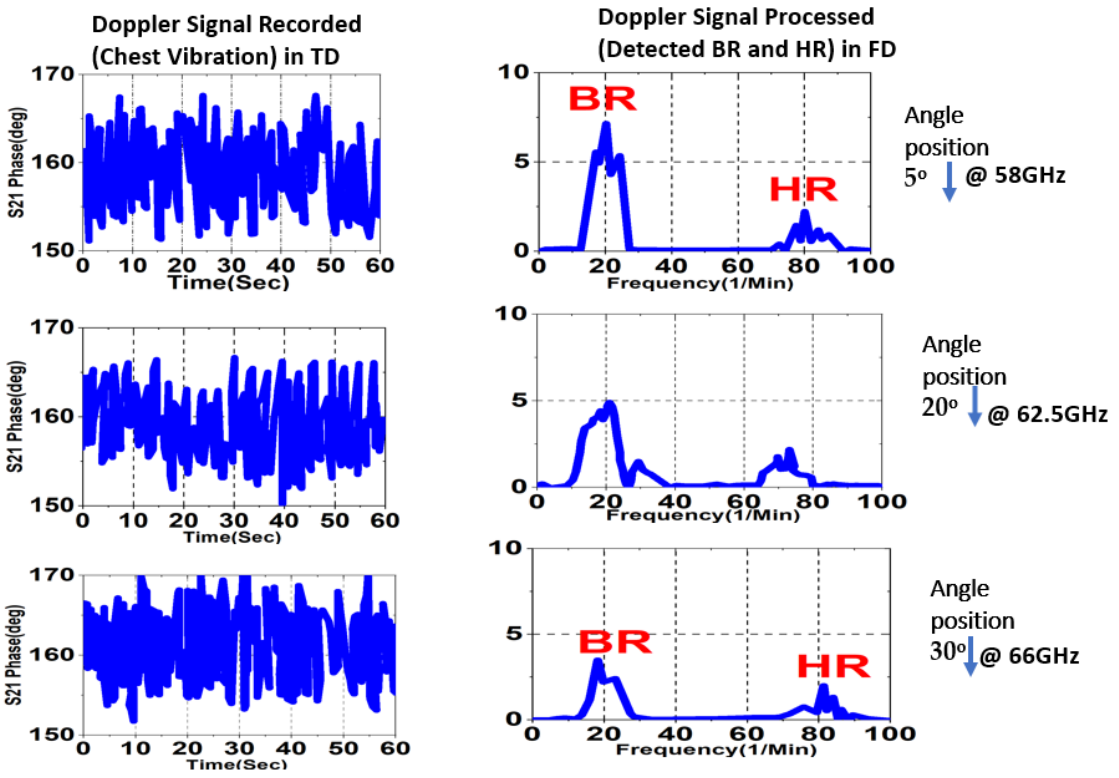


(a) (b)

Fig. 5.4.6 Validation of RVSM using (a) Non-contact device (b)Traditional blood pressure machine.

5.5.2 Remote Vital Signs Monitoring At 4 m

To show long-range operational coverage of the proposed antennas, the experiment was repeated to monitor the vital signs of the same individual seated 4 metres away from the antenna and measurements were taken at different angle positions. The other parameters of the experiment remain unchanged from what was previously reported. This time, three RVSM experiments were carried out using the best frequency and beam angle combinations that demonstrated the maximum detectability. These combinations were 58 GHz for angular positions 5^{o}, 62.5 GHz for angular positions 20^{o}, and 66 GHz for angular positions 30^{o}, as demonstrated in Fig. 5.4.7.



Fi**g. 5.4.7** Measured RVSM results from **4 m** distance at 58GHz, 62.5GHz and 66 GHz.

It can be said that the proposed antenna's RVSM detection response for an angular range of 5◦ to 25◦ at 2 m is sufficient to cover the angular range for measuring BR and HR in a patient in bed or an ambulance transported to a hospital (See Fig.5.1.1) when the operating frequency is scanned from 58 to 65 GHz accordingly. Since the antenna gain and transmit power is high enough, the angular coverage of RVSM detection can be improved by putting the antennas far away from the object [14], as shown in Fig. 5.4.7.

The presented multilayer beam scanning LWA is an excellent option for use as a contactless wireless sensor for BR and HR health monitoring at radial distances of up to 4 metres and an angular range that extends from 5^{o} to 35^{o}. In health monitoring situations where the patient is likely to move within a 2m to 4m distance of the Doppler cross-section area, the proposed multilayer LWA can perform much better than fixed-beam antennas. The proposed multilayer leaky wave antenna is compared with a horn antenna

[16] and other types of antennas used for RVSM at millimetre-wave frequencies [2], [3] and [15].

Table 5. Antenna Performance Comparison Between Recent LWA For RVSM And Proposed Multilayer LWA

	[2]	[3]	[15]	[16]	**This Work**
Antenna type	Fabry Perot	Patch Antenna	Fabry Perot	Horn Antenna	**Fabry Perot**
Frequency (GHz)	58.3 - 67.5	57.24 – 65.88	62 – 65	60	**58 – 66**
Efficiency (%)	94.5	94	95	94	**95.5**
Scanning Range(°)	27°	-	12	0	**30°**
Gain (dBi)	24	21.1	20.1	24	**24.3**
Bandwidth (GHz)	9	8.5	3.38	12	**8**
RVSM distance (m)	2	0.5	3	1	**4**
RVSM accuracy (%)	99	90.8	90.8	98.6	**93**

The main novelty of the proposed multilayer LWA is its high gain of 24.3 dBi, radiation efficiency of 95.5% and a frequency sweep of 30° over longer distances of up to 4 meters from the human body with an accuracy of 93%. This is a significant improvement over horn antennas [16], which have a gain of 24 dBi, a short-range (1 m) RVSM and suffer from beam scanning when the subject changes position. Due to the known trade-off between gain and beam aperture, our antenna has a smaller bandwidth than [16]. The proposed antenna has been shown to have higher efficiency, longer range, higher gain and higher RVSM accuracy than most other antennas. The proposed antenna is a Fabry-Perot antenna, a type of leaky-wave antenna that uses a partially reflective surface to generate multiple beams. The proposed antenna uses a multilayer structure to improve the radiation characteristics and reduce the size of the antenna. The proposed antenna is suitable for applications such as radar, communication, and navigation systems that require high gain, wide bandwidth, and beam scanning capability.

5.6 Conclusions

In situations where the subject is not in a fixed position, it has been demonstrated that a multilayer Fabry-Perot type LWA with a high gain of 24.3 dBi, radiation efficiency of 95.5%, and a frequency sweep of 30° outperforms horn and other antenna designs for RVSM. The antenna operates in the low-noise 60 GHz spectrum and is constructed using standard, low-cost PCB techniques. Two identical antennas were constructed, tested, and measured. The measured and simulated results agree perfectly, and the antennas have successfully detected breathing and heartbeat at radial distances of 2 m to 4 m and angular positions of 5^{o} to 35^{o} from the human body with 93% accuracy. The design method may be very beneficial for developing low-cost, high-gain antennas for much higher mm-wave frequencies and larger coverage regions.

References

[1] M. S. Rabbani and H. Ghafouri-Shiraz, "Frequency selective surface antenna for remote vital sign monitoring with ultra-wideband Doppler radar," Microw. Opt. Technol. Lett., vol. 59, no. 4, pp. 818-823, Apr. 2017.

[2] S. Mingle, "Frequency Scannable Leaky-Wave Antenna Design for Remote Vital Signs Radar Application at 60GHz Band." *International Conference on Electrical, Communication, and Computer Engineering (ICECCE)*, pp. 1- 4. IEEE, 2021.

[3] M. S. Rabbani and H. Ghafouri-Shiraz, "Ultra-wide patch antenna array design at 60GHz band for remote vital sign monitoring with Doppler radar principle," J. Infr., Millim., Terahertz Waves, vol. 38, no. 5, pp. $548-566,\ 2017$.

[4] M. S. Rabbani and H. Ghafouri-Shiraz, "Accurate remote vital sign monitoring with 10 GHz ultra-wide patch antenna array," AEU-Int. J. Electron. Commun., vol. 77, pp. 36-42, Jul. 2017.

[5] A. D. Droitcour et al., "Non-contact respiratory rate measurement validation for hospitalized patients," in Proc. Аппи. Int. Conf. IEEE Eng. Med. Biol. Soc., Sep. 2009, pp. 4812-4815.

[6] M. Villarroel et al., "Continuous non-contact vital sign monitoring in neonatal intensive care unit," Healthcare Technol. Lett., vol. 1, no. 3, pp. 87-91, 2014.

[7] S. Suzuki, T. Matsui, M. Kagawa, T. Asao, and K. Kotani, "An approach to a non-contact vital sign monitoring using dual-frequency microwave radars for elderly care," J. Biomed. Sci. Eng., vol. 6, no. 7, p. 704, 2013.

[8] T.-Y.-J. Kao and J. Lin, "Vital sign detection using 60-GHz Doppler radar system," *in Proc. **IEEE** Int. Wireless Symp. (IWS),* pp. 1– 4, Apr. 2013.

[9] T. Hall et al., "A phased array non-contact vital signs sensor with automatic beam steering," *in IEEE MTT-S Int. Microw. Symp. Dig*., pp. 1– 4, May 2015.

[10] T. Hall et al., "Non-contact sensor for long-term continuous vital signs monitoring: A review on intelligent phased-array Doppler sensor design," Sensors, vol. 17, no. 11, pp. 2632, Nov. 2017.

[11] A. P. Feresidis, J. C. Vardaxoglou, "A broadband high-gain resonant cavity antenna with single feed", Proc. EuCAP 2006, Nice, France, 2006.

[12] C. Gu, C. Li, J. Lin, J. Long, J. Huangfu and L. Ran, "Instrument-Based Noncontact Doppler Radar Vital Sign Detection System Using Heterodyne Digital Quadrature Demodulation Architecture," in *IEEE Transactions on Instrumentation and Measurement*, vol. 59, no. 6, pp. 1580-1588, June 2010.

[13] C. Li and J. Lin, "Optimal carrier frequency of non-contact vital sign detectors," in Proc. IEEE Radio Wireless Symp, pp. 281-284. Jan. 2007.

[14] B. Biglarbegian, M. Fakharzadeh, D. Busuioc, M.-R. Nezhad-Ahmadi, and S. Safavi-Naeini, "Optimized microstrip antenna arrays for emerging millimeter-wave

wireless applications," IEEE Trans. Antennas Propag., vol. 59, no. 5, pp. 1742–1747, May 2011.

[15] M. S. Rabbani, J. Churm and A. P. Feresidis, "Fabry–Perot Beam Scanning Antenna for Remote Vital Sign Detection at 60 GHz," in IEEE Transactions on Antennas and Propagation, vol. 69, no. 6, pp. 3115-3124, June 2021.

[16] Z. Yang, P.H. Pathak, Y. Zeng, X. Liran, P. Mohapatra. "Vital sign and sleep monitoring using millimetre wave". *ACM Trans. Sens*. Netw. **2017.**

Chapter 6: Bidirectional LWA Design Based On Dielectric Image-Line For Remote Vital Sign Monitoring At Millimeter-Wave Frequencies

Abstract: In a dynamic setting, a novel bidirectional dielectric image-line leaky wave antenna (LWA) for remote vital sign monitoring (RVSM) based on Doppler radar technology is presented. It is made of a copper dielectric image line with conductor backing on which two layers of the same dielectric material have been stacked on top of one another to improve the device's performance. The two uppermost layers consist of a substrate (RO6010) with a high value of the dielectric constant and sufficient permeability. A low permeability substrate (RT /Duroid 5880) was used for the bottom layer to prevent higher-order modes from developing in the dielectric image line (DIL) antenna during excitation. By introducing holes into the DIL at regular intervals, the dominant mode of the DIL can be excited to resonate, resulting in the generation of fast-wave spatial harmonics. The proposed antenna has a wide scan range of 70.19^{o} (- 42.49^{o} to 27.7^{o}) across the broadside. Other features of this antenna include an impedance bandwidth of 15 GHz (50-65 GHz), an optimum fast-wave gain from 15.5 dBi to 19.79 dBi, and adequate radiation efficiency of 83.8% at 57.5 GHz. Extensive experiments on remote vital sign monitoring (RVSM) with the proposed DIL antenna have been presented, which are consistent with conventional devices. We demonstrate that multiple targets' respiratory rate (BR) and heart rate (HR) can be measured within 70^{o} of the angular range by tunning the operating frequency from 50 GHz to 65 GHz.

6.1 Introduction

Accurate monitoring of physiological signals is critical in a variety of disciplines, including healthcare, medical procedures, and others. In particular, the ability to reliably

measure respiration and heart rate is critical [1]. Conventional measuring devices had to be in direct contact with the subject being measured, which required the use of wires to collect accurate data. An example of this is the use of sensors worn close to the patient's body, which is uncomfortable for patients and causes them discomfort. Doppler radar is a technique that permits remote monitoring of a person's vital signs, such as heart rate and breathing. This approach is less obtrusive and more pleasant than the conventional contact-based devices which are invasive. Doppler radar technology can be useful for remotely measuring the breathing and heartbeat of a patient who is in distress or suffering from skin burns [1].

Regular healthcare diagnostics, emergency services, security, and military applications are just a few of the fields where the suggested LWA may be used [1], [2], [3], [4], [5], [6], [8], [9], [10], [11]. However, the quality and consistency of the data acquired by RVSM must be successfully addressed before it can be employed in clinical settings. This is crucial when a patient is prone to erratic movement [7]. To satisfy the needs of these systems, planar antennas must have a high gain, wide scanning angles, a low profile, be lightweight and be simple to connect with other technologies [12].

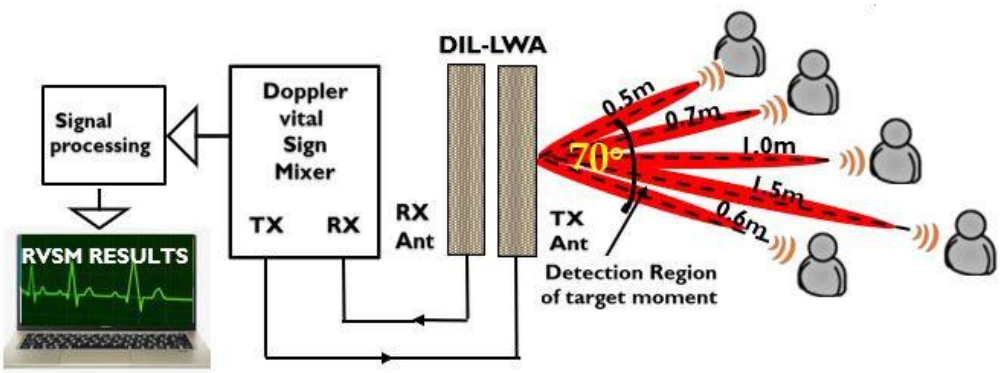


Fig. 6.1.1 Bidirectional LWA application for RVSM multiple targets through broadside.

Leaky wave antennas are excellent candidates for use in wireless frequency sensing due to their ease of feeding, high gain, and ability to operate over a wide frequency range [13]. This makes leaky wave antennas desirable candidates for use in frequency-scanning wireless systems. One of the features of the LWA is that it can perform a frequency sweep

in both directions simultaneously. Dielectric supercell grating was used in [14] to achieve dual-band LWA performance at 60 GHz. The grating consisted of two different grating layers with different diameters. The dual ray radiating in opposite directions is generated by two spatial harmonics with n = -1 and n = -2, respectively. According to reference [15], a long-wavelength antenna (LWA) for the W-band is made by placing rectangular dielectric gratings on both sides of a dielectric image line (DIL) on a single substrate.

Antennas that are based on DIL have several benefits, some of which are frequency scanning, low-loss performance, simple mounting, and the ability to integrate with other technologies. In [16], [17], and [18], a DIL leaky wave antenna array is fed through a hole in the ground plane. These antenna arrays are based on an internal dielectric waveguide operating in the mm-wave frequency range (50–85 GHz) [16], [17], [18]. In the sub-THz frequency band, DIL antennas are also produced with some radiation problems [19]. All of the above designs have semi-open structures, which means they have some power loss which prevents radiation at the broadside but the radiation they emit can be regulated to meet the requirements of a variety of applications. The term "open stop band (OSB) phenomenon" is used to describe this occurrence, which demonstrates how the internal resonance of LWAs equipped with dielectric gratings inhibits emission in the precise direction of the broadside frequency [20], [21]. Another factor contributing to the complexity of the process is the wide variety of dielectric gratings used in the fabrication of these LWAs [22, 23]. Not much work has been done on frequency-steered antenna designs at mm-wave frequencies for health monitoring applications based on DIL antenna. This is likely because the operating frequencies of commercially available electronic components are limited. The authors are aware of this, but the scope is relatively limited. Recent publications [24] show basic research on the frequency scanning characteristics of LWA based on DIL.

In this chapter, we present a bidirectional LWA with a wide beam scanning range from 50 GHz to 65 GHz that can be frequency-scanned, has no stopband and is easy to build for applications like remote vital sign monitoring. The required antenna radiated power for RVSM is calculated through broadside in a typical scenario where the target is sitting on a chair and is expected to move left, right, and centre, as shown in Fig. 6.1.1.The proposed antenna has a variable gain of 15.7 dBi to 19.79 dBi in the E-plane and a beam scanning range of 70.1^{o} (-42.4^{o} to +27.7^{o}) for non-contact detection of vital signs for two or more targets up to 1.5 m away. Because of this, the antenna can pick up vital signs from targets within the angular range without having to touch them directly.

The organisation of this chapter is outlined in the following paragraphs: In Section 6.2, we discuss the overall architecture of the DIL leaky wave antenna. The results of the measurements performed on the antennas are shown and discussed in Section 6.3. Section 6.4 covers vital signs monitoring measurements, and Section 6.5 summarises.

6.2 Leaky Wave Antenna Design Procedure

In the first place, we provide the analysis and design of the unit cell based on leaky wave theory. We then propose the feeding network and leaky wave antenna for a finite-size system.

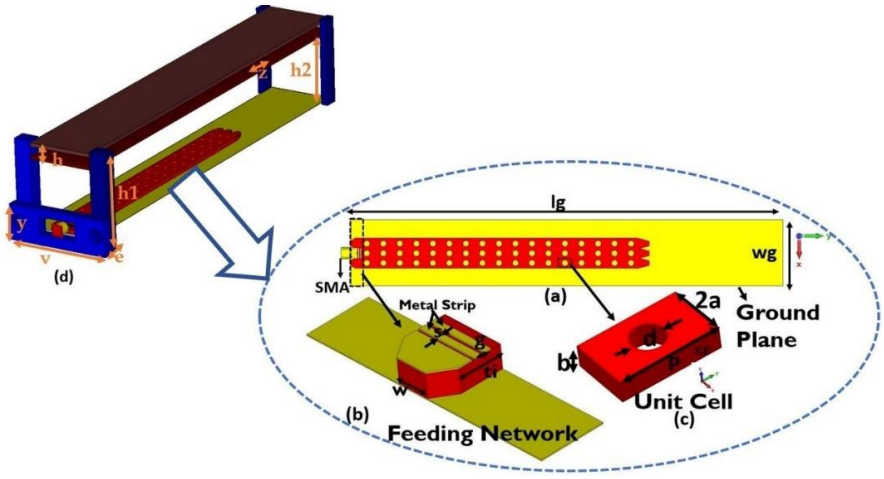


Fig. 6.2.1 Proposed representation of (a) DIL antenna, (b) feeding network (c) unit cell (d) Full complete structure.

Table 1. Dimensions Of Proposed Antenna

Parameters	Value (mm)	Parameters	Value (mm)
v	10.9	2a	1.6
z	4.8	b	0.6
h	0.9	p	2.7
h_1	6.3	d	1
h_2	5.13	w	0.6
y	4.03	i	0.9
e	2	g	0.09
lg	61.2	s	0.18
wg	7.1		

6.2.1 Dielectric Image Line Unit Cell Analysis And Design

Figure 6.2.1 depicts the proposed unit cell arrangement for the DIL antenna. It is defined by a set of parameter studies in which the width of the DIL is denoted by **2a**, the thickness of the substrate by ***b,*** the perturbation period by ***p,*** and the diameter of the hole ***d*** on the RT/duroid6010LM substrate ($\epsilon_r = 10.7, \tan\ \delta = 0.0023$). A substrate with a high enough dielectric constant is selected to maintain the fields in DIL and reduce the amount of radiation that escapes into the environment.

After selecting the substrate, the next step is to settle on the dimensions of the DIL in terms of its thickness and breadth. Since not all substrate thicknesses are commercially available, we first selected the suitable DIL thickness. After that, we used numerical equations such as $\boldsymbol{\alpha/\lambda_0}$ to determine whether single-mode or multimode exists in the DIL where $\boldsymbol{\lambda_0}$ is the free space wavelength as a function of frequency. This ratio is what determines field confinement as well as predicts single-mode or multimode in DIL. For an aspect ratio of 1:1 ($\boldsymbol{b = a}$), the formula for calculating the single-mode function which keeps the fields intact is shown as follows: [25]:

$$\frac{a}{\lambda_0} \approx \frac{0.32}{\sqrt{\varepsilon_r - 1}} \qquad (6.2-1)$$

where λ_0 represents the wavelength in free space at the operating frequency and ε_r represents the dielectric constant of Roger RT/duroid6010^{LM}.

The value of ***a*** is predicted to be ***0.54mm***, which is equivalent to the value of ***b*** that was determined by making use of the V-band centre frequency (57.5 GHz), the unit aspect ratio and eq. (6.2-1**).** In our design, the thickness of 0.62 mm available on the market is used, and the width (2a = 1.08 mm) is chosen accordingly. Table 1 lists the optimum parameter values for the unit cell structure. For the performance of high-gain and broadband antennas, leaky-wave theory, which can now be used to study the unit cell, provides some useful design recommendations. This assumption presupposes that the array is infinite, that its component elements all have similar patterns, and that it is uniformly excited in amplitude but not necessarily in phase. These three assumptions are necessary for the analysis. The analysis of large arrays is simplified by making the infinite array assumption and the similar pattern assumption for each element. The superposition equation of the Bloch-Floquet theory, which states that periodic structures can sustain an infinite number of spatial overtones, is simplified, and clarified by this.

$$\beta_n = \beta_0 + \frac{2n\pi}{p} \qquad (6.2-2)$$

Where the period is represented by $\boldsymbol{p}$, $\boldsymbol{n}$ is an integer, β_n *and* β_0 represent propagation constants of nt^{h}-order spatial harmonics for the fundamental unit cell respectively.

The space harmonic ***n = -1*** is fast and radiates in free space, whiles the fundamental spatial harmonics is a slow wave. It is generally accepted that fast waves are required for leakage to occur. In the current structure, fast spatial harmonics are generated by periodic perturbations of cylindrical holes along the axial line of the basic structure. The following formula for ***n = -1*** space harmonic is used to determine the main beam's direction in the proposed DIL LWA:

$$\theta = \sin^{-1}\left(\frac{\beta_0(\omega)}{k_0} - \frac{2\pi}{k_0 \times p}\right) \qquad (6.2-3)$$

where $\boldsymbol{\theta}$ represents the angle seen when viewed from the z-axis (Fig.6.1.2) and $\boldsymbol{K_o}$ represents the wavenumber in free space. Using the equation (6.2-3), we can get an approximation for the period $\boldsymbol{p}$ given the main beam direction and frequency (6.2-3). At 57.5 GHz, the broadside ($\theta = 0^o$) radiation of the main beam is what we are looking for. An investigation of the full-wave dispersion characteristics of the unit cell under discussion is carried out. The study was carried out with the assistance of a reliable tool that was first shown in [26]. This instrument has since been effectively used to research a variety of leaky wave antennas [27],[28].

To carry out a full-wave simulation of the unit cell depicted in Fig. 6.1.2(c) using CST Microwave Studio, the computational domain is configured as follows: periodic boundaries along the **x** and **y** axes, PEC on the axis that runs counterclockwise, and free space on the axis that runs clockwise **+*z*-**axis. There is a phase shift ξ from the negative to the positive boundaries because the leakage mode moves along the **+*y*** axis. This is a result of the leakage mode's tendency to propagate along the positive y-axis. The cell is excited by a very small dipole source located in the unit cell region. The phase constant $\boldsymbol{\beta}$ can be calculated by first locating the resonant frequency $\boldsymbol{f_r}$ at which the electric field component $\boldsymbol{E_y}$ is at its maximum value, and then working backwards from that value. According to the formula for calculating the phase constant, the phase shift $\boldsymbol{\xi}$ is required to find this maximum:

$$\beta = k_0(f_r)p \qquad (6.2-4)$$

The phase shift, represented by $\boldsymbol{\xi}$, is varied over the entire range from 0^o to 180^o. In the calculation of the attenuation constant $\boldsymbol{\alpha}$, a configuration consisting of two-unit cells is used. The highest values of the E-field components measured at two different locations

differ by one period $\boldsymbol{p}$. We established these maximum values at different locations. One method of determining the attenuation constant of the leaky mode is to calculate the exponential decline of the electric fields between these two sample sites.:

$$\alpha = -\frac{1}{p}\ln\frac{E_1}{E_0} \qquad (6.2-5)$$

where $\boldsymbol{E_1}$ is the electric field measured at the unit cell that is situated p units away from the first unit cell in the equation, and $\boldsymbol{E_0}$ is the electric field, measured in V/m at the unit cell that is receiving power from the source.

At the unit cell that the source is supplying, both fields are measured. By following the previously described procedure, it is feasible to determine the dimensions of the unit cell, which are shown in Fig. 6.2.1(c) and Table 1. Fig. 6.2.2. illustrates the wavenumber corresponding to the leaky mode. For an infinite DIL antenna fed in only one direction (where the value $\boldsymbol{\beta}$ = 0), broadband radiation is expected to be near 57.5 GHz. The primary beam travels from the rear quadrant, which operates at frequencies below 57.5 GHz, to the front quadrant (after 57.5 GHz). At 57.5 GHz, where $\boldsymbol{\beta}$ = 0, $\boldsymbol{\alpha}$ is greater than zero, which means that the open stopband has been eliminated. Because the finite-size model can never approach infinity, it is reasonable to anticipate that there will be a little variance in the computed parameters. It is essential to remember that the antenna length L should be $0.18\lambda_0/\alpha$[13] for a transmission power of 90%. This is the recommended value. In CST, periodic boundary conditions are set for the unit cell in the x and y directions. The unit cell is fed by a dipole in the domain, and E-field probes are placed at appropriate points (usually where the strength of the E-field is greatest). A phase shift is introduced across the x and y boundaries as the frequency of the maximum E-field shifts. This results in the propagation constant along the x or y-axis, the data collected is used in Matlab to plot the propagation constant shown in the graph in Fig. 6.2.2.

For the alpha calculations, two DIL unit cells with two probes exactly one period apart was used over the holes [28]. The decay of the electric field between the probes provides an estimate of alpha. Alpha is generally difficult to calculate because it is sensitive to the position of the probes, so many simulations were required before it became less sensitive. The air above the unit cell, which is important for the calculation, presents a challenge for this method. However, the advantage of this method is that it can apply to any unit cell geometry.

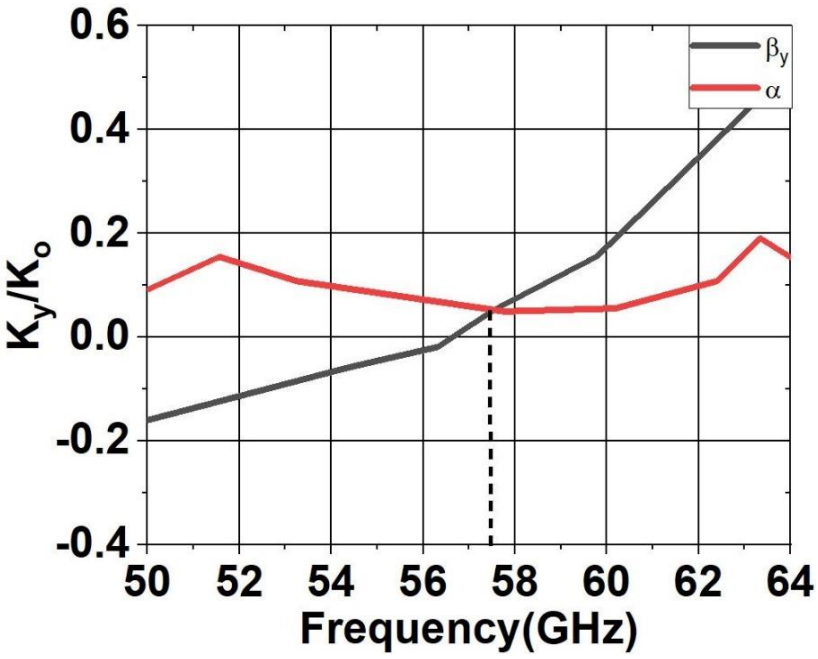


Fig.6.2.2. The computation of the DIL unit cell's leaky mode wavenumber.

6.2.2 Dielectric Image Line Feed Network

Fig. 6.2.1(b) is a representation of the suggested feeding network for the limited-size DIL. This network is made up of two additional substrate-truncated metal strips in addition to a planar substrate-truncated microstrip line-to-DIL. The length of the tapered microstrip line, denoted by ***ti*** as well as the width of the metal strip, denoted by ***s*** and the inter-element gap, denoted by ***g*** were modified in accordance with generalized empirical equations that were published in [23] for the substrate and frequency band that was chosen. Using these equations, we were able to determine the best possible values for

each of these parameters. The optimal measurements have been listed in Table 1, which can be found above.

6.2.3 Proposed Dielectric Image Line Antenna Design

Figure 6.2.1a provides a comprehensive illustration of the proposed leaky wave antenna. The DIL has 42 holes in the form of cylinders, each with a diameter of one meter, and is made up of 3x17 unit cells that are arranged along the x and y-axis. The total dimensions of the antenna, which are $Lg \times wg = 61.2 \times 7.1\ mm^2$, make it possible to achieve an acceptable radiation quality without pushing the boundaries of what is now possible with manufacturing technology. The gain and efficiency of the proposed antenna were improved by placing two dielectric plates of Taconic TLY-5 (a lossy substrate) above the DIL in a cavity height (h_1 = 6.34 mm and h_2 = 0.62 mm) between the ground plane and the first and second dielectric plates, respectively [see Fig. 6.2.1d]. This cavity height was determined by measuring the distance between the first and second dielectric plates. This is the first non-contact vital sign radar sensor leaky wave antenna that utilizes dielectric image lines, as far as we are aware.

6.3 Simulation Result

The results of a simulation performed in the CST microwave studio for the S_{11} parameters of the proposed dielectric image line LWA are shown in Fig. 6.3.1. This simulation included a modest optimization of the different hole sizes. The value of the S_{11} characteristic is less than -10 dB from 50 GHz to 68 GHz across the spectrum. Figure 6.3.2 shows that the realised gain varies as a function of the hole diameter used in the experiment. This can be interpreted in several ways. The simulated antenna maintains a gain of 19.9 dBi between 58 and 62 GHz, which is the highest possible value. A constant gain is obtained between 58 GHz and 63 GHz, which corresponds to the frequency range where the open stopband suppression occurs. The suppression of the open aperture is

demonstrated by the constant gain throughout this range. The hole diameter of ***d = 1 mm*** is the best option because, in comparison to other hole diameters, it offers a greater advantage in terms of compliance with the manufacturing limits discussed in Chapter 1.

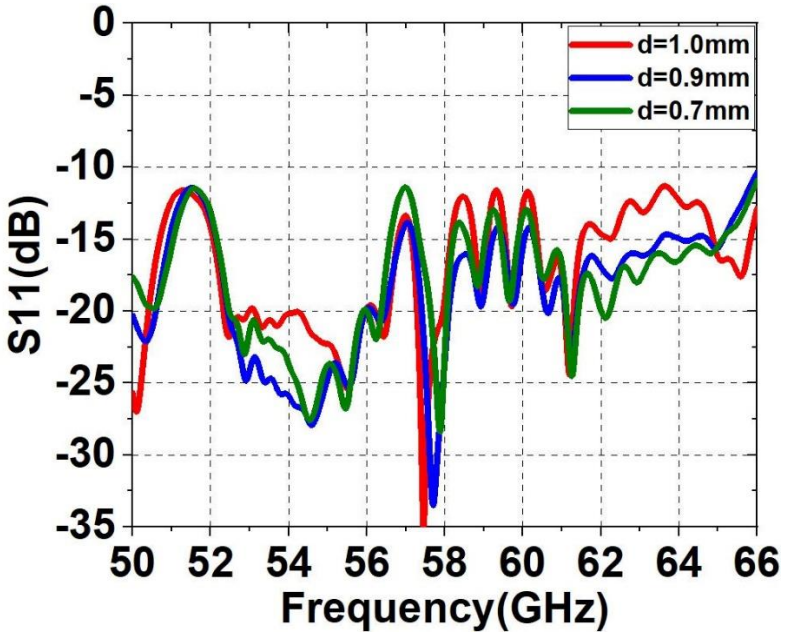


Fig.6.3.1. S_{11} Properties of DIL Antenna with a different diameter Hole size.

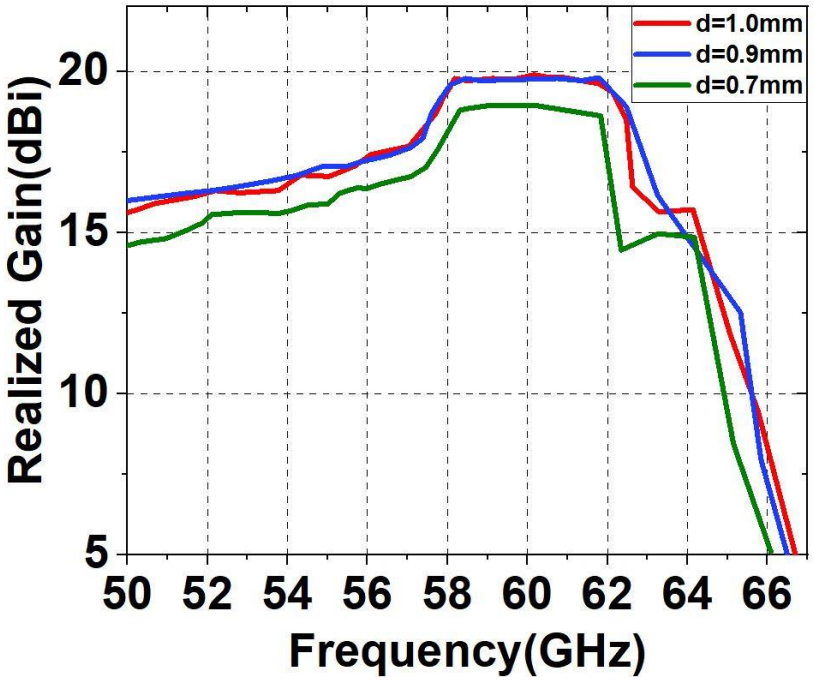
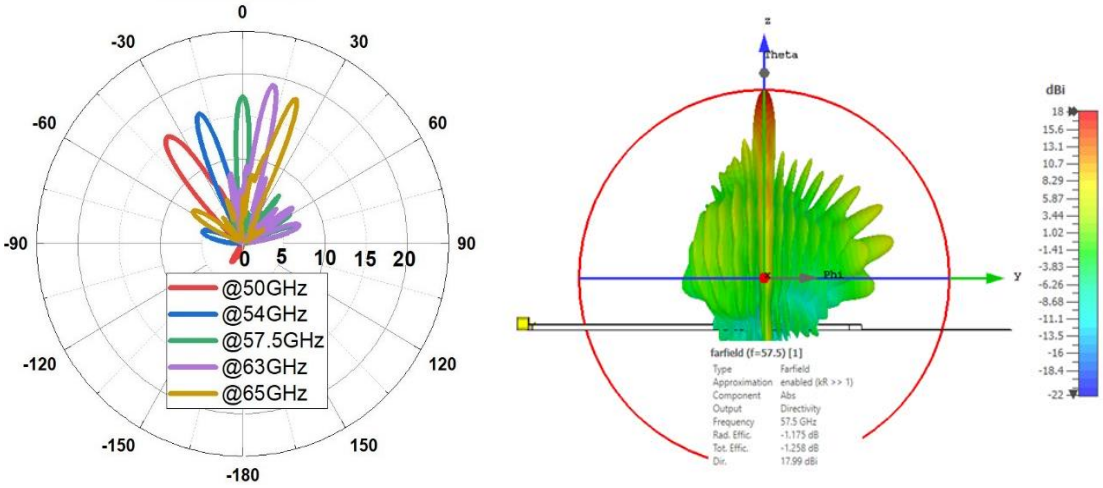


Fig.6.3.2. Realized antenna gain with different ***d***-hole size values.

The proposed antenna can simultaneously execute continuous frequency scanning in the yz plane, producing a fan beam, while maintaining its radiation characteristics. The main beam is aimed at the broadside frequency of 57.5 GHz, which coincides with the unit cell dispersion curve shown in Fig. 6.2.2 and overcomes the open stop band problem at the broadside. The two-dimensional and three-dimensional radiation patterns that were simulated can be shown in Fig. 6.3.3(a-b) in the E-plane.

The simulation results show that the main beam can be scanned through the broadside in an angular range of 70.19^{o} (from -42.49^{o} to 27.7^{o}) with only a 3 dB loss in signal strength. The result of this simulation is consistent with the predicted result. In all cases, the sidelobe level is less than -10 dB. The radiation starts from the rear at 50.8 GHz through the broadside radiation at 57.5 GHz, where the propagation constant is zero, and then proceeds toward the front and ends at 66 GHz. It is important to note that the forward and backward frequency sweeps of the beam are not identical. If the impedance matching can be improved to 68 GHz, the forward scan range can be increased while the position of the backward beam stays the same. This can make the beams symmetrical in both planes.



(a) (b)

Fig. 6.3.3 (a) 2-D radiation pattern at few frequencies in E-plane and (b) 3-D radiation main beam 57.5 GHz.

6.4 Measured Antenna Results And Discussion

The coaxial feed and antenna construction are both housed in a low-loss synthetic polymer enclosure. This makes it possible to install and test the antenna in a real-world setting. In addition, a small plastic spacer was used to keep the boards parallel to the surface of the base plate while maintaining the necessary height above the base plate to avoid obstructing the antenna's radiation. An image of the antenna prototype is provided in Fig. 6.4.1. This image shows the antenna both with and without additional dielectric layers. The proposed antenna with extra dielectric layers was chosen for RVSM because it has a high gain and does a good job of scanning the beam. Spacers of 6.34 mm and 0.62 mm were used to determine the resonance distance between the ground plane and the first and second dielectric layers respectively. The spacers and the material used to manufacture the antenna housing both have the same tolerance of ± 0.05%. The connection to the outside world is made with a 1.85 mm Female connector flanged launcher equipped with a GB 185 glass bead. Fabrication of the PCBs using traditional methods that were relatively inexpensive was used to produce the antenna layers. For remote vital signs monitoring (RVSM), two prototypes of identical multilayer leaky-wave antennas (LWAs) were made, as shown in Figure 6.4.2. (ant.A and ant. B).

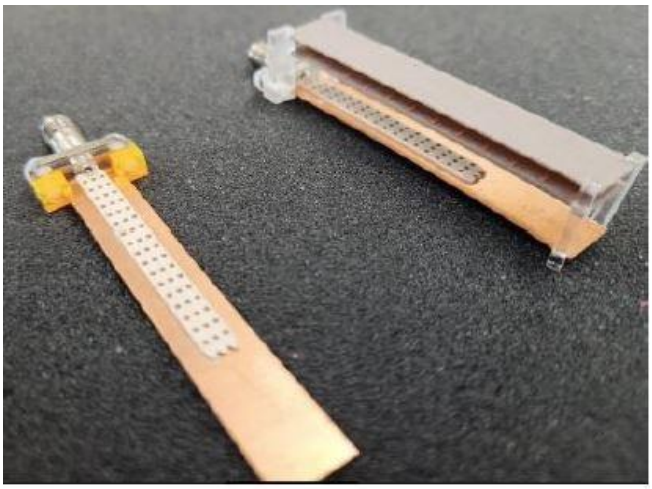
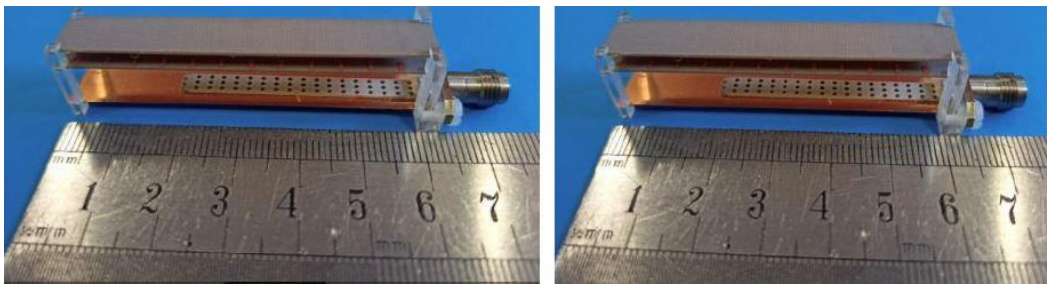


Fig. 6.4.1 Photo of DIL LWA with and without extra layers.



ant. A ant. B

Fig.6.4.2. Two identical LWA prototypes for RVSM application.

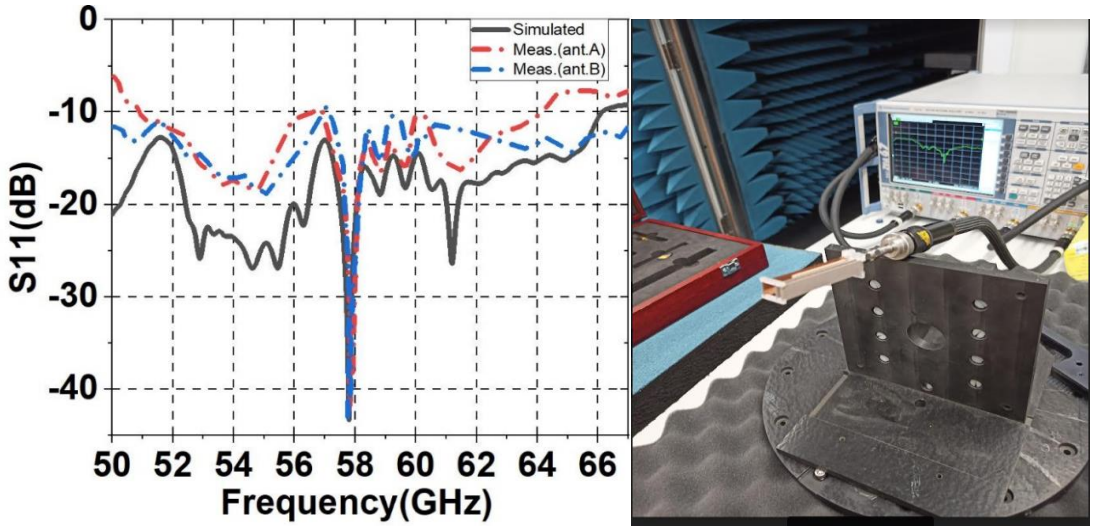
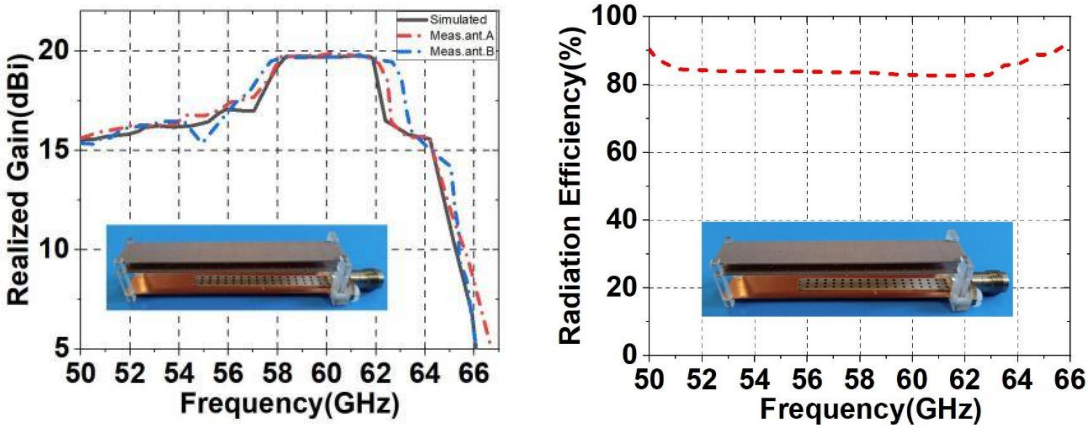


Fig. 6.4.3 S-parameters and photo of measured S_{11} DIL LWA.



(a) (b)

Fig. 6.4.4 LWA measurements (a) realized gain and (b) proposed antenna radiation efficiency.

The simulated and observed S_{11} responses of the proposed DIL LWA show an exceptionally high degree of consistency (Figure 6.4.3). Figure 6.4.4(a) also shows that the simulated gain response and the measured gain response are very close to each other.

The antenna radiation patterns were measured in an anchor chamber using a rotatable base connected to the computer for data acquisition. We calibrate the VNA to 0 dB insertion loss and then rotate the antenna 0°, 30° to 360° and took measurements for each rotation until we return to the starting point. The data is then collected and recorded to predict the signal strength.

The efficiency of the antenna was measured within the frequency range of interest. This was done by first applying some power to the antenna terminals and then determining the intensity of the emitted electromagnetic field in the environment. At 57.5 GHz, where the radiation at the broadside is achieved, this value is 83.8% (Fig. 6.4.4.b). The simulated results of the antenna are close to the expected values. The concept of bidirectional LWA was demonstrated when the main beam began scanning from behind at an angle of -42.49° through the broadside at 0° and continued with a forward scan up to 27.7°, which is consistent with all the analytical equations discussed in the previous sections. As can be seen in Figure 6.4.6, the cross-polar level maintains a satisfactory level in both E-plane and H-plane, with excellent agreement between the simulations and the measurements. Other frequencies may be predicted to have a similar cross-polar level. Table 2 summarises the two antennas' performance which will be used for the RVSM application in the next section. Co-polarisation and cross-polarisation are terms that describe the polarisation of electromagnetic waves. Polarisation means how the electric field of a wave is aligned in space. Co-polarisation is when the polarisation of the transmitting and receiving antennas (or devices) is the same. In the measurements, for example, co-polarisation was measured when both antennas are vertically polarised. Cross-polarisation was also measured when the polarization of the two antennas (or devices) was different or orthogonal. One of the antennas was vertically polarised and the other horizontally, and the cross polarisation was measured. We measured both the E-plane and the H-plane, which are perpendicular to each other and contain the propagation

direction of a wave. The reason for these measurements is to evaluate the antenna performance and compatibility with the RVSM application.

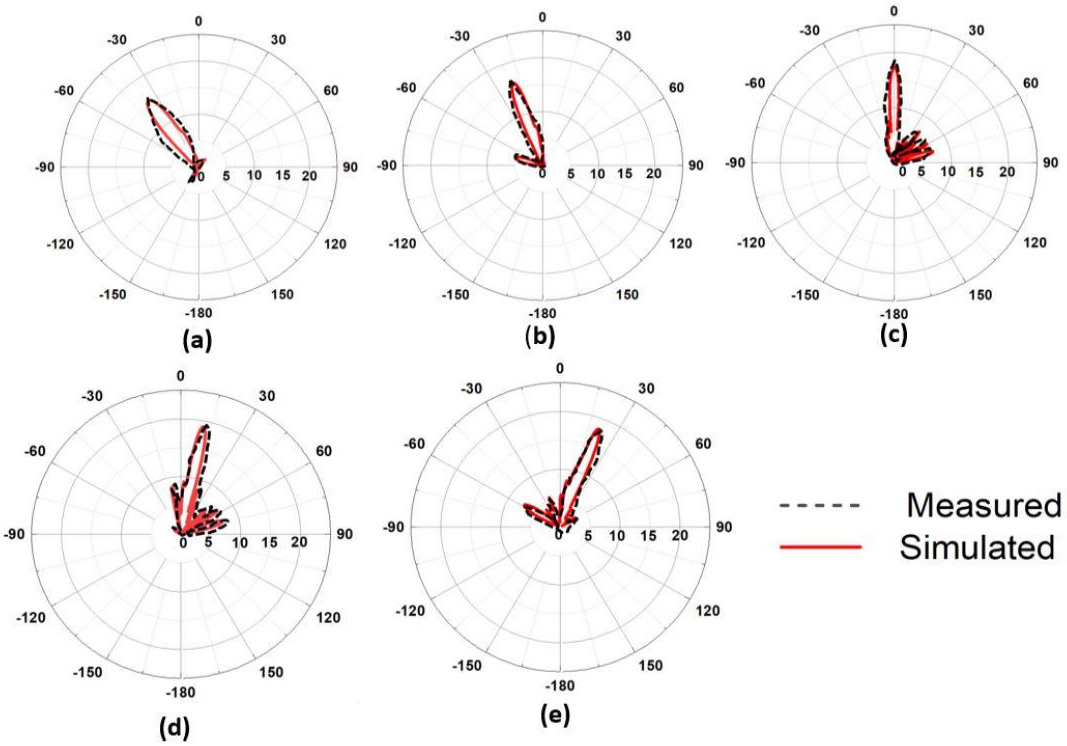


Fig. 6.4.5 Far-field radiation pattern measured and simulated antenna E-plane at (a) 50 GHz, (b) 54 GHz, (c) 57.5 GHz, (d) 63 GHz, and (e) 65 GHz.

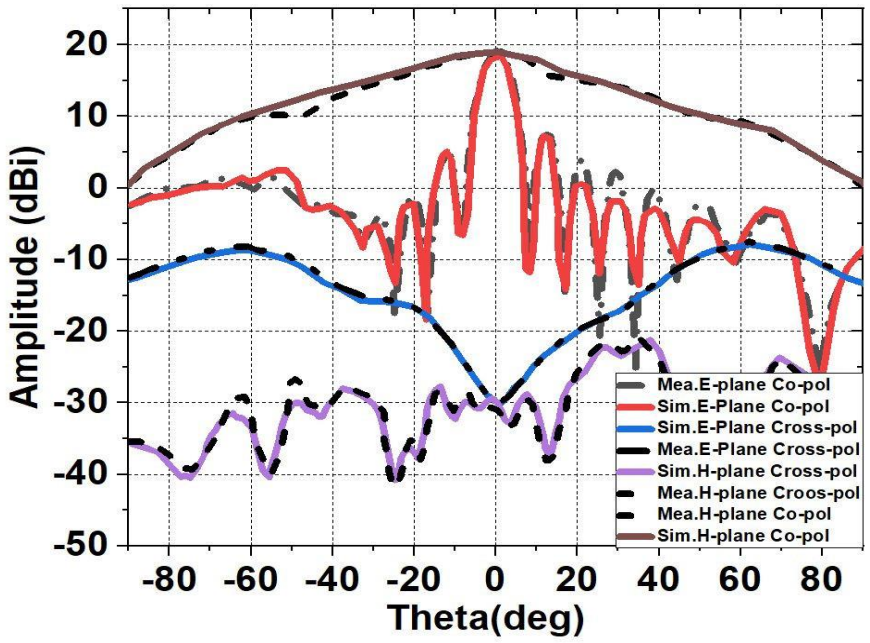


Fig. 6.4.6 Cross and co-pole measurement and simulation in the E-plane and H-plane of the proposed antenna at 57.5 GHz.

Table 2. Measured Antennas' Performances.

Parameters	Ant. A	Ant. B	Simulated
BW ($S_{11} < -10\,dB$)	50 - 64 GHz	50 - 66 GHz	50 - 67 GHz
Max. Gain (dBi)	19.7 @63 GHz	19.8 @ 63 GHz	18.5 @ 57.5 GHz
Scanning Range (50 - 65 GHz)	-42^o to +27^o	-43^o to $+26.3^o$	-47^o to $+23^o$
HPBW Variation	12^o - 5^o	14^o - 7^o	9^o - 6^o

The proposed LWA is compared in Table 3 with other published studies that are similar. Our proposed design demonstrates a suitable configuration that is capable of functioning as an LWA and possesses superior characteristics when operating at millimetre-wave frequencies. The majority of antennas described in the existing papers have a certain degree of difficulty to scan at the broadside due to the characteristics of the open stopband phenomenon. Our proposed DIL LWA does not have an open stopband, it also has a larger scanning range and a lower manufacturing cost. In [14] and [15], for instance, the results obtained from the simulated and the actual measured data did not agree 100%. These discrepancies were caused by an air gap that naturally occurred between the base plate and the dielectric layer during manufacture; consequently, broadside radiation was not taken into consideration. In [16] and [17] less gain was recorded due to the open stop band characteristics at the broadside.

Table 3. Comparison Of Proposed Antennas With Literature

	[14]	[15]	[16]	[17]	[18]	**This work**
Freq.(GHz)	57-63	97-103	8-12	50-85	9-14	**50-66**
Number of beams	Dual ($n=-1, n=-2$)	Single ($n=-1$)	Single ($n=-1$)	Single ($n=-1$)	Single ($n=-1$)	**Single** ($n=-1$)
Radiation at $\theta = 0^o$	No	No	Yes	Yes	Yes	**Yes**
Scanning range	-30^o to -20^o	-20^o to -2^o	-35^o to $+35^o$	-9^o to $+40^o$	-40^o to $+35^o$	-42.29^o **to** $+27.7^o$
Gain (dBi)	23	18	10.5 to 12.5	9.1 to 14.2	8 to 13	**15 to 19**
BW%	10	6	40	58	41.6	**25.6**
Length of antenna	$58\lambda_0$ @ 60 GHz	$5\lambda_0$ @ 100 GHz	NA	$8\lambda_0$ @ 60 GHz	$6\lambda_0$ @ 12 GHz	**11**λ_0 @ **57.5 GHz**

6.5 Measurement Of Remote Vital Signs With DIL LWA

This Section repeats the procedures for extracting vital signs using Doppler radar technology that was previously described in Chapter 4, Section 4.3, but with a different antenna. The baseband signal approximation used to extract vital signs is available in [29–30]. The setup for remote vital sign monitoring (RVSM) to detect a person's vital signs using Doppler radar technology with the proposed dielectric image line (DIL) leaky wave antenna (LWA) is shown in Fig. 6.5.1, where the transmitter and receiver ports VNA are connected to the scan antenna system for measurement. The human target is seated in front of the transmitter (Tx) and the receiver antennas (Rx) at five different distances: 0.5m, 0.7 m, 1m, 1.5 m, and 0.6 m, relating to five different angular positions: - 43º, - 25º, 0º, +13º, and +27º. As a consequence of this, a set of five S_{21} phase data, also known as the demodulated Doppler signal in the time domain (TD), are obtained at corresponding frequencies: 50 GHz, 54 GHz, 57.5 GHz, 63 GHz, and 65 GHz at each appropriate angular position.



Fig. 6.5.1 Setup for RVSM experiment.

To extract the vital signs, the signal coming from the VNA was first passed through a bandstop filter which is an 8^{th}-order Butterworth filter set for a minimum heart rate per detection of 61(1/Min) and also set at a maximum cutoff frequency of 98(1/Min). Then, for the breathing rate, the signal was sent through a bandpass filter which is 10^{th}-order Butterworth with a predictable breathing rate per minute range of 10 GHz – 41 GHz.Following the completion of the data analysis, the filters were rearranged into the sequence that generated the most precise results [31]. After the data analysis was complete, a fast Fourier transform (DFFT) was discretely utilized to ascertain both the heart rate and the respiration rate over the course of a few seconds. The thresholds were determined by taking the average of the highest and lowest heart and breathing rates recorded during the testing. These results are shown in Fig. 6.5.2 through 6.5.6. It is important to point out that the S_{21} phases obtained in this experiment represent the raw data.

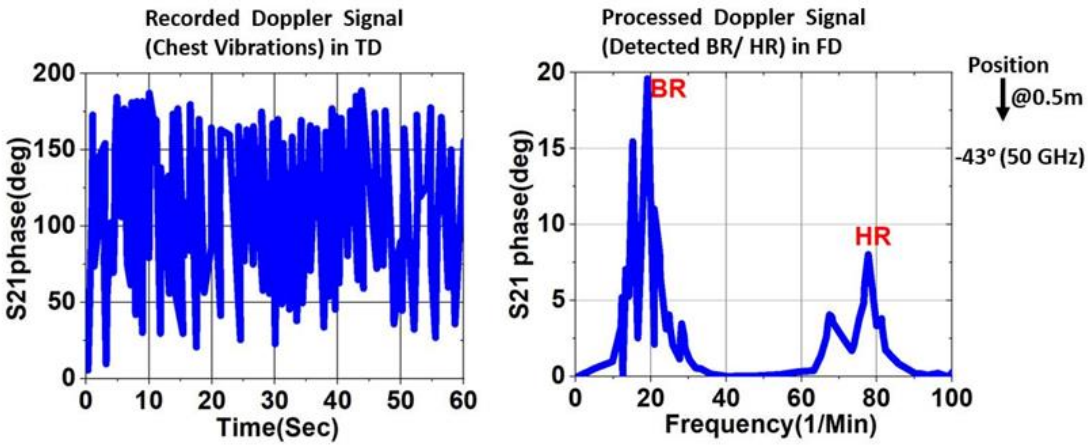


Fig. 6.5.2 Measured RVSM from **0.5 m** distance at 50 GHz (LWA main beam at - 43° with 6° HPBW).

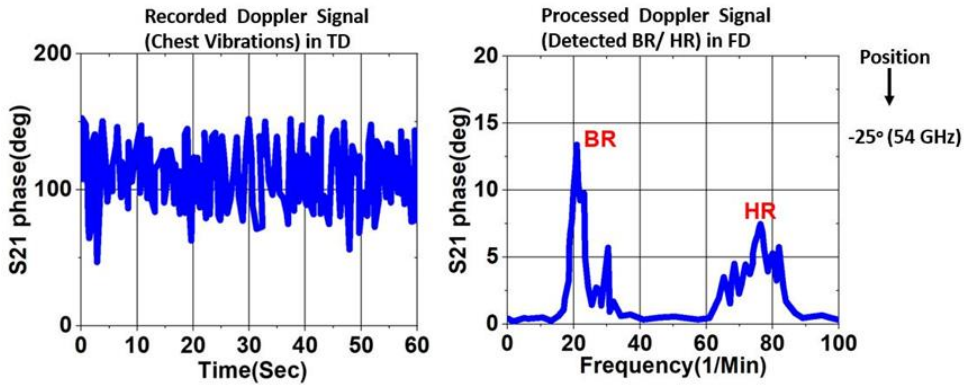


Fig. 6.5.3 Measured RVSM from **0.7 m** distance at 54 GHz (LWA main beam at **-25**° with 8° HPBW).

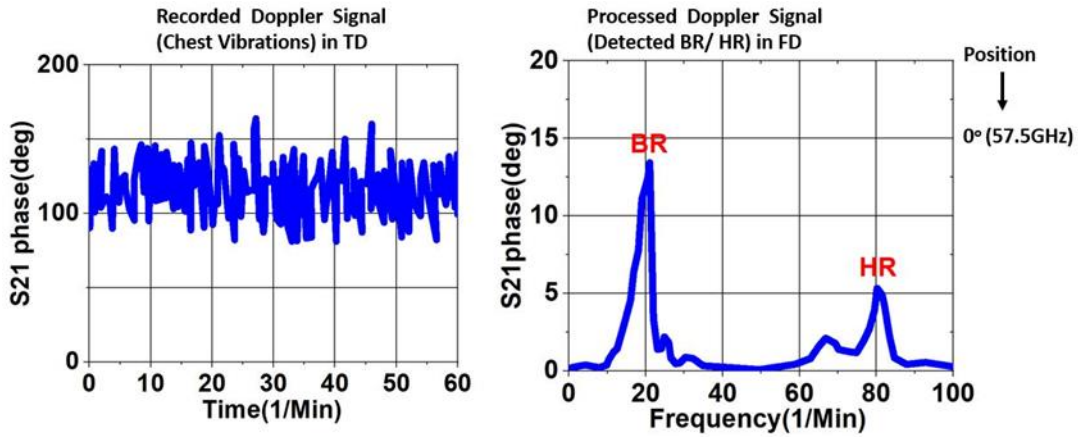


Fig. 6.5.4 Measured RVSM from **1 m** distance at t 57.5 GHz (LWA main beam at **0**◦ with 11° HPBW.

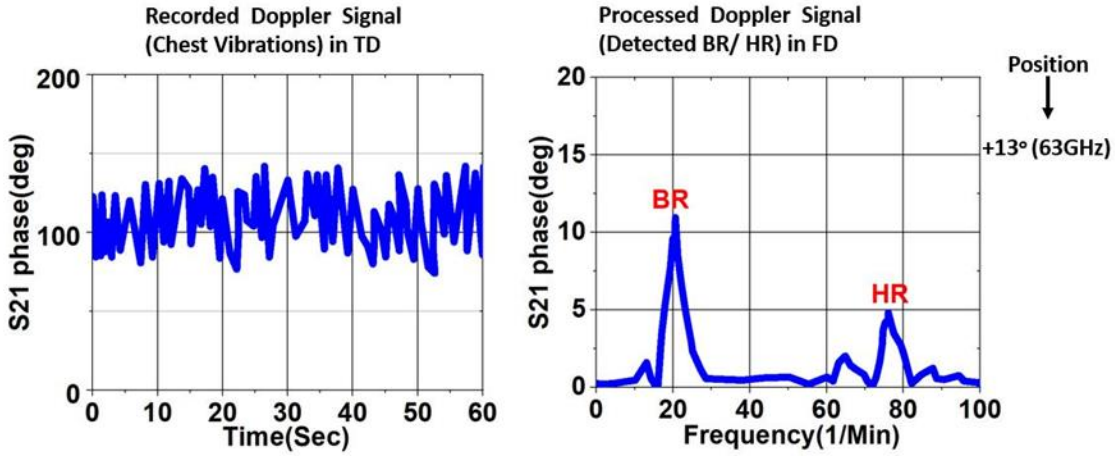


Fig. 6.5.5 Measured RVSM from a **1.5** m distance at 63 GHz (LWA main beam at **13**◦ with 8◦ HPBW).

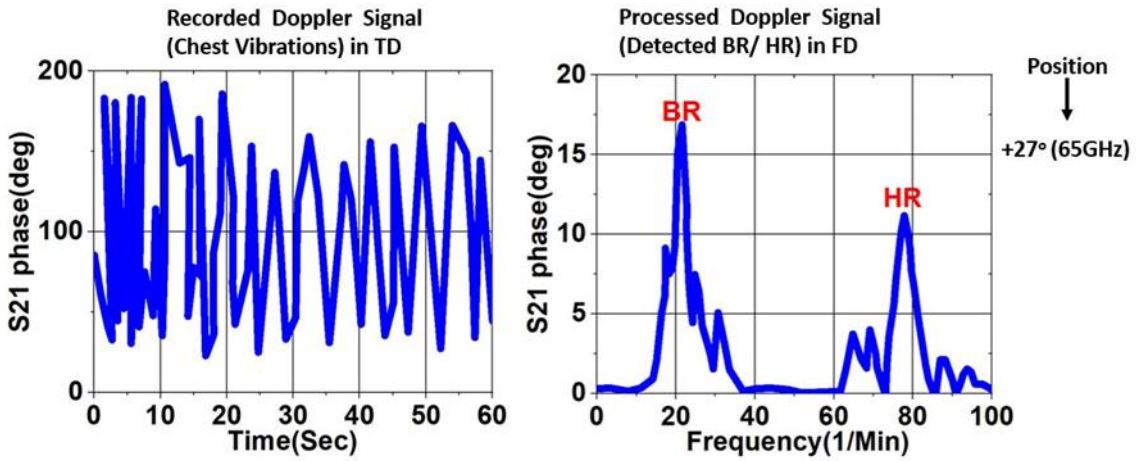


Fig. 6.5.6 Measured RVSM from **0.6 m** distance at 65 GHz (LWA main beam at **+27°** with 5° HPBW).

Table 4. Measured BR And HR At Various Distances And Positions

50GHz (-43°)	54GHz (-25°)	57.5GHz (0°)	63GHz (+13°)	65GHz (+27°)	Manual counter BR Contact device HR		Max.-Min Error
BR-HR (1/Min) @0.5m	BR-HR (1/Min) @0.7 m	BR-HR (1/Min) @ 1 m	BR-HR (1/Min) @1.5 m	BR-HR (1/Min) @0.6 m	BR-HR (1/Min)	BR-HR (1/Min)	BR-HR (1/Min)
19-79	20-78	20-80	20-79	19-74	19-20 (Avg.20)	78-81 (avg.79.5)	5% - 1.9%

The plots on the left side and the right side of each plot correspond, respectively, to the Doppler signal that was recorded in the time domain (TD) and the related processed signal that was recorded in the frequency domain (FD). The first measured peak at approximately 19 -20 (1/Min) in each plot of processed data represents the predicted amplitude of the respiratory rate signal (BR), whereas the projected amplitude of the heart rate (HR) signal is represented by the second peak, which occurs at a frequency of approximately 79 – 80 (1/min). The same amount of time was used to extract the two peaks. At lower-angle recording sites, the amplitudes of the recorded BR and HR signals were both sufficiently greater than the levels of noise that were produced. This was relevant information for both the BR and HR signals. Given that the beam centre of the

antenna radiation at 57.5 GHz is approximately 0^o, these findings validate what was hypothesized to be the case [see Fig. 6.4.5(c) and Fig. 6.4.6].

For high-frequency signals, measurements with wider angles result in the recording of the Doppler signal with the maximum amplitude compared to the background noise level. This is shown by Figures 6.5.2–6.5.6, which demonstrate this phenomenon. This is especially the case at 65 GHz for the little peak of the heart rate (HR), which is more vulnerable to noise entrapment than the larger peaks. Table 4 displays the findings of all of the measurements that were taken for BR and HR on a single target from a variety of various angles and distances. The proposed approach was validated by using a conventional blood pressure monitor [see Fig. 6.5.7] to measure the HR of the same individual. The non-contact radar approach is consistent with the majority of the results obtained with the traditional device. It can be concluded that the proposed antenna can detect the vital signs of a single target or multiple targets over an angular range of -43^o to -27^o up to 1.5 m, which corresponds to 70^o [see Fig. 6.1.1], when scanning the operating frequency from 50 GHz to 65 GHz.

It is possible to use this antenna for RVSM at distances over 2 metres due to the high gain it has and the sufficient amount of transmitting power it possesses. Inaccuracies in the VNA calibration, as well as cable tolerances for connections and wear, were found to be the cause of a slight error in the respiratory rate (BR), as well as the heart rate (HR).

One way to eliminate these errors is to use multiple transceivers with MIMO signal processing. This can open up these devices to a variety of new applications, such as monitoring people who are constantly moving, as they are currently only suitable for applications where the person is almost stationary. In addition, advanced signal processing techniques such as adaptive filtering can improve the accuracy of these devices and even remove unwanted motion artefacts.

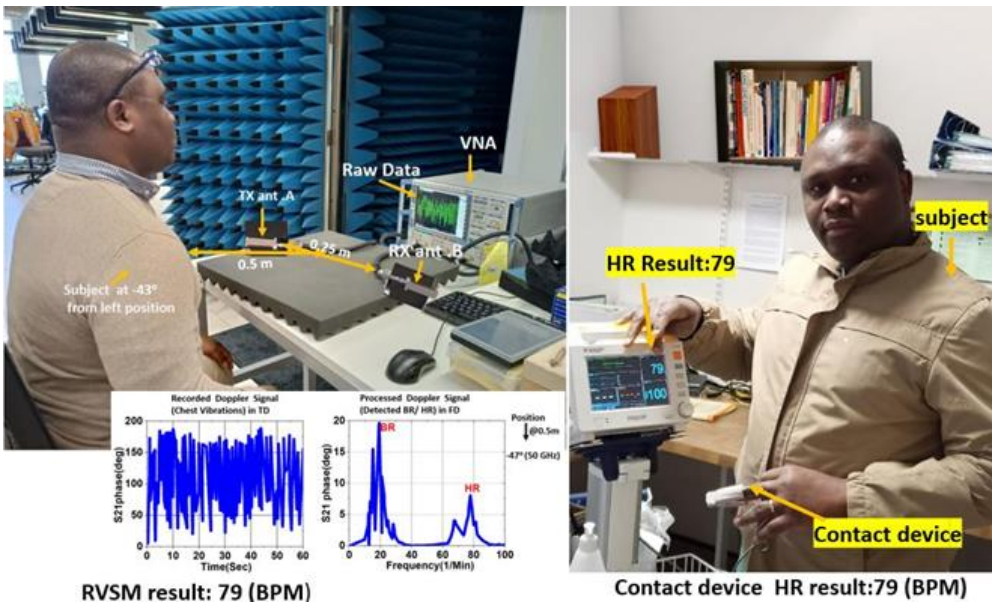


Fig. 6.5.7 Validation of measured heart rate data vs conventional approach.

6.6 Antenna Performance Comparison

In this section, a comparison of the proposed four leaky wave antennas developed in Chapters 4, 5 and 6 is carried out. The four antennas under study are shown in Fig.6.6.1. Antennas (i) and (ii) were used in Chapter 4, while antennas (iii) and (iv) were used in Chapters 5 and 6 respectively.

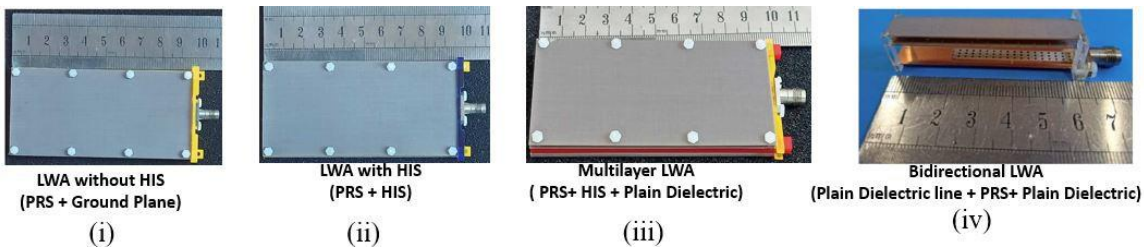


Fig. 6.6.1 Four different LWAs for RVSM.

To make an accurate comparison between the four different antenna designs, we examine the overall lateral dimensions of each antenna., their S_{11} return losses, directivity and beam scanning capabilities. It must mention here that antennas (i), (ii) and (ii) have the same dimensions with 50×15 PRS and HIS array elements printed on the same Roger 5880 dielectric $\varepsilon_r = 2.2$ and $tan\delta = 0.009$. In the case of the antenna (iv), The two upper layers are made of two different types of high-permeability dielectric substrates. To

maintain the integrity of the radiation and stop higher-order modes from being activated in the DIL channel, the bottom layer makes use of a low dielectric constant in conjunction with a low permittivity. To make an accurate comparison, the structures studied were designed to operate in the same frequency band and achieve the same level of maximum directivity.

The directivity of each of the four different designs that were investigated is depicted as a function of frequency in Figure 6.6.2. At a frequency of 62.5 GHz, the multilayer Fabry-Perot LWA antenna achieves a maximum directivity of 24 dBi while maintaining a 3 dB bandwidth of 25.6%. Due to its high gain, the multilayer LWA is better suited for RVSM applications over longer distances (4 m) than antennas (i), (ii), and (iv), which are well suited for RVSM applications over short distances (0.5 m – 2 m). This is the case because the multilayer LWA can cover longer distances.

Table 5 shows that the radiation bandwidth at the -10 dB is more than twice as large for the bidirectional LWA antenna compared to antennas (i), (ii), and (iii). Finally, figure 6.6.3 illustrates the different radiation patterns produced by each of the four antennas. As can be seen from the illustration, a noticeably reduced level of sidelobe is achieved with each of the proposed antennas, particularly for the E-plane pattern configurations. It can be extracted from the figure that the proposed bidirectional LWA outperforms the three Fabry Perot LWA antennas in terms of radiation at the broadside while keeping the same total profile ($\lambda/2$). In comparison to the other antennas, the bidirectional LWA has a large scan angle of 70° across the broadside. More specifically, the bidirectional LWA can remotely measure the vital signs of two or more subjects from 0.5 m up to 2 m. The results in Table 5 show that all four proposed LWAs have demonstrated good performance and can be used for RVSM applications.

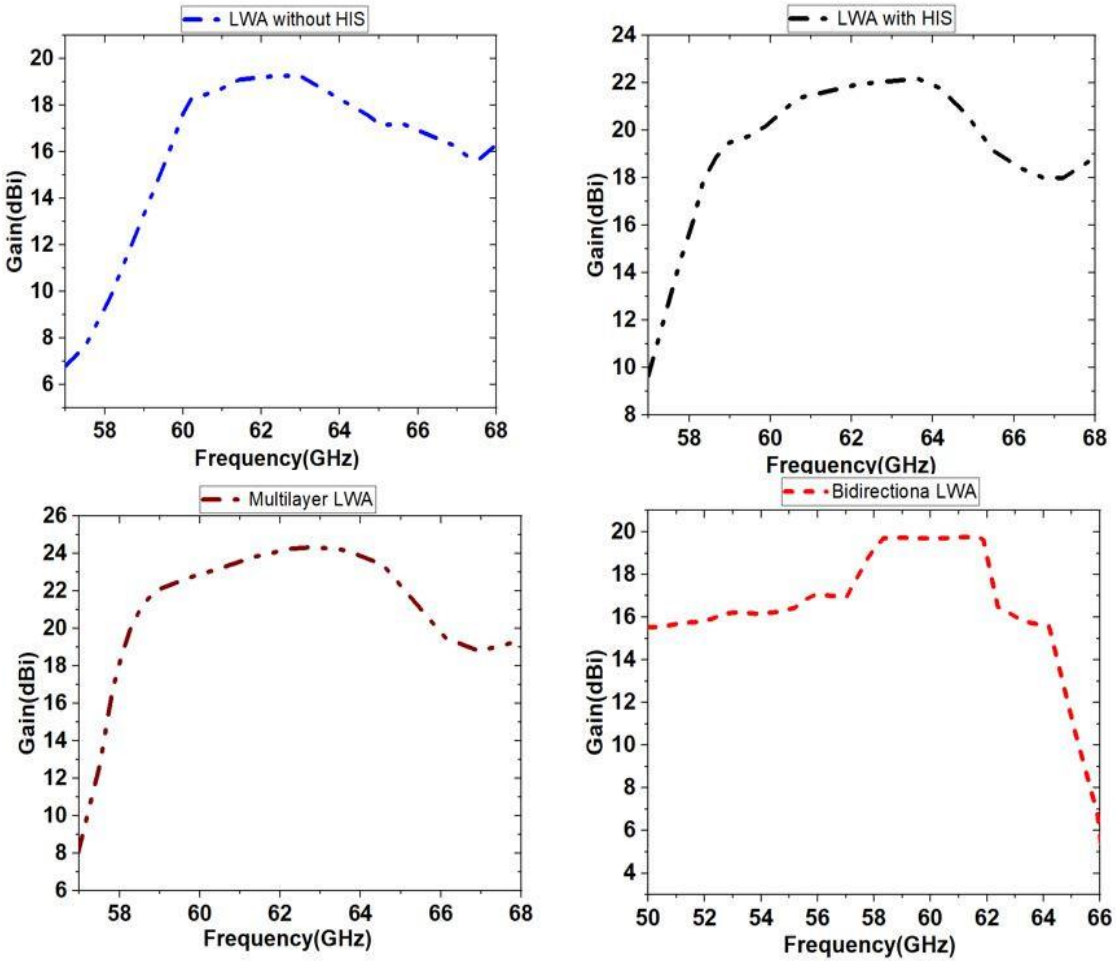


Fig.6.6.2. Measured Gain comparison of the four different LWAs.

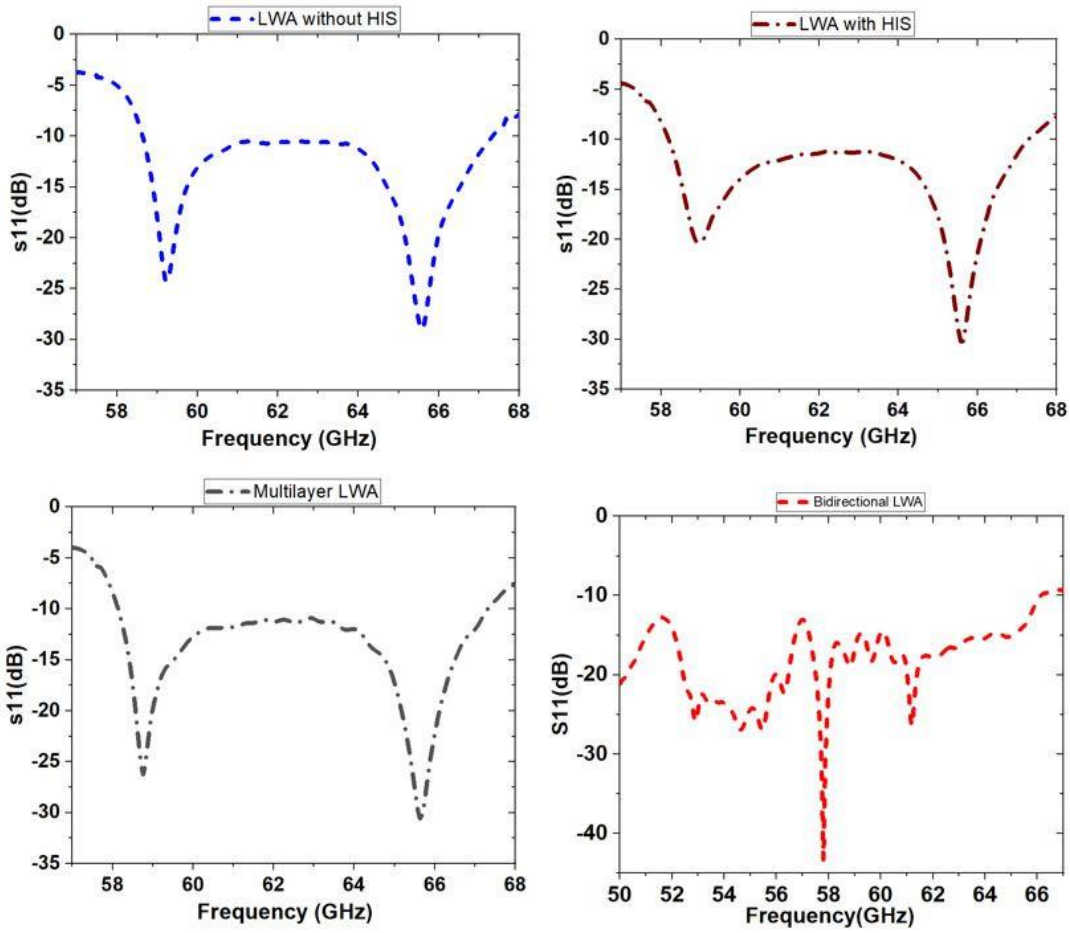


Fig.6.6.3. Measured S_{11} comparison of the four different LWAs.

Table 5. Four LWA Performance Comparison

Antenna Design Structure	Maximum Directivity (dBi)	Operating band (S_{11}< -10dB)	Beam scanning (θ)
PRS and Ground Plane	19.89	7.2	18°
PRS and HIS	22	8.50	30°
Multilayer	24	8.65	30°
Bidirectional	19 .45	16	70°

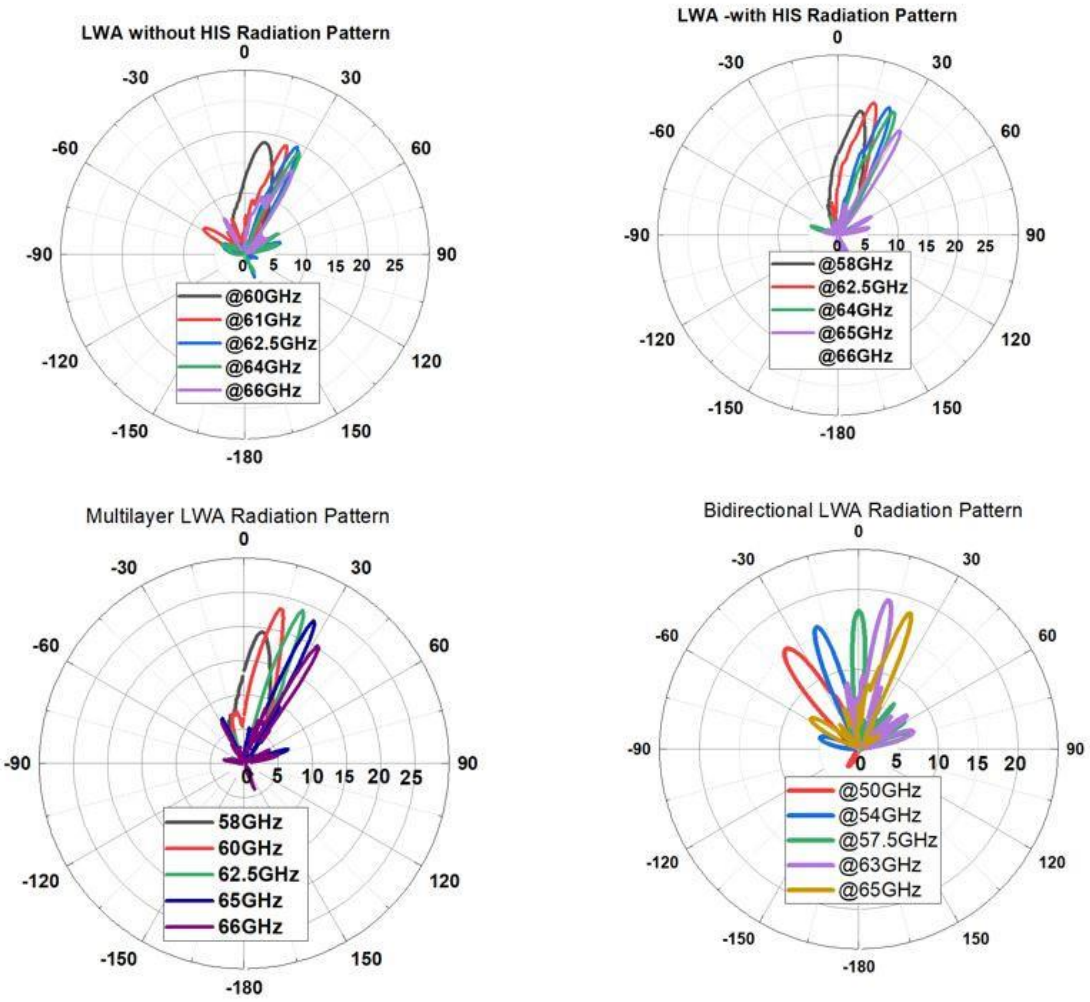


Fig. 6.6.4 Radiation pattern comparison of the four different LWAs.

6.7 Conclusions

This chapter presents a novel LWAs based on the technique known as dielectric image Line (DIL) conduction This design uses holes in DIL rather than a dielectric grating on the top or side, which allows the antenna to be easily fabricated and takes up less space. The impedance bandwidth of the antenna was designed to be quite wide (36% of the fast-wave range), and it also has a wide continuous beam scan of 70º. Other features of the DIL LWA include a high gain, a high efficiency, and the capability to scan through broadside with frequency. It has also been utilized for RVSM with multiple targets in scenarios in which the object is moving in different directions. The results of the

simulation and the measurements are consistent with one another. The RVSM measurement distance for the DIL LWA ranges from 0.5 m up to 1.5 m with good results when compared with conventional antennas. Finally, Fig. 6.6.2 compares the measurement results of all four leaky wave antennas used in Chapters 4, 5, and 6. The maximum gain is above 19 dBi for all antennas, but the multilayer LWA (Fig. 6.6.1(iii)) outperforms all other antennas with a gain of 24 dBi, which can be used for long-range RVSM. It is obvious that the bidirectional LWA has a larger beam sweep of 70^{o} and is suitable for remote monitoring of single or multiple target vital signs.

References

[1] D. Obeid, G. Zaharia, S. Sadek and G. El Zein, "Microwave Doppler radar for heartbeat detection vs electrocardiogram", *Microw. Opt. Technol. Lett*., vol. 54, no. 11, pp. 2610-2617, Nov. 2012.

[2] A. D. Droitcour et al., "Non-contact respiratory rate measurement validation for hospitalized patients," in Proc. 31st Annu. Int. Conf. *IEEE Eng. Med. Biol. Soc. Eng. Future Biomed*., pp. 4812-4815, 2009.

[3] M. S. Rabbani and H. Ghafouri-Shiraz, "Ultra-wide patch antenna array design at 60GHz band for remote vital sign monitoring with Doppler radar principle," *J. Infrared, Millimeter, Terahertz Waves*, vol. 38, no. 5, pp. 548 – 566, 2017.

[4] M. Villarroel et al., "Continuous non-contact vital sign monitoring in neonatal intensive care unit", *Healthcare Technol. Lett.*, vol. 1, no. 3, pp. 87-91, 2014.

[5] M. S. Rabbani and H. Ghafouri-Shiraz, "Accurate remote vital sign monitoring with 10 GHz ultra-wide patch antenna array," *AEU Int. J. Electron. Commun*., vol. 77, pp. 36-42, Jul. 2017.

[6] S. Suzuki, T. Matsui, M. Kagawa, T. Asao and K. Kotani, "An approach to a non-contact vital sign monitoring using dual-frequency microwave radars for elderly care", *J. Biomed. Sci. Eng.*, vol. 6, no. 7, pp. 704, 2013.

[7] Z. Yang, P. H. Pathak, Y. Zeng, X. Liran, and P. Mohapatra, "Vital sign and sleep monitoring using millimetre wave," *ACM Trans. Sensor Network*., vol. 13, no. 2, p. 14, Jun. 2017.

[8] M. S. Rabbani and H. Ghafouri-Shiraz, "Frequency selective surface antenna for remote vital sign monitoring with ultra-wideband doppler radar," *Microw. Opt. Technol. Lett.*, vol. 59, no. 4, pp. 818-823, 2017.

[9] C. Gu, "Short-range noncontact sensors for healthcare and other emerging applications: A review", *Sensors*, vol. 16, no. 8, pp. 1169, Jul. 2016.

[10] C. Li, V. M. Lubecke, O. Boric-Lubecke and J. Lin, "A review on recent advances in Doppler radar sensors for noncontact healthcare monitoring", *IEEE Trans. Microw. Theory Techn*., vol. 61, no. 5, pp. 2046-2060, May 2013.

[11] M. S. Rabbani, J. Churm, and A. P. Feresidis, "Fabry-Perot beam scanning antenna for remote vital sign detection at 60GHz," *IEEE Trans. Antennas Propag*., vol. 69, no. 6, pp. 3115-3124, Jun. 2021.

[12] A. Agarwal, R, A. Dwivedi, A. Sharma, "Leaky wave antenna for millimeter-wave utilization". *J. Phys. Conf.* Ser. 1921, 012026. Sep. 2021.

[13] D. R. Jackson and A. A. Oliner, "Leaky-wave antennas," in Modern Antenna Handbook. Hoboken, NJ, USA: Wiley, 2007.

[14] Z. L. Ma, K. B. Ng, C. H. Chan, and L. J. Jiang, "A novel supercell-based dielectric grating dual-beam leaky-wave antenna for 60-GHz applications," *IEEE Trans. Antennas Propag*., vol. 64, no. 12, pp. 5521–5526, Dec. 2016.

[15] A. Zandieh, A. S. Abdellatif, A. Taeb, and S. Safavi-Naeini, “Low-cost and high-efficiency antenna for millimetre-wave frequency scanning applications,” *IEEE Antennas Wireless Propag*. Lett., vol. 12, pp. 116–119, 2013.

[16] A. S. Al-Zoubi, A. A. Kishk, and A. W. Glisson, “Aperture coupled rectangular dielectric resonator antenna array fed by dielectric image guide,” *IEEE Trans. Antennas Propag.,* vol. 57, no. 8, pp. 2252–2259, Aug. 2009.

[17] X. Bai, S. W. Qu, K. B. Ng, and C. H. Chan, “Sinusoidally modulated leaky-wave antenna for millimetre-wave application,” *IEEE Trans. Antennas Propag.,* vol. 64, no. 3, pp. 849–855, Mar. 2016.

[18] A. Mallahzadeh and S. Mohammad-Ali-Nezhad, “Periodic collinear slotted leaky-wave antenna with open stopband elimination,” *IEEE Trans. Antennas Propag*., vol. 63, no. 12, pp. 5512–5521, Dec. 2015.

[19] Y. Torabi, G. Dadashzadeh, A. Lalbakhsh, and H. Oraizi, "High-gain and low-profile dielectric-image-line leaky-wave-antenna for wide-angle beam scanning at sub-THz frequencies," *Opt. Laser Technol.,* vol. 150, Jun. 2022, Art. no. 107968.

[20] X. Huang, Y. Lai, Z.H. Hang, H. Zheng & C.T Chan, “Dirac cones induced by accidental degeneracy in photonic crystals and zero-refractive-index materials”. *Nat. Matter.* **10**, 582–586. Sep. 2011.

[21] P. Moitra, et al., “Realization of an all-dielectric zero-index optical metamaterial”. *Nat. Photonics* **7**, 791–795, 2013.

[22] F. K. Schwering and S. T. Peng, “Design of Dielectric Grating Antennas for Millimeter-Wave Applications”. *IEEE Trans. Microw. Theory Tech*., 31, 199–209. Fab. 1983.

[23] C. S. Prasad, A. Biswas, “Dielectric Image Line-Based Leaky-Wave Antenna for Wide Range of Beam Scanning Through Broadside”..*IEEE Trans. Antennas Propag*., 65, 4311–4315. Sep. 2017.

[24] S. Mingle, D. Kampouridou, and A. Feresidis, “Beam-Scanning Leaky-Wave Antenna Based on Dielectric Image-Line for MillimetreWave Applications,” in 2021 51st *European Microwave Conference (EuMC)*, 2022, pp. 261–264.

[25] P. Bhartia and I. J. Bahl, *Millimeter Wave Engineering and Applications*.New York, NY, USA: Wiley, 1984.

[26] T. Kokkinos, C. D. Sarris, and G. V. Eleftheriades, "Periodic FDTD analysis of leaky-wave structures and applications to the analysis of negative-refractive-index leaky-wave antennas," IEEE Trans. Microw. Theory Techn., vol. 54, no. 4, pp. 1619-1630, Jun. 2006.

[27] J. R. Kelly, T. Kokkinos, and A. P. Feresidis, “Analysis and design of sub-wavelength resonant cavity type 2-D leaky-wave antennas,” *IEEE Transactions on Antennas and Propagation*, vol. 56, no. 9, 2008.

[28] D. Kampouridou and A. P. Feresidis, "Full-Wave Leaky-wave Analysis of 1-D Periodic Corrugated Metal Surface Antennas," *IEEE Antennas and Wireless Propagation Letters*, 1-4. Sep. 2021.

[29] C. Gu, C. Li, J. Lin, J. Long, J. Huangfu, and L. Ran, “Instrumentbased noncontact Doppler radar vital sign detection system using heterodyne digital quadrature demodulation architecture,” *IEEE Transactions on Instrumentation and Measurement*, vol. 59, no. 6, 2010.

[30] C. Li, and J. Lin, “Optimal carrier frequency of non-contact vital sign detectors”. *In Radio and Wireless Symposium*.IEEE.pp. 281-284. IEEE. Jan.2007.

[31] M. S. Rabbani, "Microstrip antenna design with improved fabrication tolerance for remote vital signs monitoring and WLAN/WPAN applications at mm-Wave and THz frequencies," PhD dissertation, Dept. Electron. Electr. Syst. Eng., Univ. Birmingham, Birmingham, U.K., 2018.

Chapter 7: Conclusion And Future Prospectives

In this thesis, experiments have shown that, for RVSM applications, frequency scanning with LWA Doppler radar technology is a viable alternative to commercially available heart and respiratory rate monitors. High-gain leaky wave antennas (LWAs) are still the subject of intensive research today, as they are needed for various applications in imaging, sensing and communication systems. A frequency scanning study was conducted for the Doppler radar, considering different distances and angular positions between the radar and the object. It was found that the Doppler radar becomes more sensitive to heartbeat movements as the frequency increases, which has a positive effect on detection accuracy. The accuracy of the heart signal is significantly compromised above a certain frequency (66 GHz), due to harmonic and intermodulation interference. The connectors, cables, antennas, and VNA set this limit because the performance of these devices beyond 66 GHz was unreliable and noisy. It has been found that at specific frequencies (58-65 GHz), Doppler radar can measure heart rate with accuracy. It was also found that reliable heart rate monitoring was only possible up to 4 m, although in some cases good accuracy was achieved beyond 4 m. A power of only -20 dBm was sufficient for reliable monitoring, and this fact can be used to develop low-power devices, which is a very desirable commercial feature.

All tested frequencies (58-66 GHz) were found to be suitable for monitoring respiratory rate with Doppler radar. The radar system was sensitive enough to detect chest movements at lower and higher frequencies. Intermodulation and harmonic interference with heart rate had no effect at high frequencies (58-65 GHz) because the respiratory signals are dominant at those frequencies. The respiratory frequency could be detected even at a distance of 4 m and beyond with a power of -45 dBm.

The scope of this PhD dissertation was to research and propose a novel leaky wave antenna with enhanced frequency scanning capabilities, exhibiting wide-angle scanning within a reasonable frequency range, and with high gain and low losses for RVSM.

In Chapter 1, a novel Fabry-Perot-type leaky wave antenna and significantly improved bandwidth performance based on periodic metasurfaces for remote vital sign monitoring applications were discussed. Fabry-Perot type LWAs (FP) can be formed using various topologies based on single and multilayer periodic surfaces and metasurfaces. These topologies provide the frequency-scannable operation that is desired along with a high gain at millimetre-wave frequencies. The above structures were analyzed, and their performance was estimated using the theoretical approaches described in Chapter 2.

In Chapter 3, we established through simulations and tests that low-loss, high-impedance surfaces (HIS) and partially reflecting surfaces (PRS) work effectively at mm-wave frequencies. As a direct consequence of this, the phase and magnitude responses of the structures to reflected waves were fine-tuned with frequency. Simulation results have shown that the structure is capable of functioning as a low-loss structure. A prototype capable of operating at around 62.5 GHz has been constructed. A dipole antenna for excitation of the LWA has also been demonstrated in the proposed HIS-PRS structures. Based on the work presented in this chapter, further research has resulted in the development of two different LWAs for use in millimetre wave applications.

Leaky-wave antennas of the Fabry-Perot type for RVSM applications were introduced in Chapter 4. These antennas use PRS and HIS elements separated by air cavities of half a wavelength. Other different prototypes consisting of PRS and ground planes were built and evaluated, each using the same feeding methods. The concept of the FPC-type antenna was validated through simulations and measurements. Both antennas were designed with highly direct responses for RVSM applications in mind. As a result of the work that was done in this chapter, it has been possible to measure a person's breathing

and heart rate with accurate results at 2 m, and these data have been compared with those obtained from traditional contact devices with good agreement.

In Chapter 5, an improvement of the previous designs was made based on the Multi-layer FP antenna designs to address the narrow-band performance and gain enhancement that these antennas naturally possess but at the expense of raising the antenna profile. To improve bandwidth performance while maintaining a low antenna profile, a novel multilayer FP antenna design consisting of PRS-HIS arrays and a plain dielectric was presented. The plain dielectric was put on top of an optimized PRS to make an LWA antenna with multiple layers.

The proposed multilayer LWA design was then compared with four different FPC antennas in CST simulation to validate the design concept. It was found that the proposed design outperforms the other designs of the same profile in terms of gain and beam scanning. Based on the performance of the proposed multilayer LWA, two prototypes were fabricated and used for RVSM applications with good results.

Further comparisons of the proposed FP antenna with horns and other antennas were made based on research from the literature. It was found that a multilayer Fabry-Perot type LWA with a high gain of 24.3 dBi, radiation efficiency of 95.5%, and a frequency sweep of 30° performs better than the horn and previous antenna designs for RVSM at longer distances of up to 4 m with good results in a dynamic scenario.

Chapter 6 concludes with a report on bidirectional leaky wave antennas operating at millimetre wave frequencies. This work is novel because it is the first to be designed and implemented as a frequency-scannable leaky-wave antenna for RVSM based on a dielectric image line in the V-band (50 - 68 GHz). A highly professional fabrication technique has been applied, taking into account several design aspects, which makes this antenna different from the prototypes published in the literature at mm-wave frequencies. This novel antenna offers an interesting new solution for low-cost, high-gain planar

antennas at high frequencies. A prototype was fabricated and experimentally tested to validate the simulations.

The proposed antenna has a wide scan range of 70.19^{o} (-42.49^{o} to 27.7^{o}) across the broadside. This antenna also has an impedance bandwidth of 15 GHz (50-65 GHz), an optimum fast-wave gain of 15.5 dBi to 19.79 dBi, and a reasonable radiation efficiency of 83.8% at 57.5 GHz. Extensive remote vital sign monitoring (RVSM) experiments have been conducted with the proposed antenna DIL, which is consistent with conventional devices. It was demonstrated that by adjusting the operating frequency from 50 GHz to 65 GHz, the respiratory rate (BR) and heart rate (HR) of multiple targets can be measured with 95% accuracy within an angular range of 70°.

Future work on this research could explore alternative designs that provide greater beam scanning while making the antenna less susceptible to manufacturing defects. To compensate for tolerances in micromachining, high-precision spacers could be used to connect and seal the space between PRS and the ground plane. The multilayer LWA approach presented in this work can be used to realise single-source frequency scanning antennas with high gain. Another design that allows beam scanning in two planes—azimuth and elevation—could be a single new antenna or based on a combination of the antennas presented in this thesis. This could lead to a low-cost, high-gain antenna with little complexity to manufacture, as the structure is based on a micromachining process. Furthermore, future research may focus on tuning methods for these antenna types that are appropriate for THz frequencies. The research described in this thesis paves the way for the creation of a new class of THz antennas with low losses and radiation patterns that can be changed electronically when combined with an appropriate reconfiguration method. To control the radiation angle of the antenna at a fixed frequency, piezoelectric actuators could be integrated to move one of the surfaces and alter the resonance condition.

The limitations of this technology are the effects of unwanted movements (other than those of the chest, such as arm or leg movements) or the presence of people entering the laboratory during Doppler radar monitoring. This resulted in unexpected spikes and additional noise in the acquired signals. In some cases, several unwanted signals (from other people or unwanted movements of the person tested) are mixed with the desired signal. All this contributes to a significant increase in the error rate. One way to eliminate these errors is to use multiple transceivers with MIMO signal processing. This can open up these devices to a variety of new applications, such as monitoring people who are constantly moving. Currently, this can only work for applications where the subject is almost stationary and changes position after each measurement.

Another limitation is the difficulty in accurately measuring vital signs through clothing or other materials. Doppler radar signals can penetrate some fabrics and materials, but this can also result in false readings if the signal is reflected or absorbed by the material.

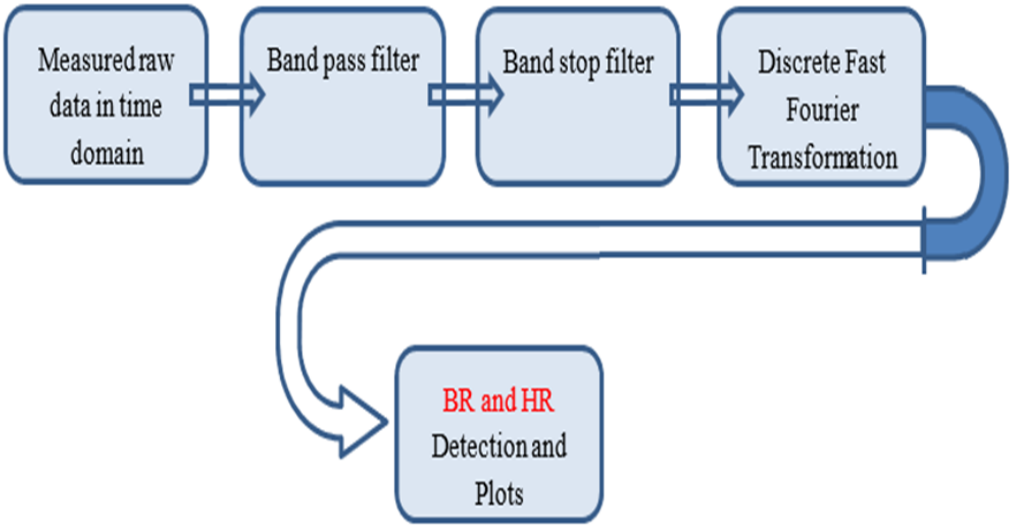
Furthermore, the distance between the person and the radar system can also impact the accuracy of the measurements. Doppler radar technology relies on the reflection of electromagnetic waves from the body, and the strength of the signal decreases as the distance between the person and the radar system increases. This can lead to reduced accuracy in measurements and the need for more sophisticated radar systems.

Areas for improvement in Doppler radar technology for remote vital sign monitoring include the development of more advanced signal processing algorithms to reduce the impact of movement artefacts and improve accuracy in measurements. Another area of improvement is the use of multiple radar systems to increase the coverage area and reduce the impact of distance on accuracy. Additionally, the integration of Doppler radar technology with other monitoring technologies such as cameras and sensors could help provide a more comprehensive picture of a person's health status.

Overall, the research presented in this thesis has been successful in addressing some of the key issues related to leaky wave antennas, especially at mm-wave frequencies for remote vital sign monitoring. This dissertation's findings have been presented at several international conferences, including the European Conference on Antennas and Propagation (EuCAP) and the European Microwave Conference (EuMC). Additionally, portions of this work in Chapter 6 have already been published in the IEEE Open Journal of Antennas and Propagation (OJAP), furthermore, Chapters 4 and 5 have also been published in the MPDI Sensor, Antennas and Propagation journal.

Appendix A: Matlab Programme for RVSM

The RVSM data is processed in Matlab by using the following main signal processing steps:



a. Matlab Code:

```
close all;
clear all;
clc;

f0=63.4*10^9; % used tone frequency
c=3*10^8;
l0=c/f0;        % wavelength
pi=3.1416;

file1=xlsread('VSM165.xls');  % measured RVSM data

                % Define the filters's cutoff frequencies based on
                % the expected BR and values (1/min)

fB1=10;                  % Expected min respiration rate/min
fB2=41;                  % Expected max respiration rate/min
fH1=61;                  % Expected min heart rate/min
fH2=98;                 % Expected max heart rate/min
f1=10;
f2=98;          % (f1 and f2 define the range of total expected frequencies

%%%%%%%%%%%%%%%       Time domain Plot           %%%%%%%%%%%

ST=60.18;            %in sec   60GHz experiment
ST=ST/60;       %  in Min
L=length(file1(1:1:end,2))-1;    % Total No. of samples (-1 when L is odd)



Fs=L/ST;                % sampling frequency
y1=0:ST/L:ST;
y2=file1(1:1:end,2);

figure(1)
subplot(311)
plot(y1.*60,y2,'-k','LineWidth',3)
title('Measured Raw Data', 'FontSize', 14);
xlabel('Time (sec)','FontSize', 12);
ylabel('S21 phase (degree)','FontSize', 12);
set(gca,'FontSize',12);
grid on
```

```
                %%      Band Pass Filter %%


NF=Fs/2;          % Nequest Frequency in min

[b1,a1]=butter(10,[f1/NF,f2/NF],'bandpass');
y2=filter(b1,a1,y2);

H1=freqz(b1,a1,floor(NF));
Wn=0:1/(NF-1):1;

figure(2)
subplot(211)
plot(Wn.*NF,abs(H1),'-k','LineWidth',3);
title('BPF Response','FontSize', 14)
xlabel('Frequency (1/min)','FontSize', 12);
ylabel('Magnitude','FontSize', 12);
set(gca,'FontSize',12);
grid on



                %%      Band Stop Filter   %%

 [b2,a2]=butter(10,[30/NF,65/NF],'stop');
 y2=filter(b2,a2,y2);

 H2=freqz(b2,a2,floor(NF));
 Wn=0:1/(NF-1):1;

 subplot(212)
 plot(Wn.*NF,abs(H2),'-k','LineWidth',3);
 title('BSF Response','FontSize', 14)
 xlabel('Frequency (1/min)','FontSize', 12);
 ylabel('Magnitude','FontSize', 12);
 set(gca,'FontSize',12);
 grid on

 figure(1)
 subplot(312)
 plot(y1.*60,y2,'-k','LineWidth',3)
```

```
title('Filtered Data','FontSize', 14);
xlabel('Time (sec)','FontSize', 12);
ylabel('S21 phase (deg.)','FontSize', 12);
set(gca,'FontSize',12);
grid on

figure(1)
subplot(312)
plot(y1.*60,y2,'-k','LineWidth',3)


title('Filtered Data','FontSize', 14);
xlabel('Time (sec)','FontSize', 12);
ylabel('S21 phase (deg.)','FontSize', 12);
set(gca,'FontSize',12);
grid on


                %% DFFT calculations  %%

f = Fs*(0:(L/2))/L;
Y = fft(y2);

P2 = abs(Y/L);
P1 = P2(1:round(L/2+0));  %% instead of 1 add 0 for for 20 sec datawhen
                          %every third sample is chosen

if length(P1)~=length(f) %% just to match the length of vetors "f" and "P1"
P1 = P2(1:round(L/2+1));
end

P1(2:end-1) = 2*P1(2:end-1);
P1=2*P1; % P1 is the magnitude to top half cycle of the wave( phase change)
         % total phase change due to the respiration is twice

fmax=max(f);
Lf=length(f);
gf=fmax/(Lf-1);              %   Freq interval(freq. bin)

B1=round(fB1/gf);            %% Breathing window start freq.
B2=round(fB2/gf);            %% Breathing window end freq.
H1=round(fH1/gf);            %% Heart window start at freq.
H2=round(fH2/gf);            %% Heart window end freq.
W1=round(f1/gf);             %% overall window start freq.
W2=round(f2/gf);             %% overall window end freq.
```

```
            %%%         Breathing Rate calculation      %%

[maxB, indxB]=max(P1(B1:B2,1));

BR=(indxB+B1-2)*gf;
fprintf('\nBreathing Rate =%f /min\n',round(BR));

meanB=mean(P1);
DPhB=maxB;                  %%  Delta Phase in Breathing
fprintf('\nPhase variation with Breathing =%f Deg.\n',DPhB);

%DxB=DPhB*l0/4/pi;           %% Chest movement (delta x)without
                            %intermodulation
%fprintf('\nChest movement with Breathing =%f mm\n\n\n',DxB*10^3);

            %%%         Heat Rate       %%

[maxH, indxH]=max(P1(H1:H2,1));



HR=(indxH+H1-2)*gf;
fprintf('\nHeart Rate =%f /min\n',round(HR));

meanH=mean(P1);
DPhH=maxH;                  %%  Delta Phase in Breathing
fprintf('\nPhase variation with Heart =%f Deg.\n',DPhH);

%DxH=DPhH*l0/4/pi;           %% Chest movement (delta x)without
                            %intermodulation
%fprintf('\nChest movement with Heart =%f mm\n\n\n',DxH*10^3);

figure(1)
subplot(313);
plot(f(1,W1:W2),P1(W1:W2,1),'-k','LineWidth',3)
title('Breath/Heart Rate Peaks','FontSize', 14);
xlabel('Frequency (1/Min)','FontSize', 12);
ylabel('S21 phase (deg)','FontSize', 12);
set(gca,'FontSize',12);
grid on

%%      End
```

A2. Results:

a.Extracted Data

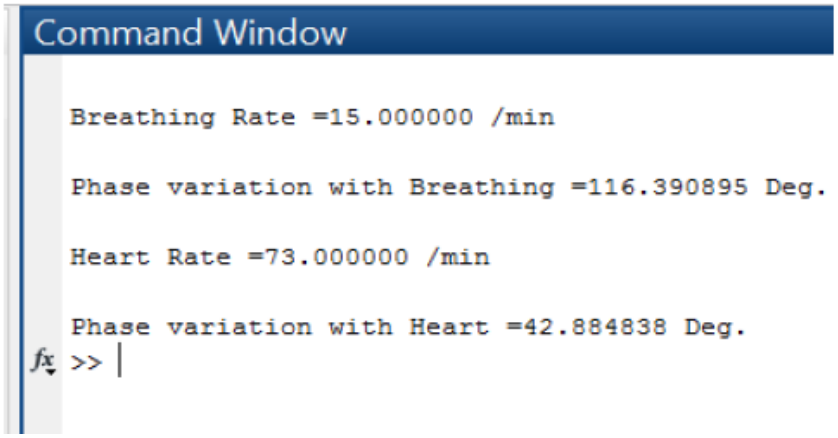
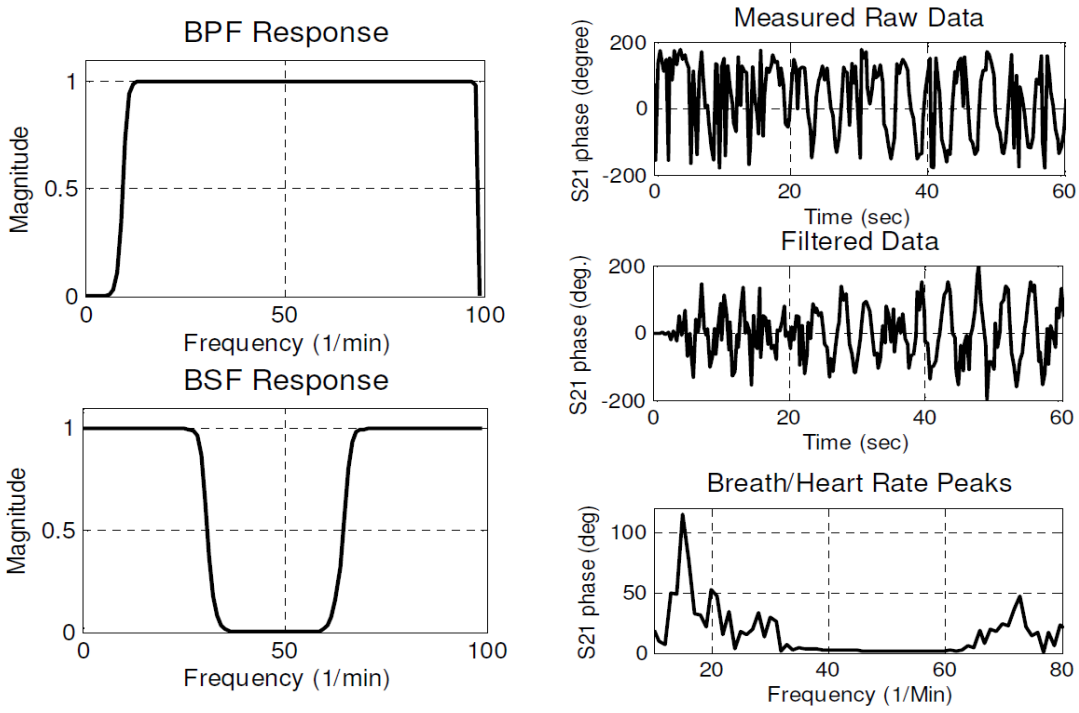


Fig. A1. Extracted data.

b. Results Plots:



(a) (b)

Fig. A2. Results Plots. (a) A bandpass filter (top) and band stop filter (bottom) responses, and (b) RVSM results